



HAL
open science

INVESTIGATION OF Ge SURFACE DIFFUSION AND SiGe NANOSTRUCTURES BY SPECTRO-MICROSCOPY TECHNIQUES

Giovanni Maria Vanacore

► **To cite this version:**

Giovanni Maria Vanacore. INVESTIGATION OF Ge SURFACE DIFFUSION AND SiGe NANOSTRUCTURES BY SPECTRO-MICROSCOPY TECHNIQUES. Materials Science [cond-mat.mtrl-sci]. Politecnico di Milano; Ecole Polytechnique X, 2011. English. NNT: . tel-00725427

HAL Id: tel-00725427

<https://pastel.hal.science/tel-00725427>

Submitted on 27 Aug 2012

HAL is a multi-disciplinary open access archive for the deposit and dissemination of scientific research documents, whether they are published or not. The documents may come from teaching and research institutions in France or abroad, or from public or private research centers.

L'archive ouverte pluridisciplinaire **HAL**, est destinée au dépôt et à la diffusion de documents scientifiques de niveau recherche, publiés ou non, émanant des établissements d'enseignement et de recherche français ou étrangers, des laboratoires publics ou privés.

POLITECNICO DI MILANO

Dipartimento di Fisica

Dottorato di Ricerca in Fisica

XXIII ciclo



**INVESTIGATION OF
Ge SURFACE DIFFUSION AND
SiGe NANOSTRUCTURES BY
SPECTRO-MICROSCOPY TECHNIQUES**

Relatore (Politecnico di Milano): Dr. A. TAGLIAFERRI

Relatore (École Polytechnique, Paris): Prof. H.-J. DROUHIN

Relatore (CEA-Saclay): Dr. N. BARRETT

Co-relatore (Politecnico di Milano): Dr. M. ZANI

Tutor e Coordinatore: Prof. F. CICCACCI

Tesi di Dottorato di:

Giovanni Maria VANACORE

Matr. 723937

Anno Accademico 2010-2011

To Milena and my family

There are two possible outcomes: if the result confirms the hypothesis, then you've made a measurement. If the result is contrary to the hypothesis, then you've made a discovery.

(Enrico Fermi)

Contents

Introduction	1
1 Basic concepts in hetero-epitaxial growth	4
1.1 Introduction	4
1.2 Modes of film growth	5
1.3 “Capillary model” of 3D island nucleation	8
1.4 Stability of a hetero-epitaxial system	10
1.5 Growth methods	11
1.6 Conclusions	12
Bibliography	13
2 Ge diffusion on a clean and C covered Si(001) surface	14
2.1 Introduction	14
2.2 Theory of Surface Diffusion	15
2.2.1 Random walk motion	15
2.2.2 Fick’s laws	16
2.2.3 Diffusion from a source of constant concentration	17
2.3 State of the art	19
2.4 Experiment and methods	20
2.5 Ge diffusion on a C-free Si(001) surface	22
2.5.1 Discrete Layer Model of the SiGe over-layer	23

2.5.2	Temperature dependence of the diffusion parameters	25
2.5.3	Time dynamics of the diffusion flux	27
2.5.4	Scaling behavior of the surface diffusion from a stripe	29
2.6	Ge diffusion on a C covered Si(001) surface	33
2.6.1	Diffusion parameters vs C coverage	33
2.6.2	Physical origin of the C-induced modulation of atomic mobility	37
2.7	Conclusions	39
	Bibliography	40
3	Self-assembled SiGe islands grown by Surface Thermal Diffusion on Si(001)	43
3.1	Introduction	43
3.2	Epitaxial growth of SiGe islands on Si(001) by MBE and CVD	44
3.2.1	Strain relaxation before the onset of 3D growth	44
3.2.2	3D island formation and faceting	45
3.2.3	SiGe intermixing	48
3.2.4	Plastic relaxation	49
3.2.5	Spatial ordering	50
3.2.6	Surfactant mediated growth	51
3.3	Growth of SiGe islands on Si(001) by surface thermal diffusion	52
3.3.1	Experiment	53
3.3.2	Growth modes	54
3.3.3	Interplay among C incorporation, Ge diffusion and island nucleation	57
3.3.4	Equilibrium shape and size	60
3.3.5	Density evolution: 1D model of nucleation	63
3.3.6	Size evolution: capture zone growth and SiGe intermixing	68
3.3.7	Carbon-induced modulation of island size and density	74
3.3.8	Delayed plastic relaxation	77
3.3.9	Ordered growth on a pit-patterned Si surface	81
3.4	Conclusions	85
	Bibliography	87

4	Nanoscale mapping of composition, strain and valence band structure in SiGe nano-stripes	92
4.1	Introduction	92
4.2	Experiment and methods	93
4.2.1	Sample preparation	93
4.2.2	TERS experiment	95
4.2.3	Energy Filtered PEEM experiment	96
4.3	Nanoscale mapping of composition and strain	97
4.4	Work function and Valence Band mapping	106
4.5	Conclusions	114
	Bibliography	115
5	Nanoscale elastic strain relief in SiGe nano-ridges studied by X-Ray Diffraction	117
5.1	Introduction	117
5.2	Experiment and methods	118
5.2.1	Sample preparation	118
5.2.2	Diffraction experiment	120
5.2.3	Construction of the reciprocal space maps	121
5.3	Strain relaxation at the step edge of a large square	123
5.4	Strain relaxation of a single nano-ridge	126
5.5	Conclusions	130
	Bibliography	130
	Conclusions	132
	Panel A – Scanning Auger Microscopy	136
A.1	Introduction	136
A.2	Scanning electron microscopy (SEM)	136

A.3	Auger effect and chemical analysis	138
A.4	Instrumentation	140
A.5	Quantification of Auger Spectra	142
	Bibliography	143
Panel B – Atomic Force Microscopy		144
B.1	Introduction	144
B.2	Basic principles	144
B.3	AFM instrumentation	146
	B.3.1 AFM scanners	146
	B.3.2 Light Lever Force Sensors	147
	B.3.3 Cantilevers and tips	148
B.4	Imaging modes	149
	B.4.1 Contact mode	150
	B.4.2 Vibrating mode	150
Panel C – Transmission Electron Microscopy		153
C.1	Introduction	153
C.2	Conventional TEM	153
	C.2.1 Basic principles	153
	C.2.2 Instrumentation	154
	C.2.3 Image contrast	157
C.3	Scanning TEM	159
C.4	Energy Filtered TEM	159
C.5	Cross-section TEM sample preparation by FIB	160
C.6	Imaging dislocations in a Ge/Si system	162
	Bibliography	163
Panel D – micro-Raman Spectroscopy		164
D.1	Introduction	164
D.2	Raman effect: general theory	164

D.3	Experimental setup	166
D.4	Application to a strained SiGe/Si system	167
	Bibliography	169
Panel E – Tip Enhanced Raman Spectroscopy		170
E.1	Introduction	170
E.2	Surface plasmon polaritons	171
E.3	Electromagnetic enhancement at the tip apex	173
E.4	Instrumentation	176
	E.4.1 TERS configuration	176
	E.4.2 Scanning tunnelling microscopy (STM)	177
	E.4.3 Tip fabrication	178
	Bibliography	179
Panel F – PhotoElectron Emission Microscopy		180
F.1	Introduction	180
F.2	Basic principles of photoemission spectroscopy	181
F.3	Photon sources	182
F.4	The NanoESCA spectro-microscope	183
	F.4.1 Energy resolution and transmission	184
	F.4.2 Spatial Resolution	186
	Bibliography	187
Panel G – X-Ray Diffraction		188
G.1	Introduction	188
G.2	Basic principles	188
G.3	Reciprocal space mapping of a Ge/Si(001) system	189
	Bibliography	191

Introduction

SiGe nanostructures on crystalline Si substrates with (001) orientation are among the most studied system in condensed matter physics and nanoscience. The subject has an h -index of 104 over about ten thousand papers from late 1980s to 2010[§] (research on spintronics, cuprates superconductors and graphene have h -indexes of 88, 117 and 160, respectively). This interest has been mainly driven by the important potential applications in micro, opto and nanoelectronic devices thanks to the improvement of the optical and electronic properties compared to bulk systems, while preserving a wide compatibility with the existing technology. These features come essentially from the possibility of engineering the strain field within the nanostructures using the lattice mismatch of $\sim 4.2\%$ between Ge and Si and from the spatial confinement, capable of modifying the electronic band structure leading to an increase of the charge carrier mobility. It is obvious that these applications largely depend on the control of surface processes during the growth of the nanostructures, and their performance (above all, operating speed) are strongly dependent on strain relaxation and dislocation injection.

Besides the technological interest, the SiGe/Si(001) system has received much attention since it is also a model for understanding the fundamental processes occurring during three-dimensional (3D) island formation and self-organization phenomena. In fact, the lattice mismatch between Ge and Si introduces a stress field which has dramatic effects on the growth process and is responsible for a number of structural and electronic phenomena. In particular, the stored elastic energy can be partially relieved by spontaneous formation of 3D objects of nanometric size on top of a pseudomorphic SiGe wetting layer. This growth mode, called Stranski-Krastanov (SK), is a way of easily forming self-assembled nanostructures, which can be used to obtain quantum confinement of charge carriers in nanoelectronics device applications.

In recent years, considerable efforts have been devoted to the growth of hetero-epitaxial SiGe nanostructures with well controlled size, shape and positioning, and with defined stoichiometry and strain state, all critical issues for both fundamental understanding and the future device engineering. However, some aspects still need to be addressed for a complete understanding of this system, including: (i) the competition between kinetic and thermodynamic factors for island formation and their stability, (ii) the mechanisms governing the relative growth of individual nanostructures, (iii)

[§]A h -index of 104 means that 104 papers have been cited at least 104 times (from ISI Web Of Knowledge).

the elastic and plastic strain relaxation, and (iv) the Si incorporation occurring during the growth (SiGe intermixing).

In the present work, we carry out an experimental investigation of the relationship between morphology, elemental composition, strain state and electronic structure of self-assembled and lithographically defined SiGe nanostructures by means of several spectro-microscopy techniques. The Si and Ge diffusion dynamics and the self-organization phenomena during the growth of SiGe islands have been studied by Scanning Auger Microscopy (SAM) and Atomic Force Microscopy (AFM). Micro-Raman, SAM and Scanning Transmission Electron Microscopy coupled with Electron Energy Loss Spectroscopy (STEM-EELS) techniques have been used for the investigation of the interplay between strain relaxation mechanisms and SiGe intermixing phenomena in self-assembled islands. The effects of strain and composition on the electronic band structure in lithographically defined SiGe nanostructures, in layout very close to those used in prototype devices, have been characterized with nanoscale spatial resolution joining information from Tip Enhanced Raman Spectroscopy (TERS), nanofocused X-Ray Diffraction (XRD) and Energy-Filtered PhotoElectron Emission Microscopy (PEEM).

The thesis is conceptually divided in two main parts: the first, to which belong Chapters 1, 2 and 3, deals with the experimental investigation of the Ge surface diffusion and of the self-organization phenomena of SiGe islands grown in a bottom-up approach; the second, including Chapters 4 and 5, is based on the experimental characterization of the strain state and of the strain-induced effects on the electronic band structure of lithographically defined SiGe nanostructures obtained in a top-down approach. A more detailed description of the arguments treated within each Chapter is presented here below.

Chapter 1 presents an overview on the basic processes occurring during hetero-epitaxial growth of thin solid films obtained by depositing a crystalline material on a likewise crystalline substrate of a different material, and describes the principles which determine the structure and the morphology of a particular film.

In the **Chapter 2** the surface diffusion of Ge on a clean and carbon-covered Si(001) surface promoted by annealing at high temperatures in ultra-high vacuum (UHV) of lithographically etched pure Ge stripes, acting as solid state sources directly placed on the Si substrate, is experimentally investigated by means of *in-situ* Scanning Auger Microscopy. After having introduced the analytical description of the rate of mass transport over a surface, we present the experimentally monitored temperature dependence of the diffusion coefficient on a microscopic length scale for Ge on a C-free Si surface. Then the influence of a controlled carbon coverage on the thermal surface diffusion is quantitatively studied, showing that the diffusion coefficient presents a strong

dependence on carbon coverage. To understand the origin of this dependence, we critically discuss the role played by the chemical interactions among Si, C and Ge, the surface roughness, and the local strain field induced by the C surfactant.

Chapter 3 deals with the experimental investigation of the growth process of self-assembled SiGe islands on Si(001). First, a short review of the results achieved by previous studies of islands grown by Molecular Beam Epitaxy (MBE) and Chemical Vapor Deposition (CVD) is presented. Then we focalize on the experimental investigation of the self-organization phenomena occurring during island growth by surface thermal diffusion of Ge from a Ge stripe. The total surface coverage of Ge strongly depends on the distance from the source stripe, so that the method allows to investigation of the island growth over a wide range of dynamical regimes at the same time. The results obtained are compatible with those reported until now in literature, but at the same time they also shine more light on some intriguing aspects of the Ge/Si(001) self-assembly. In particular, we discuss the island growth modes in the cases of C-free and C covered Si surfaces, giving an experimental evidence of a C-induced continuous transition between the two different regimes. From the size and density evolution exhibited by the nucleated islands as a function of the distance from the source stripe and for different C coverage, we propose a scenario where island growth is essentially driven by kinetic factors within a diffusion limited regime. Finally, we investigated the interplay among SiGe intermixing and plastic relaxation, showing that the surface thermal diffusion growth method leads to the formation of coherent islands (dislocation-free), larger than those attainable by MBE and CVD.

Chapter 4 presents the mapping with nanoscale resolution of strain, composition, local work function and valence band structure of lithographically defined SiGe *embedded* nano-stripes using TERS and Energy-Filtered PEEM techniques. The strain profile across a single nano-stripe is experimentally determined and compared to the strain data obtained from Finite Element Modeling (FEM) calculations. The local work function and the valence band mapping allowed the determination of the electronic structure modifications with respect to the case of bulk Ge induced by the strain field inside the nano-stripes.

In **Chapter 5** are presented the first results of a *direct* characterization of the strain state of lithographically defined SiGe nano-ridges using the recently developed nanofocused XRD technique. Strain values are extracted from the experimental diffraction profiles measured on a single nanostructure, which are then compared with kinematical simulations performed on strain data obtained from Finite Element Modeling (FEM) calculations.

A detailed description of the experimental techniques used in this work is reported in dedicated Panels: A - Scanning Auger Microscopy; B - Atomic Force Microscopy; C -

Transmission Electron Microscopy and STEM-EELS; D - micro-Raman Spectroscopy; E - Tip Enhanced Raman Spectroscopy (TERS); F - PhotoElectron Emission Microscopy (PEEM); G - X-Ray Diffraction (XRD). For each technique the underlying physical principles and the main characteristics and performances of the related instrumentations are described.

The work presented in this thesis is the outcome of an experimental PhD research project developed at the Politecnico di Milano (Milano, Italy) in co-tutorship with the École Polytechnique (ParisTech, France) and the French Atomic Energy Commission (CEA-Saclay, France). The achieved results yield from a very effective joint effort of several experimental groups working together in a strict collaboration. The author has represented the *fil rouge* among them, establishing a strong interaction with all the people involved in the project and directly performing and actively participating in every measurement presented in the following.

Scanning Auger Microscopy (SAM) and Atomic Force Microscopy (AFM) have been performed at Department of Physics of the Politecnico di Milano. Micro-Raman Spectroscopy has been carried out at the Materials Science Department of the Università di Milano-Bicocca. Energy-Filtered PEEM measurements have been realized at CEA and during two standard experimental runs at the TEMPO beamline of SOLEIL Synchrotron (France). Tip Enhanced Raman Spectroscopy (TERS) and preliminary Transmission Electron Microscopy (TEM) analysis have been performed at the École Polytechnique, while more extensive TEM and STEM-EELS measurements have been developed at IMM-CNR in Catania. The nanofocused-XRD experiment has been carried out during a standard experimental run at ID13 beamline of the European Synchrotron Radiation Facility (ESRF). The close collaboration with the laboratory L-NESS in Como made available the set of the lithographically-defined investigated samples. The experimental results have been exploited in close collaboration with a theory group at the Materials Science Department of the Università di Milano-Bicocca for a deeper insight into the atomic level mechanisms during island growth process.

Chapter 1

Basic concepts in hetero-epitaxial growth

1.1 Introduction

Thin solid films obtained by depositing a crystalline material on a likewise crystalline substrate of a different material (hetero-epitaxial growth) are routinely produced and employed in modern technology. Thus it is useful to look briefly at the process of film growth and the underlying principles which determine the structure and morphology of a particular film.

First the individual processes occurring on the substrate surface during hetero-epitaxial growth are described. Considering the process in a phenomenological way, different growth modes are discussed in terms of the surface free energies. A simple but intuitively very appealing theoretical approach (the *capillary theory of nucleation*) is presented allowing to define the energetic of the growth process. Then the stability of a hetero-epitaxial system is critically investigated. Finally, the basic concepts of the most used experimental growth methods are presented.

1.2 Modes of film growth

The individual atomic processes which determine hetero-epitaxial film growth in its initial stages are illustrated in Fig. 1.1. Once a particle has condensed from the vapor phase, it might immediately re-evaporate or it may diffuse along the surface. This diffusion process might lead to adsorption at special sites like edges or other defects, or the diffusing particle may re-evaporate. In all these processes, characteristic activation energies must be overcome, i.e. the probability per unit time, p , that a particular process occurs is given by an Arrhenius-type exponential law:

$$p \propto \exp\left(-\frac{E}{K_B T}\right) \quad (1.1)$$

where E is the activation energy of the process, K_B is the Boltzmann constant, and T is the substrate temperature. Besides adsorption at special sites and surface diffusion, nucleation of more than one

absorbed particle might occur, as might further film growth by addition of particles to an already formed nucleus.

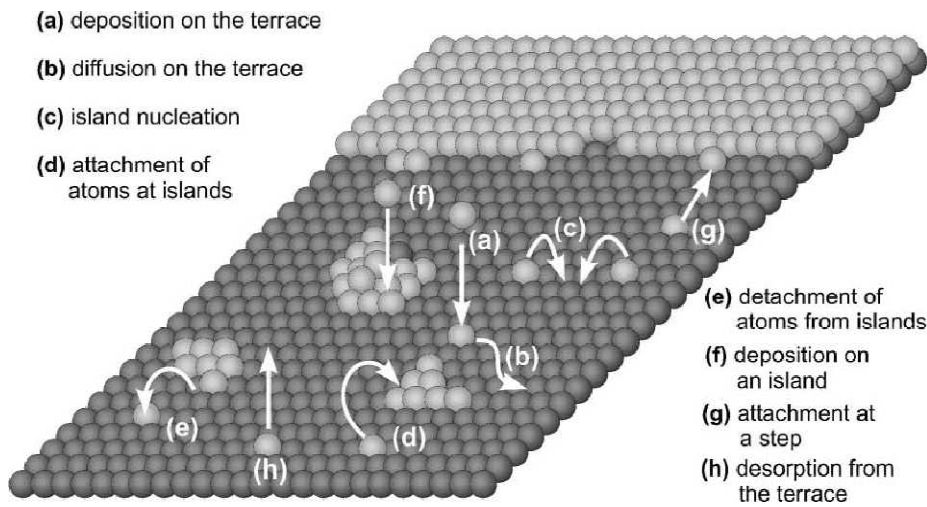


FIG. 1.1. Main surface processes occurring during epitaxial growth. Atoms from the source can be *adsorbed* (a) and diffuse on the surface as *adatoms* (b), they can meet and lead to the formation of islands (c) or attach to preexisting islands (d) or steps (g). Atoms belonging to islands or terraces can detach and diffuse again (e) or desorb (h). (From Ref. 1)

At thermodynamic equilibrium all processes proceed in two opposite directions at equal rates, as required by the principle of “detailed balance”. Thus, for example, surface processes such as condensation and evaporation, decay and formation of cluster nuclei must counterbalance. Therefore, at equilibrium, there cannot be any net growth of the film. Hence, crystal growth must clearly be a non-equilibrium process. The final macroscopic state of the system depends on the route taken through the various paths indicated in Fig. 1.1. The state which is obtained is not necessarily the most stable one, since kinetic limitations could prevent the achieving of the thermodynamic equilibrium.

Considering the process of film growth in a phenomenological way, three markedly different modes can be distinguished² (see Fig. 1.2). In the *layer-by-layer* mode (or Franck-van der Merve, FM) the interaction between substrate and layer atoms is stronger than that between neighboring layer atoms. Thus, each new layer starts to grow only after the completion of the previous one. The opposite case, in which the interaction between neighboring film atoms exceeds the overlayer-substrate interaction, leads to the *island growth* mode (Volmer-Webber, VW). The *layer-plus-island* mode (Stransky-Krastanov, SK) is an interesting intermediate case. After the formation of several complete monolayers (MLs), island nucleation occurs and 3D structures grow on the top of the first full layers (also called Wetting Layer, WL).

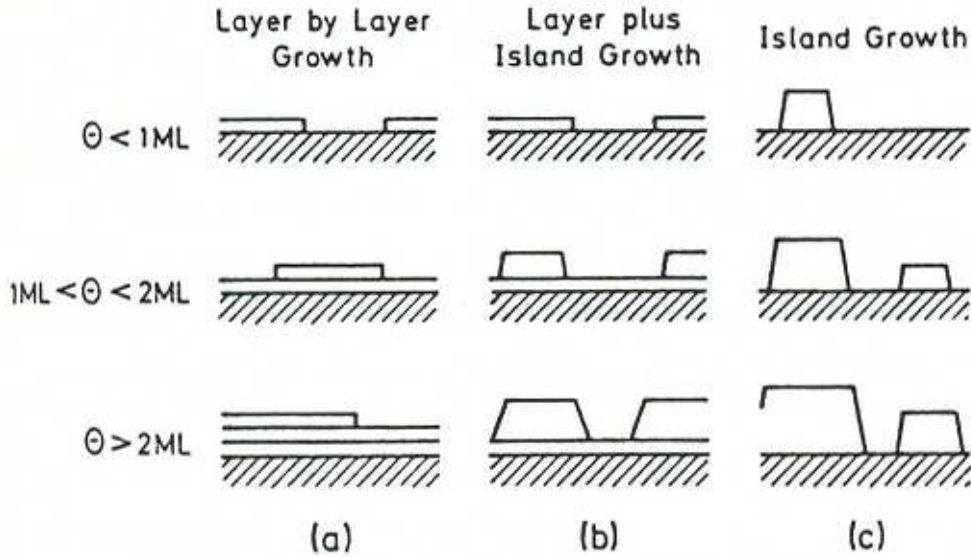


FIG. 1.2. Schematic representation of the three important growth modes of a film for different coverage, Θ , regime. (a) *Layer-by-layer* mode (or Franck-van der Merve, FM); (b) *island growth* mode (Volmer-Webber, VW); (c) *layer-plus-island* mode (Stransky-Krastanov, SK) (from Ref. 3).

Many factors might account for this intermediate growth mode, but a certain lattice mismatch between the film and the substrate is the most common case. At initial stages, the growing flat film pseudomorphically deforms in order to match the substrate lattice, accumulating some elastic energy. When this deformation energy becomes too high, the system will relieve it in some way. One possible way is to nucleate 3D islands on top of the flat film, where the absence of lateral constraints allows for an outward bending of the lattice planes inducing a partial elastic strain relief (see Fig. 1.3).

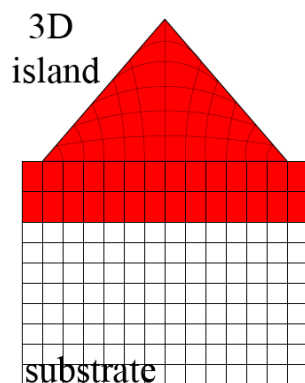


FIG. 1.3. Schematic representation of the elastic relaxation of the strain stored into the wetting layer by means of the formation of a 3D island during SK growth in a lattice mismatched system.

A simple formal distinction between the conditions for the occurrence of the various growth modes can be made in terms of the surface energy, γ , defined as the characteristic free energy per unit area to create an additional unit of surface or interface. Since γ can also be interpreted as a

force per unit length of boundary, force equilibrium at a point where substrate and a 3D island of the deposited film touch (see Fig. 1.4) can be expressed as:

$$\gamma_S = \gamma_{S/F} + \gamma_F \cos \phi \quad (1.2)$$

where γ_F , γ_S , $\gamma_{S/F}$ are the surface free energies of the film/vacuum, substrate/vacuum, and film/substrate interfaces, respectively. Using Eq. (1.2) the two limiting growth modes, layer-by-layer (FM) and island growth (VW), can be distinguished by the angle ϕ :

$$\text{layer growth: } \phi = 0 \quad \gamma_S \geq \gamma_{S/F} + \gamma_F \quad (1.3)$$

$$\text{island growth: } \phi > 0 \quad \gamma_S < \gamma_{S/F} + \gamma_F \quad (1.4)$$

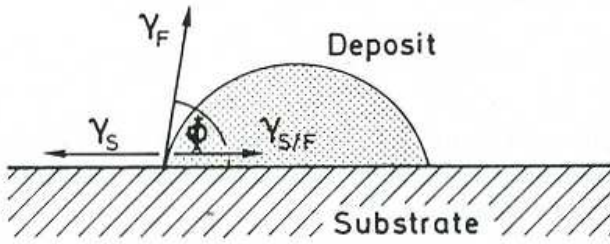


FIG. 1.4. Simplified picture of an island of a deposited film; γ_F , γ_S , $\gamma_{S/F}$ are the surface free energies of the film/vacuum, substrate/vacuum, and film/substrate interfaces, respectively; ϕ is the contact angle. (From Ref. 3)

1.3 “Capillary model” of 3D island nucleation

A simple, but intuitively very appealing theoretical approach was proposed by Bauer to describe the nucleation of 3D islands on a ideal, defect-free, surface during hetero-epitaxial growth. Since this approach uses only the thermodynamically defined surface energies γ_F , γ_S , $\gamma_{S/F}$, it is called the *capillary theory of nucleation*². In this model the total free energy for the formation of a 3D nucleus is considered as a function of the volume (or alternatively of the number of constituting atoms) only. The free energy of the system is given by two contributions: (i) one taking into account the energy gain upon the formation of the island from the flat film, and (ii) one considering the energy cost for the formation of new surfaces and interfaces. In case of an island with n atoms, the free energy ΔF is:

$$\Delta F = -n\Delta f + n^{2/3}X \quad (1.5)$$

where Δf is the difference between the bulk energies of the n atoms contained into the 3D island and the 2D flat film phases. X contains the contributions of the interface energies, and can be written as:

$$X = \sum_k C_k \gamma_F^{(k)} + C_{S/F} (\gamma_{S/F} - \gamma_S) \quad (1.6)$$

where C_k and $C_{S/F}$ are geometric constants. The first term on the right side of Eq. (1.6) is related to the various facets, with different crystallographic orientations, exhibited by the island. C_k relates $n^{2/3}$ to a part of the surface of the nucleus (adjacent to the vacuum) having the surface energy $\gamma_F^{(k)}$. The outer surface of the nucleus, i.e. the part exposed to the vapor phase (or vacuum), is assumed to be decomposed of several patches of different crystallographic orientation with different surface energies $\gamma_F^{(k)}$. The second term in Eq. (1.6) is related to the energy variation due to the replacement of a portion of free substrate surface with a new interface with the film. $C_{S/F}$ is a simple geometric constant which relates the basis area of the nucleus, $A_{S/F}$, with the number of atoms according to $A_{S/F} = C_{S/F}n^{2/3}$.

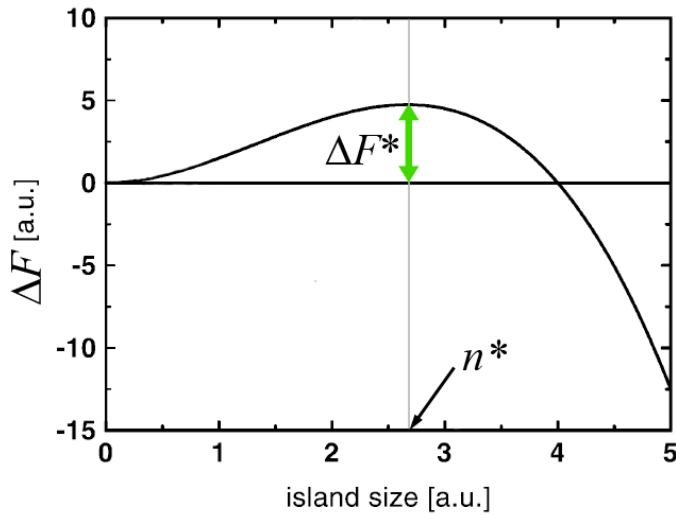


FIG. 1.5. Free energy as a function of the island size as described within the capillary model of nucleation (from Ref. 1).

Fig. 1.5 shows a qualitative plot of the free energy ΔF as a function of the number of atoms forming the 3D nucleus. The superposition of the negative term due to the energy gain following the island formation, and the positive term due to energy cost following the formation of the interfaces, generates a non-monotonic dependence of ΔF on the number of atoms n ; i.e. there exists a critical size, n^* , of the nuclei for 3D nucleation, at which the free energy ΔF becomes maximum. In this picture, 3D islands are the results of local fluctuations of the density of adatoms. During growth, nuclei composed of groups of adatoms form and may either (i) dissolve, if they contain less than n^* atoms (in this case they are called *subcritical*), or (ii) expand, if their size is larger than that of the *critical nucleus* containing n^* atoms. The process involves an activation energy $\Delta F^* = \Delta F(n^*)$ given by:

$$\Delta F^* = \frac{4X^3}{27\Delta f^2} \quad (1.7)$$

Alternatively, instead of using the total free energy of the island, the nucleation concept can be better understood by using the chemical potential $\Delta\mu = \frac{\partial\Delta F}{\partial n}$, i.e. the free energy “gained” by each adatom attaching to the nucleus. When $n < n^*$, $\Delta\mu$ is positive and thus it is not favorable for the adatom to attach to the nucleus. However, if the nucleus is supercritical, $\Delta\mu$ will be negative and the island will tend to increase its size.

1.4 Stability of a hetero-epitaxial system

The equilibrium state of a hetero-epitaxial system, i.e. its configuration with the minimum energy, is a delicate issue, since in general the deposited material can partially diffuse inside the substrate possibly lowering the energy of the system. However, it is interesting to discuss here the local minimum of the surface free energy in case of SK growth, where the system is constituted of 3D islands formed on a flat wetting layer which does not appreciably intermix with the substrate. Although in real cases significant intermixing in 3D islands has been experimentally demonstrated⁴, the case of negligible intermix is very instructive since it allows to get the main aspects of the problem. In particular, the question is whether islands form a thermodynamically-controlled equilibrium ensemble within the phase space defined by their orientation, shape and size, or if they evolve according to a kinetic coarsening mechanism. In fact kinetic limitations, in the form of low surface diffusivities or high deposition rates, can roughen a film that is energetically favored to be flat or lead to the formation of many small islands for a system in which the thermodynamically stable configuration is a single large crystallite sitting on the substrate⁵. In the latter case, the islands are only metastable; as the growth proceeds, the smallest ones dissolve as the relatively larger ones grow. This process is known as coarsening because both the average island size and the width of the size distribution increase with time as the number density decreases.

Shchukin *et al.*⁶ derived an expression for the energy of a strained nanocrystal on a lattice mismatched substrate which can be parameterized as⁷:

$$\Delta E = Cn + Bn^{2/3} + An^{1/3} \quad (1.8)$$

where ΔE is the difference between the energy of the partially relaxed (and defect free) 3D nanocrystal containing n atoms and the energy of those n atoms if they formed a single monolayer patch (2D island) on the wetting layer. The volume coefficient C is related to the bulk strain, the surface coefficient B includes the facet and interface energies, and the linear coefficient A depends on the elastic interaction of the edges. It can be demonstrated that with a suitable choice of these parameters⁷, ΔE exhibits at least one minimum. Therefore, a thermodynamic interpretation could be

given for the growth process. In this picture, the size distribution of the ensemble of islands would be represented by some discrete values associated with the free energy minima. The width of the size distribution around each minimum would depend on the thermal broadening. However, it has been emphasized by several authors^{8,9} that island growth on a lattice mismatched substrate evolves toward the equilibrium state through a kinetic rather than a thermodynamic path, and the size evolution is essentially controlled by several thermally activated processes. It is possible that some kinetic barrier will prevent the evolution of the system towards its equilibrium state or that the system will not have enough time to reach the equilibrium, if the experimental time scale is too short. The involved mechanism is very similar to the Ostwald ripening, i.e. the coarsening of the size distribution of an ensemble of islands driven by the Gibbs-Thomson effect^{10,11}. Within this framework an abrupt drop of the chemical potential occurs when the islands grow past a critical volume, triggering a coarsening process where the driving force depends on the mean curvature radius of the islands¹². In practice, it is supposed that atoms detach more readily from smaller islands and condense faster on larger ones. The main result is that, at a fixed amount of material, larger islands grow at the expense of smaller ones.

1.5 Growth methods

The most used techniques for epitaxial deposition of semiconductors are Molecular Beam Epitaxy and Chemical Vapor Deposition. Thus it is useful to discuss briefly their main basic concepts.

In MBE some materials are heated in special ovens, the *effusion cells*, from where the evaporated particles travel more or less collision-less (molecular regime) to a heated substrate where they are incorporated in a growing film (see Fig. 1.6) after a number of elementary processes, many of which are similar for any growth method (see Fig. 1.1). What is special about MBE is that the substrates are kept in an UHV environment. This assures low impurity incorporation even though typical growth rates are rather low, of the order of $\text{\AA}/\text{s}$. The UHV environment also makes it easy to use tools for *in-situ* monitoring of the growth.

To some extent the simplicity of MBE rests on the fact that surface chemistry plays a relatively minor role. This is one of the main reasons for which the technique can be applied to different materials with relative ease. With few exceptions for special applications, MBE is not, however, a technique for the *industrial production* of epitaxial semiconductor layers because of the expensive UHV technology and slow deposition rates. When it comes to large-scale production of

epitaxial semiconductors *chemical vapor deposition* (CVD) is the technique of choice. In CVD one or several reactive gases are thermally decomposed on a hot substrate in a reactor chamber.

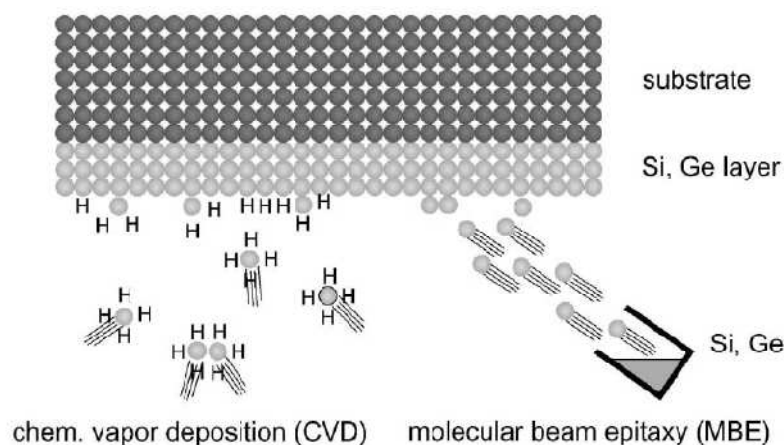


FIG. 1.6. Schematic representation of the basic principles of CVD (left) and MBE (right) for SiGe growth on Si substrate (from Ref. 1).

One of the disadvantages of the thermal CVD is the exponential decrease of the growth rate with decreasing the substrate temperature. This drawback can be eliminated by supplying the energy necessary for cracking the precursors in some form other than thermal, such as by ion bombardment. This is involved automatically in case of a plasma discharge, and then the growth by gas precursor decomposed by a hot plasma is generally called *plasma assisted* or *plasma enhanced* CVD (PECVD). As a consequence, epitaxial growth may proceed at lower substrate temperatures compared to purely thermal deposition. There is, however, a downside associated with ion bombardment in the sense that for most plasmas ion energies are high enough for causing crystal damage. One way to lower these ion energies is by using a low-voltage arc discharge to sustain the plasma, giving rise to the so-called Low Energy PECVD¹³.

1.6 Conclusions

In this chapter, an overview of the basic processes occurring during hetero-epitaxial growth of thin solid films obtained by depositing a crystalline material on a likewise crystalline substrate of a different material have been described and discussed within the framework of the capillary theory of nucleation. The equilibrium state of a hetero-epitaxial system has been critically discussed with particular attention to the case of Stanski-Krastanov (SK) growth. The concepts described here represent the essential background for the investigation of the self-organization phenomena occurring during epitaxial growth of SiGe islands presented in the following of the thesis.

Bibliography

- ¹ B. Voigtlander, *Surf. Sci. Rep.* **43**, 127 (2001).
- ² E. Bauer, *Z. Kristallogr.* **110**, 372 (1958).
- ³ H. Luth, *Solid Surface, Interfaces and Thin Films*, Springer-Verlag Berlin Heidelberg 2001
- ⁴ A. Rastelli, M. Stoffel, A. Malachias, T. Merdzhanova, G. Katsaros, K. Kern, T. H. Metzger, and O. G. Schmidt, *Nano Lett.* **8**, 1404-1409 (2008)
- ⁵ M. Zinke-Allmang, L. C. Feldman, M. H. Grabow, *Surf. Sci. Rep.* **16**, 381 (1992).
- ⁶ V. A. Shchukin, N. N. Ledentsov, P. S. Kopé, and D. Bimberg, *Phys. Rev. Lett.* **75**, 2968 (1995).
- ⁷ G. Medeiros-Ribeiro, A. M. Bratkovski, T. I. Kamins, D. A. A. Ohlberg, and R. S. Williams, *Science* **279**, 353 (1998).
- ⁸ F. Ross, J. Tersoff, and R. Tromp, *Phys. Rev. Lett.* **80**, 984 (1998).
- ⁹ F. Ross, R. Tromp, and M. Reuter, *Science* **286**, 1931 (1999).
- ¹⁰ W. Thomson, *Phylos. Mag.* **43**, 448 (1871).
- ¹¹ J. W. Gibbs, *Trans. Connect. Acad.* 3, **108** (1876).
- ¹² B. K. Chakraverty, *J. Phys. Chem. Solids* **28**, 2401 and 2413 (1967).
- ¹³ M. Kummer, *Device-grade SiGe heterostructures grown by plasma assisted techniques*, PhD dissertation, Swiss Federal Institute of Technology, ETH Zurich, 2002.

Chapter 2

Ge diffusion on clean and C covered Si(001) surface

2.1 Introduction

In this chapter, the surface diffusion of Ge on a clean and carbon covered Si(001) surface is experimentally investigated by means of Scanning Auger Microscopy (SAM). The epitaxial growth of elemental semiconductors (Si and Ge) is of considerable scientific and technological significance because Si and Ge are base materials used in electronic devices and serve also as ideal model systems for studying semiconductor surfaces and growth from a fundamental point of view. Within this scenario measurements of adatom surface diffusion can offer key insights into the thermodynamics and kinetics of surface processes occurring during the self-assembled growth of SiGe islands. In fact, the growth process is strongly dependent on the surface diffusion coefficients of Ge and Si atoms, which are both rapidly varying with the temperature^{1,2} and sub-monolayer amounts of surface impurities³.

After having introduced the analytical description for the rate of mass transport over a surface, the main experimental and theoretical results achieved so far in literature for the Ge surface diffusion on Si(001) are briefly reported. Then the temperature dependence of the diffusion length for Ge on a C-free Si surface, experimentally monitored by means of Auger spectro-microscopy, is presented allowing for a direct determination of the diffusion coefficient on a microscopic length scale. The time dynamics and the scaling behaviour of the obtained diffusion profiles have been also investigated. Finally, the influence of a controlled Carbon coverage of the Si(001) surface on the thermal surface diffusion of Ge is quantitatively studied.

2.2 Theory of surface diffusion[§]

2.2.1 Random walk motion

Surface diffusion is the motion of adatoms over the surface of a solid substrate. An ideal crystal surface is comprised of a periodic array of adsorption sites corresponding to the positions of minimum potential energy. Due to thermal excitations, a chemisorbed adatom can hop from one adsorption site to the next (see Fig. 2.1(a)). The adatom motion along the surface can be visualized as a random site-to-site hopping process (random-walk), for which the mean-square displacement of the hopping atom in time t is given by:

$$\langle \Delta r^2 \rangle = \nu a^2 t \quad (2.1)$$

where a is the jump distance and ν is the frequency of hops. The time independent ratio of the mean square displacement $\langle \Delta r^2 \rangle$ to time t is known as the *diffusion coefficient*, D :

$$D = \frac{\langle \Delta r^2 \rangle}{4t} = \frac{\nu a^2}{4} \quad (2.2)$$

Atom hopping from site to site requires surmounting the potential barrier between two neighbouring sites as shown in Fig. 2.1(b). This means that surface diffusion is a thermally activated process following an Arrhenius behaviour as a function of the temperature, T , of the substrate. If the oscillation frequency of the atom in the potential well of the adsorption site (which is essentially an attempt frequency to overcome the barrier) is ν_0 and the barrier height is E_A , the hopping frequency can be expressed as:

$$\nu = \nu_0 \exp\left(-\frac{E_A}{K_B T}\right) \quad (2.3)$$

where K_B is the Boltzmann constant.

As one can see in Fig. 2.1(b), the activation energy E_A is represented by the difference in potential energy of the adatom in the equilibrium adsorption site and in the transition saddle point. From Eq. (2.2) and (2.3) the diffusion coefficient results accordingly:

$$D = \frac{\nu_0 a^2}{4} \exp\left(-\frac{E_A}{K_B T}\right) \quad (2.4)$$

where the pre-exponential factor $D_0 = \frac{\nu_0 a^2}{4}$ is generally known as *diffusion constant*.

[§] An extensive treatment of this argument can be found in: K. Oura, V.G. Lifshits, A.A. Saranin, A.V. Zotov, M. Katayama, *Surface Science – An Introduction*, Springer Verlag (2003).

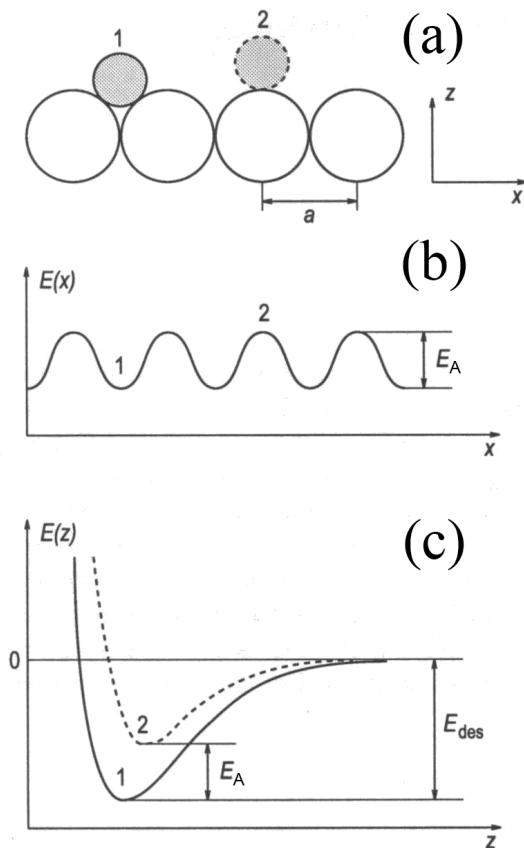


FIG. 2.1. One-dimensional schematic diagram showing (a) a substrate (open circles) and adatom (hatched circle) in an adsorption site (labelled 1) and in a transition saddle point (labelled 2). z is the distance normal to the surface and x is the coordinate along the surface. (b) Schematic potential energy diagram for adatom motion along the surface. (c) Schematic diagram of the adatom potential energy as a function of z for positions 1 and 2 as in (a). The activation energy of the surface E_A equals the difference of the minima of the curves 1 and 2. The desorption energy E_{des} is shown for comparison.

2.2.2 Fick's Laws

In presence of a gradient of the atom concentration, c , the random walk motion of many atoms results in their net diffusion motion towards the region with a lower concentration in such a way as to remove the gradient. The main regularities of such a diffusion process are described by the Fick's laws. If the atomic jumps are random and independent of each other, the flux J of atoms diffusing on the surface is proportional to concentration gradient ∇c , with the diffusion coefficient D as a factor of proportionality:

$$J = -D\nabla c \quad (2.5)$$

Eq. (2.5) is known as *Fick's first law* and is one of a class of laws (including Ohm's law, for instance) which applies when the effect is proportional to the cause.

Fick's second law describes the non-steady state situation when the diffusion flux and the concentration varies with time. It can be derived by applying the constraint of mass conservation (continuity condition) to Eq. (2.5). The continuity argument states that the rate at which material is accumulating in an element of volume dV must be equal to the rate at which it is flowing in, minus the rate at which is leaving:

$$\nabla \cdot \mathbf{J} = -\frac{\partial c}{\partial t} \quad (2.6)$$

which is essentially the expression in local form of the mass conservation. If D is a constant Eq. (2.6) becomes:

$$D\nabla^2 c = \frac{\partial c}{\partial t} \quad (2.7)$$

Eq. (2.7) is generally called *Fick's second law* (or *diffusion equation*), and reflects the preservation of the mass during the diffusion process, i.e. it shows that if the number of atoms reaching a given local area differs from the number of atoms leaving it, the local concentration varies by the difference value.

2.2.3 Diffusion from a source of constant concentration

The knowledge of the diffusion coefficient is fundamental in many contexts going from the atomic to the macroscopic length scale. In practical cases, its value is profitably obtained by studying the diffusion process in a one-dimensional (1D) geometry, where a simple analytical solution of the diffusion equation is available.

If a concentration gradient is present along the x -axis, the Fick's second law reduces to:

$$D \frac{\partial^2 c}{\partial x^2} = \frac{\partial c}{\partial t} \quad (2.8)$$

The mathematical solution to Eq. (2.8) depend on the initial and boundary conditions, which are determined by the physical conditions of the experiment in question. In this section the problem of the one-dimensional diffusion from a source of constant concentration is investigated, since it will represent the theoretical framework in which the diffusion experiment will be discussed. Within this framework the initial and boundary conditions are the following: (i) the initial concentration distribution has a step-like shape, and (ii) the concentration at the boundary is maintained at a constant value c_0 :

$$c(x, t) = c_0 \quad \text{for } x < 0 \quad (2.9)$$

$$c(x, 0) = 0 \quad \text{for } x > 0 \quad (2.10)$$

The simplest way to solve this problem is to imagine the source to be made up of an infinite number of point-like sources in the spatial range $-\infty < x < 0$. The solution of Eq. (2.8) under this conditions can be thus determined using the *superposition principle*, i.e. summing up the contribution coming from each point source. The diffusion profile of a point source after a time t is given by a Gaussian distribution:

$$c(x, t)_{point} = \frac{c_0}{\sqrt{\pi Dt}} \exp\left(-\frac{x^2}{4Dt}\right) \quad (2.11)$$

and thus the solution of the diffusion equation in case of a constant concentration source will be:

$$c(x, t) = \int_x^{+\infty} c(\xi, t)_{point} d\xi = \int_x^{+\infty} \frac{c_0}{\sqrt{\pi Dt}} \exp\left(-\frac{\xi^2}{4Dt}\right) d\xi \quad (2.12)$$

Changing the variable to $\eta = \frac{\xi}{2\sqrt{Dt}}$, this becomes:

$$c(x, t) = \int_{\beta}^{+\infty} \frac{2c_0}{\sqrt{\pi}} \exp(-\eta^2) d\eta \quad (2.13)$$

where $\beta = \frac{x}{2\sqrt{Dt}}$. This can be re-written as:

$$c(x, t) = \int_0^{+\infty} \frac{2c_0}{\sqrt{\pi}} \exp(-\eta^2) d\eta - \int_0^{\beta} \frac{2c_0}{\sqrt{\pi}} \exp(-\eta^2) d\eta \quad (2.14)$$

Since,

$$\int_0^{+\infty} \exp(-\eta^2) d\eta = \frac{\sqrt{\pi}}{2} \quad (2.15)$$

and,

$$\text{erf}(\beta) = \frac{2}{\sqrt{\pi}} \int_0^{\beta} \exp(-\eta^2) d\eta \quad (2.16)$$

$c(x, t)$ results accordingly:

$$c(x, t) = c_0 \left[1 - \text{erf}\left(\frac{x}{2\sqrt{Dt}}\right) \right] \quad (2.17)$$

Fig. 2.2 shows a plot of Eq. (2.17) for four different values of $L = 2\sqrt{Dt}$. This quantity, often denoted as the *diffusion length*, is a scaling factor for the diffusion and in an atomistic view represents the root mean square displacement of an atom moving on the surface according to a random walk mechanism.

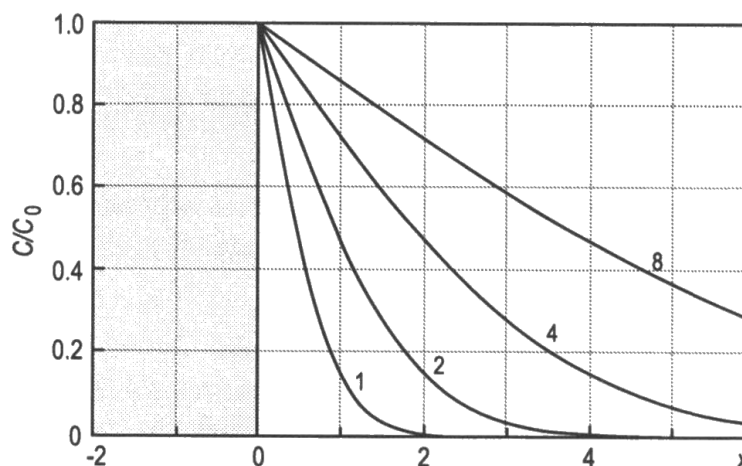


FIG. 2.2. Diffusion profiles from a source of constant concentration. The concentration normalized to the constant initial concentration c_0 is plotted for four different values of the diffusion length L .

2.3 State of the art

The main results achieved so far in literature for the surface diffusion of Ge atoms on Si(001) surface are presented here below.

Mo and Lagally⁴ experimentally showed that the diffusion process follows an anisotropic Arrhenius behaviour due to the 2×1 reconstruction with dimer rows occurring on the (001) surface. The surface mass transport of Ge on Si has been experimentally studied on a *macroscopic* scale (about 10^{-3} m) by directly measuring the diffusion length using Auger Electron Spectroscopy⁵, while diffusion activation energies on a *microscopic* length scale (varying in the range 0.7 eV – 1.3 eV) have been obtained by monitoring the island density distribution around preferential nucleation sites^{4,6,7}. The latter method exploits the formation of denuded zones free of 3D islands originated by the competition between the random nucleation on a flat surface and the preferential nucleation at energetically favoured sites. The width of this denuded zones is essentially determined by the local kinetics of diffusion, and thus its temperature dependence gives direct access to the activation energies for adatom surface diffusion.

Theoretical studies of the diffusion of Ge atoms on Si(001)- 2×1 surface were generally carried out by molecular dynamics methods^{8,9}. These studies confirmed that the diffusion follows an anisotropic Arrhenius behavior with the direction of easy diffusion parallel to the dimer rows on the (001)- 2×1 surface. According to this calculations the diffusion along the dimer rows, the *easy diffusion*, is characterized by an activation energy $E_A = 0.73$ eV, while in perpendicular direction, the *hard diffusion*, the activation energy is $E_A = 1.17$ eV. In *ab initio* studies by Density Functional

Theory (DFT) in the Local Density Approximation (LDA)¹⁰ the activation barriers for diffusion in fast and slow directions were found to be 0.62 and 0.95 eV, respectively.

The surface diffusion, and more generally the growth mode of Ge on Si, can be controlled by using surface-active species (surfactants)^{11,12}, that strongly modifies the surface free energy of both Ge and Si¹³. Tromp and Reuter¹⁴ showed that As and Sb surfactants are energetically driven to float at the surface during growth, thus providing a large driving force for the Ge atoms to incorporate into the surface which can suppress the surface diffusion and prevent island formation. An opposite behaviour is expected when carbon is used as a surfactant, since the repulsive chemical interaction between Ge and C atoms¹⁵ forces carbon into the shallow layers of the substrate¹⁶. Thus Ge atoms lie in the top-layer on the rough and strained interface created by the underlying C-rich layers. It has been proposed by several authors^{17,18} that this scenario would be responsible for a strong reduction of the Ge diffusion coefficient. However, a direct experimental demonstration of the modulation of the diffusion length of Ge adatoms on a carbon pre-covered Si(001) surface is still lacking and will be addressed in this work.

2.4 Experiment and methods

To study the surface diffusion of Ge on Si(001) surface, we made use of Ge stripes (width $\sim 3\div 5\ \mu\text{m}$) obtained by a photo-lithographic patterning of pure Ge thin films (thickness $\sim 50\ \text{nm}$) and acting as sources for Ge diffusion on the Si substrate (see Fig. 2.3). The Ge film has been grown by Low Energy Plasma Enhanced Chemical Vapour Deposition (LEPECVD)¹⁹ at $700\ ^\circ\text{C}$ with a deposition rate of $0.15\ \text{nm/s}$. An AZ5214 photo-resist has been spin-coated on its surface at $4000\ \text{rpm}$ (thickness $\sim 1.8\ \mu\text{m}$), and then exposed for $20\ \text{s}$ to a pattern of intense UV light to define the stripe features. A broad-band Hg lamp in a Karl Suss MA56 mask aligner (Hg lamp power $\sim 350\ \text{W}$) has been used. A post-exposure bake at $105\ ^\circ\text{C}$ is performed before developing with AZ400K developer, able to remove the soluble exposed part of the resist. Finally, a reactive ion etching (RIE) has been performed to define the Ge stripes avoiding significant undercutting.

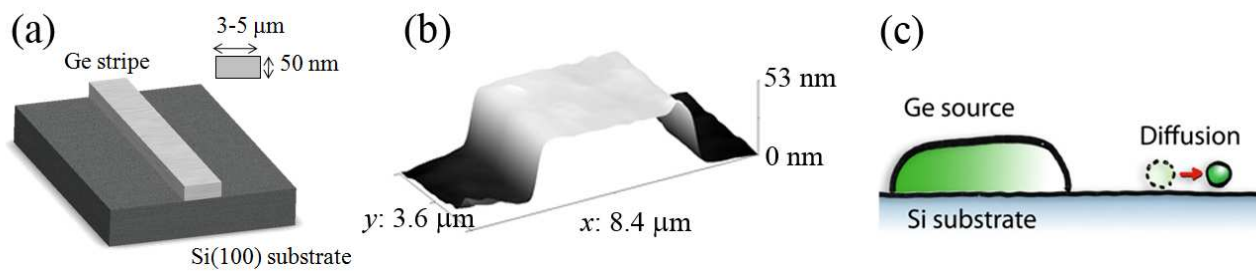


FIG. 2.3. (a) schematic representation of a Ge stripe obtained by a photo-lithographic patterning of pure Ge thin films grown by LEPECVD on a Si(001) substrate. (b) Representative 3D Atomic Force Microscopy image of a portion of a Ge stripe. (c) Schematic cartoon showing the main idea of the diffusion experiment: the stripe acts as Ge source for atom surface diffusion directly placed on the sample surface.

Before to insert the samples in the Ultra High Vacuum (UHV) analysis chamber of the SAM microscope (base pressure 5×10^{-10} torr), removal of native silicon oxide and germanium oxide has been obtained by using a diluted HF solution at 10 % for 30 s at room temperature (RT). Surface contaminations have been removed by *in-situ* low-temperature out-gassing ($T \leq 500$ °C) and Ar⁺ ion sputtering. The ions were accelerated to 4 keV kinetic energy with a beam current of ~ 0.4 μA; the ion beam had a spot size of about 0.5×1 mm² and has been rastered over an area of 10×10 mm² (greater than the whole sample surface), hitting the sample with a takeoff angle of 30°. A PHI 660 Scanning Auger Microscope has been used for the spatially resolved chemical characterization of the samples (for an extensive discussion of the basic physical principles and of the analysis methods underlying the Scanning Auger Microscopy (SAM) the reader is invited to make reference to Panel A).

To investigate the surface diffusion in presence of carbon, we exploited the presence of C on the Si surface due to adsorption of CO, CO₂ and carbon hydrogenates, as revealed by Auger analysis performed after the insertion of the sample in the vacuum system. A pure carbon layer has been then obtained by an *in-situ* low-temperature out-gassing. In fact, a several minutes long out-gassing performed at 500 °C results in a complete O desorption leaving a C layer on the surface. No residual oxygen was observed within the detection sensitivity limit of 1 %. The residual carbon layer has been reproducibly found on several samples after the out-gassing. Hydrogen contamination, undetectable with the Auger probe, is reasonably eliminated during the out-gassing²⁰.

The stripes act as Ge sources directly placed on the sample surface, and a continuous diffusion profile is obtained after annealing at high temperatures (600, 625, 650, 670 and 700 °C) in the UHV analysis chamber of the SAM microscope. The samples have been annealed by Joule heating running a DC current through the Si substrate, using a home-made sample heater (see Fig. 2.4). The temperature has been measured using a single wavelength optical pyrometer opportunely

calibrated using a type-N thermocouple. The temperature stabilization takes less than 30 s, and the temperature spatial distribution is highly uniform in the investigated area, as demonstrated by the reproducibility of the diffusion profiles measured in different zones of the sample surface. The base pressure during the annealing time was always better than 1×10^{-9} torr. The use of lithographically defined Ge stripes as sources of diffusion allows for a direct measurement of the long and short range diffusion parameters at the same time.

To characterize *in situ* the Ge diffusion profiles and the thickness of the Carbon layer, we have monitored the intensities of Ge LMM (~ 1150 eV), Si LMM (~ 90 eV), Si KLL (~ 1610 eV) and C KLL (~ 270 eV) Auger lines as a function of distance from the Ge stripe.

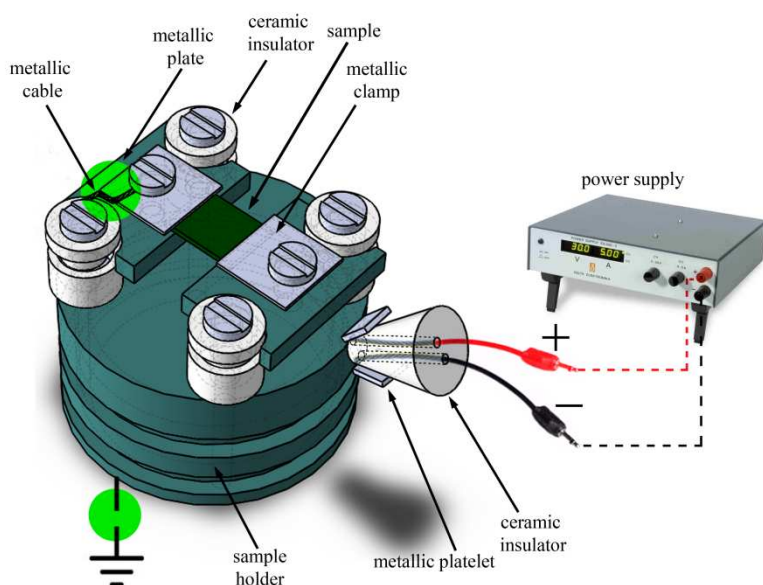


FIG. 2.4. The sample is free-standing with its edges resting on two metallic plates isolated from the metallic sample holder using ceramic nuts and washers. The sample is then blocked by means of metallic clamps tightened with metallic screws. One side of the sample (the left one in the image) is electrically connected to the sample holder through a metallic wire (highlighted by the green circle). The annealing is performed by running a direct current into the sample. The current is supplied by an external power generator connected to the sample by means of an *electric finger* made of a ceramic insulator and two metallic platelets as terminals. The positive terminal is connected to the right side of the sample through the metallic plate, while the negative one is connected to the left side through the sample holder.

2.5 Ge surface diffusion on a *C-free* Si(001) surface

During the annealing process the Ge moving from the stripe diffuses on the Si surface forming a continuous over-layer (OL). Fig. 2.5(a) shows the SEM micrograph of the stripe before (upper inset) and after (main panel) a 10 min annealing at 600 °C. Before the annealing, the surface contaminants have been completely removed by using an *isotropic* ion sputtering (see inset). After annealing, surface roughness was about 0.2 nm as determined by Atomic Force Microscopy (AFM) analysis. The shading at the sides of the stripe in Fig. 2.5(a) result from the compositional contrast of the secondary electron emission between Ge, diffused on the surface, and Si in the substrate.

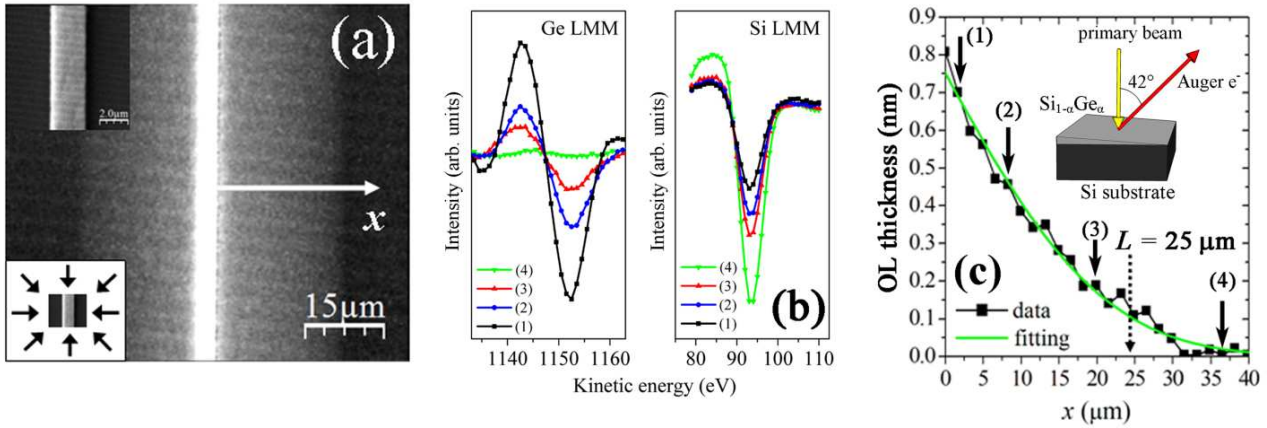


FIG. 2.5. (a) SEM image of the stripe after annealing at 600 °C for 10 min showing a bilateral diffusion (grey shaded area). Surface contaminations have been removed by using an isotropic ion sputtering (as schematically shown in the inset in the bottom-left corner). In the top-left corner is shown the SEM image of the stripe before the annealing. (b) Ge LMM and Si LMM Auger lines measured at different distances from the stripe as indicated by the solid black arrows in the panel (c). (c) Over-layer thickness as a function of the distance from the source as determined by SAM analysis (black squares). The green curve is the best fitting of the experimental data using the analytical solution of a 1D diffusion model (see text). Inset: schematic of the detection geometry and of the diffusion region as represented within the discrete layer model.

2.5.1 Discrete layer model of the SiGe over-layer

Spatially resolved Auger analysis allowed to measure the thickness and composition of the OL along the diffusion profile as a function of the distance, x , from the stripe. Fig. 2.5(b) shows the Ge LMM and Si LMM Auger lines (kinetic energy of 1150 eV and 90 eV) measured at different distances from the stripe after a 10 min annealing at 600 °C and Fig. 2.5(c) represent the corresponding OL behaviour. The determination of the OL thickness has been obtained by fitting the Ge LMM and Si LMM peak-to-peak intensities²¹ measured as a function of x , with a discrete layer model²² where the OL is approximated by a $\text{Si}_{1-\alpha}\text{Ge}_\alpha$ thin film of variable thickness and uniform composition α . Within this discrete layer model the Si LMM and Ge LMM Auger line intensities are given by the following relations:

$$I_{\text{Si}}(x) = \int_0^{h(x)} I_0^{\text{Si}} \exp\left(-\frac{z}{\lambda_{\text{Si}} \cos \delta}\right) dz + \int_{h(x)}^{+\infty} I_0^{\text{Si}} \exp\left(-\frac{z}{\lambda_{\text{Si}} \cos \delta}\right) dz \quad (2.18a)$$

$$I_{\text{Ge}}(x) = \int_0^{h(x)} I_0^{\text{Ge}} \exp\left(-\frac{z}{\lambda_{\text{Ge}}^{\text{SiGe}} \cos \delta}\right) dz \quad (2.18b)$$

where $h(x)$ is the over-layer thickness, I_0^{Si} and I_0^{Ge} include the atomic volume densities, the primary beam intensity, the spectrometer efficiency and Auger process-related parameters for the given transitions (see Panel A for the complete analytical expression); $\lambda_{\text{Ge}}^{\text{Si}} = 2.66 \text{ nm}$ ²³,

$\lambda_{Ge}^{Ge} = 2.16 \text{ nm}^{23}$, and $\lambda_{Ge}^{SiGe} = \alpha \lambda_{Ge}^{Ge} + (1 - \alpha) \lambda_{Ge}^{Si}$ are the Inelastic Mean Free path (IMFP) for Ge LMM Auger electrons propagating in a Si, Ge and SiGe matrix, respectively; $\lambda_{Si} = 0.52 \text{ nm}^{23}$ is the IMFP for Si LMM Auger electrons (in this case the dependence from the matrix is negligible due to the low kinetic energy, 90 eV, of this electrons); $\delta \approx 42^\circ$ is the angle between the normal to the surface and the outgoing direction of Auger electrons collected by the energy analyzer (see inset in Fig. 2.5(c)). The first term in the Eq. (2.18a) is related to the contribution to the Si LMM intensity of the Si intermixed inside the OL, while the second term accounts for the attenuation of the substrate signal due to the presence of the OL. The Eq. (2.18b) for the Ge LMM intensity contains only the term related to Auger electrons originated inside the over-layer (see inset in Fig. 2.5(c)). The data analysis takes advantage of the following facts: (i) the Ge LMM Auger electrons bring information from the whole OL because their IMFP is greater than its maximum thickness, and (ii) the Si LMM decay channel is more suitable than the Si KLL one for the investigation of the OL, because the Si LMM intensity is strongly affected by the OL thickness (Si LMM electrons have an IMFP 5 times shorter than that of Si KLL ones²³).

The expressions for the Si LMM and Ge LMM Auger line intensities in Eqs. (2.18) can be made usefully independent from the instrumentation and Auger process related parameters by the normalization with the standard intensities acquired on bulk samples at the same primary beam intensity:

$$I_{Ge}^{STD} = I_0^{Ge-STD} \lambda_{Ge} \quad (2.19a)$$

$$I_{Si}^{STD} = I_0^{Si-STD} \lambda_{Si} \quad (2.19b)$$

where I_0^{Si-STD} and I_0^{Ge-STD} include the atomic volume densities, the primary beam intensity, the spectrometer efficiency and Auger process-related parameters in case of bulk emission (see Panel A for the complete derivation of these expressions).

Resolving the integrals and normalizing $I_{Si}(x)$ and $I_{Ge}(x)$ with I_{Si}^{STD} and I_{Ge}^{STD} , respectively, the expressions in Eqs. (2.18) become:

$$\frac{I_{Si}(x)}{I_{Si}^{STD}} = \frac{(n_V^*)_{Si}}{(n_V)_{Si}} \left[1 - \exp\left(-\frac{h(x)}{\lambda_{Si} \cos \delta}\right) \right] + \exp\left(-\frac{h(x)}{\lambda_{Si} \cos \delta}\right) \quad (2.20a)$$

$$\frac{I_{Ge}(x)}{I_{Ge}^{STD}} = \frac{(n_V^*)_{Ge}}{(n_V)_{Ge}} \left[1 - \exp\left(-\frac{h(x)}{\lambda_{Ge}^{SiGe} \cos \delta}\right) \right] \quad (2.20b)$$

where n_V is the volume atomic density in the bulk materials (44.2 atoms/nm³ for Ge, and 49.9 atoms/nm³ for Si), and n_V^* is the elemental volume atomic density in the SiGe over-layer. Since the Ge concentration within the OL is given by:

$$\alpha = \frac{(n_V^*)_{Ge}}{(n_V^*)_{Si} + (n_V^*)_{Ge}} \quad (2.21)$$

the atomic densities n_V^* for Ge and Si in the OL fulfil the relation:

$$(n_V^*)_{Si} = (n_V^*)_{Ge} \frac{1 - \alpha}{\alpha} \quad (2.22)$$

Moreover, supposing that the atomic density of Ge in the OL is linearly correlated with its value in the bulk case, i.e.:

$$(n_V^*)_{Ge} \approx \alpha (n_V)_{Ge} \quad (2.23)$$

then the normalized Si LMM and Ge LMM Auger intensities become:

$$\frac{I_{Si}(x)}{I_{Si}^{STD}} = (1 - \alpha(x)) \frac{(n_V)_{Ge}}{(n_V)_{Si}} \left[1 - \exp\left(-\frac{h(x)}{\lambda_{Si} \cos \delta}\right) \right] + \exp\left(-\frac{h(x)}{\lambda_{Si} \cos \delta}\right) \quad (2.24a)$$

$$\frac{I_{Ge}(x)}{I_{Ge}^{STD}} = \alpha(x) \left[1 - \exp\left(-\frac{h(x)}{\lambda_{Ge}^{SiGe} \cos \delta}\right) \right] \quad (2.24b)$$

By solving numerically the Eqs. (2.24), the two unknown values $\alpha(x)$ and $h(x)$ can be determined at a given position x . For the annealing at 600 °C an average Ge relative concentration of about $0.81 \pm 0.05^{**}$ has been found, in good agreement with the values found in literature for the case of MBE deposition²⁴. The value of composition, as obtained by the discrete layer model, exhibits a relative dispersion between the several data sets of about 12 %. This dispersion is comparable with 1) the uncertainty introduced by the physical quantities of the model (namely the IMFPs, for which has been assumed an error of lower than 5%, which is commonly accepted) and 2) the possible systematic errors induced by a gradient of the composition inside the over-layer along its depth. It has been verified that, even in the extreme case of a triangular profile of the composition inside the OL, the mean composition predicted by the model lies within the dispersion boundaries.

2.5.2 Temperature dependence of the diffusion parameters

The dependence of the OL thickness as a function of x (Fig. 2.5(c)) is attributed to the diffusive motion of the atoms from the source, and can be well understood within the framework of the analytical diffusion model presented in the Section 2.2 applied to the one-dimensional case (1D) due to the geometry of the experiment. The model strictly applies for the case of negligible intermixing between the migrating species and the substrate atoms. The hypothesis is not strictly verified in the present case as we found a partial Si incorporation inside the over-layer from the

** The behaviour of the Ge concentration α as a function of the distance x from the stripe as determined with the discrete layer model is shown in Fig 3.7(b) of Chapter 3.

Auger analysis (see above). Indeed, considering that the local atomic motion is fast compared with the Ge flux²⁵, the Si intermixing occurs on a time scale much shorter than the diffusion motion of the Ge atoms from the stripe, and the model can be generalized by supposing that the Ge surface diffusion is mediated by Si incorporation inside the over-layer. The correspondent diffusion parameters obtained by the model are essentially related to a SiGe alloy with high Ge content, and we will refer to them as Ge effective diffusion parameters.

Within this scenario the gradient in the chemical potential induced by the difference of Ge surface concentration between the stripe and the surrounding regions is the driving force for the surface diffusion. In our case the Ge volume atomic density does not vary significantly as a function of the distance from the stripe and thus the Ge surface concentration is essentially proportional to the Ge coverage h , which thus follows the 1D Fick's second law expressed by Eq. (2.8):

$$D \frac{\partial^2 h}{\partial x^2} = \frac{\partial h}{\partial t} \quad (2.25)$$

where t is time, and D is the diffusion coefficient. The Ge stripe has an initial surface concentration distribution with a step-like shape, and the height at the boundary is essentially maintained at a constant value during the annealing:

$$h(x, t) = 0 \quad t = 0, \quad x > 0 \quad (2.26)$$

$$h(x, t) = h_0 \quad \forall t \in [0, \tau], \quad x < 0 \quad (2.27)$$

where τ is the annealing time. This initial and boundary conditions represent the case of diffusion from a source of constant concentration, as discussed in Section 2.2.3. The solution of the diffusion equation, and thus the Ge coverage along the diffusion profile is borrowed from the Eq. (2.17) and given by the following relation:

$$h(x, t) = h_0 \left[1 - \operatorname{erf} \left(\frac{x - x_0}{L} \right) \right] \quad (2.28)$$

where x_0 is the position of the stripe edge and $L = 2\sqrt{D\tau}$ is the diffusion length. The green curve in Fig. 2.5(c) is the best fitting of the experimental data using Eq. (2.28) for a 10 minutes annealing at 600 °C. The diffusion lengths represented in Fig. 2.6(a) were determined similarly for each couple of temperature and annealing time on data taken at three temperatures with several annealing times. Then the diffusion coefficient at each temperature is extracted by linearly fitting the $L^2/4$ values for each temperature in Fig. 2.6(a). They are shown in Fig. 2.6(b) as an Arrhenius plot of D ($\ln D$ vs $1/T$), and the green line is the fitting of the data with the corresponding Arrhenius law:

$$D = 6.4 \times 10^{-2} \exp \left(-\frac{1.24 \text{ eV}}{K_B T} \right) \frac{\text{cm}^2}{\text{s}} \quad (2.29)$$

The values found for the diffusion constant $D_0 = 6.4 \cdot 10^{-2} \text{ cm}^2/\text{s}$ and for the activation energy $E_A = 1.24 \text{ eV}$ are in good agreement with both the experimental^{5,6} and theoretical^{9,10} literature. A strong anisotropy of the surface diffusion has been experimentally demonstrated⁴ and a theoretical model has been proposed^{9,10}, where the diffusion parallel to the dimer rows, the *easy diffusion*, is characterized by an activation energy $E_A = 0.73 \text{ eV}$ and a diffusion constant $D_0 = 4.3 \times 10^{-4} \text{ cm}^2/\text{s}$, and in perpendicular direction, the *hard diffusion*, by $E_A = 1.17 \text{ eV}$ and $D_0 = 2.8 \times 10^{-3} \text{ cm}^2/\text{s}$ ⁹ (see Fig. 2.3(c) and 2.3(d)). We notice that in our setup Eq. (2.28) is used to describe the surface mass transport over a length scale of a few tens of micrometers, which exceeds significantly the typical width of single terraces and of the dimer rows domains. Thus, the measured diffusion coefficient describes the diffusion averaged over both dimer orientations domains and across their boundaries.

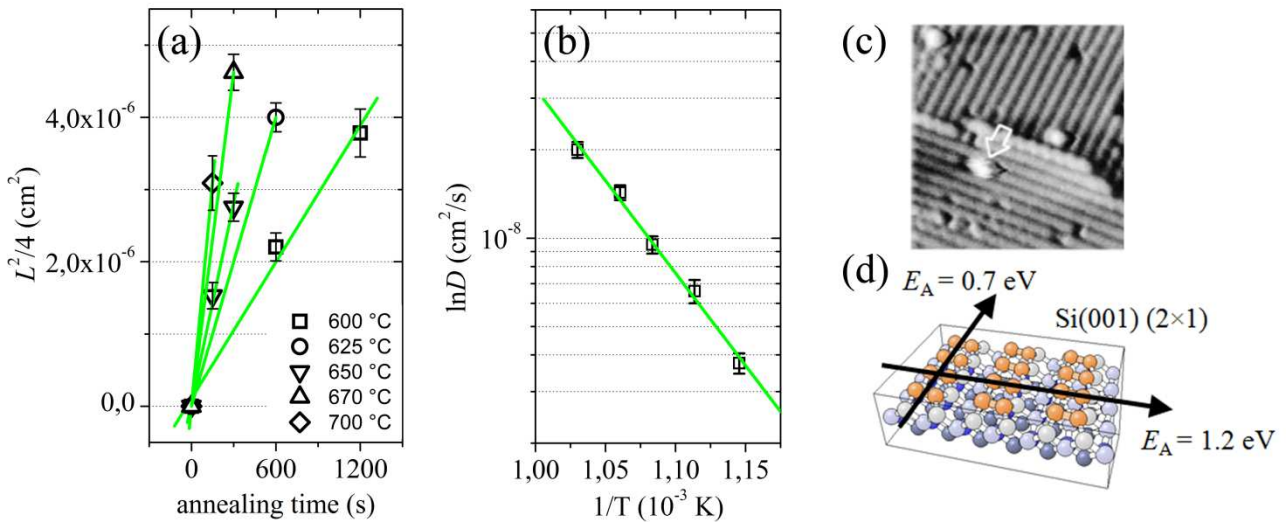


FIG. 2.6. (a) $L^2/4$, with L diffusion length, plotted as a function of the annealing time, τ , for different temperatures (600, 625, 650, 670, and 700 °C). Linear fittings of the experimental data were used to extract the values of the diffusion coefficient, D , at different temperatures ($L^2 = 4D\tau$). (b) The diffusion coefficient has an exponential temperature dependence given by an Arrhenius law: diffusion constant $D_0 = 6.4 \cdot 10^{-2} \text{ cm}^2/\text{s}$, activation energy $E_A = 1.24 \text{ eV}$. (c) STM image of the Si(001) surface showing the 2x1 reconstruction with dimer rows²⁶; different terraces show a different orientation of the dimer rows. (d) Schematic representation of the diffusion anisotropy on the reconstructed (001) surface⁹.

2.5.3 Time Dynamics of diffusion flux

In this section we present the analytical description of the time dynamics of the atomic fluxes during surface diffusion from a source stripe. This results will be useful in the following discussion of the self-assembly growth process of SiGe islands originated along the continuous diffusion profile (see Chapter 3).

The flux of diffusing atoms $J(x,t)$ represents the net number of Ge atoms that in unit time t cross a section of unit length parallel to the stripe at a distance x from it. In the one-dimensional case $J(x,t)$ can be written as:

$$J(x,t) = -D \frac{\partial}{\partial x} c(x,t) = -D \frac{\partial}{\partial x} [h(x,t) \cdot (n_V^*)_{Ge}] \quad (2.30)$$

where $(n_V^*)_{Ge}$ is the volume atomic density of Ge atoms inside the over-layer and can be derived by the Eq. (2.23). The diffusion profile $h(x,t)$ assumes the form given by the Eq. (2.28) in case of diffusion from a source stripe of constant height having its edge at $x_0 = 0$:

$$h(x,t) = \int_{\xi}^{+\infty} \frac{h_0}{\sqrt{\pi Dt}} \exp\left(-\frac{\xi^2}{4Dt}\right) d\xi \quad (2.31)$$

Assuming that:

$$g(\xi,t) = \frac{h_0}{\sqrt{\pi Dt}} \exp\left(-\frac{\xi^2}{4Dt}\right) \quad (2.32)$$

and,

$$\frac{\partial}{\partial \xi} G(\xi,t) = g(\xi,t) \quad (2.33)$$

then,

$$h(x,t) = G(+\infty,t) - G(x,t) \quad (2.34)$$

The flux $J(x,t)$ can be then obtained accordingly:

$$J(x,t) = D(n_V^*)_{Ge} \frac{\partial}{\partial x} G(x,t) = D(n_V^*)_{Ge} g(x,t) \quad (2.35)$$

and thus using the Eq. (2.32):

$$J(x,t) = h_0(n_V^*)_{Ge} \sqrt{\frac{D}{\pi}} \left(\frac{1}{\sqrt{t}}\right) \exp\left(-\frac{x^2}{4Dt}\right) \quad (2.36)$$

which represents the time and spatial dependence for the flux of diffusing atoms from the stripe.

Fig. 2.7 shows the flux $J(x,t)$ as a function of the time t as derived by the Eq. (2.36) for different distances x from the stripe in case of annealing at 600 °C and 700 °C. The parameters h_0 and D have been deduced by fitting the experimentally measured diffusion profiles with the Eq. (2.28). For both temperatures, in case of spatial positions close to the stripe edge, the atomic flux is huge and very intense showing a super-elongation at earlier times and then a progressive reduction for longer times. On the contrary for positions farther away from the stripe edge, $J(x,t)$ is very low without showing any super-elongation at the beginning of the annealing process. This different

behavior is one of the main causes for the spatial dependence of density and size of SiGe islands nucleated during the diffusion process, as it will be discussed later on the Chapter 3.

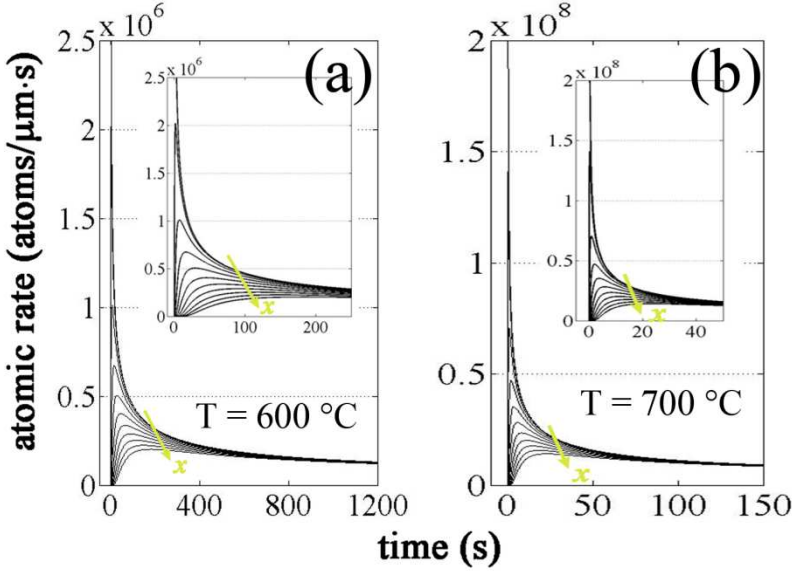


FIG. 2.7. Flux $J(x,t)$ of diffusing Ge atoms as a function of the time t as derived by the Eq. (2.36) for different distances x from the stripe in case of annealing at 600 °C (a) and 700 °C (b). The parameters h_0 and D have been deduced by fitting the experimentally measured diffusion profiles with the relation (2.28).

2.5.4 Scaling behavior of surface diffusion from a stripe

The formation of an interface is a complex process influenced by a large number of different factors, nevertheless in some situations, like in thin film growth, there is a small numbers of basics laws determining the dynamics of the process and its dependence on time and length scales of observation. The aim of this paragraph is the investigation of the scaling behavior of the surface diffusion process from a stripe source, which will be described and interpreted using the language of fractals.

Isotropic fractals are *self-similar*: they are invariant under *isotropic* scale transformations. In contrast, surfaces are generally invariant under *anisotropic* transformations and belong to the broader class of *self-affine* fractals. For investigating the scaling behavior of a surface it should be introduced a special subclass of anisotropic fractals, described by single-valued functions called *self-affine functions*²⁷. The height function $u(x,t)$ is self-affine if it respects the following relation:

$$u(x,t) = b^{-\alpha} u(bx, b^z t) \quad (2.37)$$

where α is called self-affine exponent, and z is the dynamic exponent. This equation formulates in general terms the fact that a self-affine function must be rescaled in a different way horizontally, vertically and in time: if the function is blown up with a factor b horizontally $x \rightarrow bx$ () and a factor

b^z in time ($t \rightarrow b^z t$), it must be blown up with a factor b^α vertically ($h \rightarrow b^\alpha h$) in order that the resulting object overlaps the object in the previous generation. To describe the evolution of the surface quantitatively, one can compute the time dependent height-height correlation function

$$U(x, t) = \langle [u(x + \hat{x}, t) - u(\hat{x}, t)]^2 \rangle \quad (2.38)$$

which contains most of the relevant statistical information about the surface. The averaging is done over the \hat{x} variable. If $u(x, t)$ is self-affine the height-height correlation function has the form²⁸:

$$U(x, t) = 2[w(t)]^2 f\left(\frac{x}{\chi(t)}\right) \quad (2.39)$$

where $f(x)$ is called scaling function. Here $w(t)$ is the interface width defined by $w(t) = \langle [u(x, t) - \bar{u}(t)]^2 \rangle$, where $\bar{u}(t)$ is the average height of the profile obtained over a length scale l , and $\chi(t)$ is the lateral correlation length. By looking at how these parameters evolve with time, one can characterize the dynamic behavior of the process. Since $u(x, t)$ obeys the Eq. (2.37), this is valid also for $w(t)$ and $\chi(t)$. The solutions of the corresponding ‘functional equations’ are in the form of power laws:

$$w(t) \approx t^\beta \quad (2.40)$$

$$\chi(t) \approx t^{1/z} \quad (2.41)$$

where $\beta = \alpha/z$ is called growth exponent.

We are now interested in determining the scaling exponents characterizing the surface diffusion process from a source stripe. In this scenario, the height interface, $u(x, t)$, is determined by the diffusion profile $h(x, t)$ given by the Eq. (2.28). If this profile is *self-affine*, then on rescaling it vertically:

$$h \rightarrow b^\alpha h \quad (2.42)$$

horizontally:

$$x \rightarrow bx \quad (2.43)$$

and in time:

$$t \rightarrow b^z t \quad (2.44)$$

we should obtain an interface that is statistically invariant from the original one. Substituting the Eqs. (2.42)-(2.44) into the Eq. (2.28), we find:

$$b^\alpha h(x, t) = h_0 \left[1 - \operatorname{erf}\left(\frac{bx}{2\sqrt{Db^z t}}\right) \right] \quad (2.45)$$

and thus,

$$h(x, t) = b^{-\alpha} h_0 \left[1 - \operatorname{erf}\left(b^{1-\frac{z}{2}} \frac{x}{2\sqrt{Dt}}\right) \right] \quad (2.46)$$

To find the correct exponents we require that the profile $h(x,t)$ must be invariant under the transformation (2.45), and thus each term on the right side of the Eq. (2.46) must be independent of b , which implies:

$$\alpha = 0, \quad \beta = 0, \quad z = 2 \quad (2.47)$$

In this particular case where α and β are equals to zero, and $z = \alpha/\beta$ is a singularity assuming an integer value, the dynamic evolution of the height profile $h(x,t)$ is no longer described by a power law as defined by the Eq. (2.40), but indeed the interface width $w(t)$ scales logarithmically with time at early times²⁹.

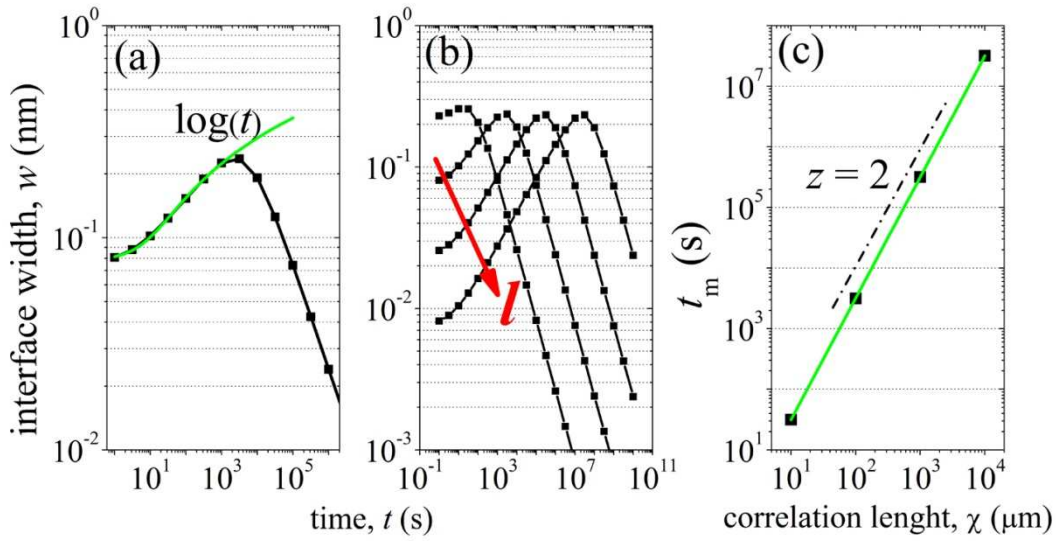


FIG. 2.8. (a) Log-log plot of the interface width w (black squares) obtained in case of diffusion at 600 °C ($h_0 = 0.8 \text{ ML}$, $D = 0.3 \mu\text{m}^2/\text{s}$) over a length scale $l = 10^2 \mu\text{m}$ as a function of the time t . The green curve is the best fitting of the portion at early times using a logarithmic function. (b) Time dependence of the interface width w (black squares) at 600 °C obtained over different length scales $l = 10, 10^2, 10^3$, and $10^4 \mu\text{m}$. (c) Log-log plot of the time t_m at which w reaches its maximum as a function of the correlation length $\chi = l$.

In the context of surface diffusion exploring here, the interface is represented by the separation surface between the SiGe over-layer induced by the diffusion and the vacuum. The interface width w can be thus mathematically determined as:

$$w(t) = \sqrt{\frac{1}{l} \int_0^l \left[h_0 \left(1 - \operatorname{erf} \left(\frac{x}{2\sqrt{Dt}} \right) \right) - \frac{1}{l} \int_0^l h_0 \left(1 - \operatorname{erf} \left(\frac{x}{2\sqrt{Dt}} \right) \right) dx \right]^2 dx} \quad (2.48)$$

where l is the length scale over which the diffusion is studied, and h_0 and D are the Ge coverage at $x = 0$ and the Ge diffusion coefficient, respectively, experimentally determined by fitting the measured diffusion profile with the solution of the diffusion equation (see Section 2.5.2). In Fig.

2.8(a) the interface width w obtained in case of diffusion at 600 °C ($h_0 = 0.8 \text{ ML}$, $D = 0.3 \mu\text{m}^2/\text{s}$) over a length scale $l = 10^2 \mu\text{m}$ is plotted as a function of the time t . It is clearly seen that as t approaches to zero, w is well fitted by a logarithmic function of the time. Fig. 2.8(b) reports the time dependence of the interface width obtained over different length scales $l = 10, 10^2, 10^3, 10^4 \mu\text{m}$, showing a similar behaviour irrespectively from the value of l . The attainment of a maximum and the following decrease are both features common to all curves, while the time positions, t_m , at which this maximum is reached depends on the length scale l , suggesting that this phenomenon constitutes a *finite size effect*. In fact, during the diffusion process the portion of surface whose height profile depends on that of the neighbouring regions grows with time, i.e. the lateral correlation length $\chi(t)$ increases as a function of time. When $\chi(t)$ reaches the length scale l over which the system is studied, the entire profile becomes correlated and the interface width w starts to decrease. In Fig. 2.8(c) the time t_m at which w reaches its maximum is plotted as a function of χ . This dependence is well described within the power law:

$$\chi \approx t_m^{1/2} \quad (2.49)$$

confirming that $z = 2$ as derived by the previous scaling argument. Comparing the Eq. (2.49) with $L = 2\sqrt{Dt}$, it is easy to understand that the diffusion length L plays the role of the correlation length during the diffusion process.

The set of scaling exponents defined by the Eq. (2.47) for the diffusion process from a source stripe and the correlation logarithmically decaying shown in Fig. 2.8 are also shared by the solutions of the Edwards-Wilkinson (EW) equation³⁰ in a (2+1)-dimensional space. This means that they belong to the same universality class, and thus they share the same symmetry properties and conservation laws. The EW equation can be seen as the stochastic version of the diffusion equation given in Eq. (2.7), and describes all the processes where a conservative relaxation mechanism is involved. A logarithmic scaling appears in case of Molecular Beam Epitaxy (MBE) when nucleation starts on the surface³¹, or negative Schwoebel barriers characterizes the step edges of the surface³². Drotar et al.³³ sustain that the scaling exponents defined by the Eq. (2.47) applies also in case of Low Pressure Chemical Vapour Deposition (LPCVD) when reemission phenomena of the vapour particles are taken into account. Moreover, theoretical approaches to domain-wall dynamics in magnetic ultrathin films³⁴, and in general the motion of driven interfaces in disordered media³⁵, are typically based on the EW equation with quenched disorder. In medicine, the dynamics of the tumor growth after stimulating the immune response with a strong neutrophilia around the tumor is compatible with EW universality class³⁶.

In this paragraph we studied the scaling behaviour of the surface diffusion process from a source stripe. We found that the diffusion profile is self-affine with a given set of scaling exponents (Eq. 2.47) belonging to the same universality class of the solutions of the EW equation. This opens to the possibility that the results found here, as for instance the law which regulates the modulation of diffusion as a function of a surfactant (see Section 2.6), could be applied also in cases of magnetic domain-wall and tumor growth dynamics, which are very different contexts from atom diffusion and SiGe growth.

2.6 Ge diffusion on a C covered Si(001) surface

2.6.1 Diffusion parameters vs C coverage

We discuss here the dependence of the Ge surface diffusion from the C coverage. It has been proposed by several authors^{17,18} that C surfactant can be used in order to control the size and density of self-assembled islands exploiting the C-induced reduction of the Ge diffusion coefficient. However, a direct experimental demonstration of the modulation of the diffusion length of Ge adatoms on a carbon pre-covered Si(001) surface is still lacking and will be addressed here below.

In order to compare the effect of different coverage in the same environmental conditions, we have produced a carbon coverage varying continuously from zero to about few mono-layers (MLs) along the direction y parallel to the stripe (see Fig. 2.9) according to the following procedure. An homogeneously carbon covered surface has been obtained as described in the experimental section (Section 2.4). Then, we used a metallic shutter plate parallel to the sample surface and placed between the sample and the Ion gun. In this way the portion of the sample surface masked by the shutter is not exposed to the ion beam irradiation. Thus the surface has been ion sputtered while the shutter, having an edge perpendicular to the stripe and parallel to the sample surface, was moved along the y direction. This allowed the exposure of an increasing portion of the surface with time. The sputtering direction has been kept fixed with projection along x in this case (instead of using the isotropic bombardment adopted before) in order to exploit the shutter motion. As a side effect, the C film is not removed from the area shadowed by the stripe (the right side of the stripes shown in Fig. 2.9 and in Fig. 2.10). The C coverage before Ge diffusion as a function of y has been determined by measuring the C KLL Auger line (kinetic energy of 270 eV and IMFP of 1 nm²³). Then its intensity variation has been fitted with a discrete layer model²² similar to the one used for Ge in the previous section, where C is considered to be at the top-most of the surface. This is

supported by the fact that for coverage greater than 0.2 ML carbon is preferentially found at surface sites³⁷.

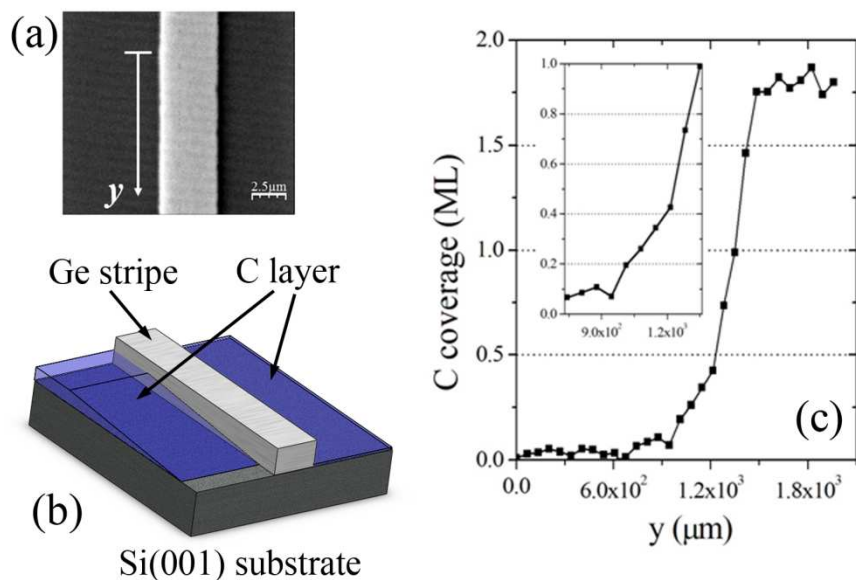


FIG. 2.9. (a) SEM image of the stripe before annealing: y coordinate is parallel to the stripe edge. (b) Schematic representation of the wedged carbon layer close to the stripe region as obtained by means of the anisotropic spatially modulated ion sputtering (see text). (c) Quantification of the wedged layer: the C coverage varies continuously from zero to about few mono-layers (MLs) along the direction y parallel to the stripe as determined by measuring the C KLL Auger line and fitting its intensity variation with a discrete layer model.

Fig. 2.10 shows the diffusion region for two different stripes after annealing for 10 min at 600 °C, where the modulation of the carbon coverage goes from the top (C-free) to the bottom (C-rich) of the figure. The effect of the carbon coverage on the Ge diffusion is dramatic: (i) the diffusion is fully inhibited on the right side of the stripe due to the shadowing effect on the ion beam produced by the stripe itself, which prevents the C removal from the Si surface; (ii) on the left side the diffusion is completely quenched when the coverage exceeded a critical value (which is about 1 ML), while in the C-free region the diffusion is favoured and a continuous variation of the diffusion length with the C coverage goes from one extreme to the other. This behaviour experimentally confirms the crucial role played by carbon in determining the Ge atomic mobility on Si(100).

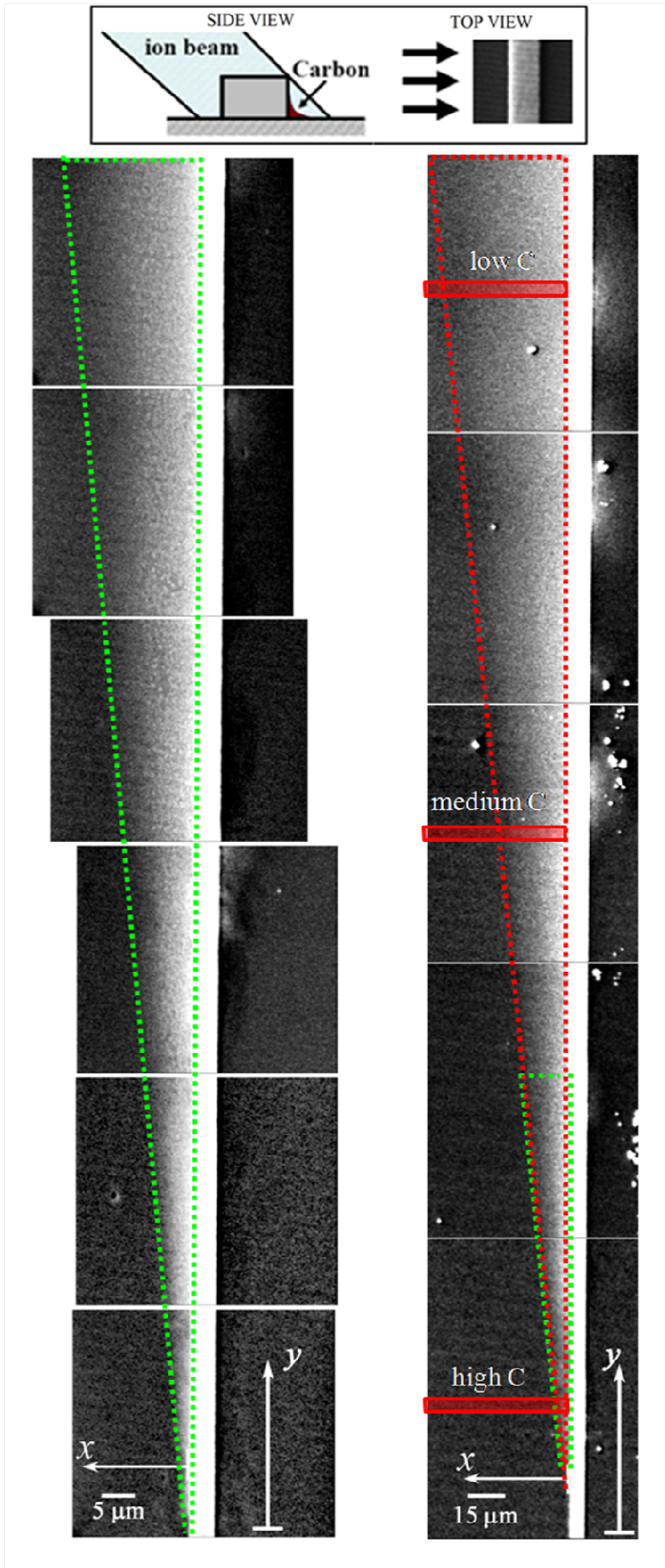


FIG. 2.10. Diffusion regions for two different stripes after annealing for 10 min at 600 °C in presence of a wedged C coverage. Transversal sputtering has been used in this case (see inset on top). For both stripes, in the C-rich region (at the bottom) the diffusion is inhibited, while in the C-free region (at the top) the diffusion is favoured with a continuous transition between these two extremes. The limit of the diffusion region as a function of the Carbon coverage is outlined by the green contour (left panel) and red contour (right panel, where the rescaled green contour is also reported as a comparison). The regions with low, medium and high C coverage used in Chapter 3 are shown by red shaded areas.

Spatially resolved Auger analysis allowed to obtain the Ge coverage profiles after annealing as a function of the distance from the stripe, x , for different pre-existing C thickness in the submonolayer regime, whose complete mapping is shown in figure 2.11(a). For the determination of the coverage profiles, the same model exploited in the C-free case is used. Then by applying again the 1D diffusion model already described, the diffusion length behaviour can be extracted by the map of the diffusion profiles. The correlation between the diffusion coefficient and the C coverage, shown in Fig. 2.11(b), is finally obtained by the relation $L = 2\sqrt{D\tau}$. It is worth noting here that the analytical solution of the 1D diffusion model used in the case of *C-free* diffusion still represents a good approximation for the experimental behaviour of the Ge coverage as a function of x . Although this model strictly applies only in case of perfect translational symmetry along the stripe, as in the C-free diffusion described in Section 2.5, it is still a good approximation in the present case: in fact the diffusion length varies slowly along the y direction from 0.35 μm to 30 μm over a 500 μm range (see right panel in Fig. 2.10). It is worth noting as well that by changing the C coverage from about 1 ML to 0.1 ML, a variation of about 4 orders of magnitude in the diffusion coefficient is obtained (see inset in Fig. 2.11(b)). This experimentally shows the possibility to tune the surface diffusion of Ge by using a controlled coverage of carbon, opening interesting perspectives in technological applications and device fabrication.

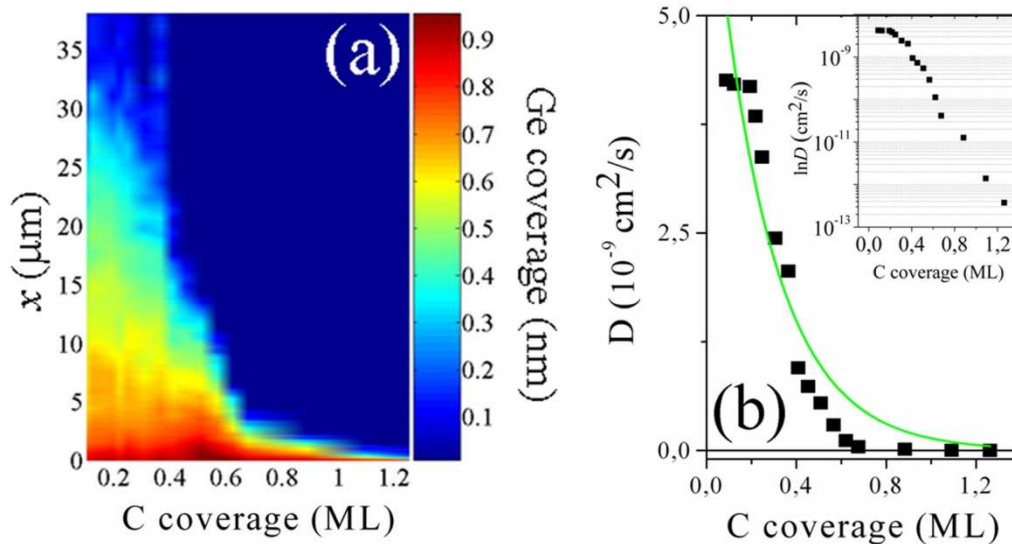


FIG. 2.11. (a) Auger mapping of the Ge diffusion profiles as a function of the C coverage. (b) Quantitative correlation between the Ge diffusion coefficient and the carbon coverage (linear plot): the green curve is the best fit of the experimental data (black squares) using a model where the activation energy for surface diffusion linearly depends on the carbon coverage (see text). The free parameters D_0^* and E_A^1 result from the fitting to be $5.68 \pm 0.33 \times 10^{-2} \text{ cm}^2/\text{s}$ and $0.29 \pm 0.04 \text{ eV}$, respectively. Inset: logarithmic plot of the diffusion coefficient vs the carbon coverage.

2.6.2 Physical origin of the C-induced modulation of atomic mobility

In this section the measured variation of the diffusion coefficient of Ge at 600 °C as a function of the carbon coverage in sub-monolayer regime is critically discussed. In Fig. 2.11(b) it is shown that the coefficient strongly decreases while increasing the surfactant coverage. The reduction of the atomic mobility in presence of carbon has been generally related to the strong chemical interactions among Si, C and Ge, and to the increment of surface roughness due to the C presence^{38,39,40}. Moreover, the activation energies for the surface diffusion have been theoretically shown to strongly depend on the local strain field experienced by the diffusing atoms on the substrate surface along their diffusion pathway^{41,42,43,44,45}.

It is shown here that a first order expansion of the activation energy $E_A = E_A^0 + E_A^1(\vartheta - \vartheta_0)$ as a function of the C coverage, ϑ (defined as the ratio between the thickness of the Carbon layer as determined by the discrete layer model and the thickness of one monolayer in the C diamond crystalline structure), is good enough to reproduce the gross features of the experimental dependence. The coverage threshold, ϑ_0 , is found to be 0.16 ± 0.06 ML according to the analysis developed in Section 3.3.3 of Chapter 3. Its physical origin is related to the tendency of carbon to intermix with Si into the shallow layers of the substrate rather than stay at the surface, as it will be extensively discussed later on in this section. The diffusion coefficient results accordingly:

$$D(\vartheta, T) = D_0^* \exp\left(-\frac{E_A^0}{K_B T}\right) \exp\left[-\frac{E_A^1}{K_B T}(\vartheta - \vartheta_0)\right] \quad (2.50)$$

where the pre-exponential factor, D_0^* , represents an average effective value of the diffusion constant in presence of a carbon coverage.

The main panel in Fig. 2.11(b) shows the best fit of the experimental data using Eq. (2.50), where E_A^0 was set to the value found in the case of C-free diffusion, and D_0^* and E_A^1 have been considered as free parameter, resulting to be $5.68 \pm 0.33 \times 10^{-2}$ cm²/s (the same as in the case of C-free diffusion within the experimental uncertainty) and 0.29 ± 0.04 eV, respectively.

On the basis of the experimental results reported here, we are not able to identify quantitatively a predominant factor among the chemical interactions, the surface roughness and the strain field determining the reduction of the Ge atomic mobility. However, combining our observations with well established results from the literature we propose that the most reasonable picture of the experiment is the diffusion of a SiGe top-layer with high Ge concentration ($\approx 80\%$) on a rough and compressively strained substrate surface. This scenario is discussed in the following paragraphs.

The increase in surface roughness with the carbon coverage can be induced by the tendency of C atoms to diffuse into the Si substrate^{46,47}. In fact, the C incorporation in Si is essentially driven by the competition between the tendency of C atoms to occupy favourable sites and the minimization of the lattice elastic energy associated with the c(4×4) reconstruction strain field³⁷. This process can result in the formation of separated reconstruction domains and in the increase of the roughness. Torigoe *et al.*⁴⁸ gave experimental and theoretical evidence for a monotonic dependence of the activation energy for surface diffusion by the surface roughness, which is shown to increase for higher carbon coverage at a Si surface. We measured by AFM the post-annealing surface rms roughness, which increases with the C coverage from 0.20 ± 0.04 nm in the C-free regions up to 0.35 ± 0.05 nm in the C-rich regions. Thus the roughness seems to play a role in the observed variation of the diffusion parameters.

In the case of further coverage with Ge as in our experiment, we have to take into account the existence of a strong repulsive chemical interaction between Ge and C atoms, which has been both theoretically predicted^{15,47} and experimentally demonstrated⁴⁹. This interaction is able to force C into the shallow layers¹⁶ where it is principally incorporated substitutionally⁵⁰, forming stable Si-C bonds and giving rise to a strong compressive strain field. This C-induced strain field increases with the carbon content at the surface¹⁶ and can be obtained at the first order within the Vegard law as being proportional to the carbon coverage. The enhancement of compressive strain of the substrate has been shown^{41,42,43,44,51} to be responsible for an increase of the surface diffusion energy barrier leading to a decrease of the mobility. Huang *et al.*^{43,44}, based on first principles calculations, found a linear correlation between this diffusion energy barrier and the substrate strain field.

Thus we propose a scenario where the decrease of the Ge diffusion coefficient between the C-free and the C-covered Si(001) substrate originates from the modulation of the activation energy induced by two contribution: 1) the roughness at the interface and 2) the increased compressive strain within the substrate. Both contributions determine a linear dependence of the activation energy, thus they are both described by the coefficient E_A^1 in the exponential factor of Eq. (2.50).

The fitting in Fig. 2.11(b) reveals that the Ge diffusion constant, $D_0^* = 5.68 \times 10^{-2}$ cm²/s, does not significantly change with respect to the C-free case, $D_0 = 6.4 \times 10^{-2}$ cm²/s, showing that the main cause of the strong dependence of the diffusion coefficient from the C-coverage comes from the activation energy.

The above discussion shows that Si-C bonds influence deeply the SiGe diffusion in our experiment so that the value of E_A^1 estimated here cannot be directly compared to the theoretical calculations of the diffusion on externally strained pure Si substrates. However a qualitative

explanation of the main trends is possible within the approximation that E_A^1 is determined only by the C-induced strain field. This needs to account for the real strain field induced by C atoms in the surface layer, whose determination requires the knowledge of the Carbon concentration in the top-most layer. This issue will be properly addressed in the following discussion about the island self-assembly (Section 3.3.3 of Chapter 3), and thus the reader is referred there also for the discussion about the term E_A^1 .

These results should be considered as a preliminary attempt to have a deeper insight in the comprehension of the processes governing the C-induced modulation of the atomic mobility. They give an experimental basis on both the identification of the factors influencing the surface diffusion and the quantitative prediction of the C-induced trend for the activation energy and the diffusion constant. Moreover, they represent a solid background for the comprehension of the self-organization phenomena during SiGe islands growth, which will be treated in the Chapter 3. We hope that these systematic results will motivate further experimental and theoretical works.

2.7 Conclusions

We have investigated the surface diffusion of Ge on both C-free and C-covered Si(001) surface by means of Scanning Auger Microscopy. First, the temperature dependence of Ge diffusion coefficient on a microscopic scale has been directly measured in case of a *C-free* Si surface, interpreting the results within a one-dimensional diffusion model. The scaling behaviour of the resulting diffusion profile has been investigated, showing that it belongs to the universality class defined by the solutions of the Edwards-Wilkinson equation in a (2+1)-dimensional space. Then, the Ge diffusion coefficient at 600 °C has been monitored as a function of the carbon coverage, exploiting a continuous spatial modulation obtained by ion sputtering a homogeneous carbon layer during a time increasing with the longitudinal position along the stripe. The increase of the carbon coverage from 0.1 ML to 1 ML, corresponds to a decrease of the diffusion coefficient from $\sim 3 \cdot 10^{-9}$ cm²/s to $\sim 3 \cdot 10^{-13}$ cm²/s. This huge dependence is discussed within a physical scenario where carbon is incorporated within the shallow volume of the Si substrate inducing a surface roughness and a compressive local strain field. These two phenomena, together with the chemical interactions among Si, C and Ge are the main factors influencing the diffusion modulation and are described through a linear dependence of the diffusion activation energy on the C coverage.

Bibliography

- ¹ J. Drucker and S. Chaparro, *App. Phys. Lett.* **71** 614 (1997)
- ² T.I. Kamins and R.S. Williams, *App. Phys. Lett.* **71** 1201 (1997)
- ³ O. Schmidt, C. Lange, K. Eberl, O. Kienzle, F. Ernst, *App. Phys. Lett.* **71** 2340 (1997);
- ⁴ Y.-M. Mo and Lagally, *Surf. Sci.* **248**, 313 (1991)
- ⁵ A. E. Dolbak and B.Z. Olshanetsky, *Central European Journal of Physics* **4** 310 (2006)
- ⁶ T. Schwarz-Selinger, Y. L. Foo, David G. Cahill and J. E. Greene, *Phys. Rev. B* **65**, 125317 (2002)
- ⁷ H.J. Kim Z. M. Zhao, J. Liu, V. Ozolins, J. Y. Chang,b) and Y. H. Xie , *J.Appl. Phys.* **95**, 6065 (2004)
- ⁸ C. Roland and G.H. Gilmer, *Phys. Rev. B* **47**, 16286 (1993)
- ⁹ D. Srivastava and B. Garrison, *Phys. Rev. B* **46**, 1472 (1992)
- ¹⁰ V. Milman, D.E. Jesson, S.J. Pennycook, M.C. Payne, M.H. Lee, I. Stich , *Phys. Rev. B* **50**, 2663 (1994)
- ¹¹ M. Copel, M.C. Reuter, E. Kaxiras, and R. M. Tromp, *Phys. Rev. Lett.* **63** 632 (1989)
- ¹² M. Copel, M.C. Reuter, M. Horn von Hoegen, and R.M. Tromp, *Phys. Rev. B* **42** 11682 (1990)
- ¹³ R.D. Bringans, R.I.G. Uhrberg, M. A. Olmstead, and R.Z. Bachrach, *Phys. Rev. B* **34**, 7447 (1986)
- ¹⁴ R.M. Tromp and M.C. Reuter, *Phys. Rev. Lett.* **68**, 954 (1992)
- ¹⁵ P.C. Kelires, *Phys. Rev. Lett.* **75**, 1114 (1995); *Int. J. Mod. Phys. C* **9**, 357 (1998)
- ¹⁶ G. Hadjisavvas, Ph. Sonnet, and P.C. Kelires, *Phys. Rev. B* **67**, 241302(R) (2003)
- ¹⁷ O. Schmidt, S. Schieker, K. Eberl, O. Kienzle, F. Ernst, *App. Phys. Lett.* **73** 659 (1998)
- ¹⁸ O. Leifeld, E. Muller, D. Grutzmacher, B. Muller and K. Kern, *App. Phys. Lett.* **74** 994 (1999)
- ¹⁹ G. Isella, D. Chrastina, B. Rössner, T. Hackbarth, H-J. Herzog, U. König, H. von Känel, *Solid-State Electronic* **48**,1317-1323 (2004)
- ²⁰ N. Watanabe, S. Yamahata, T. Kobayashi, *J. Cryst. Growth* **200** 599 (1999); T. Hallam, F. J. Rueß, N. J. Curson, K. E. J. Goh, L. Oberbeck, M. Y. Simmons, and R. G. Clark , *App. Phys. Lett.* **86**, 143116 (2005)
- ²¹ Auger spectra have been treated according to the following procedure: 1) high frequency noise reduction with an average filtering (5 points smoothing); 2) first order differentiation; 3) determination of the Auger line intensity as difference between the maximum and the minimum intensities (peak-to-peak intensity).

- ²² C. S. Fadley, Prog. Surf. Sci. **16**, 275 (1984)
- ²³ S. Tanuma, C. J. Powell, D. R. Penn, Surf. Interface Anal. **21**, 165 (1993)
- ²⁴ M. Brehm, M. Grydlik, H. Lichtenberger, T. Fromherz, N. Hrauda, W. Jantsch, F. Schäffler, and G. Bauer, App. Phys. Lett. **93** (2008) 121901
- ²⁵ Medeiros Ribeiro, A.M. Bratkovski, T.I. Kamins, D. A. A. Ohlberg, R. S. Williams., Science **279** 353 (1998)
- ²⁶ X. R. Qin, B. S. Swartzentruber, and M. G. Lagally, Phys Rev. Lett **85**, 3660 (2000)
- ²⁷ Michael Barnsley, *Fractals Everywhere*, Boston [etc.] Academic Press, 1988, p.43
- ²⁸ F. Family and T. Vicsek, J. Phys. A **18**, L75 (1985); F. Family, Physica A **168**, 561 (1990)
- ²⁹ A.-L. Barabasy, H.E. Stanley, *Fractal Concepts in Surface Growth*, Cambridge University Press (2002)
- ³⁰ S.F. Edwards and D.Wilkinson D R 1982 Proc. R. Soc. A **381** 17–31
- ³¹ S. Pal and D.P. Landau, Phys. Rev. B **49**, 10597 (1994)
- ³² M. Siegert and M. Plischke, Phys Rev E **50**, 917-931 (1994)
- ³³ J. Drotar, Y.-P. Zhao, T.-M. Lu, and G.-C Wang, Phys Rev B **64**, 125411 (2001)
- ³⁴ A. B. Kolton, A. Rosso, E. V. Albano, and T. Giamarchi, Phys. Rev. B **74**, 140201(R) (2006).
- ³⁵ L.A. Nunes Amaral, A.-L. Barabási, H. A. Makse, and H. E. Stanley Phys. Rev. E **52**, 4087–4104 (1995)
- ³⁶ A. Bru´, S. Albertos, J. A. Lo´pez Garcı´a-Asenjo, and I. Bru´, Phys Rev Lett **92**, 238101 (2004)
- ³⁷ I.N. Remediakis, E. Kaxiras, and P.C. Kelires, Phys. Rev. Lett. **86**, 4556 (2001)
- ³⁸ O. Schmidt, S. Schieker, K. Eberl, O. Kienzle, F. Ernst, App. Phys. Lett. **73** 659 (1998)
- ³⁹ O. Leifeld, E. Muller, D. Grutzmacher, B. Muller and K. Kern, App. Phys. Lett. **74** 994 (1999)
- ⁴⁰ O. Leifeld, R. Hartmann, E. Muller, E Kaxiras, K. Kern and D. Grutzmacher, Nanotechnology **10** 122 (1999)
- ⁴¹ D.J. Shu, F. Liu, and X. G. Gong, Phys. Rev. B **64** 245410 (2001)
- ⁴² A. van de Walle, M. Asta, and P. W. Voorhees, Phys. Rev. B **67** 041308(R) (2003);
- ⁴³ L. Huang, F. Liu, and X. G. Gong, Phys. Rev. B **70** 155320 (2004)
- ⁴⁴ L. Huang, F. Liu, Guang-Hong Lu and X. G. Gong *et al.*, Phys. Rev. Lett. **96** 016103 (2006);
- ⁴⁵ R. Grima, J. DeGraffenreid, J. A. Venables, Phys. Rev. B **76** 233405 (2007)
- ⁴⁶ J. Tersoff, Phys. Rev. Lett. **74** 5080 (1995)
- ⁴⁷ P.C. Kelires, Surf. Sci. **418** L62 (1998)
- ⁴⁸ K. Torigoe, Y. Ohno, H. Kohno, T. Ichihashi, S. Takeda, Surf. Sci. **601** 5103 (2007)

⁴⁹ O. Leifeld, A. Beyer, D. Grutzmacher, and K. Kern, Phys. Rev. B **66**, 125312 (2002)

⁵⁰ S. C. Jain, H. J. Osten, B. Dietrich, and H. Rucker, Semicond. Sci. Technol. **10** 1289 (1995)

⁵¹ V. Cherepanov and B. Voigtlander, Phys. Rev. B **69** 125331 (2004)

Chapter 3

Self-assembled SiGe islands grown by Surface Thermal Diffusion on Si(001)

3.1 Introduction

Crystalline silicon and germanium have the same lattice structure, i.e. that of diamond. However, the lattice constant of Ge is about 4.2 % larger than that of Si. This difference is called *misfit* and is defined as $f = (a_{\text{Ge}} - a_{\text{Si}})/a_{\text{Si}}$, where $a_{\text{Si}} = 5.43 \text{ \AA}$ and $a_{\text{Ge}} = 5.64 \text{ \AA}$ are the lattice constants of Si and Ge, respectively. Because of this lattice mismatch, the growth of Ge on Si evolves in layer-by-layer mode for only few monolayers (MLs), after which 3D islands form. This system is a classical example of Stranski-Krastanov (SK) growth mode¹.

The SiGe system has been extensively studied in recent years. The main results achieved in the growth of Ge on Si(001) by means of CVD and MBE are briefly reported in Section 3.2, where it is shown that a rather coherent picture emerges out of many experiments. In Section 3.3, we will focalize more deeply on the investigation of self-assembled SiGe islands on Si(001) grown by an original method making use of a lithographically etched Ge stripe used as solid state source directly placed on the sample surface. The obtained results can be described in their mainlines within the same framework developed for MBE and CVD grown systems, however they open a new region of the parameter space and shine more light on some intriguing aspects of the Ge/Si(001) *self-assembly*.

3.2 Epitaxial growth of SiGe islands on Si(001) by MBE and CVD

As the dangling bonds of Ge atoms are less energetic than those of Si atoms, the surface energy of Si is larger than that of Ge, and thus in the initial phase of the growth process the Ge wets the Si substrate forming a flat compressively strained film (wetting layer, WL). Ge grows flat until a critical thickness of around 3 - 4 ML is reached^{1,2}, at which the effects of the Si interface are no longer felt. Above this thickness, coherent stable 3D islands are formed in order to lower the elastic energy of the system with respect to the pure 2D WL configuration, where a tetragonal distortion is the only possible reaction to the applied biaxial strain. At the critical thickness the free energy for the formation of an extra-surface is sufficiently lower than the elastic strain energy due to the lattice mismatch, and thus the system spontaneously evolves toward the formation of 3D clusters where the outward bending of the lattice planes leads to a partial elastic strain relaxation (see Fig 1.3 in the Chapter 1).

3.2.1 Strain relaxation before the onset of 3D growth

On the ideal Si(100) surface, as obtained by truncation of the bulk, each atom has two broken (or *dangling*) bonds and two backbonds connecting it to the subsurface sites. Because of the huge number of dangling bonds, the surface is structurally unstable and an atomic rearrangement occurs through the formation of buckled dimers generating a (2×1) reconstruction (see Fig. 2.6(d) in the Chapter 2).

During the initial stages of Ge deposition a compressively strained wetting layer is formed. The main effect of Ge deposition on the surface structure is an abrupt change of the surface reconstruction. At low Ge coverage, the surface shows a disordered structure exhibiting many missing dimers³. When the coverage reaches about 1 ML, dimer vacancies arrange themselves into an ordered array of lines (dimer vacancy lines, DVL's)⁴ (see Fig 3.1(a)). The surface reconstruction has now changed from (2×1) to (2×N), where the Nth dimer is missing. Tersoff⁵ has demonstrated that the formation of DVL's is a very efficient way of partially relieving the compressive strain within the wetting layer. At even higher Ge coverage (about 2 ML), terraces fragment into small patches bounded by DVL's and by larger trenches perpendicular to the DVL's, the so-called dimer row vacancies (DRV's)^{6,7} (see Fig. 3.1(b)). The surface structure has now changed into a (M×N) reconstruction, where M is the number of rows within each patch.

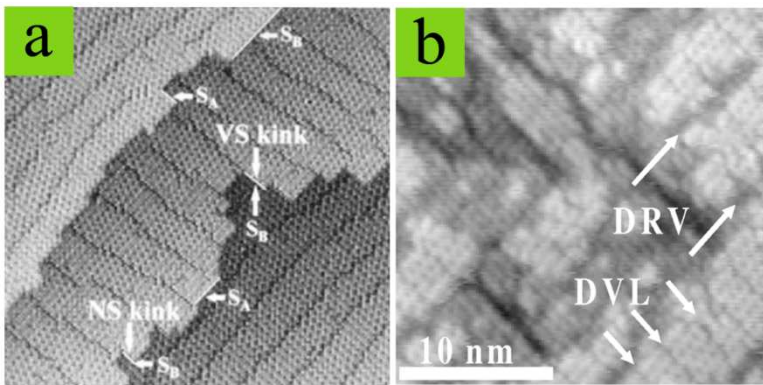


FIG. 3.1. (a) STM image ($45 \times 45 \text{ nm}^2$) of the $(2 \times N)$ reconstruction (from Ref. 4). Dimer Vacancy Lines (DVL's) are visible as dark lines perpendicular to the dimer rows. (b) STM image of the $(M \times N)$ reconstruction (from Ref. 8). DRV's represent the dimer row vacancies.

3.2.2 3D island formation and faceting

The spontaneous formation of 3D islands on the top of the compressively strained wetting layer is a result of the competition between the release of the elastic strain energy and the increase of the surface energy due to presence of an extra-surface with respect to a 2D configuration. At initial stages islands appear first as unfaceted shallow mounds (generally referred to as *pre-pyramids*), and then with increasing deposition coverage they transform in completely faceted *pyramids*, bounded by four $\{105\}$ facets⁹ (see Fig. 3.2). When the wetting layer thickness exceeds its critical value, a morphologic instability (known as Asaro-Tiller-Grinfeld, ATG, instability¹⁰) develops with the formation of a ripple structure, made of regularly spaced cells, able to partially relieve the strain stored into the wetting layer^{11,12}. This cell-like structure is composed of rounded, rough and not regularly stepped mounds, exhibiting a very low height-to-base aspect ratio (A.R. around 0.05). Fig. 3.2 shows the evolution pathway undergone by a shallow mound leading to the formation of a complete pyramid, though an intermediate truncated pyramid morphology. Small $\{105\}$ facets nucleate at the region of the pre-pyramid surface located at a height intermediate between the base and the top⁹ (see Fig. 3.2(a)); since the $\{105\}$ facets exhibit a very low surface tension^{13,14}, they expand in order to reduce the surface energy of the whole structure, and the unfaceted remnants of the parent pre-pyramid disappear (see Fig. 3.2(b)); finally, the apex of the pyramid forms since material is likely to be attracted from the surrounding to the partially relaxed top, rising the aspect ratio up to around 0.1 (see Fig. 3.2(c)). Tersoff *et al.*⁹ suggested that the pre-pyramid-to-pyramid transition is a first order transition, occurring when the island size reaches a critical value. At this point on the pre-pyramid morphology becomes unstable since its total energy becomes higher than that of a truncated pyramid.

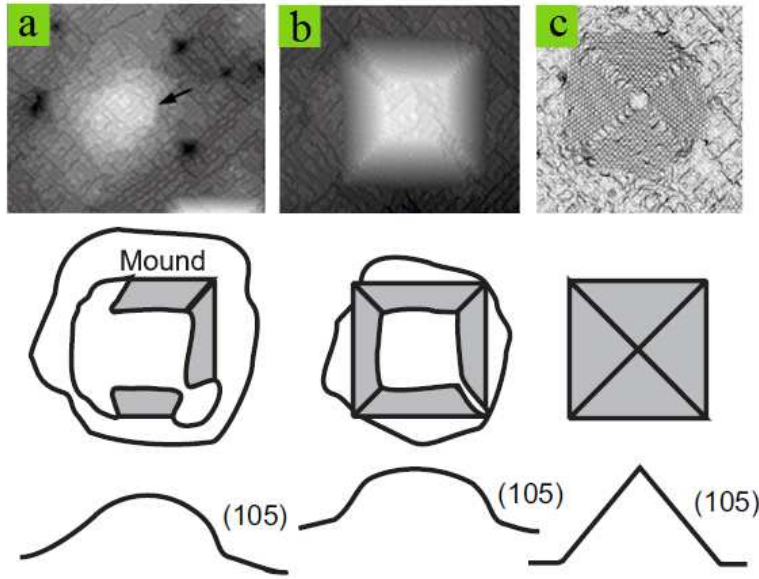


FIG. 3.2. Pre-pyramid to pyramid transition. STM images and corresponding schematic representation of an unfaçeted mounds (a), a transition pyramid (b) and a {105} faceted complete pyramid. Scale in STM images are: (a) $118 \times 95 \text{ nm}^2$, (b) $92 \times 80 \text{ nm}^2$, (c) $80 \times 80 \text{ nm}^2$. (From Ref. 12)

As, with increasing deposition, complete pyramids with {105} facets reach a critical volume, they undergo a second morphological change to multifaceted islands dubbed *domes* exhibiting steeper {113} and {15 3 23} facets (A.R. around 0.2)^{15,16}. Ross *et al.*¹⁶ used real-time Low Energy Electron Microscopy (LEEM) to experimentally observe all the transition states and intermediate shapes between pyramids and domes (see Fig. 3.3(a)-(c)). This evolution can be understood by considering that steeper islands better release elastic energy, while exposing more extra-surface with respect to a 2D configuration. The balance between these two terms yields to the following expression for the free energy difference² between an island and an area of flat WL of equal volume V :

$$\Delta = V[\rho_{is} - \rho_{WL}] + V^{2/3}(c_S^{is}\gamma_{is} - c_B^{is}\gamma_{WL}) \quad (3.1)$$

where is refers to *island*, S to *surface* and B to *base* so that ρ_{is} and ρ_{WL} are the elastic energy densities in the island and in the WL, respectively; γ_{is} and γ_{WL} are the average surface energy densities of the island facets and of the WL, respectively; c_S^{is} and c_B^{is} are the facets and base areas normalized to $V^{2/3}$, respectively. At large volumes, the surface energy term is negligible, so that steep islands will be favored, while shallow morphologies are expected in the limit of small V . Fig. 3.3(g) illustrates the behavior of Δ as a function of the island size for pyramids and domes based on Eq. (3.1). Pyramids are more stable than the WL for any volumes. Both shapes are degenerate in energy at the critical size V^* , where domes becomes more energetically favorable with respect to pyramids and thus a transition occurs.

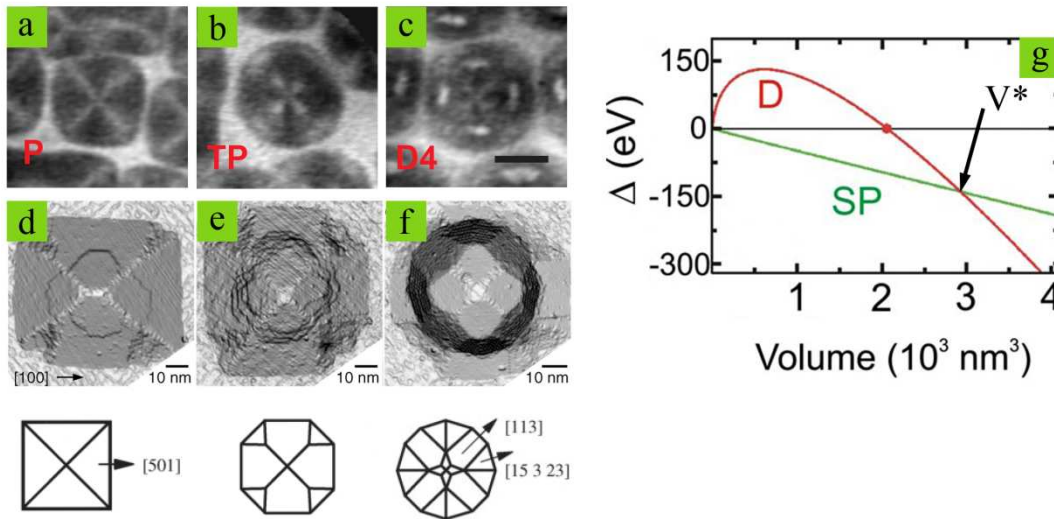


FIG. 3.3. Panels (a)-(c): LEEM images recorded during SiGe growth on Si(001), showing the pyramid (P), transition (TP), and dome (D4) shapes (from Ref. 16). Panels (c)-(d): STM images illustrating the pathway of the pyramid-to-dome evolution (from Ref. 17). At the bottom, schematic diagram showing the facets present in P, TP and D4 shapes. Panel (g): calculated energy difference of shallow pyramids (SP) and domes (D) with respect to the flat WL. V^* defines the critical volume at which transition occurs. (From Ref. 2)

Medeiros-Ribeiro *et al.*¹⁵ gave a thermodynamic interpretation of the growth process considering this bimodal size distribution (pyramids and domes) to reflect an equilibrium state of the system. Pyramids and domes would be associated to two free energy minima at discrete islands volume, and the width of the bimodal distribution around each minimum is due to thermal broadening¹⁵. The transition between pyramids and domes would be thus a thermally activated process, occurring relatively abruptly, able to overcome the energetic barrier between the two minima. However, Ross *et al.*^{16,18} and Daruka and Tersoff¹⁹ proposed a kinetic rather than a thermodynamic model, whereby the island growth is related to a mechanism very similar to Ostwald ripening (see Section 1.4 in Chapter 1). An abrupt drop of the chemical potential occurs when the islands grow past the critical volume, triggering a coarsening process able to increase larger islands at the expense of the smaller ones. Indeed, some observations^{20,21} for Ge/Si(001) show that the size distribution does not behave exactly as predicted by the Ostwald ripening model²², nor by the thermodynamic equilibrium model. In this sense the identification of the factors governing the relative growth of individual nanostructures, i.e. the competition mechanisms among different nuclei to gather the mass present on the surface is still an interesting open issue.

Montalenti *et al.*¹⁷ investigated the microscopic mechanism of the shape transition. They showed that the island growth proceeds from top to bottom. Pyramids grows by the successive addition of complete layers until they reach a critical size. From this point on, atoms accumulate only on the partially relaxed topmost region of the island, which is an energetically favourable position, creating a series of steps able to bunch together. As the island volume increases, an

extended step bunching leads to the formation of steeper facets, and the transition to dome shape is attained (see Fig. 3.3(d)-(f)).

3.2.3 SiGe intermixing

During the island growth process, Si penetrates into the growing Ge islands leading to the formation of alloyed nanocrystals. Si intermixing is mainly driven by the entropy of mixing²³ and offers a path toward the elastic strain relaxation since alloying effectively reduces the lattice misfit between the island and the substrate. It has been shown to drive the increase of the mean island size and the increase of the critical volume for the insertion of extended defects (plastic relaxation)^{24,25}. The final degree of intermixing is thus modulated by both energetic and kinetic factors, and is associated to a significant mass transport during the growth related to only genuine surface diffusion phenomena^{26,27}.

Using Anomalous X-Ray Scattering^{28,29,30,31} a vertical gradient of composition was deduced both for pyramids and domes, showing a Ge-rich topmost region of the island and a Si-rich bottom region. Baranov *et al.*³² with polarized micro-Raman spectroscopy studied the alloying process in large islands grown in the range 700 °C - 800 °C. Their experimental observations are in agreement with an island model consistent with a Si-rich boundary region and a Ge-rich core. By combining selective wet chemical etching and AFM measurements, 3D compositional profiles of individual islands have been experimentally determined^{33,34,35,36}, finding that pyramids have highly Si intermixed base corners while the edges, the centre and the apex are rich in Ge, whereas domes show a ring-shaped periphery region with a higher Si content (see Fig. 3.4(a)). The core of the islands, both for pyramids and domes, appears to be richer in Ge while the boundary regions seems to be richer in Si, with a vertical gradient of composition in which the Ge fraction drops moving from the island top toward the substrate. Very recently, 3D compositional maps have been obtained by using grazing incidence x-ray diffraction (GIXD) combined with finite element method (FEM) calculations³⁷ showing results fully compatible with selective etching data.

All of these results are consistent with an intermixing process associated with only surface diffusion phenomena without the need of considering other mechanisms, like defects nucleation which even occurs. In this picture, the strain driven formation of lateral trenches^{27,38,39,40} digging into the substrate could identify a possible kinetic pathway for the enrichment in Si of the outermost region of the islands. The evolution of the SiGe intermixing during the growth process has been theoretically studied by Tu and Tersoff²⁷ using continuum modelling. Fig. 3.4(b)-(i) summarizes their results. When the wetting layer thickness exceeds its critical value, the ATG linear instability¹⁰

develops perturbing laterally the flat surface of the strained layer and giving rise to the ripple structure (Fig. 3.4(c)). As the ripples increase in amplitude, they pinch off and form distinct islands. Their aspect ratio continue to increase until the formation of defined facets, due to surface energy anisotropy⁹ (Fig. 3.4(d)). The faceted islands exhibits a lower chemical potential⁹, so they grow rapidly at the expense of smaller islands via a coarsening process¹⁸. At this point, trenches form around the largest island, digging deeply into the substrate (Fig. 3.4(e)). Once the trench cuts into the substrate, the ejected Si mixes with Ge being captured by the growing island. As a result subsequent island growth, occurring mainly through surface diffusion along the island walls, generates an outer layer with a dilute composition (Fig. 3.4(f)). Further Si intermixing leads to the increase of the size of the largest island at the expense of the smaller ones (Fig.3.4(g)-(i)). It is worth noting the strict similarity between the experimentally measured cross-sectional Ge concentration map shown in Fig. 3.4(a), and the last run of the simulation shown in Fig. 3.4(i).

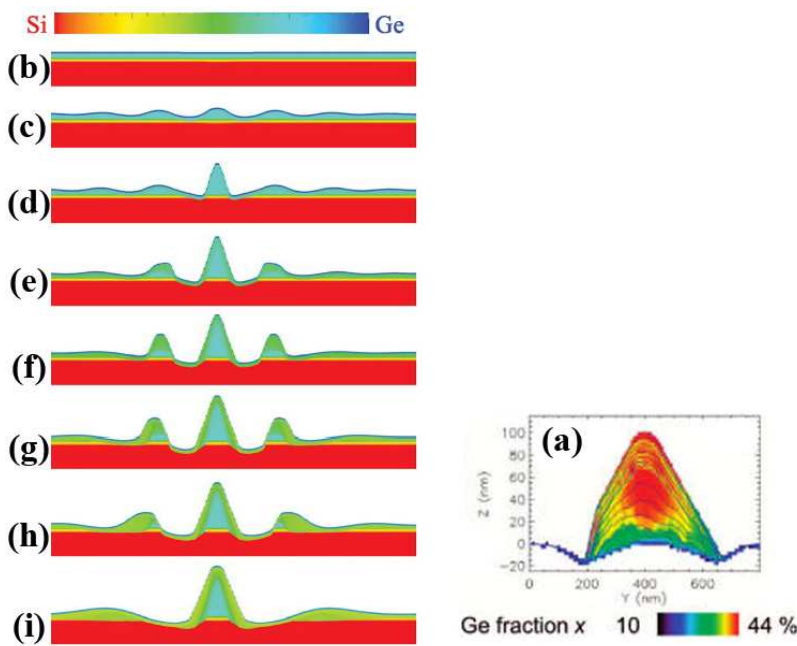


FIG. 3.4. Panel (a): Vertical cross-section of the Ge concentration map of a single island as derived by selective wet chemical etching (from Ref. 36). Panel (b)-(i): Selected snapshots at different times from the simulation of the evolution of Si intermixing during island formation process. The vertical scale is exaggerated by a factor of 5. The color bar shows the composition scale. (From Ref. 27).

3.2.4 Plastic relaxation

As described in section 3.2.2, a morphologic transition with deposition from shallow unfaceted pre-pyramids (A.R. around 0.05), to shallow pyramids (AR around 0.1), to steeper large domes (AR around 0.2) has been experimentally reported^{15,16}. This experimental observation of a progressive transition towards islands with higher aspect ratio (AR) with increasing volume¹⁵, seems to confirm the qualitative prediction based on Eq. (3.1). However, this simple model only works under the assumption of a constant and uniform Ge concentration within the islands, and in the absence of plastic relaxation by injection of misfit dislocations. Actually, plasticity onset by

means of dislocation injection beyond a critical volume^{41,42,43} (see Fig. 3.5(a)-(b)) has been clearly demonstrated, as well as, a strain-driven SiGe intermixing^{41,44} and lateral and vertical composition gradients³⁶ as reported in Section 3.2.3. In fact both SiGe alloying and dislocation injection effectively lower the elastic energy of the islands by relieving the misfit strain.

The tendency towards higher aspect ratios with increasing size predicted by Eq. (3.1) is interrupted by the nucleation of dislocations⁴². During the growth, a dislocation has formed near the edge of the island, and thus the island boundaries become a sink for new material because of the sudden lowering of elastic energy. Thus the island rapidly expands in lateral direction, producing a flattening of its shape by formation of low-index facets on top of it⁴¹. This is experimentally evidenced by a discontinuity in the slope of the aspect ratio distribution as a function of the island base width (see Fig. 3.5(c)).

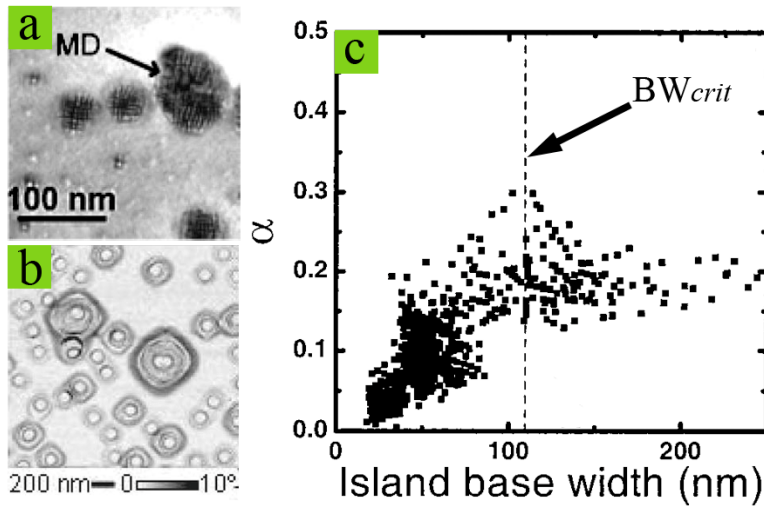


FIG. 3.5. Panel (a) TEM image of islands grown by CVD. The arrow marks the interruption of the regular interference pattern due to a misfit dislocation (MD) (from Ref. 41). Panel (b) AFM image (gradient mode) of dislocated islands grown by MBE after selective wet chemical etching, showing the typical ring-structure induced by dislocation injection (From Ref. 45). Panel (c) Island aspect ratio plotted as a function of the island base width for islands grown by CVD. The critical base for the dislocation insertion BW_{crit} is indicated. (From Ref. 41)

3.2.5 Spatial ordering

For many technological applications⁴⁶, which require the individual addressability of the islands, the random positioning following the Ge deposition on a flat Si substrate impose serious limitations. Spatial ordering of self-assembled islands can be controlled by different energetic parameters.

The short range elastic interactions between islands can improve both uniformity in dimensions and spatial ordering, inducing a chemical potential gradient between different islands and within a single island^{47,48,49}. Capellini *et al.*⁵⁰ have demonstrated that, by exposing randomly positioned Ge islands to a Si flux, in-plane ordering can be achieved. This has been explained by means of real lateral displacements, as originated by the elastic interactions and surface diffusion driven by a chemical potential gradient across neighboring islands, for both Ge and Si atoms.

A pre-existing stress pattern induced in the wetting layer has been shown to allow for a direct control of order and disorder effects at short and long ranges^{51,52}. Self-organization driven by the elastic strain field in multilayered structures has been indicated one possible way to achieve this^{53,54,55}. A Ge island epitaxially buried in a Si capping layer is assumed to generate a tensile strain field at the surface of the Si layer, providing preferential nucleation sites for further nucleation of Ge islands⁵⁶.

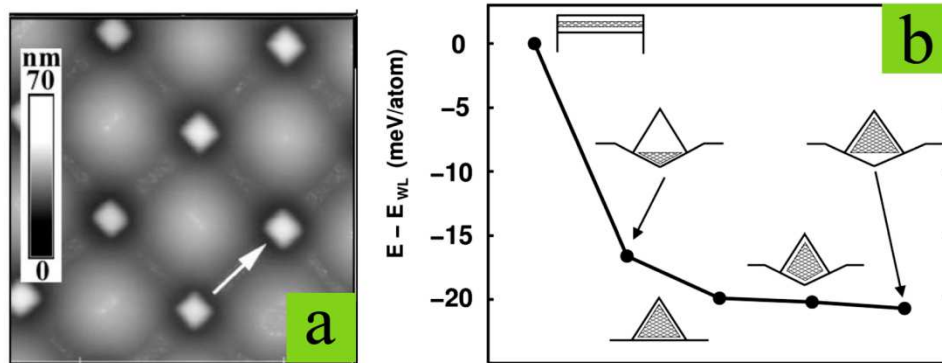


FIG. 3.6. Panel (a): $1 \times 1 \mu\text{m}^2$ AFM images of ordered grown islands by MBE in a pit-patterned Si(001) substrate. Panel (b): calculated elastic energy per atom for different simulated geometries. From left to right: flat wetting layer, downward pyramid, pyramid on flat substrate, island in pit, upward pyramid. The elastic energy difference per atom between the pyramid on a flat substrate and in the pit is about 0.3 meV/atom. (From Ref. 57)

Substrate two-dimensional patterning has been shown to induce an ordered growth process with a controlled positioning⁵⁸. Usually, the templates consist of a 2D array of pits where only a single island develops at the pit bottom, which represent a preferential nucleation site since the elastic energy per atom becomes minimum at this position⁵⁷ (see Fig. 3.6).

3.2.6 Surfactant mediated growth

In a lattice-mismatched system the use of a surface active specie (surfactant) can enhance island formation by modifying the energy and the strain state of the surface, and opens to the possibility of controlling shape, size and density of self-assembled islands^{59,60}.

A recent bottom-up strategy towards the engineering of the self-assembly process of Ge islands involves the use of carbon as a surfactant. The growth of C-induced SiGe islands has been extensively studied^{61,62,63,64,65,66} for the possibility to tailor their properties for potential application in nanoscale devices⁶⁷. The growth mode of Ge on a Si(100) surface pre-covered with a sub-monolayer amount of carbon, generating $c(4 \times 4)$ reconstructed domains, has been studied by Stoffel *et al.*⁶⁸, showing that the growth proceeds via a Volmer–Weber mode. This growth mode has been observed also by Leifeld *et al.*⁶⁹ using Scanning Tunneling Microscopy, and by Dentel *et al.*⁶⁶ and

Bernardi *et al.*⁷⁰ through Reflection High Energy Electron Diffraction studies. However, the microscopic mechanism of surfactant effect upon the growth process evolution is still under investigation, and the identification of the microscopic factors governing the relative growth of individual nanostructures is an important issue that still needs to be addressed for a complete understanding of the process. Bernardi *et al.*⁷¹ recently demonstrated that by depositing a carbon layer over a SiGe buffer layer it is possible to manipulate the epitaxial growth of Ge dots in a kinetically-limited deposition regime. In comparison with Ge islands directly grown on a bare Si surface, the average size of the C-induced Ge dots is generally smaller and the island density is higher^{72,73}. This is usually attributed to a decrease of diffusion length of adatoms on a C pre-covered surface⁷⁴, even if a direct experimental demonstration of the influence upon the island size of such a reduction of the Ge diffusion induced by the C surfactant is still lacking.

3.3 Epitaxial growth of SiGe islands on Si(001) by Surface Thermal Diffusion

In this section, we investigate the self-assembly of SiGe islands grown on a Si(001) surface by the surface thermal diffusion of Ge from a source stripe. This method does not involve atom condensation from a vapor phase, like happens in the cases of MBE and CVD, and the dominant process during the growth is essentially the surface diffusion of both Ge and Si. We used lithographically defined Ge stripes as solid state sources directly placed on the sample surface. The total surface coverage of Ge strongly depends on the distance from the source stripe, thus the method allows the investigation of the island growth over a wide range of dynamical regimes at the same time.

First we discuss the island growth modes in case of C-free and C covered Si surfaces, giving experimental evidence of a C-induced continuous transition from a Stranski-Krastanov mode, in the C-free case, to the Volmer-Weber regime, at higher C coverage. From the size evolution exhibited by the nucleated islands as a function of the distance from the source stripe and for different C coverage, we propose a scenario where island growth is essentially driven by kinetic factors within a diffusion limited regime. Then, we studied the correlation between the size and density evolution of the nucleated islands giving a better insight on the factors governing the relative growth among different nanostructures. We investigated the interplay among Si intermixing and plastic relaxation

during the island growth process, showing that this method leads to the formation of coherent islands (dislocation-free) larger than those attainable by MBE and CVD growth. Finally, the ordered growth of self-assembled SiGe islands on a pit-patterned Si(001) surface has been investigated. We studied the size distribution of the islands as a function of the Ge coverage. Our observations are consistent with a physical scenario where island positioning is essentially driven by energetic factors, which predominate with respect to the local kinetics of diffusion, and the growth evolution of ordered islands mainly depends on the local density of Ge atoms.

3.3.1 Experiment

We show here that surface thermal diffusion from solid state sources allows one to epitaxially grow self-assembled SiGe islands on Si(001). To this purpose we have fabricated pure Ge stripes, and annealed them in UHV at different temperatures (600, 625, 650, 670, 700 °C) inducing Ge diffusion and islands self-assembly. An extended discussion of the experimental aspects regarding to the stripe fabrication, surface cleaning, C deposition and annealing procedure is reported in Section 2.4 of Chapter 2. Here we recall briefly only those experimental details useful for the following discussion.

The samples consist of Ge stripes (width 5 μm , thickness 50 \div 150 nm) obtained by a photolithographic patterning of pure Ge thin films, grown on a Si(001) substrate by LEPECVD⁷⁵. A PHI 660 Scanning Auger Microscope (SAM) has been used for *in-situ* imaging and spatially resolved chemical analysis at the sample surface before and after thermal diffusion (see Panel A for a detailed overview regarding the SAM technique). The samples have been annealed by direct Joule heating flowing a DC current through the Si substrate using the home-made sample heater reported in Fig. 2.4 of Chapter 2. Atomic Force Microscopy (AFM), whose description is reported in the Panel B, for *ex-situ* analysis of the nucleated islands has been performed using a Veeco Inova microscope operated in tapping mode with ultra-sharp tips (nominal tip radius about 2 nm). Statistical analysis of AFM data has been performed on more than 1000 islands using freely available software tools.⁷⁶ The structural and compositional analysis of single islands has been performed by means of Transmission Electron Microscopy (TEM) using a JEOL 2010F TEM/STEM equipped with a 200 kV Schottky field emission electron gun (see Panel C for an extensive discussion about the physical principles and the analysis methods underlying the TEM and STEM-EELS techniques). The average composition of single islands has been measured by micro-Raman spectroscopy (see Panel D for a detailed description), performed on a Jasco R800

double spectrometer using backscattering geometry and 458 nm as excitation wavelength focused by a 0.9 numerical aperture objective.

3.3.2 Growth modes

During the high temperature annealing in UHV, the stripes act as Ge sources from which Ge diffuses on the Si surface forming a continuous over-layer (OL) (see Fig. 3.7(a)). The thickness and composition of such a layer, reported in Fig. 3.7(b) for the case of annealing at 625 °C, have been monitored by SAM as a function of the distance, x , from the stripe. Spontaneous nucleation of self-assembled SiGe islands is observed to coexist with the continuous surface diffusion of Ge. Figs. 3.8 show representative SEM and AFM images of the sample surface for annealing at 600 °C and 700 °C.

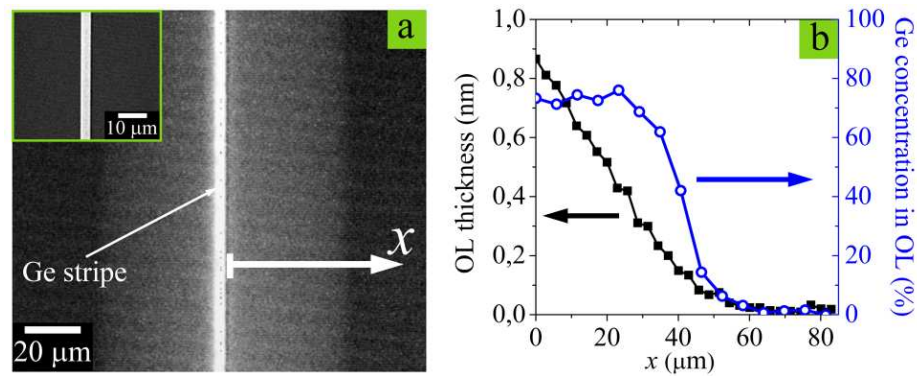


FIG. 3.7. Panel (a): SEM image of the diffusion region after annealing at 625 °C for 7.5 min; inset: SEM image of the stripe before the annealing. Panel (b): Thickness (black squares) and Ge concentration (blue open circles) of the continuous over-layer (OL) created by the diffusive motion of Ge from the stripe after annealing at 625 °C for 7.5 min measured by Scanning Auger Microscopy as a function of the distance, x , from the stripe edge.

Islands grown by surface thermal diffusion from a Ge stripe essentially develop in a defined region close to the stripe (see Fig. 3.8(b)); the spatial limit for island nucleation is essentially determined by the diffusion dynamics of Si and Ge and by the growth regime of the nucleated islands. We have investigated the island growth mode both on a C-free Si surface and in presence of carbon acting as a surfactant. The critical over-layer thickness for the setting up of island nucleation has been determined by coupling SAM analysis (giving both C coverage and OL thickness as a function of x and y) and AFM analysis (giving the density of the islands as a function of x and y). In the following we identify this critical thickness with the largest thickness of the OL at which the island density goes to zero.

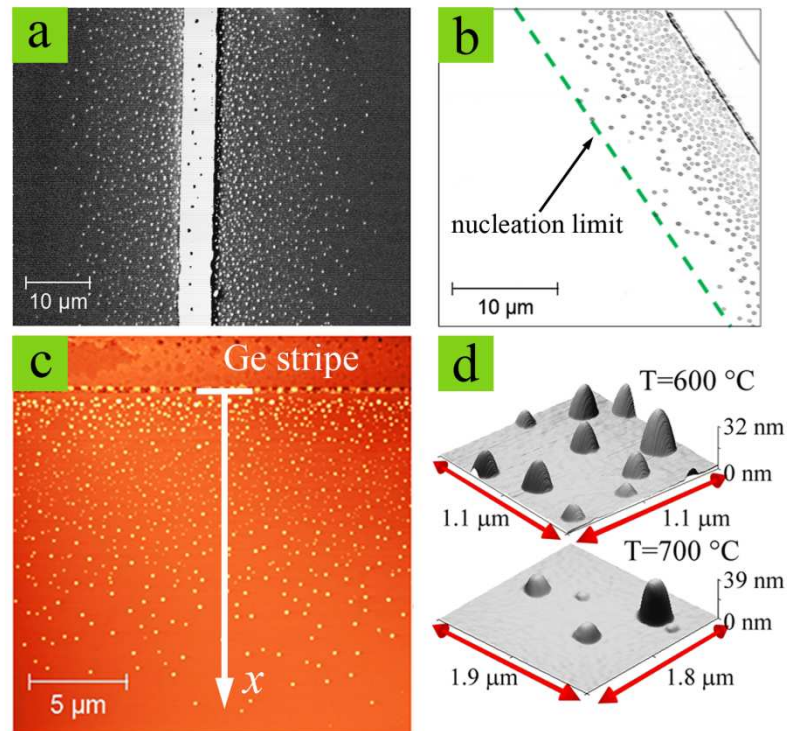


FIG. 3.8. Panel (a): SEM image of islands nucleated within the diffusion region close to the stripe (the lighter part in the centre of the image is the Ge stripe). Panel (b): AFM image (gradient mode) showing that islands develop within a defined region close to the stripe. Panel (c): AFM image qualitatively showing that nucleated islands exhibit a modulation in density and size as a function of the distance, x , from the stripe. Panel (d): 3D AFM images of islands grown after annealing at 600 °C and 700 °C.

In the case of a clean Si(001) surface, the growth mode of the SiGe islands is Stranski-Krastanov (SK)⁷⁷ in the whole range of temperature (600 ÷ 700 °C) over which the nucleation is observed, since we found the critical over-layer thickness always varying in the range 3-4 ML (see Fig. 3.9(a)). In presence of C (see Fig. 3.9(b)), we found that this critical thickness varies from 0.8 ± 0.17 ML for a pre-existing C coverage of ~ 0.7 ML (identified in Fig. 2.10 of Chapter 2 as the C-rich region of the sample), to 1.8 ± 0.25 ML at ~ 0.4 ML C coverage (hereafter called intermediate C coverage region), up to 3 ± 0.21 ML for ~ 0.2 ML C coverage (the low C coverage region). We recall here that the absolute uncertainty for the C coverage is about ± 0.1 ML. The main source of uncertainty on the critical thickness is the intrinsic error in the thickness determination as obtained within the discrete layer model presented in Section 2.5.1 of Chapter 2. The error on the critical thickness value coming from the uncertainty on the onset position for island nucleation (see Fig. 3.9) is negligible with respect to that one introduced by the discrete layer model.

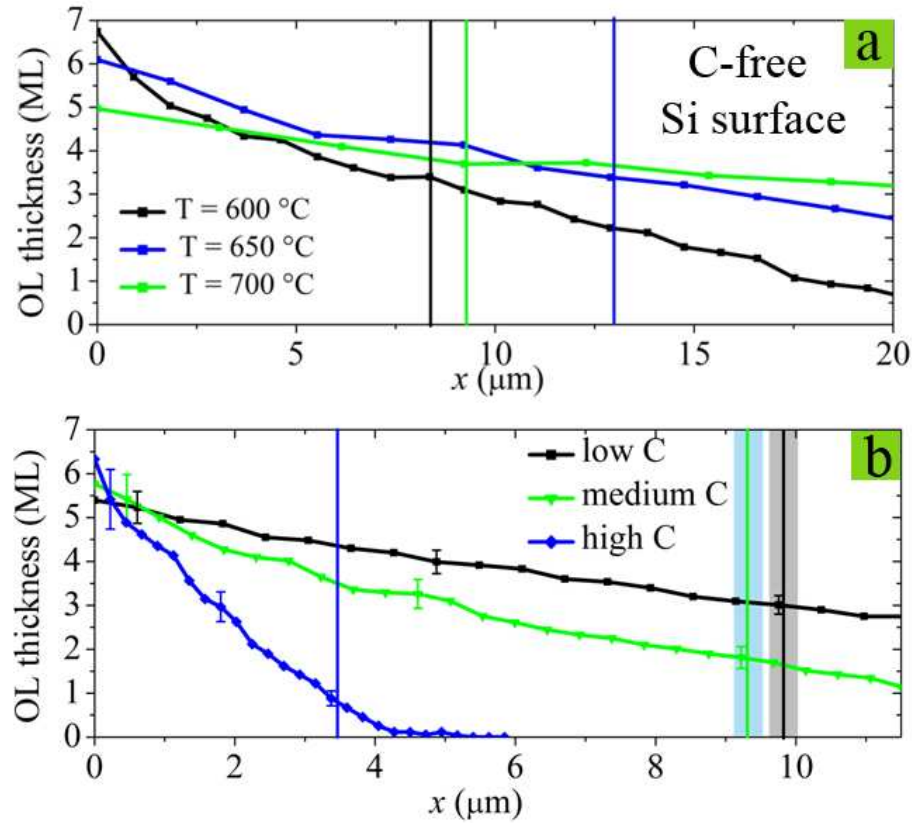


FIG. 3.9. Panel (a): over-layer (OL) thickness as a function of the distance, x , from the stripe at different annealing temperatures in case of diffusion on a C-free Si surface. Panel (b): over-layer (OL) thickness as a function of x after annealing at $600\text{ }^\circ\text{C}$ in case of diffusion on a carbon covered Si surface. The black, blue and green vertical solid lines define the position of the nucleation limit at which the island density goes to zero.

In the low and intermediate carbon coverage regions, the measurement also confirms the Stranski-Krastanov (SK) growth mode observed in the absence of surfactant, where the island formation is driven by elastic strain relaxation⁷⁷. In the high C coverage region islands are able to nucleate even with a sub-monolayer Ge coverage. This observation is consistent with a Volmer-Weber (VW) growth mode⁶⁹, where the formation of a larger Ge surface for a 3D island is energetically more convenient with respect to the accumulation of strain energy due to the formation of a continuous epitaxial layer. We attribute this to the presence of a carbon-induced local compressive strain field⁶³. In fact C atoms incorporate into the shallow volume of the Si substrate (as discussed in Section 2.6.2 of Chapter 2), thus reducing the lattice constant of the C alloyed Si surface due to their smaller size with respect to Si atoms and exaggerating the mismatch with the SiGe over-layer.

The direct measure of the critical wetting layer thickness for nucleation, allowed us to show that the island growth mode gradually evolves from Stranski-Krastanov (SK) in case of absence of surfactant, to Volmer-Weber (VW) for high surfactant coverage. Although different growth modes

have been already observed for SiGe islands, this is the first experimental demonstration of a continuous transition.

3.3.3 Interplay among C incorporation, Ge diffusion and island nucleation

The monotonic dependence of the critical thickness on the C coverage can be used to gain a quantitative estimation of the C incorporation inside the Si substrate and improve the understanding of the interplay of the diffusion and nucleation properties. The simplified scenario is the following: as discussed above, the SiGe over-layer diffuses over a Si surface partially alloyed with carbon; the alloying increases the misfit strain between the SiGe thin film and the top-most layer of the substrate, thus increasing the amount of the elastic energy stored in the OL and consequently promoting the island nucleation at lower OL thicknesses.

We now propose a semi-quantitative estimation of the carbon incorporation into the first layer of the Si substrate. The critical thickness at the 2D-3D transition corresponds to the minimization of the total free energy, F , of the system, which at first approximation can be obtained by considering only the contributions of the surface energy of the SiGe over-layer, γ , and of the elastic energy, E_{el} , stored in it⁶⁰:

$$F = \gamma + E_{el} \quad (3.2)$$

The elastic energy E_{el} stored per unit area in the SiGe over-layer can be determined using the equation based on the classical continuum model of a solid system:

$$E_{el} = 2\mu \frac{1+\nu}{1-\nu} \varepsilon^2 h \quad (3.3)$$

where μ and ν are the shear modulus and the Poisson's ratio of the over-layer, ε is the misfit strain of a SiGe thin film on a Si-C alloy layer, and h is the OL thickness.

We point out that the surface energy of the SiGe over-layer, γ , can be considered at first approximation independent from the carbon coverage of the surface: in fact, the repulsive interaction between Ge and C forces the latter to be incorporated in sub-surface sites and thus leaves unmodified the top surface of the SiGe over-layer. As a consequence at the critical thickness the reduction of the elastic energy stored in the over-layer for the case of nucleation on C-free and carbon covered regions is the same⁶⁰ and we can write:

$$\varepsilon^2 h_{crit} = \varepsilon_0^2 h_0 \quad (3.4)$$

where $h_0 \sim 3.5 \text{ ML}$ ⁷⁸ and ε_0 are the critical thickness and the misfit strain in case of absence of Carbon, while h_{crit} and ε are the similar quantities for the C-covered Si surface. Eq. (3.4) is valid provided that 3D clusters formed at the 2D-3D transition have the same morphological structure in

both cases. The misfit strain ε and ε_0 depend to a first approximation only on the lattice parameters of the substrate and of the OL:

$$\varepsilon = \frac{a_{SiGe} - a_{SiC}}{a_{SiGe}}, \quad \varepsilon_0 = \frac{a_{SiGe} - a_{Si}}{a_{SiGe}} \quad (3.5)$$

where $a_{Si} = 5.43 \text{ \AA}$ refer to Si bulk and $a_{SiGe} = a_{Si}(1-\alpha) + a_{Ge}\alpha = 5.60 \text{ \AA}$ (with $a_{Ge} = 5.64 \text{ \AA}$ and $\alpha = 0.81$ from Section 2.5.1 of Chapter 2) is the $Si_{1-x}Ge_x$ OL lattice parameter following the Vegard law. The parameter of the uppermost C alloyed Si layer of the substrate, $Si_{1-c}C_c$ (where the carbon concentration c in the uppermost layer has not to be confused with the carbon coverage), can be evaluated in agreement with theoretical⁷⁹ and experimental^{80,81} studies as:

$$a_{SiC} = a_{Si}(1-c) + a_Cc + c(1-c)\beta \quad (3.6)$$

where $\beta = -0.64 \text{ \AA}^{81}$ is the so called bowing parameter, and $a_C = 3.56 \text{ \AA}$ the lattice parameter of C in its diamond allotropes.

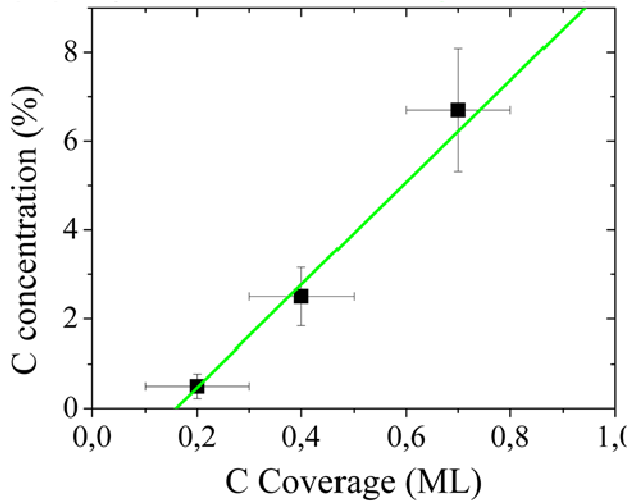


FIG. 3.10. Carbon concentration within the top-most layer of the Si substrate, derived by using the experimentally measured over-layer critical thickness with a 2D-to-3D nucleation model (see text), as a function of the carbon coverage. The green solid line is the best linear fitting of the experimental data taking into account their experimental uncertainties.

Thus combining Eqs. (3.4), (3.5) and (3.6), and using the experimentally measured critical over-layer thickness we can evaluate the carbon concentration, c , within the top-most substrate layer and compare them with the corresponding carbon coverage. As shown in Fig. 3.10, in the C-rich region c is found to be about 6.7 %, while at intermediate C coverage it becomes 2.5 %, decreasing down to 0.5 % in the low C coverage region. The experimental data are well fitted by a linear behaviour (green line in Fig. 3.10), showing that under a critical C coverage $\vartheta_0 = 0.16 \pm 0.06 \text{ ML}$ the C concentration c of the surface layer becomes negligible. These results are consistent with the picture that for low C coverage subsurface sites are more energetically stable for carbon, and justify the term $(\vartheta - \vartheta_0)$ in the activation energy expansion $E_A = E_A^0 + E_A^1(\vartheta - \vartheta_0)$ for

surface diffusion introduced in Section 2.6.2 of Chapter 2. They also support experimentally the Monte Carlo simulations and the *ab initio* calculations by Remediakis *et al.*⁸², according to which the ratio of surface to sub-surface C atoms increases monotonically with increasing C coverage and becomes greater than 1 for a carbon coverage of 0.17 ML.

We discuss now the value of the first order coefficient $E_A^1 \sim 0.29$ eV in the linear expansion of the activation energy $E_A = E_A^0 + E_A^1(\vartheta - \vartheta_0)$ used in Section 2.6.2 of Chapter 2 to fit the experimental trend of the diffusion coefficient. Based on the carbon concentration in the top-most layer of the substrate as given above, we can compare the quantitative results of our fitting in Section 2.6.2 of Chapter 2 with the values reported by Huang *et al.*⁸³ for Ge diffusion on a pure Si strained substrate. They found by first-principle calculations that the activation energy, E_A , for surface diffusion of Ge on a biaxially strained Si(001) surface has a linear dependence on the strain applied to the substrate, $\hat{\varepsilon}$: $E_A = E_A^0 - E_A^1 \hat{\varepsilon}$. In our case, the intermixing with Carbon induces a strain field $\hat{\varepsilon} \approx (a_{SiC} - a_{Si})/a_{Si}$ in the top-most layer of the substrate (not to be confused with the strain in the overlayer \mathcal{E}), which we can suppose to have a similar effect on the Ge diffusion. A comparison between the two above expressions of the activation energy E_A yields to the following relation between the first order coefficients \hat{E}_A^1 and E_A^1 :

$$E_A^1(\vartheta - \vartheta_0) = -\hat{E}_A^1 \hat{\varepsilon} \quad (3.7)$$

Eq. (3.6) can be now used to explicit in the Eq. (3.7) the lattice parameter a_{SiC} in the top substrate layer as a function of the Carbon concentration c . Thus Eq. (3.7) becomes:

$$c = \left(\frac{a_{Si}}{a_{Si} - \beta - a_C} \right) \frac{E_A^1}{\hat{E}_A^1} (\vartheta - \vartheta_0) \quad (3.8)$$

where the second order term has been neglected because of the small values of c found above. We notice that, within this approximation, Eq. (3.8) show a linear dependence between the C concentration c in the top-most layer and the carbon coverage ϑ , consistently with our previous discussion. From the fit in Fig. 3.10 and $E_A^1 = 0.29 \pm 0.04$ eV, we found $\hat{E}_A^1 = 5.45 \pm 1.32$ eV, to be compared with the values of 3.75 eV and 4.37 eV for perpendicular and parallel diffusion of Ge with respect to the dimer rows, respectively, found by Huang *et al.*⁸³ We attribute tentatively the larger value of \hat{E}_A^1 obtained here to the additional contribution of the C-induced surface roughness at the interface, which further increases the activation energy and consequently reduces the surface mobility.

3.3.4 Equilibrium shape and size

Fig. 3.11 shows the volume histograms and the related scatter plots of the projected area as a function of the volume for the whole island population in the case of annealing at extreme temperature (600 °C and 700 °C). Islands exhibit a monotonic increase of the area for larger volumes. This behaviour has been reproducibly observed for different samples and for all the temperatures investigated. We found that higher annealing temperatures lead to an increase of the mean island size, as usually reported even in the case of MBE and CVD growth^{24,25}. This is compatible with the fact that all the relevant processes governing the epitaxial growth of self-assembled islands are thermally activated. For a fixed temperature, the monotonic dependence exhibited by the scatter plot of the projected area versus the volume (see Fig. 3.11(a) and 3.11(c)) is consistent with a continuous transition from small to large islands following an Ostwald ripening mechanism (see Chapter 1 Section 1.4), where a coarsening process able to increase the size of larger islands at the expense of the smaller ones dominates during the growth. To be more quantitative, we found that at 700 °C the island area scales with the volume according to a *power-law* behaviour:

$$area \propto (volume)^\beta \quad (3.9)$$

with the exponent β equal to 0.59. This behaviour maintains also at lower annealing temperatures (T = 600 °C) but only within the limit of high volume range (β is 0.58 at 600 °C); at small volumes the size evolution of the islands is no longer described by a power law, where indeed the projected area scales with the volume by a slower logarithmic dependence (see Fig. 3.11(a)). We propose the following qualitative picture to describe these experimental results: small islands show preferential vertical growth, i.e. they increase in volume by increasing more rapidly in height rather than in base area. This is in agreement with a shape transition from pyramids with shallow facets to domes with steeper facets occurring from the top to the bottom of the island, i.e. by the progressive accumulation of Ge atoms on the partially relaxed topmost region of the island which is an energetically favourable position¹⁷. At the other limit (high volume), large islands are characterized by a homogenous growth, i.e. they increase the volume by increasing simultaneously both the area and the height whilst always maintaining the same global shape.

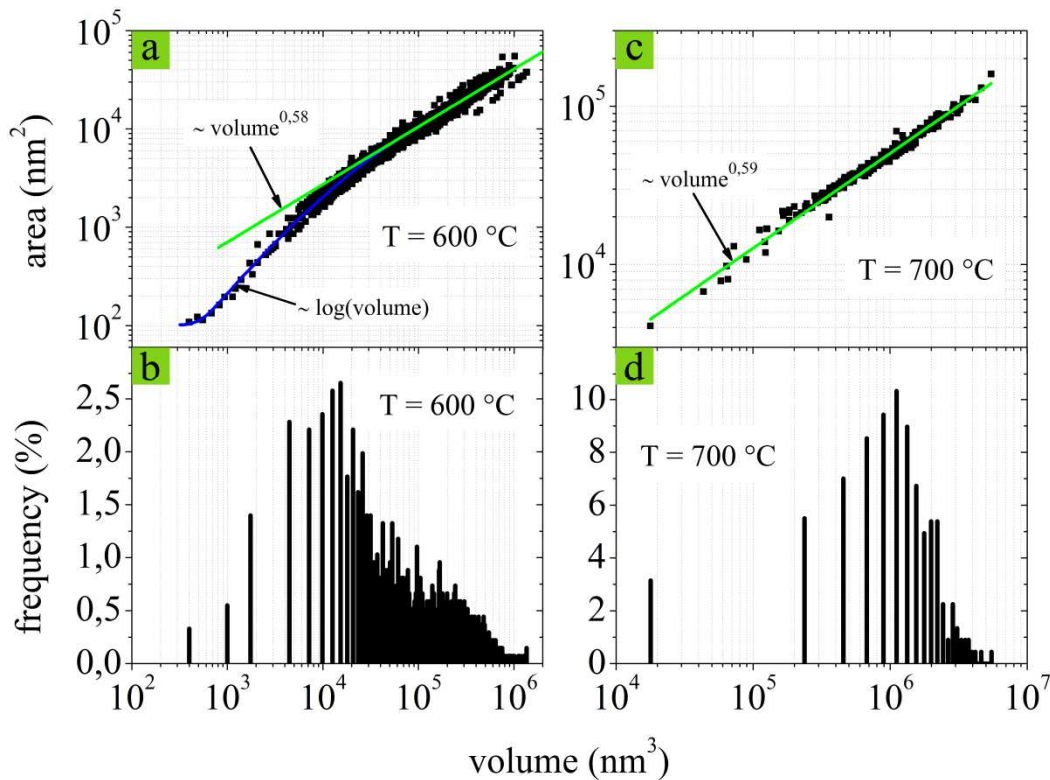


FIG. 3.11. Panel (a)-(c): scatter plots of the projected area as a function of the volume for islands grown at 600 °C (a) and 700 °C (c). The green solid lines represent a power law behaviour as described in the text, while the blue solid line is a logarithmic dependence. Panel (b)-(d): volume histograms for islands grown at 600 °C (b) and 700 °C (d).

In Fig. 3.12 are reported the typical island morphologies developed on the samples annealed at the extreme temperatures (600 °C and 700 °C). In case of annealing at 600 °C small islands are unfaceted mounds with very low aspect ratio (Fig. 3.12(a)), then evolving in square-based pyramids with shallow {105} facets (Fig. 3.12(b)). Larger islands becomes multifaceted domes exhibiting steeper {113} facets (Fig. 3.12(c)). In the case of annealing at 700 °C, the majority of the island population is still dome shaped with the further appearance of even steeper {15 3 23} facets (Fig. 3.12(d)), whose nucleation completes the pyramid-to-dome transition¹¹.

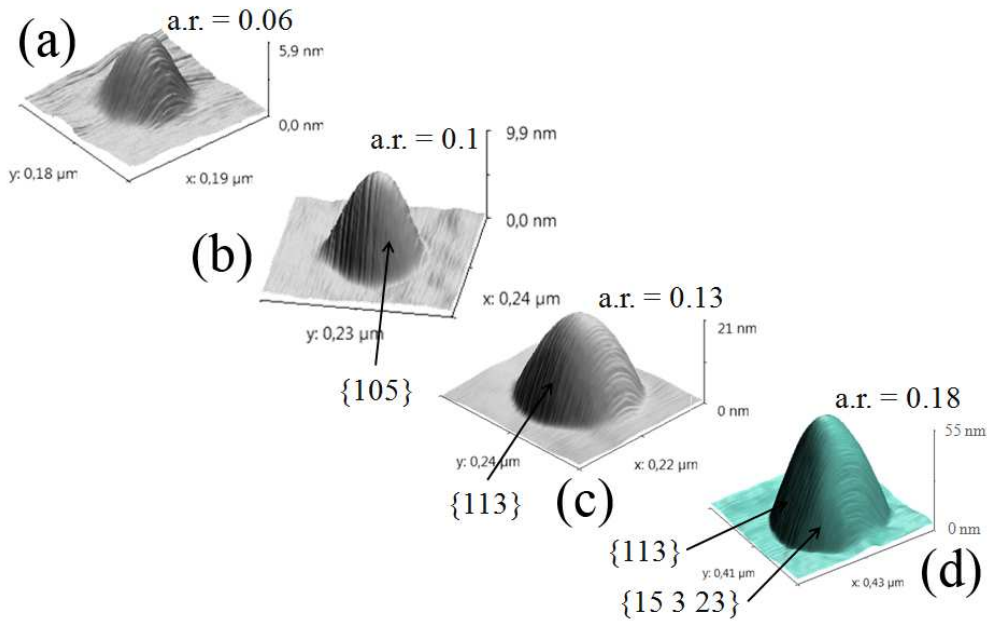


FIG. 3.12. Island morphology evolution from unfaceted mounds (a), to square-based pyramids with $\{105\}$ shallow facets, to steeper islands exhibiting $\{113\}$ facets, to complete domes with the further appearance of even steeper $\{15\ 3\ 23\}$ facets. A simultaneous increase of the height-to-base aspect ratio (a.r.) accompanies the shape evolution.

At variance with MBE, CVD and other out-of-equilibrium techniques, because of the intrinsic longer annealing time it is quite likely that the growth by surface thermal diffusion results in islands in their thermodynamic equilibrium state. The actual thermodynamic stability of the islands can be confirmed by comparing the experimental data with a calculated stability phase diagram. Experimental volume distributions measured on our samples as a function of the over-layer coverage have been obtained by coupling extensive AFM analysis with spatially resolved Auger monitoring of the continuous diffusion profile (see Fig. 3.13). Using the formulation of the free energy difference between island and WL reported in Eq. (3.1), Brehm *et al.*² have calculated the critical volumes (conventionally computed by imposing $\Delta(V) = 0$) for island appearance as a function of the wetting layer thickness shown in Fig. 3.13. They exploited density functional theory (DFT)-derived surface energies, while they evaluate the elastic energy density for pyramids and domes by continuum elasticity theory using a FEM solver. The gray regions within the calculated stability diagram indicate areas where no islands can exist. The experimental volume distributions fall well inside the stability region of dome shaped islands, except for the case of smallest islands at 600 °C which gets close to the pyramid stability region.

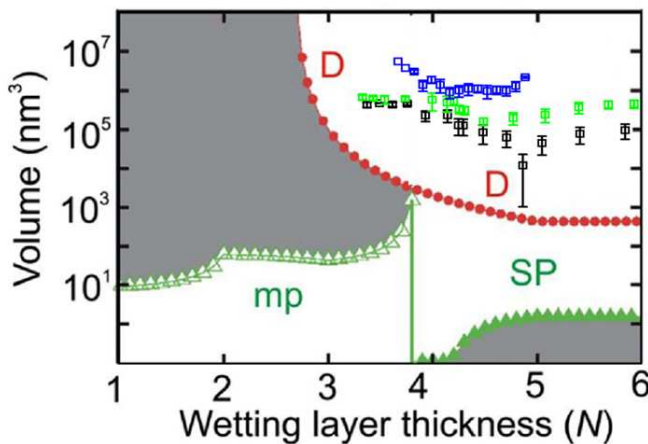


FIG. 3.13. Experimental volume distributions (open black, blue and green squares) measured on our samples plotted as a function of the over-layer coverage for the islands grown within the diffusion area. The error bars in the experimental volume distributions are determined as the standard deviation of the volume histogram for each Ge coverage. The curves represented by the empty triangles, the full triangles and the full circles are the calculated critical volumes for island appearance (from Ref. 2). The gray regions indicate areas where no islands can exist.

3.3.5 Density evolution: 1D model of nucleation

The density distribution of SiGe islands grown by surface thermal diffusion from a Ge source stripe exhibits intrinsic and peculiar properties due to the presence of the stripe and to the spatially variable Ge atomic flux (see Section 2.5.3 in Chapter 2). Using extensive AFM statistical analysis over thousands of islands for each investigated sample, we have determined the behavior of the island areal density as a function of the distance, x , from the stripe (see Fig 3.14 showing the case of annealing at 600, 625, 650, 670 and 700 °C). The density distributions present general features irrespectively from the annealing temperature: the island density exhibit a maximum few μm 's away from the stripe edge, and then slowly decreases at greater distances from it.

The physical origin of this behavior is due to the competition between two opposite processes. The first is the preferential nucleation at the stripe edge giving rise to a depleted zone free of 3D islands, and the second one is the random nucleation on a flat Si surface where the Ge coverage presents a gradient perpendicular to the stripe (1D geometry). Ge atoms moving on the surface can either meet each other to form islands, or walk toward the stripe edge where they are most likely stuck. This competition between island nucleation and the incorporation at the stripe edge leads to a depleted region, or “denuded zone”, in the spatial distribution of the islands near the stripe^{84,85}. A denuded zone is thus a band close and parallel to the stripe edge free of self-assembled islands (see Fig. 3.15(a)). The preferential nucleation at the stripe edge is thus responsible for the increase of the island density as a function of the distance, x , from the stripe. This behavior would exhibit a saturation asymptote in the case of homogeneous Ge coverage⁸⁴ (see Fig. 3.15(b)). However, in the present case the Ge coverage rapidly varies moving far away from the stripe, and thus the following decrease of the island density for distances greater than 2-3 μm , where random nucleation on the flat Si surface dominates, is due to the monotonic decrease of the local density of Ge atoms due to the mass transport from the stripe.

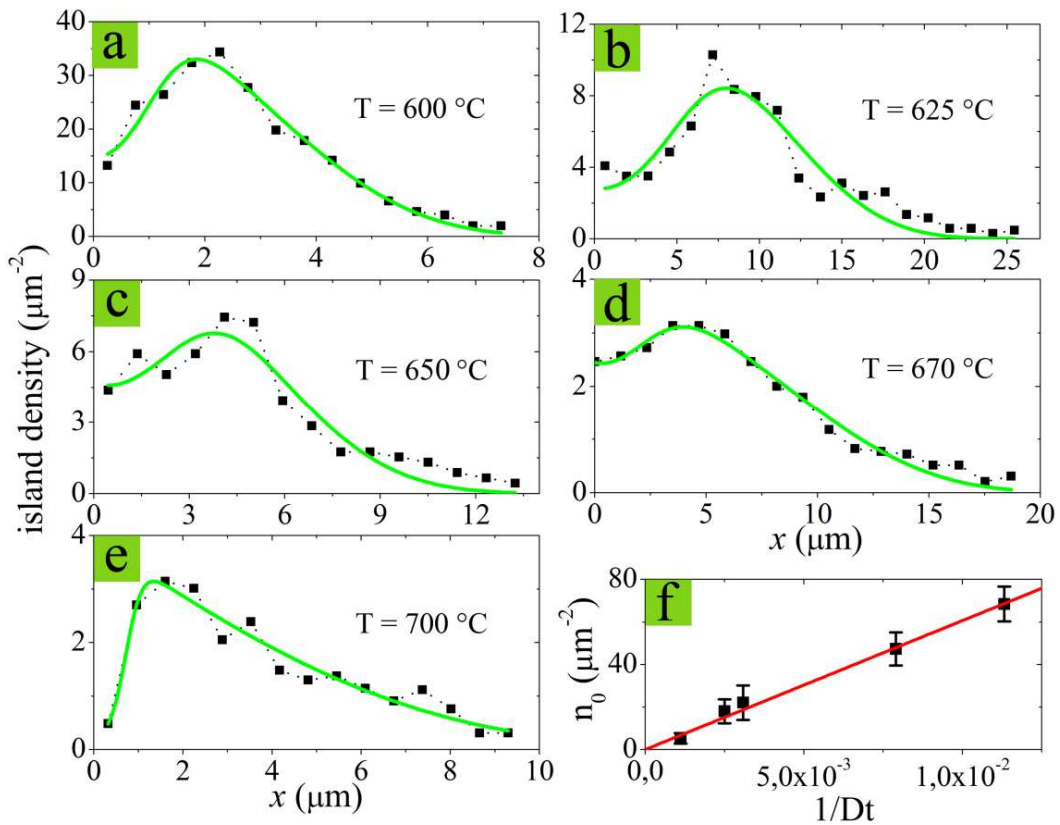


FIG. 3.14. Panel (a)-(e): areal density distributions (black squares) as a function of the distance, x , from the stripe, for islands grown at $600\text{ }^\circ\text{C}$ for 20 min (a), $625\text{ }^\circ\text{C}$ for 7.5 min (b), $650\text{ }^\circ\text{C}$ for 5 min (c), $670\text{ }^\circ\text{C}$ for 4.5 min (d) and $700\text{ }^\circ\text{C}$ 2.5 min (e). The solid green lines are the best fitting using the 1D model of nucleation presented in the text. Panel (f): linear scaling behavior exhibited by n_0 plotted as a function of $1/Dt$. n_0 is the island density in case of homogeneous Ge coverage and in absence of any preferential nucleation site; D is the diffusion coefficient and t is the annealing time.

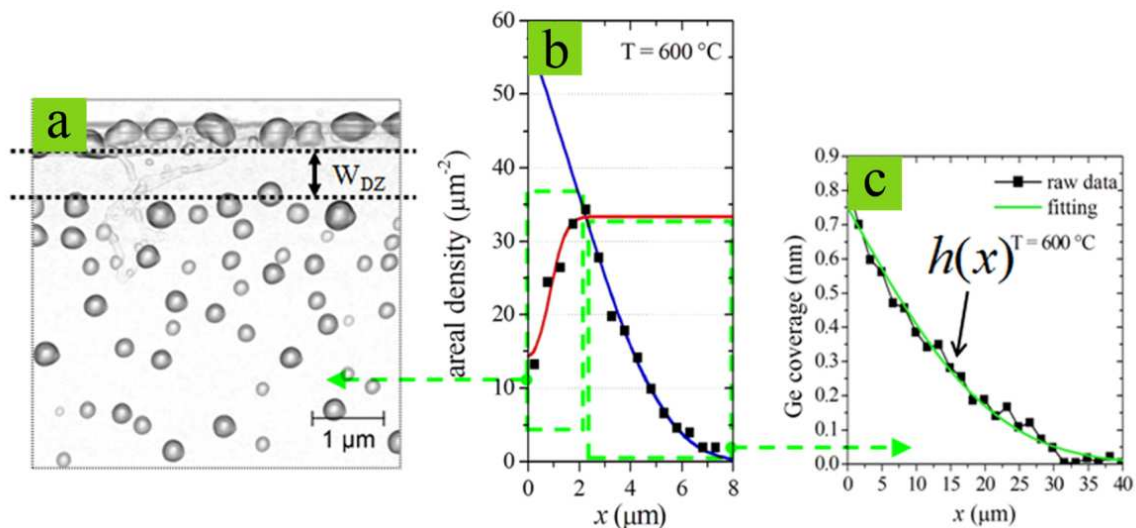


FIG. 3.15. Panel (a): island nucleation region close to the stripe. W_{dz} defines the denuded zone free of 3D islands. Panel (b): areal density distribution (black squares) for islands grown at $600\text{ }^\circ\text{C}$ as a function of the distance, x , from the stripe. The red solid line represents the increase of the island density from a preferential nucleation site to a saturation value, according to the calculations of Ref. 84. The blue solid line describes the decrease for distances greater than $2\text{--}3\text{ }\mu\text{m}$, which is monotonically correlated to the decrease of the local density of Ge atoms due to the mass transport from the stripe. Panel (c): continuous Ge coverage as a function of x after annealing at $600\text{ }^\circ\text{C}$ for 10 min.

The origin of this trend can be considered basically kinetic, and this is supported by two experimental facts: the island density decreases (i) with the distance from the source stripe at a given temperature, and (ii) with the annealing temperature at a given Ge coverage. The first observation can be attributed to the formation of a smaller number of nucleation sites due to the reduction of the local Ge atomic density for greater distances from the source. The second one is genuinely a diffusion limited effect. In fact, the rate of Ge surface diffusion, and thus the diffusion length of each atom, exponentially increases with the temperature promoting the nucleation of islands much more separated from each other, and thus inducing a smaller areal density.

We developed a one-dimensional model of mass transport and island nucleation which allows to describe the behavior exhibited by the island density, n , as a function of the distance from the source stripe. We assumed that the island density is essentially controlled by the local differences in the chemical potential $\Delta\mu$ of the wetting layer. Tersoff⁸⁶ used empirical potentials to calculate the surface energy per atom for Ge wetting layers as a function of thickness. Daruka and Barabasi⁸⁷ suggest an approximate exponential form for the change in the chemical potential with thickness:

$$\Delta\mu = -\Delta\mu_0 \exp\left(-\frac{h - h_c}{h^*}\right) \quad (3.10)$$

where h is the wetting layer thickness, h_c is the critical WL thickness at the 2D-to-3D transition (~ 4 ML), and $\Delta\mu_0$ and h^* describes the wetting forces between Ge and Si^{86,87}. By fitting Tersoff's results (plotted as square symbols in Fig. 3 of Ref. 86), we estimate $\Delta\mu_0 = 0.1$ eV and $h^* = a_{Ge}$.

In our experiment, the wetting layer thickness is determined by the 1D Fick's second law expressed by equation (2.8) of Chapter 2, according to which the gradient of the Ge concentration between the stripe and the surrounding regions is the driving force for the surface diffusion:

$$D \frac{\partial^2 c}{\partial x^2} = \frac{\partial c}{\partial t} \quad (3.11)$$

where t is the time, and D is the diffusion coefficient. The Ge stripe has an initial concentration distribution with a step-like shape, and the height at the boundary is essentially maintained at a constant value during the annealing. These initial and boundary conditions represent the case of diffusion from a source of constant concentration, as discussed in Section 2.23 of Chapter 2. The solution of the diffusion equation, i.e. the Ge coverage along the diffusion profile is borrowed from the equation (2.17) of Chapter 2 and given by the following relation:

$$h = h_0 \left[1 - \operatorname{erf}\left(\frac{x}{L}\right)\right] \quad (3.12)$$

where L is the diffusion length. Eqs. (3.10) and (3.12) describe quantitatively the random nucleation on a flat Si surface where there exist a gradient in the Ge coverage.

Now we need to introduce the preferential nucleation at the stripe edge. This can be done by artificially creating at the stripe edge a Gaussian-shaped region of limited spatial extension exhibiting a local lowering of the chemical potential:

$$\Delta\mu = -\Delta\mu_0 \exp\left(-\frac{h-h_c}{h^*}\right) - \chi \exp\left(-\frac{x}{x_0^2}\right) \quad (3.13)$$

where the stripe edge is considered at $x = 0$, and $x_0/2$ is approximately the width of the stripe edge.

Nucleation is treated in our model by considering that for each surface site the relative probability, p , of formation of a critical nucleus depends only by the local differences in the chemical potential $\Delta\mu$ of the wetting layer (and not by the absolute value of the chemical potential $\mu(x)$). Since in the nucleation process a characteristic activation energy must be overcome, the probability p follows an Arrhenius-type exponential law:

$$p = p_0 \exp\left(\frac{\Delta\mu}{K_B T}\right) \quad (3.14)$$

where $\Delta\mu$ is given by the Eq. (3.10). It is worth noting that $\Delta\mu$ should be a negative value in order that the nucleus becomes supercritical and the island will tend to increase its size. In this picture the island density is determined by the number of supercritical nuclei, and thus it depends proportionally on the relative probability p ⁸⁸:

$$n = n_0 \frac{p}{p_0} \quad (3.15)$$

where n_0 represent the island density in case of homogeneous Ge coverage and in absence of any preferential nucleation site.

By combining the Eqs. (3.10) - (3.15), the dependence of the island density on the distance from the source stripe can be finally obtained:

$$n = n_0 \exp\left[-\frac{\Delta\mu_0}{K_B T} \exp\left(-\frac{h_0 \operatorname{erfc}\left(\frac{x}{L}\right) - h_c}{h^*}\right) - \frac{\chi}{K_B T} \exp\left(-\frac{x^2}{x_0^2}\right)\right] \quad (3.16)$$

The green lines in Figs. 3.14(a)-(e) represent the best fitting of the experimental behaviour of the island density as a function of x using the analytical 1D model of nucleation discussed so far. It successfully reproduces all of the important behavior seen in the experiments. Only n_0 and χ have been considered as fitting parameters to be adjusted. In fact, h_0 and L are determined by the experimentally measured diffusion profiles for each annealing temperature; h_c and h^* are, respectively, equal to 4 ML and 1 ML⁸⁶; $x_0/2$, which represents the width of the stripe edge, is considered to be equal to $\sim 0.5 \mu\text{m}$ from AFM analysis. The χ values obtained from the fitting vary in the range 0.1-0.2 eV, very close to the value used for $\Delta\mu_0 = 0.1 \text{ eV}$ as derived by Tersoff's

results. Fig. 3.14(f) shows the linear scaling behaviour exhibited by n_0 when plotted as a function of $1/Dt$, where Dt is derived by the diffusion length ($L = 2\sqrt{Dt}$) from the experimentally measured diffusion profiles for each annealing temperature (see Section 2.5.2 of Chapter 2). This behaviour quantitatively confirms the essentially diffusive origin of the decrease of the island density for higher temperatures.

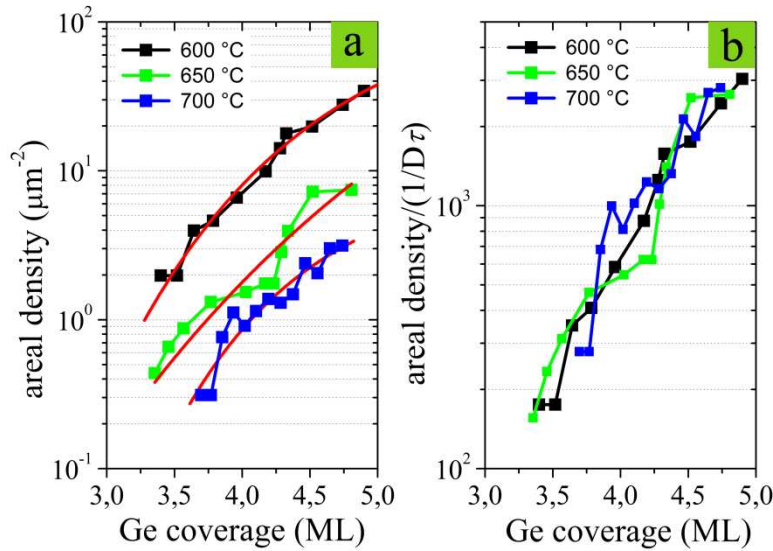


FIG. 3.16. Panel (a): areal density distributions of islands nucleated within the random nucleation area as a function of the Ge coverage obtained from fitting Auger data with a discrete layer model (see Section 2.5.1 of Chapter 2). The red solid lines represent the best fitting of the experimental data using the 1D model described in the text. Panel (b): the density distribution in (a) has been normalized to the factor $1/Dt$, where D is the diffusion coefficient and t is the annealing time.

A further stronger confirmation of this effect comes from the scaling analysis of the correlation between the island density in the random nucleation area ($x > 2\text{-}3 \mu\text{m}$) and the Ge coverage along the continuous diffusion profile (see Fig. 3.16(a)). Normalizing the island density to the factor $1/Dt$, we found that all curves follow a universal scaling distribution which depends only on the Ge coverage (see Fig. 3.16(b)). This can be easily understood assuming that the growth process evolves within a diffusion limited regime. In this case the island density can be written as the inverse of the squared distance d_{nn}^2 between nearest-neighbors islands, which scales as the diffusion length L of Ge atoms moving on the surface. In hypothesis of a random walk motion L is related to the diffusion coefficient and the annealing time by the relation $L^2 = 4Dt$. This leads to the following expression for the island density:

$$n \approx \frac{1}{d_{nn}^2} \approx \frac{1}{L^2} \approx \frac{1}{Dt} \quad (3.17)$$

confirming the experimentally observed scaling behavior.

3.3.6 Size evolution: capture zone growth and SiGe intermixing

In Fig. 3.17 the observed size evolution of the islands as a function of distance, x , from the stripe is shown in comparison with the density behaviour: the region with high Ge coverage (close to the stripe, $x \approx 2 - 3 \mu\text{m}$) where the island density reaches its maximum presents the lowest average island size, while where the coverage decreases to 3.5-4 ML larger average dimensions and lower island density are attained. The interplay among nucleation, atomic diffusion dynamics and Si intermixing is strongly affected by the gradient of the Ge coverage as induced by the mass transport from the source stripe, possibly giving rise to the observed spatial modulation of island size.

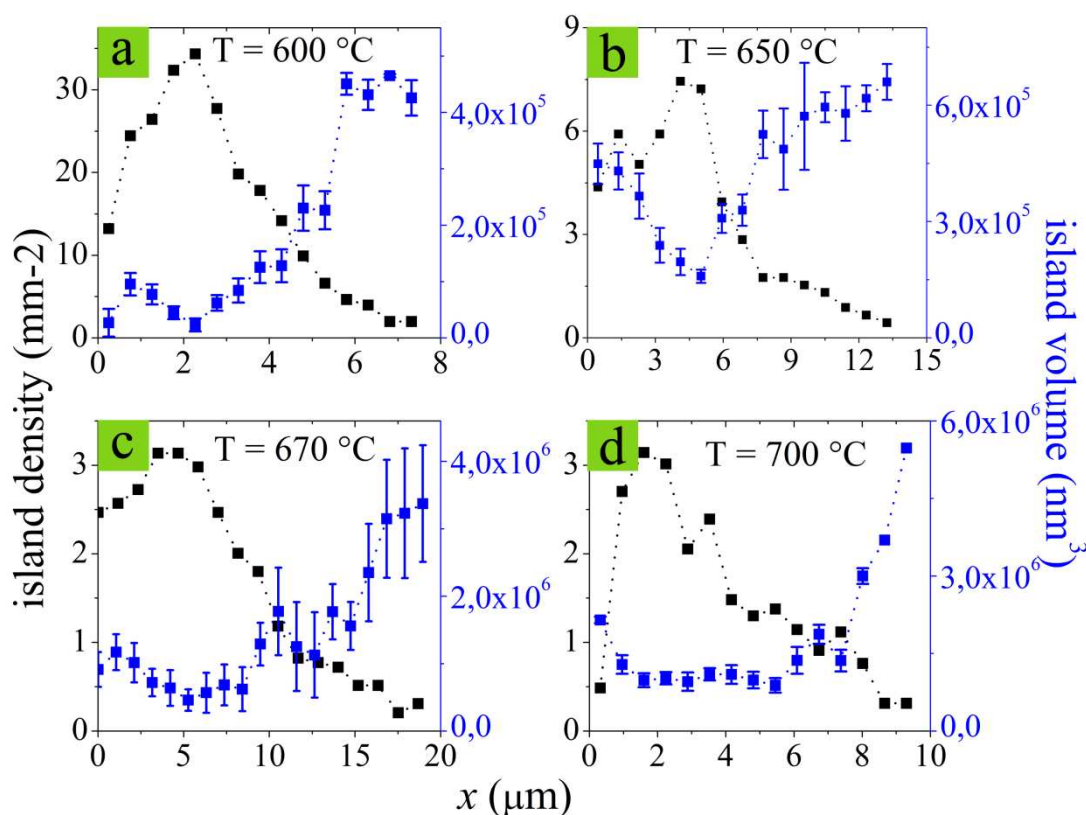


FIG. 3.17. Island density (black squares) and average island volume (blue squares) as a function of the distance, x , from the stripe for different annealing temperatures.

The understanding of the origin of this size modulation is fundamental for the comprehension of the factors governing the relative growth of individual nanostructures, and furnishes an important insight within the competition processes among different nuclei to gather the mass present on the surface. As described in Chapter 1, the growth can be essentially described in terms of kinetic processes based on diffusion, nucleation, and capture⁸⁹. The growth of a 3D island arises from the formation of a stable nucleus. The latter generally results from a collision process involving a number of diffusing atoms greater than a critical threshold⁹⁰. The occurrence probability of such a collision event is proportional to the local density of atoms⁸⁸. Upon formation, the critical nucleus

starts capturing the diffusing atoms in its neighborhood. From this point on some different scenarios could develop during the further growth of the single nucleus. The growth of the islands might be governed by diffusive phenomena⁹¹. In this context diffusing atoms would tend towards and be captured by – on average – the closest nuclei. The process could then be described by the *Mulheran capture zone model*^{92,93}, which results in a linear relationship between the growth rate of every island and the capture zone from which islands can gather mass. Thus the competition among neighboring nuclei to attract the mass supplied to the surface would follow local laws. On the other hand, a growth process not consistent with the Mulheran model could be related to energetic factors. These might prompt diffusing atoms to preferentially reach islands for reasons else than their geometric proximity as energetic interactions among islands leading to local nonuniformities in the mass density and driving an unbalanced diffusion of atoms at the surface. Under these circumstances some nuclei would reach a thermodynamically steadier structure than others and develop thereafter at a different place⁹⁴. Here we test these concepts by comparing the output of the capture zone model descriptions with our experimental results.

As discussed in the previous section, the scaling behavior exhibited by the island density as a function of the Ge coverage (see Fig. 3.16) gives strong experimental evidence that the growth process essentially evolves within a diffusion limited regime. In this scenario the island growth at microscopic length scale is determined by kinetic factors only, and thus the essence of the phenomenon would be described by the Mulheran model, where the island volume proportionally correlate with the capture zone area and the island density exhibits an inverse correlation with it:

$$V \propto A_{CZ}, \quad n \propto \frac{1}{A_{CZ}} \quad (3.18)$$

where A_{CZ} is the capture zone area, which can be mathematically defined as the area of the Voronoi cell within the Voronoi tessellation of the island network. The surface is divided into several cells that are associated with the center of mass of each island, and are defined as the sets of points that are closer to a given island rather than to any other (see inset in Fig. 3.18(a)).

The model's validity can be verified by evaluating the correlation between island volumes and the Voronoi cell areas. Our approach consists of plotting the former as a function of the latter and estimating the degree of linear correlation by the Pearson's coefficient, r . Fig 3.18(a) summarizes the results we have obtained at different temperatures for islands grown inside the random nucleation area far from the stripe ($x > 2 \mu\text{m}$), since the stripe itself could be a possible source of alteration of the hypothesis of the Mulheran model. A Pearson's coefficient of about 0.76 quantitatively attests the good linear correlation between the volume of the islands and their correspondent capture area. The validity of the Mulheran model is further confirmed by probing the

inverse correlation of the island volume as a function of the areal density ($n \approx 1/V$), as shown in Fig. 3.18(b) including results for annealing at different temperatures. This findings suggest that kinetic factors rather than energetic ones crucially affect the competition between the islands to gather the available mass and could be one of the main causes responsible for the observed island size evolution as a function of the distance from the stripe.

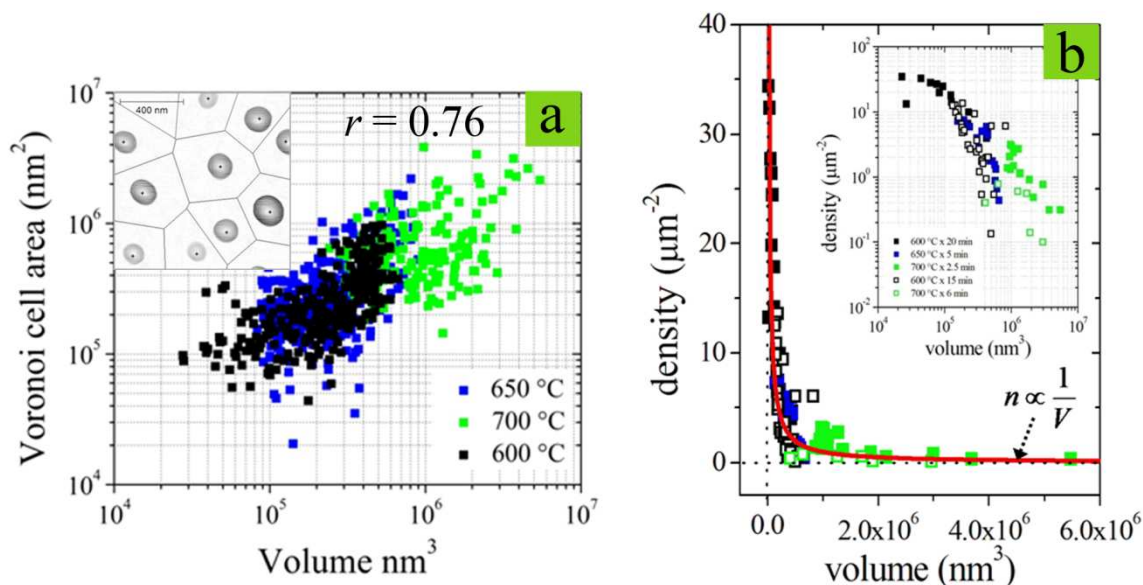


FIG. 3.18. Panel (a): scatter plot of the Voronoi cell area as a function of the island volume for different annealing temperatures. Inset: schematic representation of the Voronoi tessellation of the island network. Panel (b): island density plotted in linear scale as a function of the volume, showing an inverse correlation behavior. Inset: the density is plotted as a function of the volume using logarithmic scales.

Within the scenario described so far, the increased volume for islands grown far away from the stripe is essentially determined by the mass gathering from a greater capture area, due to the lower island density. Indeed, during the growth process the mass available for a growing island is represented by both the Ge atoms diffusing on the surface and the Si atoms coming from the substrate which penetrate into the islands leading to the formation of alloyed nanocrystals. We already observed that Si intermixing is driven by the entropy of mixing²³ and strain relaxation, and it has been shown to drive the increase of the mean island size^{24,25}. Now we will be able to draw a quantitative relationship between intermixing and the mean island size in case of islands growth by surface thermal diffusion.

To measure the composition of single islands we performed an Electron Energy Loss Spectroscopy (EELS) experiment in a Scanning Transmission Electron Microscope (STEM) (more details about this technique are reported in the Panel C). Fig. 3.19(a) shows a low angle annular dark field (LAADF) STEM image of the cross-section of a single dome-shaped island grown at 670

°C and nucleated 2.1 μm far from the stripe (see inset in Fig. 3.19(a)). The sample preparation for the cross-sectional imaging has been obtained using a Focused Ion Beam (FIB) microscope by means of the procedure described in the Section C.5 of Panel 5. In LAADF-STEM imaging mode the contrast is mainly determined by the atomic number of the elements. Figs. 3.19(b) and 3.19(c) show Energy Filtered TEM images at the SiGe (16 eV) and Au (25 eV) plasmon loss peaks, respectively. We monitored also the Si and Ge L-edges loss signals at energy loss of 99 eV and 1217 eV with respect to the elastic peak, respectively, as a function of the position along vertical and horizontal line scans. By normalizing these integral intensities to the correspondent cross-sections determined within the Hartree-Slater model, the relative composition of Si and Ge is thus obtained. Figs. 3.19(b) and 3.19(c) show the vertical and horizontal profiles of the Ge concentration across the island. The increase of the Si concentration at the extreme points of the horizontal profile is consistent with highly Si intermixed boundary regions of about 15 nm, in agreement with several experimental and theoretical results^{26,27} which consider the Si incorporation as due to only surface diffusion phenomena. Moreover, the behavior of the Ge concentration along the vertical profile is consistent with the results of Rastelli *et al.*³⁶ obtained using selective chemical etching. The rapid increase of the Ge concentration from ~5 % to ~55 % within ~10 nm for positions below the surface plane corresponds to the Si-rich SiGe material inside trenches digging into the substrate and responsible for the supply of the Si inside the island. Then a slower increase of the Ge concentration appears leading from ~55 % to ~75 % within ~ 45 nm corresponding to a vertical compositional gradient from a Si-rich bottom to a Ge-rich topmost region.

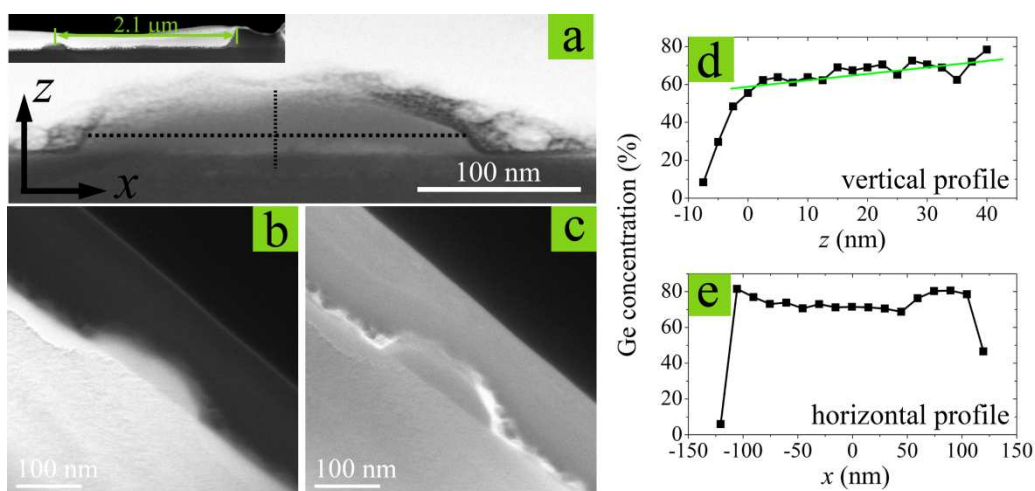


FIG. 3.19. Panel (a): cross-section LAADF-STEM image of a single island grown at 670 °C and nucleated 2.1 μm far from the stripe (see inset). Panels (b)-(c): Energy Filtered TEM images at the SiGe (b) and Au (c) plasmon loss peaks. The gold layer is used as protective layer during the sample preparation procedure. Panels (d)-(e): vertical (d) and horizontal (e) profiles of the Ge concentration within the island along the dotted lines shown in (a).

To explore the interplay between intermixing and size evolution, we measured the composition of single islands grown at 700 °C as a function of the distance from the stripe by means of micro-Raman spectroscopy (see Fig. 3.20) (a detailed discussion of the technique and its application to a biaxially strained SiGe thin film is reported in the Panel D). The measured values of Ge concentration change from 45 % to about 25 % moving farther away from the stripe, with an experimental uncertainty of about 3 %. The values of strain obtained within the same measurement range between 0.1% and -0.2 % with an experimental uncertainty of 0.2 %. The values of strain and concentration are based on the results reported in Ref. 95 (see also the Section D.3 of Panel D), and therefore they rely on coefficients calibrated from flat biaxially strained thin films, uniform in strain and composition. This is not the case for SiGe islands being inhomogeneous in both composition³⁶ and strain⁹⁶, and therefore it is difficult to quantify precisely the validity of the application of these calibrations. Nevertheless, the observation of a neat variation of composition as a function of the distance from the stripe is well distinguished from the experimental uncertainty and gives important hints about the self-assembling of the islands. Looking at the average island concentration, a greater Si incorporation has been found for islands nucleated farther away from the stripe at lower Ge coverage regions (see Fig. 3.20(b)). In the inset of Fig. 3.20(b) is shown a tentative correlation between the volume and the Ge content for islands following a thermodynamic equilibrium growth (far from the stripe, $x > 2 \mu\text{m}$).

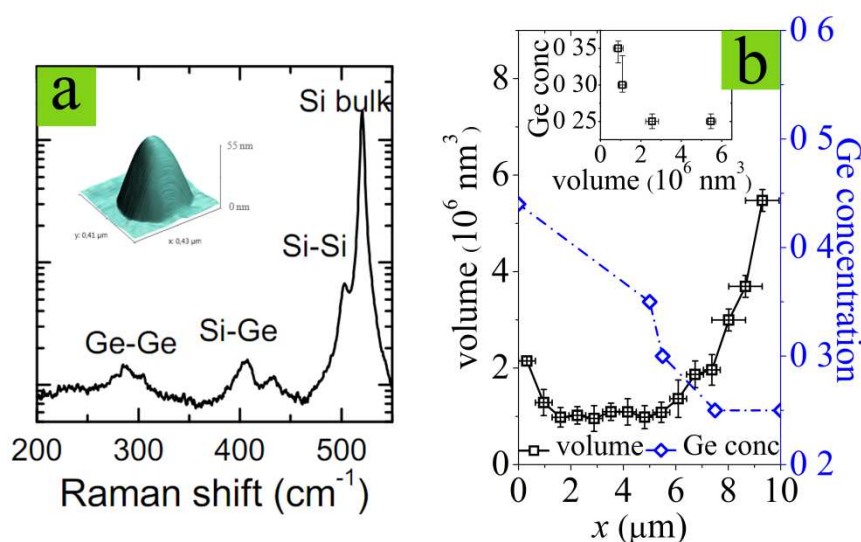


FIG. 3.20. Panel (a): Raman spectrum measured on a single dome-shaped island grown at 700 °C and nucleated 10 μm far from the stripe; the Ge-Ge, Si-Ge, Si-Si modes related to the island and the Si bulk mode are indicated. Panel (b): Ge concentration (blue open diamonds) and average volume (black open squares) of islands grown at 700 °C as a function of the distance, x , from the stripe. Inset: tentative correlation between volume and Ge content for islands following a thermodynamic equilibrium growth (far from the stripe, $x > 2 \mu\text{m}$).

The trend of the Ge concentration as a function of the distance from the stripe is quantitatively confirmed even at lower annealing temperatures, as monitored by means of Scanning Auger Microscopy (SAM) for islands grown at 670 °C. We measured the Si LMM (90 eV) and Ge LMM (1150 eV) Auger lines on single islands nucleated at different distances, x , from the stripe. By using a standard-based quantification method, where the Auger intensities have been corrected with an exponential factor in order to take in account the residual Carbon contamination, we determined the trend of the average Ge concentration as a function of x (shown in Fig. 3.21, together with the Ge concentration at the island top derived from the EELS-STEM results for a single island grown at 670 °C and nucleated 2 μm far from the stripe). It is worth noting that the Auger analysis is sensible only to the surface composition of the islands mediated over the whole area of about 100 nm in diameter with a depth sensitivity of a few nanometres, and thus the concentration values indicated in Fig. 3.21 are relative to the most external shell of the island.

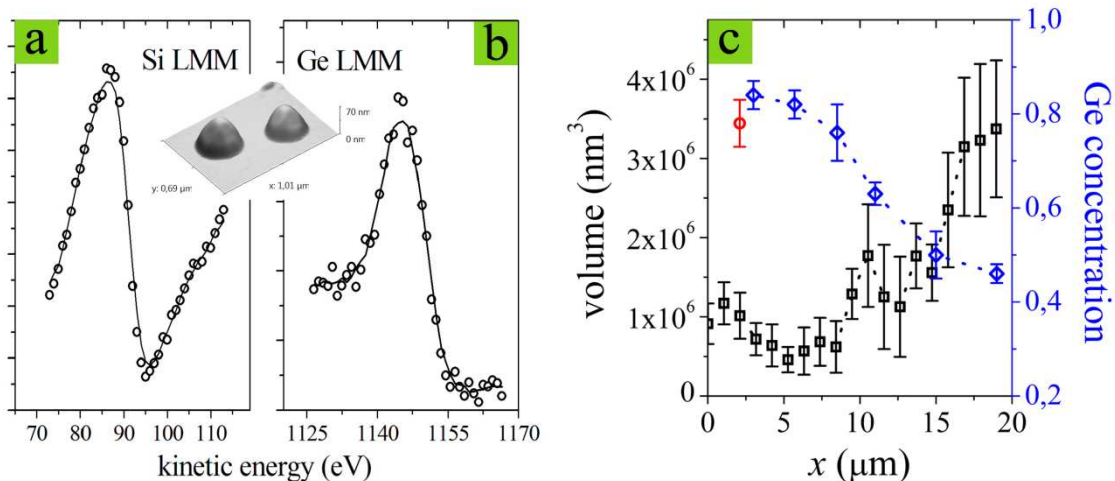


FIG. 3.21. Panel (a)-(b): Si LMM (a) and Ge LMM (b) Auger peaks measured on a single dome-shaped island grown at 670 °C. Panel (c): Ge concentration (blue open diamonds) and average volume (black open squares) of islands grown at 670 °C as a function of the distance, x , from the stripe. The red open circle data point represents the Ge concentration measured on top of a single island by means of STEM-EELS (see Fig. 3.19).

Since intermixing strongly affects the average island size⁴¹, the observed island volume evolution can be reasonably related to the measured spatial modulation of Ge composition shown in Fig. 3.7, induced by the variation of the local density of Ge atoms due to the mass transport from the stripe. The increase of the island volume going away from the stripe is thus mainly determined by the interaction of two contributions: (i) the decrease of the island density, and (ii) the increase of the Si incorporation. For regions close to the stripe the higher local density of Ge atoms with respect to the Si flux coming from the substrate leads to the formation of a high density of critical nuclei gathering mass (Si and Ge) from small capture areas. In this case only small and weakly intermixed islands are thermodynamically stable and kinetically allowed to grow. However,

far away from the stripe the local density of Ge atoms decreases considerably with respect to the Si flux. This leads to the formation of a small number of critical nuclei exhibiting wider capture areas where the flux of Ge atoms diffusing on the surface is significantly reduced with respect to the Si flux from the substrate, and thus bigger and highly intermixed islands develop.

3.3.7 Carbon-induced modulation of island size and density

In Section 2.6 of Chapter 2 we have investigated the surface diffusion on a C-covered Si(001) surface. The Ge diffusion coefficient at 600 °C has been monitored as a function of the carbon coverage. The increase of the carbon coverage from 0.1 to 1 ML corresponds to a decrease of the diffusion coefficient from 3×10^{-9} to 3×10^{-13} cm²/s. This variation of four order of magnitude is discussed within a physical scenario where carbon is incorporated within the shallow volume of the Si substrate due to the chemical interactions among Si, C, and Ge, and thus inducing an enhancement of the surface roughness and a compressive local strain field able to modulate the diffusion of Ge atoms. Spontaneous nucleation of SiGe islands coexists with the continuous surface diffusion of Ge. By directly measuring the overlayer critical thickness for nucleation, we showed (see Section 3.3.2 of this Chapter) that the island growth mode gradually evolves from SK in case of absence of surfactant to VW for high surfactant coverage.

Here we investigate the influence of carbon on the size and density of islands grown at a fixed temperature (600 °C for 10 min). Fig. 3.22 shows the volume distribution of islands developed in the regions shown in Fig. 2.10 of Chapter 2 with a different carbon coverage, and nucleated within the same area close to the stripe edge (x ranging from 0 to 3 μm). Such histograms show that smaller islands are preferentially nucleated in the C-rich region while bigger islands tend to grow where the C coverage is reduced. The spread of the distribution is also seen to increase for lower C coverage.

By using the statistical analysis of the AFM data coupled with the SAM observations, the average size and the areal density of islands nucleated in regions with different C coverage are correlated with the diffusion coefficient showing a monotonic dependence, as reported in Fig. 23. These results show that increasing the surface atomic mobility leads to the enhancement of island size and a correspondent decreasing of the areal density. This behavior is in good agreement with the results reported by different authors using MBE^{72,73} showing that the deposition of sub-monolayer carbon enables the growth of smaller islands with higher density. The islands size and density dependence on a reduced atomic mobility is qualitatively similar to the effect of a decreasing temperature in absence of surfactant⁹⁷. The same trend is also seen when Sb is used as a

surfactant at a fixed temperature⁹⁸, even if different mechanisms dominate at atomic level with respect to a C surfactant due to the diverse nature of the chemical interactions Ge-C and Ge-Sb. In fact Sb atoms tend to float over the Si surface while C atoms tend to incorporate within subsurface sites (see Section 2.3 of Chapter 2 for a more extensive discussion).

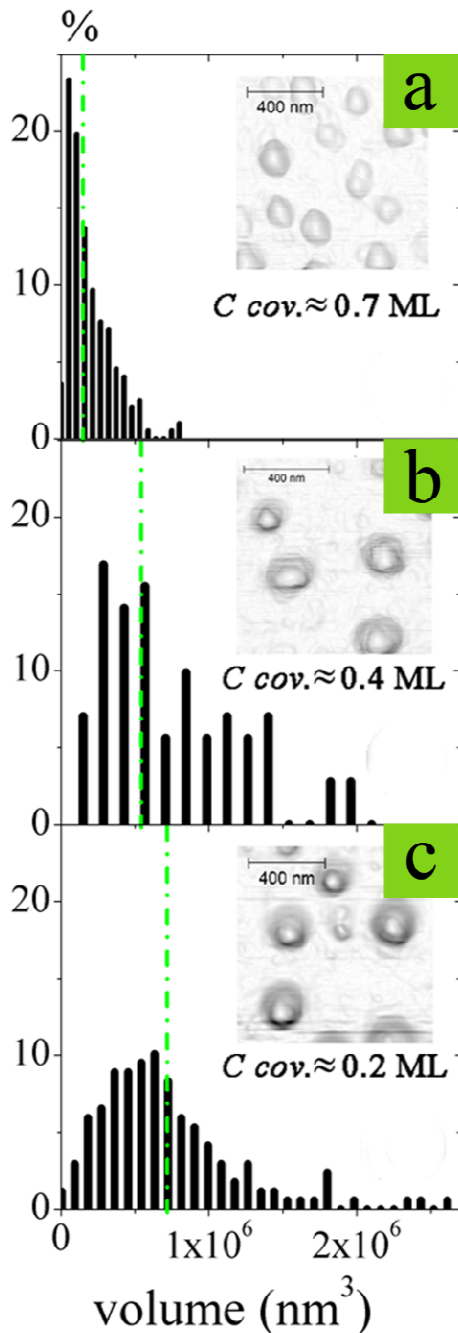


FIG. 3.22. Volume histograms of the SiGe islands nucleated in areas with different Carbon coverage. Smaller islands are preferentially nucleated in the C-rich region (panel (a)), while bigger islands grow at low C-coverage zones (panel (b) and (c)). The insets in the panels are AFM images in gradient mode of islands nucleated for different C coverage. The dash-dot green lines shown in each panel represent the average volume of the corresponding distribution.

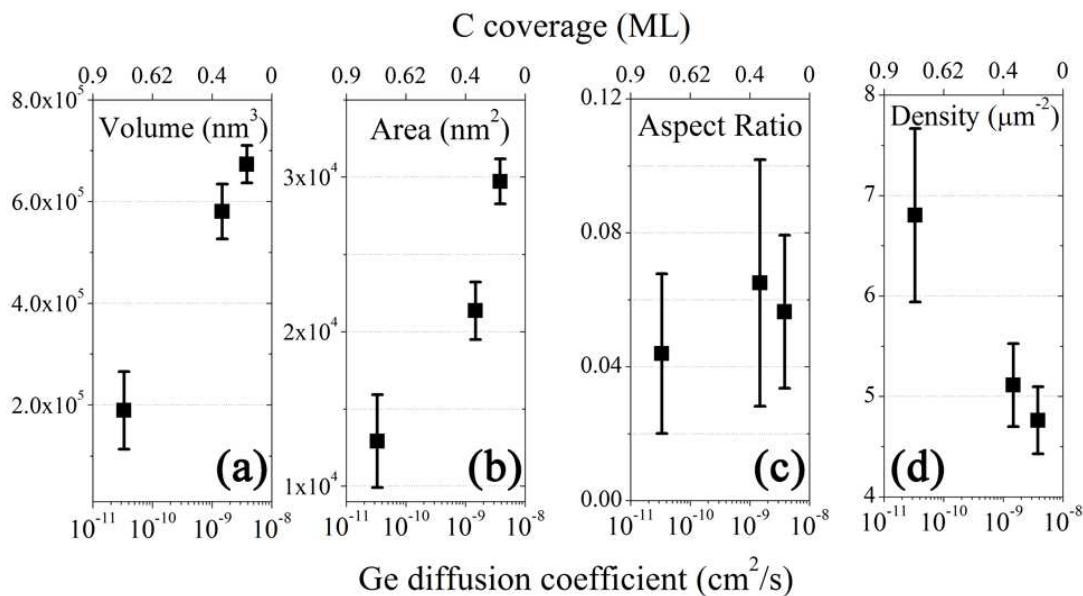


FIG. 2.23. Average volume (a), area (b), aspect ratio (c) and density (d) of the islands nucleated in areas with different C coverage correlated with the Ge diffusion coefficient.

Based on this observation and on the conclusion of the Section 2.6 of Chapter 2, we attribute the size and density dependence of the nucleated islands from the carbon surfactant coverage to the C-induced modulation of the atomic mobility of Ge atoms on the surface. This is another evidence of the diffusive origin of the growth process⁹¹, where diffusing atoms tend to be captured by the closest nuclei, and the islands grow by gathering mass essentially from a defined surrounding area. As already discussed in case of island formation on a C-free Si surface, the growth process should be well described by geometrical based models^{99,100}, and in particular by the Mulheran *capture zone model*⁹². This results are a further confirmation that the island growth should be mainly controlled by the local kinetics of diffusion which in turn determines the island density and governs the competition among the nuclei to collect Ge and Si in their surroundings. The experimental verification of the validity of the Mulheran's model is confirmed by the good linear correlation (Pearson's coefficient of 0.89) between the volume and the Voronoi cell areas for islands grown at different C coverage shown in Fig 3.24. The strict similarity between the scatter plot for islands grown at a fixed temperature but for different C coverage, and that one shown in Fig. 3.18(a) for islands nucleated at different temperatures on a C-free Si surface is a further confirmation of the C-induced modulation of the Ge surface diffusion controlling the growth process.

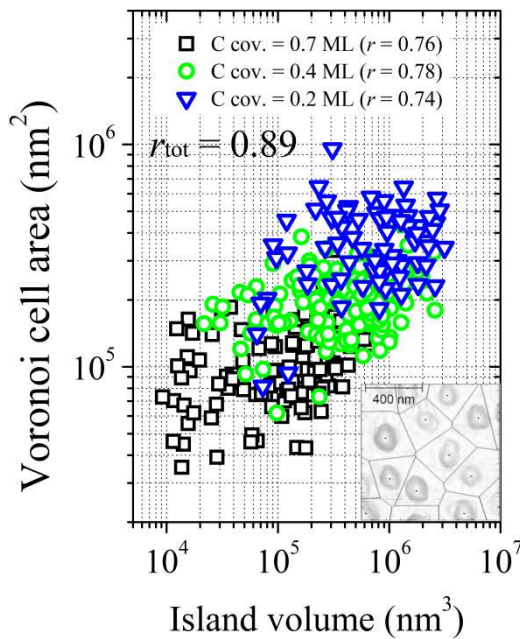


FIG. 3.24. Scatter plot of the Voronoi cell areas as a function of the volume for islands grown at 600 °C in regions with different carbon coverage. The legend reports the Pearson's coefficients for the data sets related to each C coverage; the total Pearson's coefficient is also indicated. Inset: schematic representation of the Voronoi tessellation of the island network.

3.3.8 Delayed plastic relaxation

Si intermixing offers a path to the elastic strain relaxation since alloying effectively reduces the lattice misfit between the island and the substrate. Dislocation injection leads to a similar effect since it lowers the elastic energy stored into the islands by relieving the misfit strain. Thus intermixing and dislocation injection influence each other: islands grown at higher temperatures, being more Si-rich, may display a lower tendency towards plastic relaxation, leading to larger critical sizes for dislocation injection^{41,45,96}. However the kinetics of the growth process and the time scale over which Si intermixing occurs with respect to that of the Ge supply, quantitatively influence the elemental composition and the coherence of the growing islands. Within this scenario, the interplay between intermixing and plastic relaxation is still not fully understood and represents one of the most intriguing aspects of Ge/Si(001) SK growth.

In Fig. 3.25 we present the distribution of the aspect ratio of islands grown at 600 °C and 700 °C as a function of their base width, BW . The monotonic increase of the aspect ratio going from smaller to bigger islands is consistent with the continuous transition from shallow to steeper morphologies allowing a partial elastic strain relief as qualitatively described by Eq. (3.1). The absence of any discontinuity in the aspect ratio distribution contrary to the scatter plot shown in Fig. 3.5(c), is a first indication that, in average, islands are coherently matched to the substrate and the plastic relaxation channel is quenched. Moreover, at a fixed BW , the smaller aspect ratio for islands

grown at 700 °C with respect to those obtained at 600 °C is an indication of a greater SiGe intermixing at higher temperatures^{41,43}.

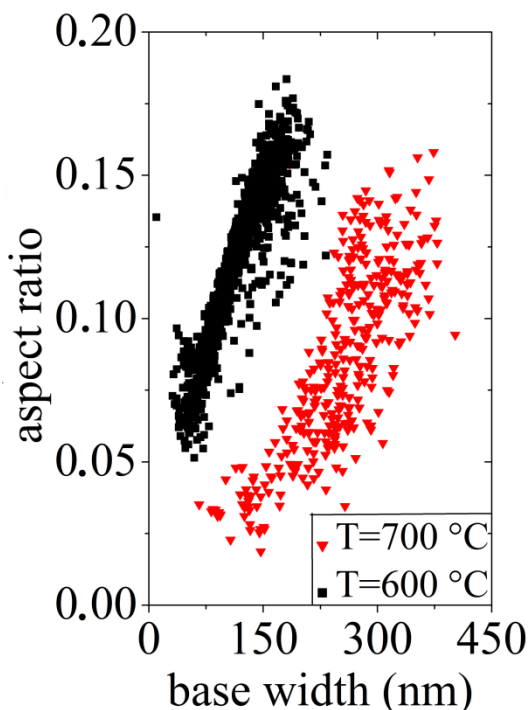


FIG. 3.25. Aspect ratio distributions as a function of the base width for islands grown at 600 °C (black squares) and 700 °C (red triangles).

To confirm the above conclusions, in the following we discuss the direct non-averaged information about the internal defect structure of SiGe islands obtained by TEM analysis. The plastic relaxation by dislocation injection is experimentally evidenced by the presence of moiré and cross-hatched patterns, as shown in Ref. 101 and in Fig. 3.26(a)-(d) (see also Section C.6 of Panel C), which represent TEM images taken on the plastically relaxed Ge stripe. The comparison of these images with those of representative islands nucleated in the diffusion region (Figs. 3.26(e)-(h)) provides clear indications on their plastic relaxation.

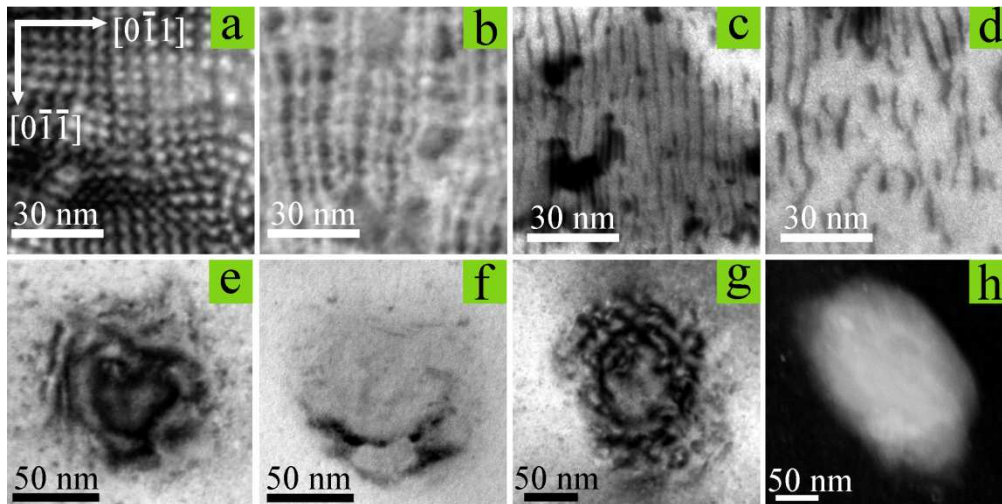


FIG. 3.26. TEM images of the sample annealed at 700 °C taken on the relaxed Ge stripe (Panels a-d) and from representative single islands in the diffusion region (Panels e-f). All images are aligned according to the directions shown in (a). Panels (a) and (b): plan view (PV) bright field (BF) images under [100] diffraction condition showing moiré patterns due to the misfit at the interface between the relaxed Ge stripe and the Si bulk (a), and a cross-hatched pattern (b) due to the 90° edge dislocations propagating along the interface. Panels (c) and (d): weak beam (WB) BF images in [022] diffraction condition. The lines parallel to the [011] direction shown in (c) are due to the 90° dislocations. The short and irregular segments in (d) come from the threading arms of the 60° dislocations. Panels (e) and (g): PV BF images under [100] axis beam condition of SiGe islands showing the absence of dislocation fingerprints as in the patterns presented in (a) and (b). Panel (f): WB BF image in [022] diffraction condition of the same island of Panel (e) showing the absence of features similar to those reported in (c) and (d). Panel (h) LAADF-STEM image of a large SiGe island: the presence of dislocations would result in brighter lines parallel to the $\langle 011 \rangle$ directions [Ref 101], not seen here.

Figs. 3.26(e) and 3.26(g) show plan view (PV) bright field (BF) TEM images of single islands grown at 700 °C taken in [001] axis beam condition (to be compared with Figs. 3.26(a)-(b) taken on the relaxed stripe). The (roughly) circular diffraction fringes visible inside the islands indicate a lateral outward bending of the lattice planes. The absence of moiré patterns exclude the plastic relaxation of the islands, in agreement with the indication derived from the aspect ratio distribution, and implies that they are still coherent with the Si substrate. This is clearly visible also in the TEM image taken in [022] diffraction condition (Fig. 3.26(f), to be compared with Fig. 3.26(c)-(d)) showing a uniform contrast inside the island without characteristic fringes as induced by the presence of dislocations. The black regions inside the island are due to portions of lattice plane families in Bragg condition with the electron beam, which move from one extreme to the other by changing the diffraction angle (not shown). A further cross check of the absence of crystalline defects is provided by LAADF-STEM imaging (Fig. 3.26(h)), where the contrast is mainly determined by the atomic number of the elements. In this imaging mode a dislocation appears as an intense white line due to the random displacement of atoms around defects which causes extra scattering in the low angle region¹⁰². In Fig. 3.26(h) a large SiGe island appears as a nearly uniform

lighter area where the absence of brighter linear features aligned along the $\langle 011 \rangle$ directions exclude the presence of dislocations or stacking faults.

Fig. 3.27 shows PV BF TEM images under $[02\bar{2}]$ axis beam condition of islands grown at 600 °C. Also in this case of lower temperature the majority of the islands appears to be dislocation-free, as seen by the uniform contrast inside them in the TEM images, even if some larger islands exhibit multiple fringes (see Fig. 3.27(b)) possibly due to the occurrence of crystal defects such as twins. Thus although the indication derived by the aspect ratio distribution about the coherence of the islands is confirmed by TEM even in the case of annealing at 600 °C, the presence of those defects do not allow one to exclude that the islands with the largest base width would be already plastically relaxed or close to the critical value for the insertion of a dislocation.

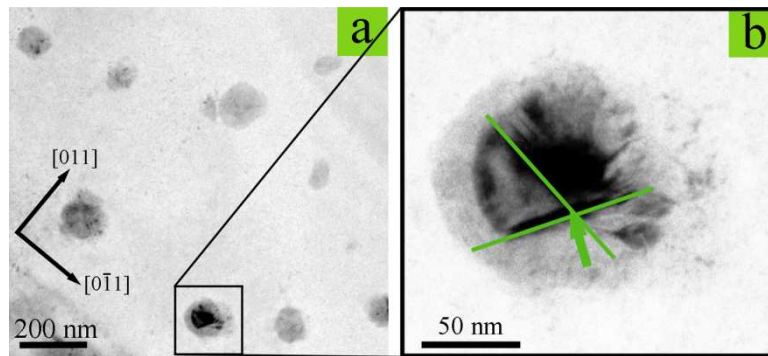


FIG. 3.27. PV bright field TEM images under $[02\bar{2}]$ axis beam condition of SiGe islands grown at 600 °C. The most of islands appears to be dislocation-free since a uniform contrast inside them is seen in the images, although some larger islands exhibit dislocations possibly due to the presence of twins, as in the square particular magnified in (b).

The results obtained from the TEM investigation (Figs. 3.26 and 3.27) and the statistical distributions of island aspect ratio derived by the AFM data (Fig. 3.25) give experimental evidence that islands grown by surface thermal diffusion do not show plastic relaxation for base width below 180 - 200 nm at 600 °C, and below 300-350 nm at 700 °C.

We focus now on the discussion of the origin of this quenching of the plastic relaxation. Since both Si intermixing and dislocation injection lead to an effective lowering of the elastic energy, the coherence and the strain state of the nucleated islands is thus a result of the interaction between these phenomena which strongly depends on the dynamics governing the growth process. By looking at typical MBE and CVD data one finds that intermixing prevents plastic relaxation only up to certain limiting values. In MBE the critical base width, BW_{crit} , has been found to evolve from 58 nm at 620 °C to 80 nm at 700 °C⁴⁵. The same trend has been seen in the case of CVD, where BW_{crit} goes from 100 nm at 600 °C to 200 nm at 700 °C⁴¹. If we compare the critical values in MBE and CVD growth with our results, we derive that the growth by surface thermal diffusion allows one to

obtain dislocation-free coherent islands whose base width is greater by a factor ~ 3 - 3.5 and ~ 1.5 - 1.8 than those obtained by MBE and CVD, respectively. In Section 3.3.6 of this Chapter we have directly measured the Ge composition of single islands grown at $700\text{ }^\circ\text{C}$ as a function of the distance from the stripe by means of micro-Raman spectroscopy. We found that the largest islands ($BW \sim 350\text{nm}$) grown at $700\text{ }^\circ\text{C}$ have an average Ge concentration, c_{Ge} , of about 25 %. This value, even within its experimental and model-related uncertainties, is smaller than the average Ge content found at the plastic relaxation onset for islands grown at $700\text{ }^\circ\text{C}$ by MBE ($c_{Ge} \sim 40\%$)⁴⁵ and CVD ($c_{Ge} \sim 50\%$)⁴¹. This enhanced intermixing in our case could be thus responsible for a further elastic strain relief able to quench the plastic relaxation channel. In fact, the growth method by surface thermal diffusion intrinsically favors a greater SiGe intermixing since the Ge supply occurs on a time scale longer with respect to the Si incorporation from the substrate. In this scenario the intermixing becomes thus the dominant process for the strain relaxation leading to the quenching of the plastic channel.

For the case of lower diffusion temperature, $600\text{ }^\circ\text{C}$, the micro-Raman measurements are very critical due to the lower island size and their higher density because of the diffraction limited spatial resolution. However, based on the above argument, we propose a tentative explanation for the lower critical base width seen at $600\text{ }^\circ\text{C}$. It is commonly agreed that the average Ge concentration contained inside the islands increases by decreasing the growth temperature^{24,103}. This leads to a reduced strain relief driven by the intermixing, which consequently lowers the critical dimension for the insertion of dislocations. This is consistent with the appearance at $600\text{ }^\circ\text{C}$ of dislocated islands for lower base width with respect to the case at $700\text{ }^\circ\text{C}$.

3.3.9 Ordered growth on a pit-patterned Si surface

In order to explore device engineering for electronics and opto-electronics applications based on self-assembled SiGe nano-structures, some crucial parameters must be controlled. From a mesoscopic point of view, island positioning and size distribution are the most important factors that need to be managed. Hence, it is imperative to understand and control the growth conditions for a rational nanostructures design.

Here, we have experimentally investigated the ordered growth of self-assembled SiGe islands obtained by means of surface thermal diffusion from a Ge stripe on a pit-patterned Si(100). The sample surface close to the stripe region has been patterned with a squared two-dimensional array of circular pits (diameter = 150 nm, depth = 25 nm, period = 1 μm) with an overall width of about 10 μm from the stripe edge, obtained by means of Electron Beam Lithography (EBL) and reactive

Ion Etching (RIE). A gradient into the Ge coverage has been induced by the diffusion process after annealing at 625 °C, strongly modulating the local density of Ge atoms upon the distance from the source stripe. In this case, we found an average Ge relative concentration of about 0.73 ± 0.03 , in good agreement with the values found in literature for the case of MBE deposition¹⁰⁴. Spontaneous nucleation of self-assembled SiGe islands coexists with the continuous surface diffusion of Ge. Figure 3.28(a)–(b) and 3.28(c)–(d) show representative SEM and AFM images, respectively, of the sample surface in the pit-patterned region after annealing at 625 °C for 7.5 min. Islands are essentially dome shaped and preferentially develop at the pit positions creating an ordered squared 2D array following the pit pattern: only about 10% of islands nucleated within the textured region are outside of the pit positions, and only around 7% of pits are empty or partially filled. The ordered island growth has been obtained by controlling the local atomic mobility by purposely choosing the growth parameters (annealing time and temperature). This allowed to make the distance over which each atom diffuses before the formation of a critical nucleus longer than the periodicity of the pit pattern. This condition favored the islands formation at pit positions, which represent preferential nucleation sites since a total elastic energy minimum is reached at the pit bottom⁵⁷.

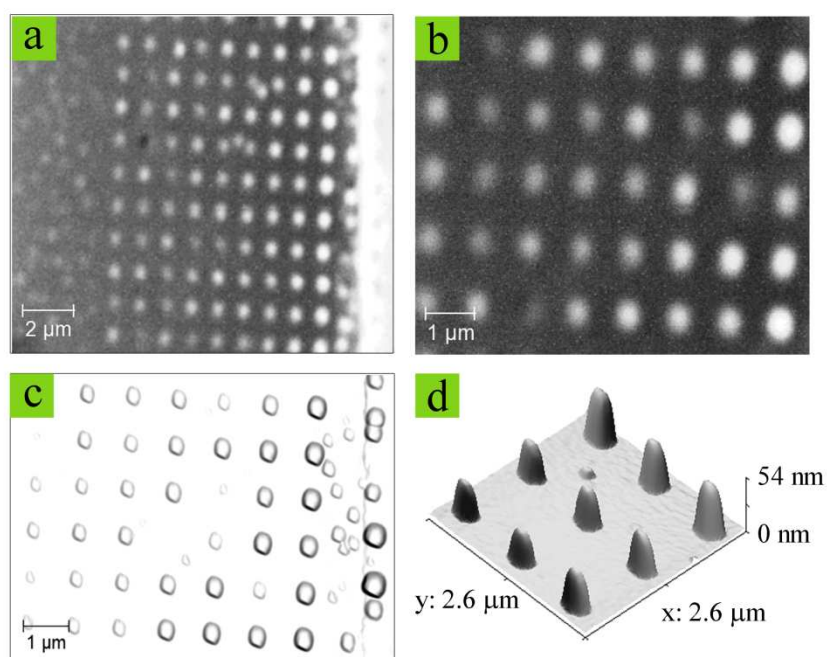


FIG. 3.28. SEM (a)–(b) and AFM (c)–(d) images of the sample surface in the pit-patterned region after annealing at 625 °C for 7.5 min. The AFM image in (c) is shown in gradient mode

Figure 3.29(a) shows the volume of individual ordered grown islands nucleated in the pit-patterning region, derived by AFM data, as a function of the distance, x , from the stripe. For the estimation of the island volume, we considered only the portion of the dome above the surrounding

2D flat surface; the contribution of Ge volume inside the pit underneath the island is negligible and has not been taken into account. Indeed, our conclusions about the factors governing the growth process will be not affected by this evaluation. Larger islands preferentially nucleate close to the stripe, while small islands grow farther away from it (see Fig. 3.29(a)), showing a continuous variation greater than one order of magnitude in their volume. In this case of ordered growth, the areal density of the nucleated islands and their positioning are essentially driven by the elastic energy minimization on a textured surface, which predominate with respect to the local kinetics of diffusion of Si and Ge atoms. We propose that this size evolution is mainly due to the gradient into the Ge coverage induced by the long-scale diffusing motion of Ge atoms from the stripe. In fact, regions farther away from the stripe exhibit a lower local density of Ge atoms and thus a smaller amount of Ge available for a growing island. A lower average Ge content could be thus responsible for a smaller island size, as experimentally demonstrated by Rastelli *et al.*³⁶ in case of randomly nucleated islands grown by Molecular Beam Epitaxy (MBE). However, as discussed in Section 3.3.6 of this Chapter, in case of island growth by Ge surface diffusion over a flat Si(001) surface without any pit patterning, we observed that the region with highest Ge coverage (close to the stripe) presents the lowest average island sizes, while where the coverage decreases to about 4 ML (farther away from the stripe), the biggest average dimensions of the islands are attained (see Fig. 3.17).

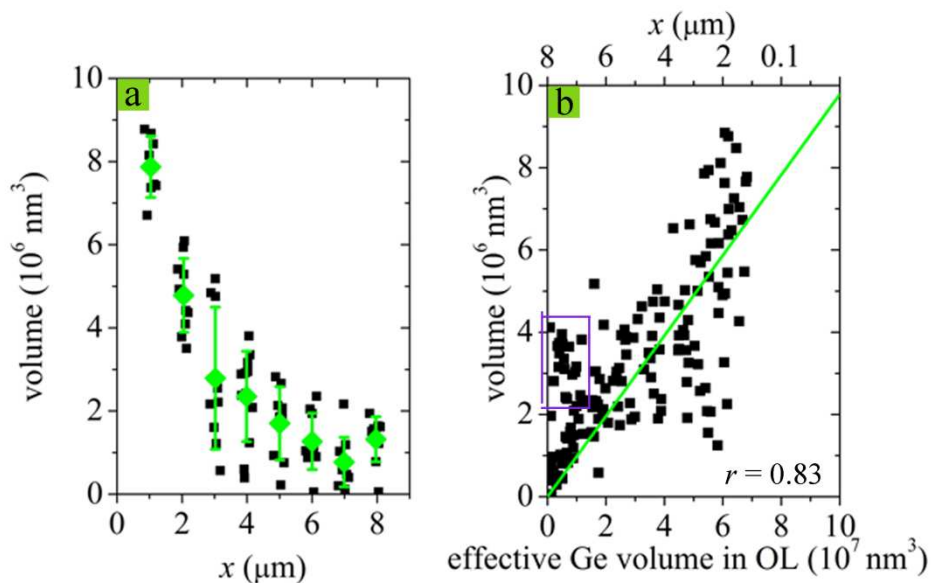


FIG. 3.29. Panel (a): volume distribution of individual ordered grown islands on a pit-patterned Si(100) surface, derived by AFM scans, as a function of the distance, x , from the stripe. Green diamonds represent average values. Panel (b) Scatter plot of the volume of ordered grown islands as a function of the effective Ge volume within the OL per island, as obtained by integrating the Ge coverage within the capture zone of each island. The green curve is the best linear fitting of the data, and r is the Pearson's coefficient. The blue square indicates a set of islands at low Ge coverage, far away from the stripe (see scale on top for a coarse indication of the distance), that deviate from the capture zone model, presenting higher volumes with respect to the linear scaling fitting (see text).

This different behavior could be explained by the following argument. The artificial pit patterning used in combination with the self-assembled growth by surface thermal diffusion allows to modulate the Ge coverage keeping at the same time fixed the island density and the capture zone area, from where islands gather mass to grow. This effectively separates the factors governing the formation of the critical nuclei from the following growth process of the islands determining their final size. In the case of random nucleation, kinetic factors influence both the nucleation mechanism and the growth process, strongly modulating the island density and the capture zone area. Actually, on a flat Si surface the island density decreases going far away from the stripe, and thus, the capture zone area increases correspondingly, inducing a progressive increase in the island volume as determined by the interplay among the local density of Ge atoms, the capture area and the Si incorporation (see discussion in Section 3.3.6 of this Chapter).

A quantitative validation of our educated guess about the factors governing the ordered growth process in presence of pit patterning can be obtained by correlating the volume of ordered grown islands with the effective Ge volume within the OL per island (see Fig. 3.29(b)). The latter is obtained by integrating the Ge coverage within the capture zone of each island. In principle, in case of a perfectly ordered 2D squared array of islands, the capture zone has the same area for all islands with a squared shape (the side is equal to the step size of the pit pattern). However, during data analysis, in order to correctly take into account the cases of not perfectly ordered growth, the capture zone for each island has been obtained by the Voronoi tessellation of the island network. A good linear correlation has been found between the volume of ordered grown islands and the effective Ge volume within the OL as given by a Pearson's coefficient, r , of about 0.83, confirming that their size evolution as a function of x is mainly driven by the gradient into the Ge coverage. Thus, as a first approximation, the growth process could be described within the capture zone model^{92,93}, extended to the case of variable Ge coverage. According to this *modified* model, the island volume scales linearly with the integral of the Ge coverage over the capture zone area (instead of the straight capture zone area as in case of homogeneous coverage).

We stress that this model does not exclude SiGe intermixing phenomena during the annealing process. Indeed, the growth process can be still well described by this scaling behavior considering that islands are in a chemical equilibrium with the wetting layer. Moreover, a detailed observation of Fig. 3.29(b) reveals a non-negligible set of islands at low Ge coverage (far away from the stripe) that deviate from the above-mentioned model, presenting higher volumes with respect to the linear scaling fitting. We think that the deviation from this linear scaling behavior could be due to an enhanced SiGe intermixing, which become significant in low Ge coverage regions far away from

the stripe, as experimentally proved in case of annealing at 700 °C. In fact, there the timescale of the growth process is slower with respect to the high coverage region close to the stripe, leaving enough time to islands to gather Si from their surroundings.

3.4 Conclusions

In this chapter we studied the spontaneous nucleation of SiGe islands coexisting with the continuous surface diffusion of Ge from the source stripe.

Joining SAM and AFM analysis the critical overlayer thickness for nucleation has been measured, showing that island growth mode gradually evolves from Stranski-Krastanow (SK) in case of absence of surfactant to Volmer-Weber (VW) for high surfactant coverage. A semi-quantitative estimation of the C incorporation inside the Si substrate is then deduced from the critical thickness. The carbon concentration inside the topmost Si substrate layer is found to increase linearly as a function of the carbon coverage, starting from a critical threshold $\theta_0 = 0.16 \pm 0.06$ ML. Below this critical coverage no sizable effect on the diffusion of Ge or on the nucleation of SiGe islands has been found.

Then, the growth process of SiGe islands obtained by the surface thermal diffusion of Ge from a source stripe on a *C-free* Si(001) surface has been experimentally investigated and discussed in details, with a particular emphasis to key aspects as the formation kinetics, the SiGe intermixing phenomena, the strain relaxation mechanisms and the islands ordering.

Using extensive AFM statistical analysis we have determined the size and density behavior exhibited by islands grown at different temperatures in the range 600 ÷ 700 °C as a function of the distance from the source stripe. Our results give experimental evidence that the growth process essentially evolves within a diffusion limited regime where the island density follows a universal scaling distribution depending only by the Ge coverage. Moreover, we showed that the density behaviour has been successfully reproduced using a 1D model of nucleation which considers the probability of formation of a critical nucleus depending only by the local differences in the chemical potential of the wetting layer. In this scenario the island growth is determined by kinetic factors only, and thus the essence of the phenomenon would be described by the Mulheran capture zone model. The model's validity has been verified by evaluating the correlation between the island volumes and the capture zone area, mathematically defined as the area of the Voronoi cell within the Voronoi tessellation of the island network. This findings suggest that kinetic factors rather than energetic ones crucially affect the competition between the islands to gather the available mass,

represented by both Ge atoms diffusing on the surface and Si atoms coming from the substrate which penetrate into the islands leading to the formation of alloyed nanocrystals (SiGe intermixing).

To measure the composition of single islands we performed a STEM-EELS experiment giving both the vertical and the horizontal concentration profiles. We found a vertical compositional gradient from a Si-rich bottom to a Ge-rich topmost region and highly Si-intermixed boundaries. To explore the interplay between intermixing and size evolution, we measured the composition of single islands as a function of the distance from the stripe by means of micro-Raman spectroscopy and Scanning Auger Microscopy. Looking at the average island concentration, a greater Si incorporation has been found for islands nucleated farther away from the stripe at lower Ge coverage regions. This modulation of Ge composition is believed to be the origin of the experimentally observed increase of the island volume as a function of the distance from the stripe.

Moreover, we have experimentally studied the plastic strain relaxation of nucleated self-assembled SiGe islands. The aspect ratio distributions as a function of the base width gave a statistical indication of the coherent nature of the nucleated islands. This has been confirmed by the structural analysis performed with TEM and LAADF-STEM on single islands. We have shown that islands grown by surface thermal diffusion remain dislocation-free for base width values greater by a factor ~ 3 - 3.5 and ~ 1.5 - 1.8 with respect to MBE and CVD, respectively. An enhanced SiGe intermixing is believed to be the origin of this suppression of the plastic relaxation. In fact the used growth method intrinsically promotes a greater intermixing since the Ge supply occurs on a time scale longer with respect to the Si incorporation from the substrate, and thus intermixing becomes the dominant process for the strain relaxation leading to the quenching of the plastic channel.

In order to explore device engineering for nanoelectronics applications based on self-assembled SiGe islands, some crucial parameters must be controlled. From a mesoscopic point of view, island positioning and size distribution are the most important factors that can be managed. Hence, we have investigated the growth of SiGe islands on a Si(001) surface patterned with a 2D squared array of circular pits. The ordered island growth has been obtained by controlling the local atomic mobility and the length of the diffusion pathway of Ge atoms by means of a correct choice of the growth parameters (annealing time and temperature). Moreover, controlling the diffusion dynamics of Ge from the source stripe, we were able to obtain a controlled size evolution of the orderly nucleated islands as a function of the Ge coverage. Our observations are consistent with a physical scenario where island positioning is essentially driven by energetic factors, which predominate with respect to the local kinetics of diffusion, and the size evolution mainly depends on the local density of Ge atoms.

Bibliography

- ¹ Y.W. Mo, D.E. Savage, B.S. Swartzentruber, and M.G. Lagally, Phys. Rev. Lett. **65**, 1020 (1990).
- ² M. Brehm, F. Montalenti, M. Grydlik, G. Vastola, H. Lichtenberger, N. Hrauda, M. J. Beck, T. Fromherz, F. Schaffler, L. Miglio, and G. Bauer, Phys. Rev. B **80**, 205321 (2009).
- ³ H. Hammar, F. LeGoues, J. Tersoff, M. Reuter, and R. Tromp, Surf. Sci. **349**, 129 (1996).
- ⁴ F. Wu, X. Chen, Z. Zhang, and M. G. Lagally, Phys. Rev. Lett. **74**, 574 (1995).
- ⁵ J. Tersoff and R. M. Tromp, Phys. Rev. Lett. **70**, 2782 (1993).
- ⁶ M. Tomitori, K. Wanatabe, M. Kobayashi, and O. Nishikawa, Appl. Surf. Sci. **76**, 322 (1994).
- ⁷ I. Goldfarb *et al.*, J. Vac. Sci. Technol. A **16**, 1938 (1998).
- ⁸ A. Vailionis *et al.*, Phys. Rev. Lett. **85**, 3672 (2000).
- ⁹ J. Tersoff, B. Spencer, A. Rastelli, and H. von Kanel, Phys. Rev. Lett. **89**, 196104 (2002).
- ¹⁰ R. J. Asaro and W. A. Tiller, Metall. Trans. **3**, 1789 (1972); M. A. Grinfeld, Dokl. Akad. Nauk SSSR **290**, 1358 (1986) [Sov. Phys. Dokl. **31**, 831 (1986)]; D. J. Srolovitz, Acta Metall. **37**, 621 (1989); B. J. Spencer, P.W. Voorhees, and S. H. Davis, Phys. Rev. Lett. **67**, 3696 (1991).
- ¹¹ I. Berbezier, A. Ronda, Surf. Sci. Rep. **64** (2009) 47-98
- ¹² A. Rastelli, PhD thesis, University of Pavia (2002)
- ¹³ P. Raiteri, D. Migas, L. Miglio, A. Rastelli, and H. von Kanel, Phys. Rev. Lett. **88**, 256103 (2002).
- ¹⁴ Y. Fujikawa *et al.*, Phys. Rev. Lett. **88**, 176101 (2002).
- ¹⁵ G. Medeiros-Ribeiro, A. M. Bratkovski, T. I. Kamins, D. A. A. Ohlberg, and R. S. Williams, Science **279**, 353 (1998).
- ¹⁶ F.M. Ross *et al.*, Science **286** (1999)
- ¹⁷ F. Montalenti *et al.*, Phys. Rev. Lett. **93** 216102 (2004)
- ¹⁸ F.M. Ross *et al.*, Phys. Rev. Lett. **80**, 984 (1998)
- ¹⁹ I. Daruka and J. Tersoff, Phys. Rev. B **66**, 132104 (2002)
- ²⁰ S. Krishna *et al.*, J. Appl. Phys. **86**, 6135 (1999).
- ²¹ P. B. Joyce *et al.*, Phys. Rev. B **62**, 10891 (2000).
- ²² B. K. Chakraverty, J. Phys. Chem. Solids **28**, 2401 - 2413 (1967).
- ²³ G. Medeiros-Ribeiro *et al.*, Nano Lett. **7**, 223 (2007)
- ²⁴ G. Capellini *et al.*, Appl. Phys. Lett. **78**, 303 (2001)
- ²⁵ J. Tersoff, Phys. Rev. Lett. **81**, 3183 (1998)
- ²⁶ U. Denker *et al.*, Phys. Rev. Lett. **94**, 216103 (2005)

-
- ²⁷ Y. Tu and J. Tersoff, Phys. Rev. Lett. **98**, 096103 (2007)
- ²⁸ R. Magalhaes-Paniago *et al.*, Phys. Rev. B **66**, 245312 (2002)
- ²⁹ T. U. Schulli *et al.*, Phys. Rev. Lett. **90**, 066105 (2003)
- ³⁰ A. Malachias *et al.*, Phys. Rev. Lett. **91**, 176101 (2003)
- ³¹ T. U. Schulli *et al.*, Phys. Rev. B **71**, 035326 (2005)
- ³² A. V. Baranov *et al.*, Phys. Rev. B **73**, 075322 (2006)
- ³³ O. G. Schmidt *et al.*, Appl. Phys. Lett. **81**, 2614 (2002)
- ³⁴ U. Denker *et al.*, Phys. Rev Lett. **90**, 196102 (2003)
- ³⁵ G. Katsaros *et al.*, Phys. Rev. B **72**, 195320 (2005)
- ³⁶ A. Rastelli *et al.*, Nano Lett. **8**, 1404 (2008)
- ³⁷ T. U. Schulli *et al.*, Phys. Rev Lett. **102**, 025502 (2009)
- ³⁸ U. Denker *et al.*, Appl. Phys. Lett. **78**, 3723 (2001)
- ³⁹ D. T. Tambe and V. B. Shenoy, Appl. Phys. Lett **85**, 1586 (2004)
- ⁴⁰ Ph. Sonnet and P.C. Kelires, Appl. Phys. Lett **85**, 203 (2004)
- ⁴¹ M. De Seta, G. Capellini, F. Evangelisti, C. Spinella, J. Appl. Phys. **92**, 614 (2002)
- ⁴² F. K. LeGoues, M. C. Reuter, J. Tersoff, M. Hammar, and R. M. Tromp, Phys. Rev. Lett. **73**, 300 (1994)
- ⁴³ T. Merdzhanova, S. Kiravittaya, A. Rastelli, M. Stoffel, U. Denker, and O.G. Schmidt, Phys. Rev. Lett. **96**, 226103 (2006)
- ⁴⁴ S.A. Chaparro, J. Drucker, Y. Zhang, D. Chandrasekhar, M. McCartney, D. Smith, Phys. Rev. Lett. **83**, 1199 (1999)
- ⁴⁵ A. Marzegalli, V. A. Zinovyev, F. Montalenti, A. Rastelli, M. Stoffel, T. Merdzhanova, O. G. Schmidt, and Leo Miglio, Phys. Rev. Lett. **99**, 235505 (2007)
- ⁴⁶ O.G. Schmidt, K. Eberl, IEEE Trans. Electron Devices **48**, 1175 287 (2001)
- ⁴⁷ H. M. Koduvely and A. Zangwill, Phys. Rev. B **60**, R2204 (1999)
- ⁴⁸ F. Liu *et al.*, Phys. Rev. Lett. **87**, 126103 (2001)
- ⁴⁹ V. A. Shchukin *et al.*, Phys. Rev. Lett. **90**, 076102 (2003)
- ⁵⁰ G. Capellini *et al.*, Phys. Rev. Lett. **96**, 106102 (2006)
- ⁵¹ I. Berbezier and A. Ronda, Phys. Rev. B **75**, 195407 (2007)
- ⁵² A. Pascale *et al.*, Phys. Rev. B **77**, 075311 (2008)
- ⁵³ J. Tersoff, C. Teichert, and M. G. Lagally, Phys. Rev. Lett. **76**, 1675 (1996).
- ⁵⁴ V. A. Shchukin and D. Bimberg, Rev. Mod. Phys. **71**, 1125 (1999).
- ⁵⁵ J. Stangl, V. Holý, and G. Bauer, Rev. Mod. Phys. **76**, 725 (2004)

- ⁵⁶ R. Marchetti *et al.*, *App. Phys. Lett.* **87** 261919 (2005)
- ⁵⁷ Z. Zhong, W. Schwinger, F. Schaffler, G. Bauer, G. Vastola, F. 291 Montalenti, L. Miglio, *Phys. Rev. Lett.* **98**, 176102 (2007)
- ⁵⁸ Z. Zhong, O.G. Schmidt, G. Bauer, *Appl. Phys. Lett.* **87**, 133111 289 (2005)
- ⁵⁹ D.J. Eaglesham, F.C. Unterwald, and D.C. Jacobson, *Phys. Rev. Lett.* **70**, 966 (1993)
- ⁶⁰ A. Portavoce, I. Berbezier, and A. Ronda, *Phys. Rev. B* **69** 155416 (2004)
- ⁶¹ O. Schmidt, C. Lange, K. Eberl, O. Kienzle, and F. Ernst, *Appl. Phys. Lett.* **71**, 2340 (1997).
- ⁶² O. Schmidt, S. Schieker, K. Eberl, O. Kienzle, F. Ernst, *App. Phys. Lett.* **73** 659 (1998);
- ⁶³ O. Leifeld, E. Muller, D. Grutzmacher, B. Muller and K. Kern, *App. Phys. Lett.* **74** 994 (1999);
- ⁶⁴ O. Leifeld, R. Hartmann, E. Muller, E Kaxiras, K. Kern and D. Grutzmacher, *Nanotechnology* **10** 122 (1999);
- ⁶⁵ A. Beyer, E. Muller, H. Sigg, S. Stutz, and D. Grutzmacher, O. Leifeld, K. Ensslin, *App. Phys. Lett.* **77** 3218 (2000)
- ⁶⁶ D. Dentel, J. L. Bischoff, and L. Kubler, M. Stoffel, G. Costelein, *J. Appl. Phys.* **93** 5069 (2003)
- ⁶⁷ J. Stangl, V. Holy, G. Bauer, *Rev. Mod. Phys.* **76**, 725 (2004)
- ⁶⁸ M. Stoffel, L. Simon, J.L. Bischoff, D. Aubel, L. Kubler, G. Costelein, *Thin Solid Films* **380**, 32 (2000)
- ⁶⁹ O. Leifeld, A. Beyer, D. Grutzmacher, and K. Kern, *Phys. Rev. B* **66**, 125312 (2002)
- ⁷⁰ A. Bernardi, M.I. Alonso, A.R. Goñi, J.O. Ossó, M. Garriga, *Surf. Sci.* **601**, 2783 (2007)
- ⁷¹ A. Bernardi, M. I. Alonso, A. R. Goñi, J. O. Ossó, and M. Garriga, *Appl. Phys. Lett.* **89** (2006) 101921
- ⁷² J.Y. Kim, S.H. Ihm, J.H. Seok, C.H. Lee, Y.H. Lee, E.-K. Suh, H.J. Lee, *Thin Solid Films* **369**, 96 (2000)
- ⁷³ Y. Wakayama, L. V. Sokolov, N. Zakharov, P. Werner, and U. Gosele, *J. Appl. Phys.* **93** 765 (2003)
- ⁷⁴ Y. Wakayama, G. Gerth, Peter Werner, U. Gosele, L. V. Sokolov *App. Phys. Lett.* **77** 2328 (2000)
- ⁷⁵ G. Isella, D. Chrastina, B. Rössner, T. Hackbarth, H-J. Herzog, U. König, H. von Känel, *Solid-State Electronic* **48**,1317-1323 (2004)
- ⁷⁶ WSXM (I. Horcas *et al.*, *Rev. Sci. Instrum.* **78** 013705 (2007)); Gwyddion (<http://gwyddion.net/>).
- ⁷⁷ Y.-W. Mo, D.E. Savage, B.S. Swartzentruber, and M. Lagally, *Phys. Rev. Lett.* **65** 1020 (1990)
- ⁷⁸ G.M. Vanacore, A. Tagliaferri, M. Zani, G. Isella (unpublished)
- ⁷⁹ P. C. Kelires, *Phys. Rev. B* **55** 8784 (1997)

- ⁸⁰ M. Berti, D. De Salvador, A. V. Drigo, F. Romanato, J. Stangl, S. Zerlauth, F. Schaffler, and G. Bauer, *App. Phys. Lett.* **72** 1602 (1998)
- ⁸¹ D. De Salvador, M. Petrovich, M. Berti, F. Romanato, E. Napolitani, and A. Drigo, J. Stangl, S. Zerlauth, M. Muhlberger, F. Schaffler, G. Bauer, P.C. Kelires, , *Phys. Rev. B* **61** 13005 (2000)
- ⁸² I. N. Remediakis, E. Kaxiras, and P. C. Kelires, *Phys. Rev. Lett.* **86**, 4556 (2001).
- ⁸³ L. Huang, F. Liu, and X. G. Gong, *Phys. Rev. B* **70**, 155320 (2004).
- ⁸⁴ H. J. Kim, Z. M. Zhao, J. Liu, V. Ozolins, J. Y. Chang, and Y. H. Xie, *J. Appl. Phys.* **95**, 6065 (2004).
- ⁸⁵ T. Schwarz-Selinger, Y. L. Foo, D. G. Cahill, and J. E. Greene, *Phys. Rev. B* **65**, 125317 (2002).
- ⁸⁶ J. Tersoff, *Phys. Rev. B* **43**, 9377 1991
- ⁸⁷ I. Daruka and A.-L. Barabasi, *Appl. Phys. Lett.* **72**, 2102 1998
- ⁸⁸ F. Ratto, A. Locatelli, S. Fontana, S. Kharrazi, S. Ashtaputre, S. K. Kulkarni, S. Heun, and F. Roseil, *Phys. Rev. Lett.* **96** 096103 (2006)
- ⁸⁹ M. Fanfoni and M. Tomellini, *J. Phys. Condens. Matter* **17**, R571 (2005).
- ⁹⁰ M. Zinke-Allmang, *Thin Solid Films* **346**, 1 (1999).
- ⁹¹ M. Brinkmann, S. Graaf, and F. Biscarini, *Phys. Rev. B* **66**, 165430 (2002).
- ⁹² P. A. Mulheran and J. A. Blackman, *Phys. Rev. B* **53**, 10 261 (1996).
- ⁹³ S. Pratontep, M. Brinkmann, F. Nuesch, and L. Zuppiroli, *Phys. Rev. B* **69**, 165201 (2004).
- ⁹⁴ P. Raiteri and L. Miglio, *Phys. Rev. B* **66**, 235408 (2002).
- ⁹⁵ F. Pezzoli, E. Bonera, E. Grilli, M. Guzzi, S. Sanguinetti, D. Chrastina, G. Isella, H. von Knel, E. Wintersberger, J. Stangl, and G. Bauer, *J. Appl. Phys.* **103**, 093521 (2008)
- ⁹⁶ R. Gatti, A. Marzegalli, V. A. Zinovyev, F. Montalenti, and Leo Miglio, *Phys. Rev. B* **78**, 184104 (2008)
- ⁹⁷ V. G. Dubrovskii, G. E. Cirlin, Yu. G. Musikhin, Yu. B. Samsonenko, A. A. Tonkikh, N. K. Polyakov, V. A. Egorov, A. F. Tsatsul'nikov, N. A. Krizhanovskaya, V. M. Ustinov, and P. Werner, *J. Cryst. Growth* **267**, 47 (2004).
- ⁹⁸ G.E. Cirlin, V. G. Dubrovskii, A. A. Tonkikh, N. V. Sibirev, V. M. Ustinov, and P. Werner, *Semiconductors* **39**, 547 (2005).
- ⁹⁹ M. Li, M. C. Bartelt, and J. W. Evans, *Phys. Rev. B* **68**, 121401 (R) (2003).
- ¹⁰⁰ J. G. Amar, M. N. Popescu, and F. Family, *Surf. Sci.* **491**, 239 (2001)
- ¹⁰¹ G. Capellini, M. De Seta, Y. Busby, M. Pea, F. Evangelisti, G. Nicotra, C. Spinella, M. Nardone, and C. Ferrari, *J. Appl. Phys.* **107**, 063504 (2010)
- ¹⁰² Y. Zhiheng, D. A. Muller, and J. Silcox, *J. Appl. Phys.* **95**, 3362 (2004).

¹⁰³ M. Floyd, Y. Zhang, K. P. Driver, J. Drucker, P. A. Crozier, and D.J. Smith Appl. Phys. Lett. **82**, 1473 (2003)

¹⁰⁴ 14. M. Brehm, M. Grydlik, H. Lichtenberger, T. Fromherz, N. Hrauda, W. Jantsch, F. Schäffler, G. Bauer, App. Phys. Lett. **93**, 305 121901 (2008)

Chapter 4

Nanoscale mapping of composition, strain and valence band structure in SiGe nano-stripes

4.1 Introduction

New materials and device concepts are required to overcome the physical limitations of the bulk Si semiconductor. The introduction of SiGe heterostructures into main-stream Si technology is such an approach, which opens new degrees of freedom via band structure engineering. High carrier mobility can be obtained by controlling the strain of the MOSFET channel¹. Improvements in mobility have been demonstrated at room temperature² and further improvement has been observed at low temperature³. When the lateral size of the channel is large compared to its thickness, the strain is biaxial and can be fully controlled using $\text{Si}_{1-x}\text{Ge}_x$ virtual substrates of appropriate composition x . However, channels of 40 nm are already used in commercial devices, while small scale nano-fabrication techniques like e-beam lithography make possible a channel width as small as the lowest thickness limit for the carrier confinement (~5 nm). In this regime, the channel strain depends also on the lateral boundary conditions due to elastic and plastic relaxation, resulting in an uniaxial strain which can further enhance the carrier mobility due to the warping of the electronic band structure⁴. Shear stress is particularly effective in modifying the band dispersion parallel to the interface plane, leading to dramatic changes in the constant-energy surfaces in k -space, and the reduction of the effective mass in the transport direction⁵.

Within this scenario it would be of fundamental importance: (i) to know and control the strain in the channel down to the nanoscale, and (ii) to understand its effect on the electronic structure in order to allow an efficient design of high performance devices with maximum carrier mobility and device operation speed.

The strain information is usually obtained by optical micro-Raman with a spatial resolution limited to $\sim 1 \mu\text{m}$. Thus the strain and mobility optimization on channels narrower than $\sim 1 \mu\text{m}$ is actually achieved through averaging and model-based interpretations⁶. As a result, the investigation of details on a single channel becomes a difficult task. Tip Enhanced Raman Spectroscopy (TERS) provides an alternative way to go beyond this barrier by performing Raman spectroscopic imaging with high spatial resolution^{7,8,9,10,11}, thanks to the local amplification and to the spatial confinement of the incoming electromagnetic radiation at the apex of a sharp metallic tip. This technique promises an unprecedented detail in the spatial strain mapping of single nanostructures, with the considerable advantage of not requiring destructive procedures for sample preparation.

Electron and hole mobility are strongly dependent upon the valence band shifting, the electronic states splitting and the bandwidth modifications induced by the strain field inside the channel. Theoretical investigations⁵ predicted valence band shifts to vary in the range $0.2 \text{ eV} \div 1 \text{ eV}$, and variations of the valence band dispersion capable of increasing the hole effective mass by a factor four. Energy-filtered PhotoElectron Emission Microscopy (PEEM) can provide full spectroscopic information (core-levels, valence band, photoemission threshold) using soft X-ray excitation, with spatial resolution better than 100 nm and an energy band width of 50-100 meV, as recently demonstrated by Ratto *et al.*¹² for the study of the elemental composition of self-assembled Ge islands on Si(111), and by De La Pena *et al.*¹³ for the chemical imaging of buried sub-oxide of doped Si patterns.

In this chapter, we present the nanoscale mapping of strain, composition and valence band structure of lithographically defined SiGe nano-stripes on Si(001) substrates, in layouts very close to those used in prototype devices, by means of TERS and Energy-Filtered PEEM techniques. The main steps for data analysis are presented and the determination of the strain profile across a single nano-stripe is discussed and compared to the strain profile obtained from Finite Element Modeling (FEM) calculations. The measured local work function and valence band maps are presented allowing the determination of the electronic structure modifications with respect to the Ge bulk case induced by the strain field inside the nano-stripes.

4.2 Experiment and methods

4.2.1 Sample preparation

SiGe *embedded* nano-stripes have been created by coupling electron-beam lithography (EBL) and Low Energy Plasma Enhanced Chemical Vapour Deposition (LEPECVD). A n+(As)-doped Si(001) substrate has been patterned with a series of trenches (depth 110 nm, width 150 nm)

aligned along the $\langle 110 \rangle$ direction by means of EBL. PMMA photo-resist has been spin-coated on Si substrate at 4000 rpm (thickness $\sim 1.8 \mu\text{m}$), and then exposed to the electron beam of a Converted Scanning Electron Microscope (SEM) along the designed pattern. A post-exposure bake at 105°C is performed before the development of the PMMA removing the soluble exposed part of the resist. A reactive ion etching (RIE) has been then performed to define the array of trenches. Finally, the epitaxial deposition of pure Ge by LEPECVD, keeping the substrate at 650°C and using a deposition rate of 1.5 nm/s , allows the filling of the trenches, and then the formation of the embedded nano-stripes.

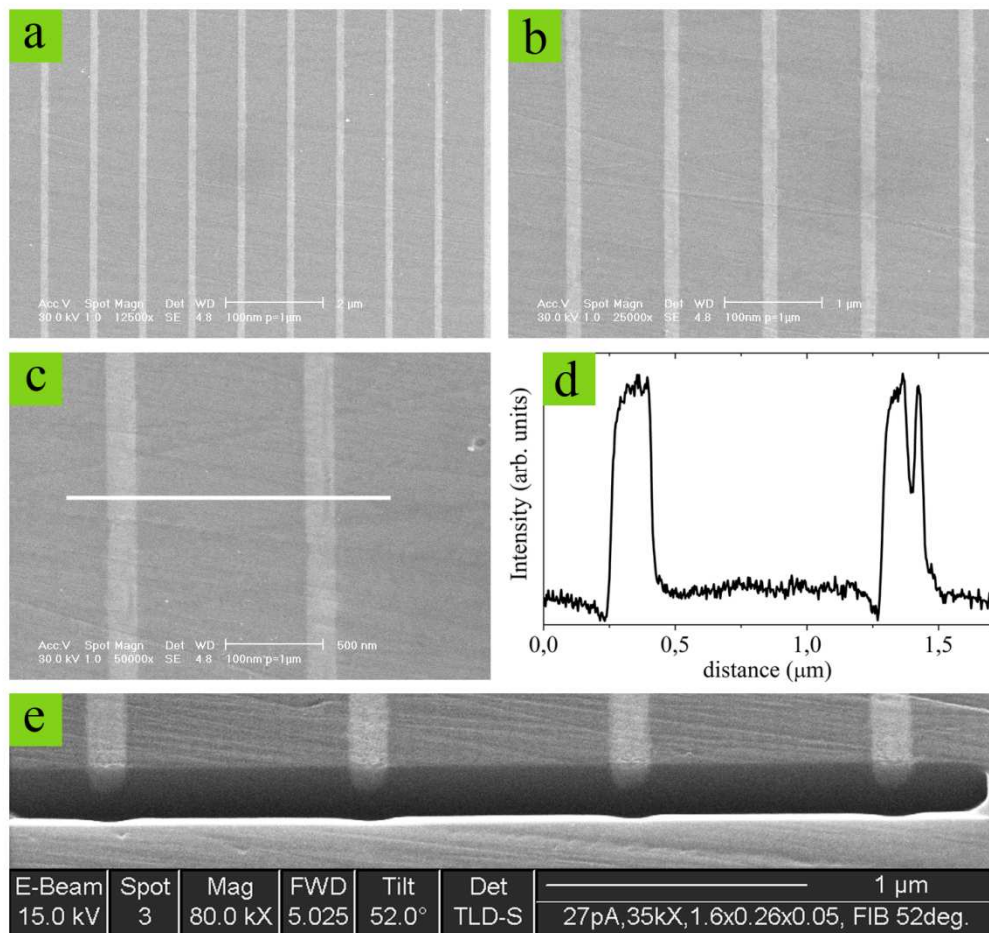


FIG. 4.1. Panel (a)-(c): plan view SEM images with different magnification of a periodic array of nano-stripes. Panel (d): intensity profile as determined along the white line in (c). The stripes exhibit a lateral width of about 150 nm , and are spaced by a periodic separation of about $1 \mu\text{m}$. Panel (e): cross-section SEM image of four nano-stripes after Focused Ion Beam (FIB) processing. During FIB processing the ion beam hit the sample surface off normal with an incidence angle of 52° . In this way the cross-section profile of the nano-stripe can be well distinguished by eventual ion-induced artifacts due to the amorphization of the cross-section surface (not present in panel (e)), since the artifacts should appear only along a 52° tilted direction with respect to the normal to the surface.

Under this growth conditions the Ge atom condensation from the vapor phase dominates with respect to the surface diffusion of both Si and Ge, thus strongly reducing Si incorporation from the substrate and leading to the formation of Ge-rich nano-stripes. In fact SiGe nanostructures with high

Ge concentration have potential applications in optoelectronics¹⁴ and thermoelectric¹⁵. The real composition of the nano-stripes has been then measured by means of Energy-Filtered PEEM (see Section 3 of this Chapter and Panel F for a more extensive discussion). The SiGe epilayer possibly formed in between the structures after the Ge growth was completely etched away by a mechanical polishing.

Fig. 4.1 shows a set of SEM images with different magnification of the periodic array of the nano-stripes. They exhibit a lateral width of about 150 nm, a thickness of 110 ± 5 nm (see Fig. 4.1(e) showing a cross-section SEM image of the nano-stripes after Focused Ion Beam (FIB) processing performed at the S3 Laboratory in Modena), and are spaced by a periodic separation of about 1 μm .

4.2.2 TERS experiment

TERS experiment has been performed at the Laboratoire de Physique des Interface et des Couches Minces (LPICM) at the Ecole Polytechnique. An extensive description of the technique is reported in the Panel E. The TERS setup is a combination of a Raman Spectrometer Horiba Jobin Yvon equipped with a 50X objective ($\text{NA} = 0.45$) optically coupled in oblique (70°) backscattering geometry to a Scanning Tunnelling Microscope (PSIA) (see Fig. 4.2(a)). The sample orientation with respect to the incident light is chosen in order to align the projection of the incident direction on the sample surface along the axis longitudinal to the stripes, corresponding to the $\langle 110 \rangle$ crystallographic direction (see Fig. 4.2(b)). A $\lambda/2$ -waveplate is inserted in the optical path of the excitation laser beam ($\lambda = 633$ nm) thus controlling the polarization of the incident radiation. In all measurements shown below, the electric field of the incoming electromagnetic radiation is set to be parallel to the incidence plane (p polarization). STM tips were prepared by electrochemically etching a 0.25 mm Au wire in a concentrated HCl/ethanol 1:1 mixture (see Section E.4.3 of the Panel E). Tips with final apex radius lower than 30 nm can be reproducibly fabricated using this technique. Tunneling experiments took place in air using a sample bias of -1 V and a current set-point of 0.1 nA. Before every measurement sequence, native silicon and germanium oxide on the sample surface have been removed by means of DHF (10 % for 30 s at RT).

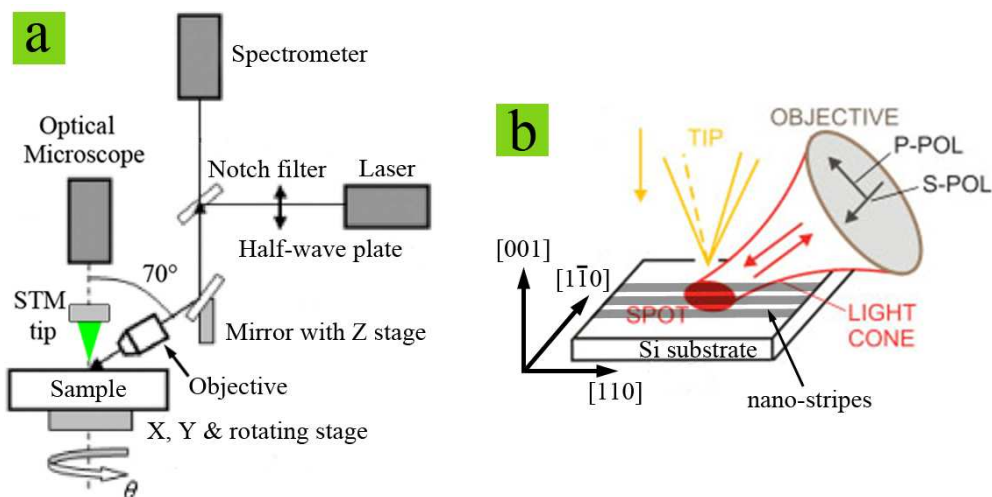


FIG. 4.2. Panel (a): schematic representation of the experimental setup for TERS experiment. The laser beam is focalized in oblique incidence on the sample surface within the region where the Au tip is in tunneling contact with the sample. An half-wave plate is used to define the polarization state of the incidence light. Panel (b): schematic diagram of the sample orientation with respect to the incidence direction and polarization of the incoming electromagnetic radiation.

4.2.3 Energy-Filtered PEEM experiment

The Energy-Filtered PEEM experiment took place at the TEMPO branch-line of SOLEIL Synchrotron using the NanoESCA photoemission microscope (Omicron Nanotechnology – see Fig. 4.3) of the CEA-LETI, whose installation has been assured by the CEA-IRAMIS and CEA-LETI institutes. The preparation protocol for the cleaning of the sample surface used during the experiment has been the following: (i) chemical etching of the native silicon and germanium oxide by DHF (10 % for 30 s at RT); (ii) UV-ozone treatment by irradiation with D₂ lamp for 15-20 min for carbon removal^{16,17}; (iii) removal of silicon oxide layer (covering the surface after UV treatment) by *in-situ* mild Ar⁺ sputtering (beam voltage ~ 500 V - 1000 V, beam current ~ 1 μA), and (iv) thermal relaxation by *in situ* annealing below the diffusion threshold temperature (~ 400 °C). Soft X-rays with photon energy ranging from 90 eV to 160 eV have been used for both band structure mapping and core-level measurements. The sample was mounted such that the normal to the (001) surface was in the horizontal plane containing the incoming wavevector. The light was hitting the surface at a grazing incidence angle of 23° respect to the (001) plane, and a horizontal linear polarization of the incident light was chosen, in order to have a preferential sensitivity along the out-of-plane direction ([001] direction). The NanoESCA spectro-microscope was operated with a contrast aperture of 70 μm, an extractor voltage of 15 kV, a pass energy of 100 eV, and an entrance analyzer aperture of 1 mm. See Panel F for an more detailed discussion of the PEEM technique and of the main characteristics of the NanoESCA microscope.

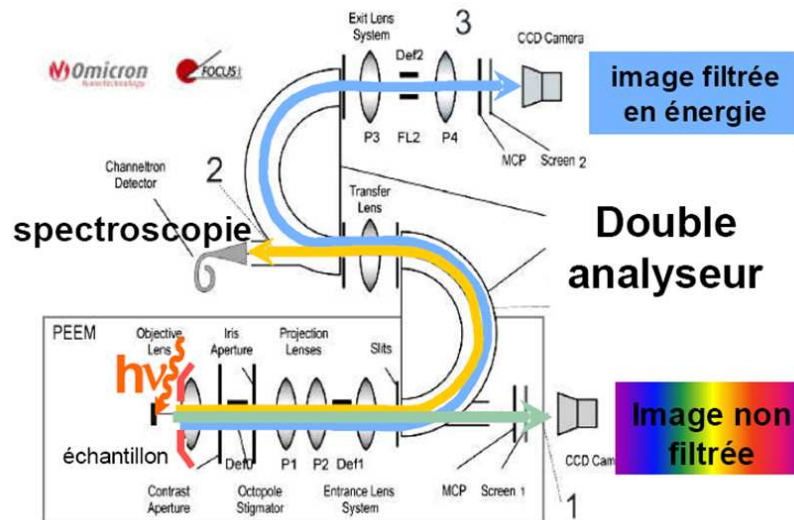


FIG. 4.3. Schematic representation of the NanoESCA spectro-microscope, composed of a fully electrostatic PEEM column together with an aberration corrected energy filter consisting of two hemispherical electron energy analyzers coupled by a transfer lens. The microscope works on three different modes: 1) non-filtered imaging mode; 2) spectroscopy mode on a small spot (around few μm); 3) energy-filtered imaging mode.

4.3 Nanoscale mapping of composition and strain

The baseline corrected Raman spectrum measured on the Si substrate with the tip retracted is shown in Fig. 4.4(a). The peak of the first order Si-Si optical mode at 520.7 cm^{-1} related to the Si substrate clearly appears in the spectrum, together with the second order overtones generating defined peaks at $\sim 300\text{ cm}^{-1}$ ($2TA$) and at $\sim 434\text{ cm}^{-1}$ ($2A_1$), a doublet structure in the range $600 \div 700\text{ cm}^{-1}$ ($TO + TA$), and a broad band between 930 and 990 cm^{-1} ($2TO$). The symmetry properties of these modes induce a defined polarization to the scattered radiation¹⁸. The use of a polarization analyzer before the spectrometer allows thus to select within the spectrum the several symmetry components of the excited II order modes and with respect to the I order peak. In the measurements presented here we did *not* use a polarization analyzer in order to avoid any possible suppression of the Raman signals related to the nano-stripes.

During the TERS experiment a region containing a single SiGe nano-stripe has been selected by STM imaging of the sample surface (see Fig. 4.5, where the contrast in the image is essentially due to the different surface roughness between the Si substrate and the SiGe nano-stripe). Fig. 4.4(b) shows the baseline corrected Raman spectrum measured on the Si substrate with the tip in tunneling position. The spectral features appearing in this spectrum are very similar to those ones present in the spectrum measured with the tip in retracted position (Fig. 4.4(a)). This can be understood by the following argument. In case of tip retracted, the Raman signal comes from the far field scattering from the total illuminated area by the laser light, roughly defined as the beam spot

size (around $1.5 \mu\text{m}$ due to the oblique geometry) multiplied with the penetration depth, l_p , of the laser light (l_p is about $1\div 2 \mu\text{m}$ in Si bulk at $\lambda = 633 \text{ nm}$ ¹⁹). Indeed, the TERS effect originates from the local amplification of the electromagnetic field at the apex of the tip due to the lightning rod effect and the resonant excitation of localized surface plasmons (LSP)²⁰ (see Section E.3 in the Panel E), converting the incoming far field radiation into an enhanced near field in a region with dimensions determined by the size of the tip apex²⁰. In case of absence of a polarization analyzer for the scattered radiation, for the Si bulk the near-field Raman signal coming from the nanoscale region below the tip is generally much weaker by orders of magnitude than the far field background of the larger spot-illuminated volume¹⁹. Thus the Raman spectrum measured on the Si substrate even with the tip in tunneling position is essentially determined by the far field contribution.

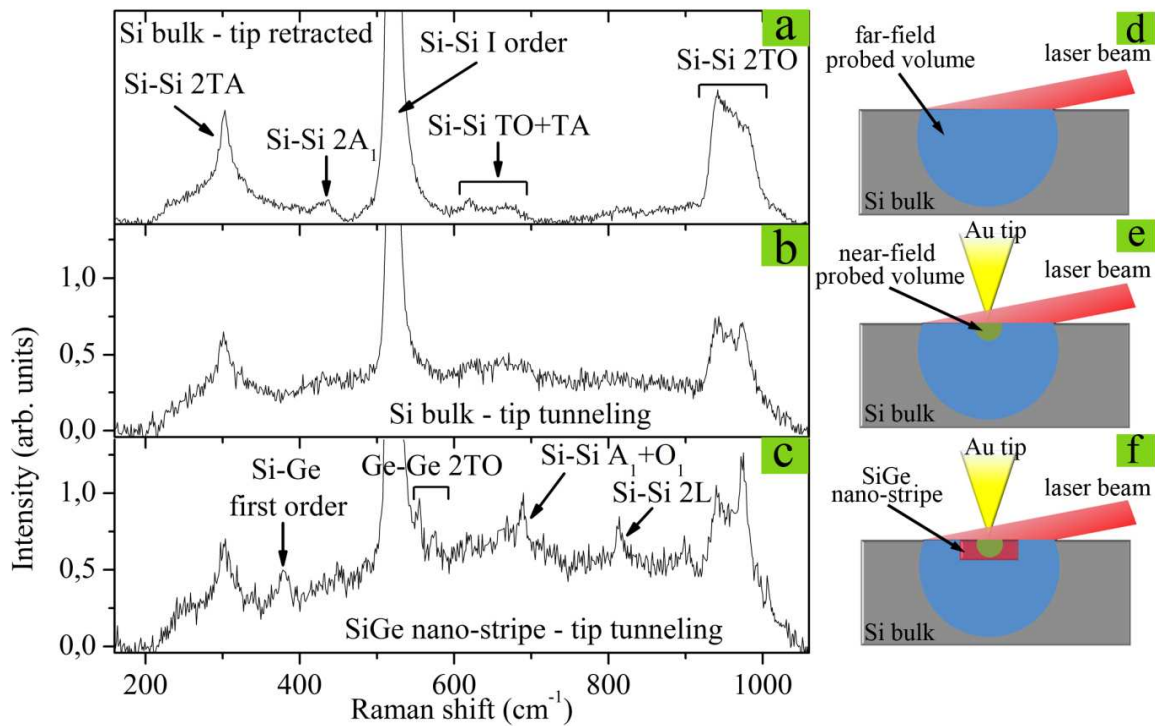


FIG. 4.4. Panels (a)-(c): baseline corrected Raman spectra measured on the Si substrate with the tip in retracted position (a), on the Si substrate with the tip in tunneling position (b), and on the SiGe nano-stripe with the tip in tunneling position (c). Panels (d)-(f): schematic sketches of the experimental geometry related to the spectra shown in (a)-(c), respectively.

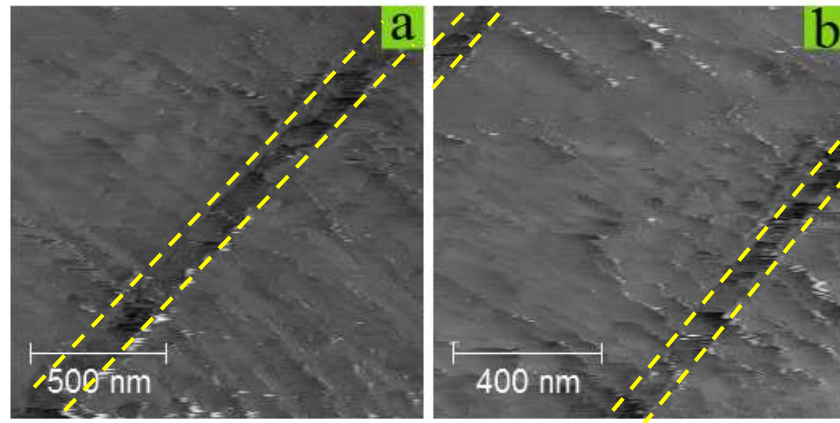


FIG. 4.5. STM images of the SiGe nano-stripes (sample bias = -1 V, current set-point = 0.1 nA). The dashed green lines define the boundaries of the SiGe nano-stripe.

Fig. 4.4(c) shows the baseline corrected Raman spectrum measured on the nano-stripe with the tip in tunneling. Here new structures appear and some weaker Si-Si overtones have enhanced intensity, while the most intense features related to the far field contribution from the Si bulk (the I order peak, the 2TA and 2TO overtones) are substantially unmodified. In this case, while the far field radiation still probes a larger scattering volume in the bulk Si, the locally enhanced near field Raman signal reasonably comes from the region below the tip occupied exclusively by the SiGe nano-stripe (see the schematic in Fig. 4.4(f)), significantly enhancing the scattering cross-section of Raman peaks related to the nano-stripe. The doublet structure appearing at 553 cm^{-1} and 575 cm^{-1} is attributed to the 2TO overtones of the Ge-Ge Raman mode²¹, while the peaks emerging at 690 cm^{-1} and 812 cm^{-1} represent the Si-Si overtones $A_1 + O_1$ and $2L$, respectively¹⁶. The enhancement of 2TO Ge-Ge mode is quite obviously due to the presence of Ge within the nano-stripe, while the enhancement of the Si-Si II order modes is not so clear. The origin of the latter effect is still under investigation and represents one intriguing aspect to be addressed in future. At the moment, we speculate that this modes, which are forbidden in the case of a flat surface, could become allowed due to the breaking of the translational symmetry because of the presence of the nano-stripe. The spatial mapping of their intensity should give thus information about the spread of the strain within the Si substrate. Concerning to the peak appearing around 380 cm^{-1} , we can exclude that it is related to the 2LA Ge-Ge overtone at 382 cm^{-1} , and we attribute this peak to the first order component of the Si-Ge Raman mode originating within the nano-stripe and enhanced by the near-field contribution. This identification is supported by the following argument. Both theoretical calculations of the Raman scattering intensities²² and experimental measurements of second order spectra²¹ report that the Ge 2TO peaks are more intense by a factor ~ 6 with respect to the Ge 2LA component. This is not the case in our spectra, where the intensity of the peak at 380 cm^{-1} is always

greater by one order of magnitude than the 2TO Ge-Ge overtones. Moreover, as reported in the experimental section (Section 4.2.1), we tuned the LEPECVD growth conditions in order to fabricate nano-stripes with high Ge concentration, whose real composition has been measured by Energy-Filtered PEEM (see the analysis below). For high Ge concentration the Si-Ge peak has been theoretically predicted and experimentally found²³ in the range of Raman shifts around 380 cm^{-1} .

Figs. 4.6(a)-(c) show the integral intensities after a linear background subtraction for the Ge-Ge 2TO (Fig. 4.6(a)), the Si-Si A_1+O_1 (Fig. 4.6(b)), and the first order Si-Ge (Fig. 4.6(c)) peaks as derived by TERS spectra monitored as a function of the position across the nano-stripe during a line scan of the tip. The intensity profiles exhibit a reproducible behavior, well above by the experimental uncertainty, and perfectly consistent with the typical stripe width of 150 nm (after considering the inclination of about 30° between the scanning direction and the axis perpendicular to the nano-stripe). Figs. 4.6(d)-(f) show the behavior of the Raman shifts as a function of the position across the nano-stripe for the monitored peaks, obtained by fitting the spectral region close to the peak maximum using a Voigt lineshape.

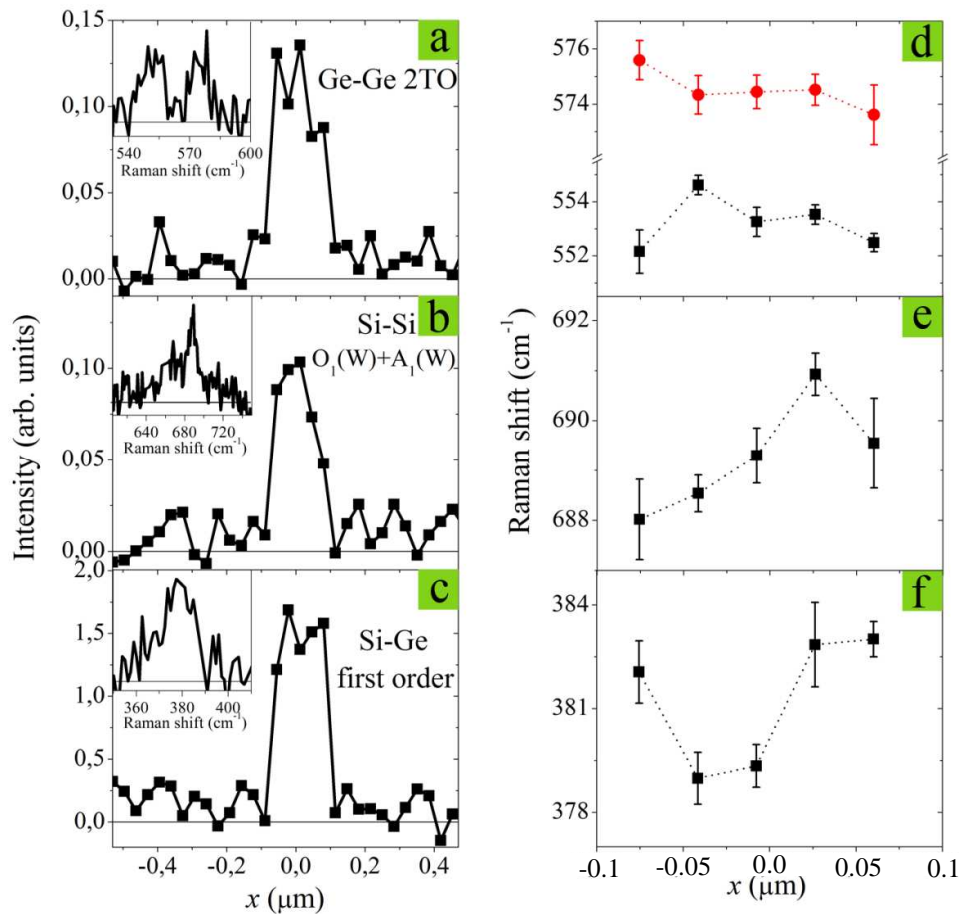


FIG. 4.6. Panels (a)-(c): integral intensities after a linear background subtraction for the Ge-Ge 2TO (a), the Si-Si A_1+O_1 (b), and the first order Si-Ge (c) peaks as derived by TERS spectra monitored as a function of the position across the nano-stripe during a line scan of the tip. Panels (d)-(f) behavior of the Raman shifts as a function of the position across the nano-stripe for the monitored peaks, obtained by fitting the spectral region close to the peak maximum using a Voigt lineshape.

In order to probe the reproducibility of the results obtained from the line scan shown in Fig. 4.6, we measured TERS spectra as a function of the position of the tip across a different nano-stripe. Fig. 4.7 shows the intensity profiles and the relative Raman shifts as a function of the position as obtained from this second line scan for the Ge-Ge 2TO, the Si-Si $2A_1$, and the first order Si-Ge peaks. The enhancement effects from the near-field contribution and the main trend of the profiles are essentially reproduced. Even in this case, the intensity profiles are well above the experimental uncertainty, and perfectly consistent with the typical dimensions of the nano-stripe. The decrease of the Si-Si $2A_1$ and of the first order Si-Ge Raman signals at the center of the stripe are possibly due to a non-homogeneous filling of parts of some trenches, for which there is evidence in the SEM images of Fig. 4.1. It is worth noting that the frequency profile for the Si-Ge peak shown in Fig. 4.7(e) for this second line scan is qualitatively and quantitatively similar to that shown in Fig. 4.6(e) for the first line scan. From the data in Figs 4.6 and 4.7, the spatial resolution obtained in the TERS results is estimated to be 30 nm, consistent with the typical size of electrochemically etched Au tips.

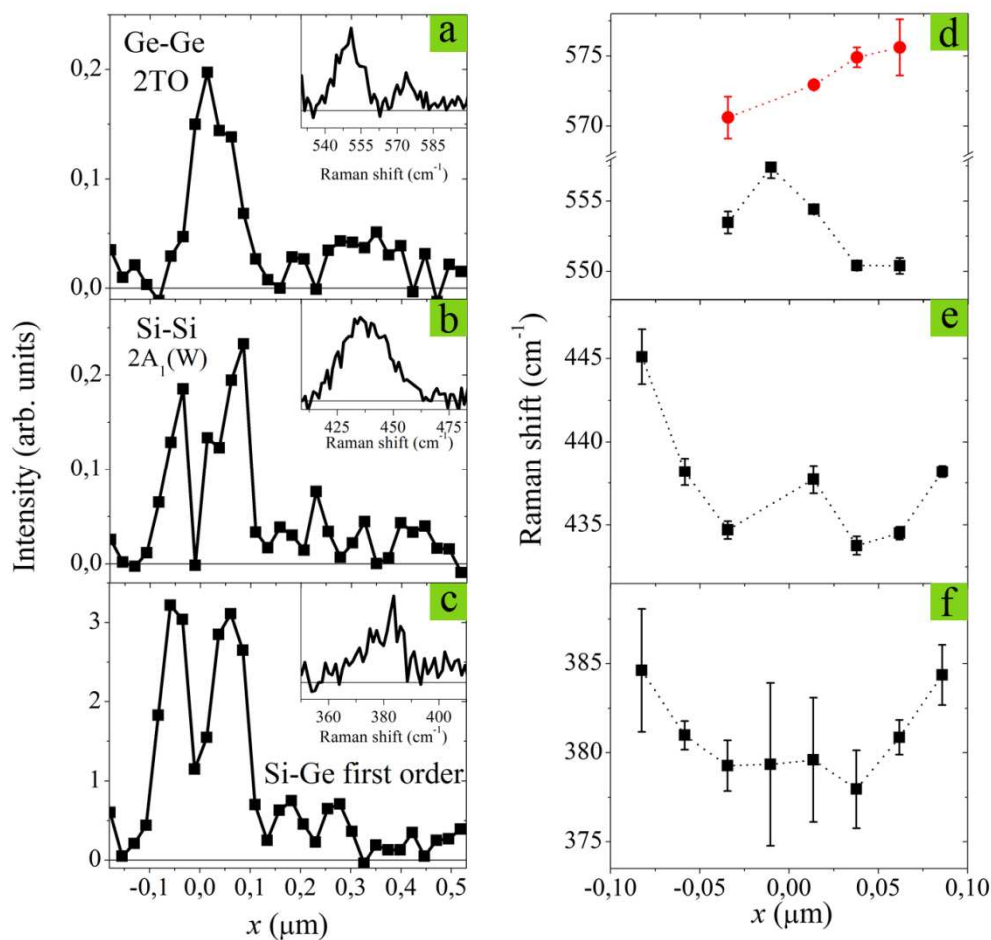


FIG. 4.7. Panels (a)-(c): integral intensities after a linear background subtraction for the Ge-Ge 2TO (a), the Si-Si $2A_1$ (b), and the first order Si-Ge (c) peaks as derived by TERS spectra monitored as a function of the position across the nano-stripe during a line scan of the tip. Panels (d)-(f) behavior of the Raman shifts as a function of the position across the nano-stripe for the monitored peaks, obtained by fitting the spectral region close to the peak maximum using a Voigt lineshape.

In SiGe structures heteroepitaxially grown on Si substrates the presence of misfit strain due to the lattice mismatch between the SiGe alloy and the Si bulk induces a shift of the Raman frequency modes²³ (see also Section D.3 in the Panel D). Very recently Hossain and Johnson²⁴ have determined by means of *ab initio* calculations the dependency of the frequency of the first order SiGe mode, ω_{Si-Ge} , on the Ge concentration, x , of the alloy and the misfit strain, ε_{zz} , along the direction parallel to the electric field of the incident radiation:

$$\omega_{SiGe} = \omega_{SiGe}^{(0)} + \beta \varepsilon_{zz} \quad (4.1)$$

where $\omega_{SiGe}^{(0)}$ and β are truncated polynomial expansions as a function of the Ge concentration x :

$$\omega_{SiGe}^{(0)} = -113.51x^2 + 107.79x + 382.82$$

$$\beta = -1163.4x^3 + 1977.8x^2 - 898.59x - 517.2$$

In this calculations, they explicitly considered the variations in bond length after strain is applied to the alloy and the effects of short range atomic ordering, including extended calculations of the equilibrium structural properties of the lattice for different compositions and of the force constants for strained supercells. In our geometry the incoming beam has a *p*-polarization (the electric field is parallel to the incidence plane), thus it is reasonable to assume that the enhanced near field is mainly polarized along the tip axis, i.e., the direction perpendicular to the sample surface, since the vertical field component along the tip axis plays the dominant role in the coupling effect between tip and radiation²⁵. Thus, the experimentally measured frequencies of the Si-Ge mode could allow for a direct determination of the misfit strain in direction perpendicular to the (001) plane inside a single nano-stripe, provided that its elemental composition is known.

We used Energy-Filtered XPEEM for the direct measurement of the Ge concentration within the nano-stripes. Photoelectrons energy filtered image series have been acquired around the Ge 3d ($E_B = 30$ eV) and Si 2p ($E_B = 99$ eV) core levels, using soft x-ray excitation at $h\nu = 90$ eV and 160 eV, respectively. In these conditions the Ge 3d and Si 2p photoelectrons have approximately the same kinetic energy, and thus they come from the same mean depth within the sample. The main panels in Figs. 4.8(a) and 4.8(b) represent the background subtracted core level images, while in the insets are shown the photoemission spectra averaged over a single nano-stripe. From the integral intensities I_{Ge} and I_{Si} of the core levels spectra determined for each pixel, we can estimate the Ge concentration in each spatial point in the field of view (FoV) by the relation:

$$x = \frac{\frac{I_{Ge}}{J_0(90 \text{ eV}) \cdot \sigma_{Ge}(90 \text{ eV})}}{\frac{I_{Ge}}{J_0(90 \text{ eV}) \cdot \sigma_{Ge}(90 \text{ eV})} + \frac{I_{Si}}{J_0(160 \text{ eV}) \cdot \sigma_{Si}(160 \text{ eV})}} \quad (4.2)$$

where σ_{Ge} and σ_{Si} are the photoionization cross-sections of Ge 3d and Si 2p transitions, and $J_0(90\text{ eV})$ and $J_0(160\text{ eV})$ are the photon beam intensities at $h\nu = 90\text{ eV}$ and 160 eV , respectively. In Eq. 2 we were able to wash out the inelastic mean free path (IMFP) of Ge 3d and Si 2p photoelectrons, thanks to the versatility of the synchrotron source which allowed to tune their kinetic energy to the same value. Moreover this choice of the excitation energies allows the measurement to be insensitive with respect to the Si oxide contamination at the surface, which is evidenced by the weak shoulder at the high binding energy side of the Si 2p spectrum (see inset of Fig. 4.8(b)). In fact the Si and Ge photoelectrons have the same kinetic energy and the same removal cross section, so that they are attenuated by the same relative amount. Taking Yeh and Lindau's cross-sections²⁶ and the transmissivity data of the x-ray monochromator at the TEMPO beamline, the spatial mapping of the Ge concentration is finally obtained (see Fig. 4.8(c)). Considering that the width of a single nano-stripe is around 150 nm, as derived by SEM (Fig. 4.1) and TERS (Figs. 4.6 and 4.7) data, the de-convolution of the experimentally measured concentration profile of single nano-stripes with a Gaussian weight function allowed to estimate the instrumental spatial resolution achieved in the XPEEM experiment to be around $96.7 \pm 3.5\text{ nm}$. Since the dimension of a single nano-stripe (around 150 nm) is significantly larger than the experimentally obtained spatial resolution, and assuming that its transverse concentration profile is approximately constant, as derived by SEM imaging (see Fig. 4.1) and TERS mapping (see Fig. 4.6(c)), the concentration value measured at the top of the PEEM profile is a good estimation of the real composition across the nano-stripe. By averaging for all the nano-stripes present in the FoV, a mean Ge concentration of about 0.91 ± 0.03 has been estimated.

Using the behaviour of the Si-Ge frequency mode as a function of the position across the nano-stripe as experimentally monitored by the TERS experiment, and the average Ge concentration as obtained by PEEM analysis, the perpendicular misfit strain across the nano-stripe can be derived by exploiting the Eq. (4.1). Fig. 4.9(a) presents the experimental strain profiles obtained from the TERS data of the two line scans (spatial resolution of 30 nm). In spite of the large experimental uncertainties for each data point, both profiles appear to be quite reproducible with a weighted mean square deviation of about 1.6×10^{-3} (equal to the 11% of the maximum measured strain). The experimental data has been compared with perpendicular strain profiles calculated using open source OpenFOAM²⁷ finite element modeling (FEM) system. For the calculations we considered a rectangular cross-section profile of the nano-stripe having a width of 150 nm and a thickness of 110 nm, as obtained from SEM imaging and FIB processing (see Fig. 4.1). Within the calculations, isotropic elastic constants were assumed, and the different composition and the lattice mismatch between the Si bulk and the SiGe nano-stripe were incorporated by means of a

modulation of the thermal expansion coefficient. In spite of the simplicity of the boundary conditions used here, interesting results have been derived and all the physical information about the system under investigation can be already deduced. The creation of the FEM mesh to exactly reproduce the cross section profile of the stripe (see Fig. 4.1(e)) is a next step foreseen for the future just to refine the calculations.

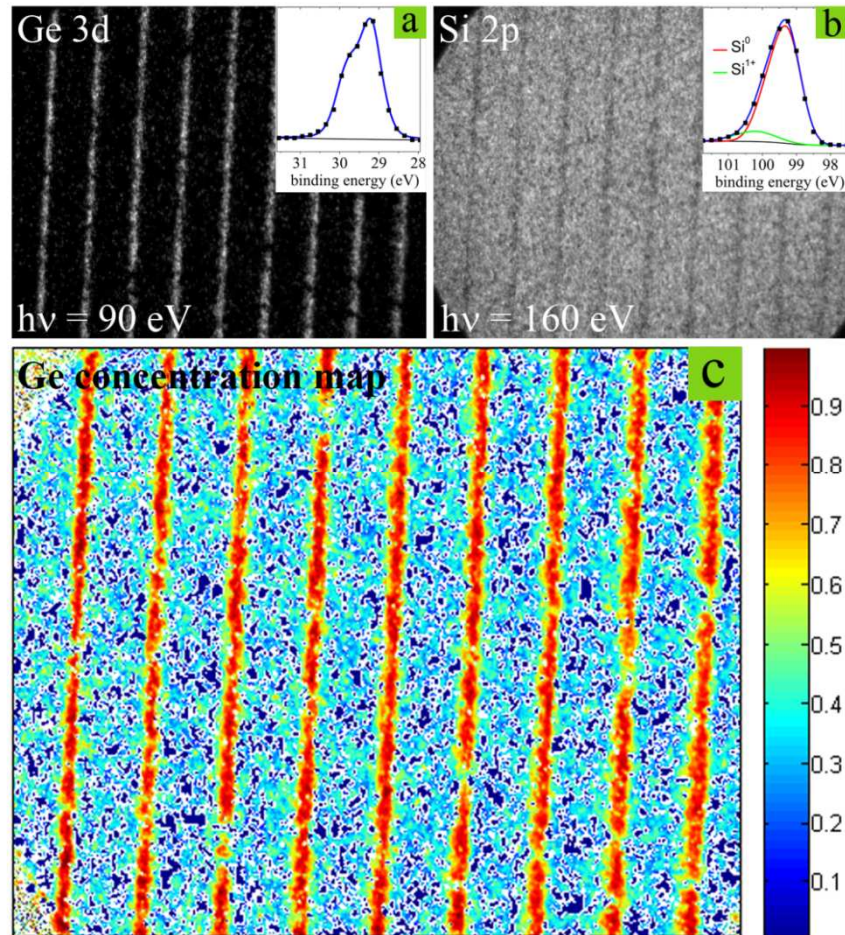


FIG. 4.8. Panels (a)-(b): background subtracted Ge 3d and Si 2p core level XPEEM images (FoV is around $15 \mu\text{m}$); insets: Ge 3d and Si 2p photoemission spectra extracted on a single nano-stripe (black squares) fitted with a Gaussian-Lorentzian lineshape (solid lines). In the case of Ge 3d spectrum two spin-orbit split structures separated by 0.6 ± 0.1 eV and with a branching ratio of ~ 1.5 have been considered. The weak component at high binding energy side within the Si 2p spectrum is consistent with a surface contamination with silicon oxide. Panel (c): spatial mapping of the Ge concentration as obtained by monitoring the Ge and Si integral intensities in every position within the FoV. The average Ge concentration within the stripes is about 0.91 ± 0.03 .

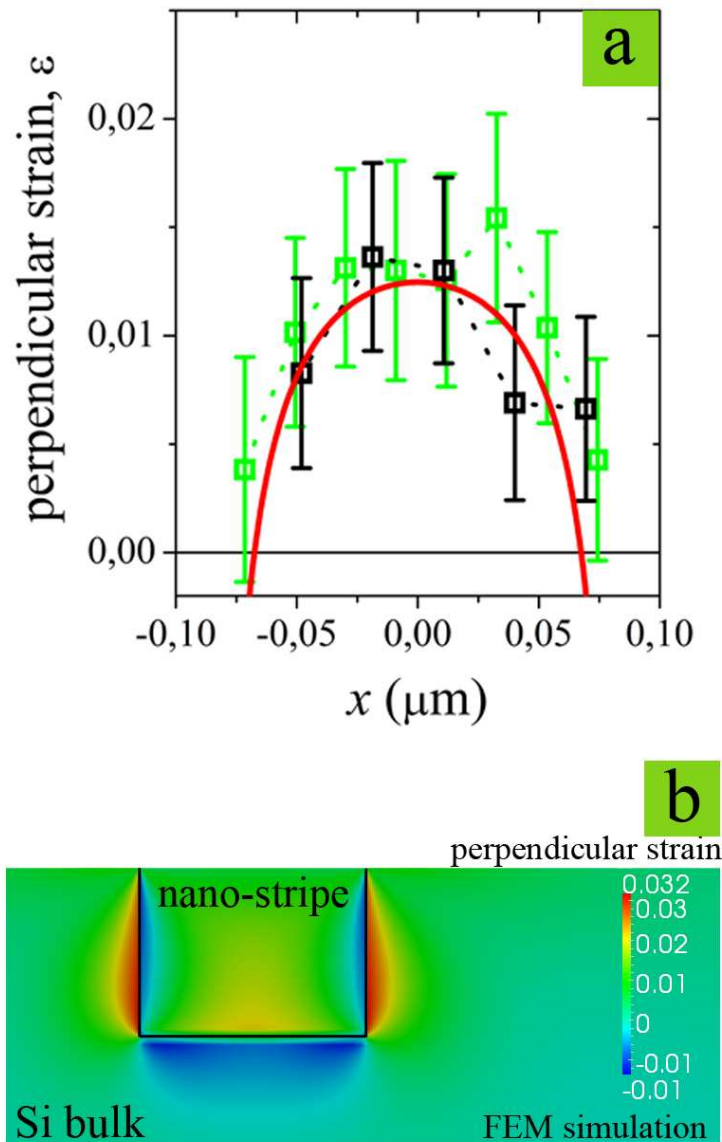


FIG. 4.9. Panel (a): experimental strain profiles (green and black squares) as obtained employing TERS data from the two measured line scans. The red solid line represent the strain profile obtained by averaging the calculated ϵ_{zz} strain along the direction perpendicular to the nano-stripe. The calculated ϵ_{zz} strain values have been also weighted at different depth with an exponential function having an attenuation length of 30 nm, in order to take into account the attenuation of the light within the sample. Panel (b): 2D cross section map of the strain perpendicular to the surface plane within a single nano-stripe with Ge concentration of 0.91 and the surrounding Si bulk regions, calculated using the OpenFOAM finite element modeling system. The colour scale goes from negative compressive strain (blue) to positive tensile strain (red). The nano-stripe has rectangular profile with a thickness of 110 nm and a width of 150 nm. Black solid lines define the limits of the SiGe nano-stripe.

Fig. 4.9(b) shows a 2D cross section map of the perpendicular strain as calculated by FEM within the nano-stripe with a Ge concentration of 0.91 and the surrounding Si bulk regions. The red solid line in Fig. 4.9(a) represent the calculated strain profile as a function of the position across the nano-stripe. This behavior has been obtained by averaging the calculated strain along the z -axis perpendicular to the nano-stripe, and weighting the strain values at different depth with an

exponential function in order to take into account the attenuation of the near-field within the sample.

The FEM calculations predict that the nano-stripe is fully strained along its axis (the [110] direction), while exhibits an elastic relaxation in the (110) plane. In fact the calculated σ_{yy} stress along the [110] direction is much greater than in-plane σ_{xx} and out-of-plane σ_{zz} stresses. This is the condition for a preferential uniaxial stress along the [110] direction. The sensitivity of our experimental results with respect to the stress field within the nano-stripe can be discussed by making reference to two limiting cases. On one hand, in case of biaxial strain in the (001) plane, the perpendicular strain ε_{zz} should be around 0.027, much greater than both the FEM calculated and the experimentally measured strain values. On the other hand, a plastic relaxation induced by a set of a network of 60° dislocations with a typical density of 10^9 cm^{-2} along the [110] direction²⁸ would cause an almost complete strain relaxation leading ε_{zz} close to zero. Therefore, the very good agreement between the experimentally measured and the calculated strain profiles is an indication that the nano-stripe would exhibit a preferential uniaxial compressive stress field along its axis (the [110] direction) predicted by the FEM simulations.

4.4 Work function and Valence band mapping

In this Section the measured local work function and valence band maps are presented allowing the determination of the conduction and valence electronic structure modifications with respect to the Ge bulk case induced by the strain field inside the nano-stripes.

Photoelectrons energy filtered PEEM images have been acquired around the photoemission threshold using soft x-ray excitation at $h\nu = 90 \text{ eV}$. Fig. 4.10(a) and 4.10(b) represent PEEM images using secondary electrons of 4.6 eV and 4.9 eV, respectively, where the inversion of the contrast between the nano-stripes and the surrounding Si bulk reflects the difference in the work function, defined as the energy needed to promote an electron from the Fermi level to the vacuum level. Fig. 4.10(c) shows the threshold spectra extracted from the Si bulk and from a single nano-stripe. The energy scale on the abscissa axis is referred to the Fermi level, E_F , of the sample surface as illustrated in Fig. 4.10(d). If E_K denotes the kinetic energy of the photoelectrons measured at the entrance of the imaging analyzer, and E denotes the final-state energy, then $E - E_F = E_K + eV_S + \Phi_A$, where Φ_A is the work function of the analyzer and V_S the bias voltage applied to the sample surface. An electron having an initial state energy E_i just below E_F , excited with photons of energy $h\nu$, will have a measured kinetic energy E_K given by $E_K = (E_i + h\nu) - eV_S - \Phi_A$. Thus, the threshold kinetic energy E_K^0 is given by $\Phi - eV_S - \Phi_A$ and the correspondent final state energy $(E - E_F)^0$ is equal to

Φ , the sample work function. The secondary electron energy distributions as a function of $E - E_F$ presented in Figure 4.10(d) are thus characterized by a sharp threshold corresponding to the local work function Φ of the emitting region under consideration. These distributions are very similar to the energy distribution of gold reported by Henke *et al.*²⁹

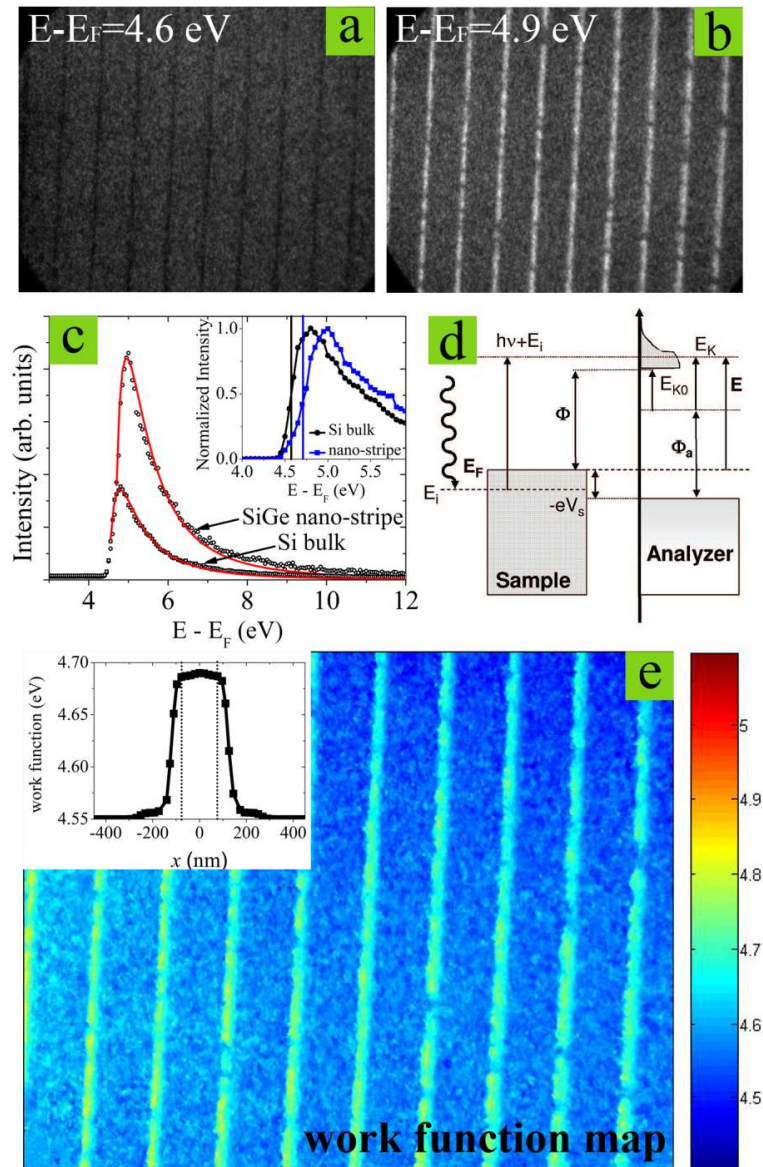


FIG. 4.10. Panel (a)-(b): PEEM images of a portion of the nano-stripes array acquired with soft x-ray excitation at $h\nu = 90$ eV using secondary electrons of 4.6 eV (a) and 4.9 eV (b). The FoV is ~ 17 μm . Panel (c): experimental secondary electron energy distributions as a function of $E - E_F$ for the Si bulk and the SiGe nano-stripes. The red curves represent the best least-square fitting of the experimental data using the Henke's model (see text). Inset: normalized spectra showing the shift of the photoemission threshold. Panel (d): schematic energy level diagram illustrating the determination of the local work function (from Ref. 30). Panel (e): local work function map obtained from the least-square-fitting of the experimental threshold spectra measured for each point within the FoV to the secondary electron distribution described by the Henke's model. Inset: work function profile measured across a single nano-stripe after deconvolution with a Gaussian weight function using the recursive Van Cittert method; the vertical dotted lines define the real width of the nano-stripe.

The local work function map (see Fig. 4.10(e)) of the Si substrate and of the SiGe nano-stripes have been thus obtained from the best least-square-fitting of the experimental threshold

spectra measured for each point within the FoV to the secondary electron distribution, $S(E-E_F)$, described by Henke *et al.*³¹:

$$S(E-E_F) = \frac{A(E-E_F-\Phi)}{(E-E_F-\Phi+B)^4} \quad (4.3)$$

where A is a scaling factor and B is a fitting parameter.

The Si substrate has a work function of 4.55 ± 0.01 eV, lower than the value reported in case of pure bulk intrinsic silicon (4.75 eV). This is attributed high level of n-type doping which shifts the Fermi level up toward the conduction band. The inset in Fig. 4.10(e) represents the work function profile measured across a single nano-stripe after de-convolution with a Gaussian weight function using the recursive Van Cittert method³². The full width half maximum (FWHM) of the Gaussian function has been chosen equal to the instrumental spatial resolution (96.7 nm) achieved in the XPEEM measurement. The work function value of the nano-stripe is 4.69 ± 0.01 , much smaller than the work function of a bulk $\text{Si}_{0.1}\text{Ge}_{0.9}$ alloy (4.98 eV). This variation is a fingerprint of the strong modification of the band structure of the nano-stripe with respect to the bulk case.

Indeed, at the Si-SiGe interface at the nano-stripe boundaries a hetero-junction between two differently doped semiconductors (the n-type Si bulk and the intrinsic SiGe nano-stripe) is formed. In the simple case of a hetero-junction between two bulk materials, after reaching the chemical/thermal equilibrium the Fermi level in each material aligns and is constant throughout the junction. To the extent that they are able, electrons from As donors leave some regions within the n-doped Si (depletion region) and accumulate within the intrinsic SiGe (accumulation region), building up an electric field able to re-establish the equilibrium. When this occurs a certain amount of band bending occurs near the interface. This doping-induced band bending can be quantified with the built-in potential given by difference of the work function between the materials constituting the hetero-junction in their bulk state (V_{bi} is around 0.43 eV for the Si-Si_{0.1}Ge_{0.9} hetero-junction of our case). Moreover, when dealing with junctions between two different materials a *natural* band offset due to the different surface charges at the interface must be also taken into account and superimposed to the built-in potential.

However, as soon as the strain is involved the situation becomes considerably more complicated. Inside the SiGe nano-stripes a not negligible strain field appears due to the lattice mismatch between Si and Ge, as experimentally shown in the last section. Such a strain field is responsible for a strong modification of the electronic band structures: the hydrostatic component affects the bands offset, while the uniaxial component is responsible for the splitting of degenerate bands. This strain-induced bands shift and states splitting have to be thus superimposed to the doping-induced band bending and to the natural band offset.

Recent experiments based on Kelvin Probe Force Microscopy (KPFM)³³ and *ab initio* density functional theory calculations for Si nanowires³⁴ showed that the work function exhibit significant changes as a function of the strain of the investigated structures. The work function modification would reflect the strain-induced variations of the surface electrostatic dipole and the shift of the Fermi Level with respect to the conduction band edge³⁵, the latter being the dominant contribution^{34,35}. Within the SiGe nano-stripes the Fermi level is pinned to the position defined by the Si bulk substrate, and thus any shift of the conduction band edge must be accompanied to a modification of the vacuum level to maintain the charge balance. At zero-order approximation, we consider that the vacuum level is modified in the same way as the conduction band edge³⁶ and we neglect the surface dipole contribution. Under this hypothesis, the difference of the local work function between the SiGe nano-stripe and the surrounding Si bulk, $\Delta\Phi$, is thus given by summing up the built-in potential V_{bi} , the *natural* conduction band offset (-0.2 eV for a Si-Si_{0.1}Ge_{0.9} hetero-junction³⁷), and the strain-induced conduction band offset ΔE_C within the SiGe nano-stripe. We measured from the PEEM images at the photoemission threshold a $\Delta\Phi$ value of about 0.14 eV, and thus a rough experimental estimation of ΔE_C is ~ -0.49 eV. It is worth noting that the width of the work function profile shown in the inset of Fig. 4.10(e) is larger than the real width of the nano-stripe (150 nm). This could be possibly due to the distortion of the extraction electric field lines by the presence of the built-in electric field across the hetero-junctions at the Si-SiGe interfaces³⁸.

In general, a uniaxial strain will deform a crystal and lift some of the degeneracies in the conduction band. In a Ge crystal the L_6 lowest conduction band minima occur along the four equivalent $[111]$, $[\bar{1}\bar{1}\bar{1}]$, $[1\bar{1}\bar{1}]$ and $[\bar{1}\bar{1}1]$ directions of the first Brillouin zone (see Fig. 4.11), so that they exhibit a four-fold degeneracy as a result of the degeneracy in the reciprocal space. A uniaxial stress applied along the $[111]$ direction will make it different from the remaining three equivalent directions. Thus, from symmetry argument one expects that a $[111]$ -oriented uniaxial stress will split the $[111]$ valley (which will form a singlet) from the other three valleys, which remain degenerate forming a triplet state.

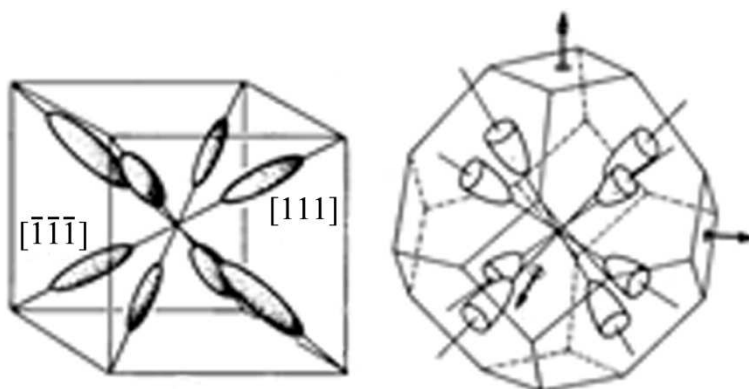


FIG. 4.11. Constant energy surface conduction band minima in Ge represented within the real space (left) and reciprocal space (right) unit cells. There are height symmetry related ellipsoids with long axes along the $\langle 111 \rangle$ directions centered on the midpoints of the hexagonal zone faces.

However a strain applied along the [001] direction will affect all four minima in the same way and leave the degeneracy unchanged, thus only a uniaxial strain along the [111] direction will be able to lift the degeneracy of the L_6 conduction band minima. In our case, the nano-stripes exhibit a preferential uniaxial strain along the [110] direction, which can be seen as the projection of a [111] uniaxial strain on the (001) plane. The problem can be expressed in terms of a uniaxial strain Hamiltonian of the form³⁹:

$$H_{uniaxial} = \Xi_u (\hat{k} \cdot \boldsymbol{\varepsilon} \cdot \hat{k}) \quad (4.4)$$

where $\boldsymbol{\varepsilon}$ is the strain tensor, \hat{k} is a unit vector along the direction of one of the equivalent [111] conduction band minima in reciprocal space, and Ξ_u is the shear deformation potential. Within this framework, the splitting of the conduction band minima as a result of a uniaxial strain $\boldsymbol{\varepsilon}_u = \sqrt{2/3}(\boldsymbol{\varepsilon}_{yy} - \boldsymbol{\varepsilon}_{xx})$ (y is the direction along the nano-stripe and x is the in-plane direction perpendicular to y) was found to be³⁹:

$$E_C - E_C^0 = \begin{cases} +\frac{2}{3}\Xi_u \boldsymbol{\varepsilon}_u \\ -\frac{1}{3}\Xi_u \boldsymbol{\varepsilon}_u \end{cases} \quad (4.5)$$

where E_C^0 is the conduction band minimum of the unstrained crystal, $\Xi_u = 16.8$ eV is derived from the *ab initio* calculations of Fischetti and Laux⁵, and $\boldsymbol{\varepsilon}_u = -0.038$ is the average uniaxial strain of the SiGe nano-stripes derived by the FEM simulations presented in the last section. So far, we have just considered the splitting of the conduction band minima resulting from the uniaxial component of the strain. In order to calculate the proper band offset, it is necessary also to consider the effect of the hydrostatic component of the strain. The problem can be expressed in terms of a hydrostatic Hamiltonian of the form³⁹:

$$H_{hydro} = \Xi_d (\text{Tr}\{\boldsymbol{\varepsilon}\}) \quad (4.6)$$

where $\text{Tr}\{\boldsymbol{\varepsilon}\}$ is the trace of the strain tensor $\boldsymbol{\varepsilon}$, and Ξ_d is the dilatation deformation potential. Thus, the shift of the conduction band due to the hydrostatic strain component was found to be:

$$\Delta_C = \left(\Xi_d + \frac{1}{3}\Xi_u \right) \frac{\Delta V}{V} \quad (4.7)$$

where $\Xi_d + \frac{1}{3}\Xi_u = 1.17$ eV⁵ is the volume deformation potential, and $\frac{\Delta V}{V} = \boldsymbol{\varepsilon}_{xx} + \boldsymbol{\varepsilon}_{yy} + \boldsymbol{\varepsilon}_{zz} = -0.023$ as derived by the FEM simulations (z is the direction perpendicular to the surface). The total strain-induced conduction band offset is thus obtained by considering the effects of both uniaxial and hydrostatic strain components:

$$\Delta E_C = +\frac{2}{3}\Xi_u \epsilon_u + \left(\Xi_d + \frac{1}{3}\Xi_u \right) \frac{\Delta V}{V} = -0.45 \text{ eV} \quad (4.8)$$

very close to the value (- 0.49 eV) experimentally estimated using the local work function results.

We focus now on the discussion of the valence band mapping measured by XPEEM. To probe the modifications of the valence electronic structure within the SiGe nano-stripes with respect to the bulk case, we measured photoelectrons energy filtered images across the valence band using soft x-ray excitation at $h\nu = 90 \text{ eV}$. Fig. 4.12(a) represent the spatial mapping of the intensity of the valence band signal obtained integrating the valence band spectra acquired for each point within the FoV over an energy range of 20 eV from the Fermi level. The contrast seen in the image is possibly due to a different filling of the valence electronic orbital for the SiGe nano-stripes with respect to the Si bulk. Fig. 4.12(c) represents the raw valence band spectrum averaged on a single nano-stripe, while in Fig. 4.12(b) the valence band spectrum of a Ge(001) bulk crystal is reported for comparison. The bulk Ge 3d core level (29.2-29.8 eV) has been used as energy reference for the measured spectra (not shown).

The broad structure within the spectrum measured on the nano-stripe centered at 2.2 eV below the valence band maximum (VBM) and 2 eV large (see Fig. 4.12(c)) could correspond to the superposition of several spectral features reported in literature to characterize a clean Ge(001) surface: the emission from dimer up atom dangling bond states at 0.4 eV⁴⁰, a peak at 1.4 eV due to back bond emission and confined to the second and third surface layers⁴¹, and the emission at 3.2 eV from valence bands of the bulk electronic structure⁴². The defined peak at 7 eV is assigned to the nonbonding O 2p orbital of silicon oxide contamination of the sample surface (also evident from Si 2p core-level spectrum shown in the inset of Fig. 4.8(b)). We exclude the presence of germanium oxide contamination since the main features due to oxygen should be observed at 5.2 eV from the VBM⁴³ and we observe no evidence for an oxide component in the local Ge 3d core level spectra of the stripes. The valence band onsets are obtained from a linear extrapolation of the valence band leading edges (see Fig. 4.12(d)). The spectrum measured on the SiGe nano-stripe exhibits a VBM shifted toward the lower binding energy side of about $\Delta E_V = 0.28 \text{ eV}$ with respect to the Ge(001) bulk case, and shows a greater energy dispersion at the valence band edge as revealed by an increase of its slope by a factor 1.5.

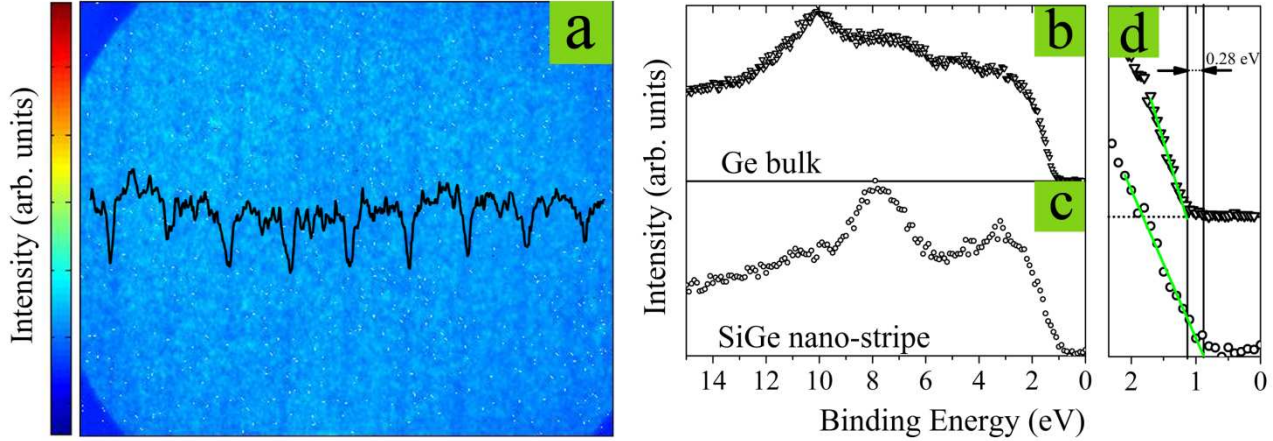


FIG. 4.12. Panel (a): spatial mapping of the intensity of the valence band signal obtained integrating the valence band spectra acquired for each point within the FoV (15 μm) over an energy range of 20 eV from the Fermi level. The black solid line is the integration of the signal perpendicular to the stripe direction. Panel (b)-(c): valence band spectra measured on a Ge(001) bulk sample (b) and on a single nano-stripe (c). Panel (d): close ups of the valence band maximum (VBM) region for the spectra shown in (b)-(c). The VBM values have been determined by a linear fitting (green lines) of the upper edge. The relative shift is about 0.28 eV.

To describe the effects of the strain on the valence band maxima at the Γ point of the first Brillouin zone of a SiGe crystal we require only three further deformation potentials. As in the case of degenerate conduction bands discussed before, the strain will deform the crystal and lift and shift the six-fold (including spin) degenerate valence band maxima. In this case it is convenient to regard these six bands as transforming like the eigenstates of a $J = 3/2$ and a $J = 1/2$ angular momentum operator⁴⁴, exhibiting a spin orbit splitting Δ_0 . The hole-strain interaction Hamiltonian can be derived by symmetrizing the angular momentum operator J through multiplication by appropriate components of the strain tensor (method of invariants). The procedure for doing this can be derived from the group theory and has been described in details by Pikus and Bir⁴⁴. The Pikus and Bir effective strain Hamiltonian for the valence bands in the zinc-blend semiconductors is given by:

$$H_{PB} = a(\epsilon_{xx} + \epsilon_{yy} + \epsilon_{zz}) + b \left[\left(J_x^2 - \frac{J^2}{3} \right) \epsilon_{xx} + \text{c.p.} \right] + \frac{2d}{\sqrt{3}} \left[\frac{1}{2} (J_x J_y + J_y J_x) \epsilon_{xy} + \text{c.p.} \right] \quad (4.9)$$

where a , b , and d are the three deformation potentials, and c.p. stands for cyclic permutation. The deformation potential $a = 2 \text{ eV}^5$ accounts for the crystal dilatation under hydrostatic strain inducing a shift of the valence band maximum of the quantity:

$$\Delta_V = a \frac{\Delta V}{V} \quad (4.10)$$

The deformation potentials $b = -2.16 \text{ eV}$ and $d = -6.06 \text{ eV}^5$ determine the splitting of the six-fold $J = 1/2$ and $J = 3/2$ valence bands at Γ under uniaxial stress. In addition to the strain the spin-orbit

interaction contributes to the splitting. The valence band splitting under the combined action of uniaxial strain and spin-orbit interaction is given by⁴⁵:

$$\begin{aligned}
 E_v \left(J = \frac{3}{2}, J_z = \pm \frac{3}{2} \right) &= \frac{1}{3} \Delta_0 - \frac{1}{2} \delta E && \text{heavy hole band} \\
 E_v \left(J = \frac{3}{2}, J_z = \pm \frac{1}{2} \right) &= -\frac{1}{6} \Delta_0 + \frac{1}{4} \delta E + \frac{1}{2} \sqrt{\Delta_0^2 + \Delta_0 \delta E + \frac{9}{4} \delta E^2} && \text{light hole band} \\
 E_v \left(J = \frac{3}{2}, J_z = \pm \frac{1}{2} \right) &= -\frac{1}{6} \Delta_0 + \frac{1}{4} \delta E - \frac{1}{2} \sqrt{\Delta_0^2 + \Delta_0 \delta E + \frac{9}{4} \delta E^2} && \text{split-off band}
 \end{aligned} \tag{4.11}$$

where $\Delta_0 = 0.29$ eV for Ge is the spin-orbit splitting, and:

$$\delta E = 2b(\varepsilon_{zz} - \varepsilon_{yy}) + \frac{1}{\sqrt{3}} d\varepsilon_{yz} \tag{4.12}$$

In Fig. 4.13 is presented the schematic change of the valence band character when SiGe is subjected to compressive strain as derived within a perturbation approach in the framework of the $k \cdot p$ interaction method. In case of compressively strained SiGe the heavy hole band lies above the light hole band, and thus the total strain-induced valence band offset obtained considering the effects of both uniaxial and hydrostatic strain components is given by:

$$\Delta E_V = \frac{1}{3} \Delta_0 - \frac{1}{2} \left[2b(\varepsilon_{zz} - \varepsilon_{yy}) + \frac{1}{\sqrt{3}} d\varepsilon_{yz} \right] + a \frac{\Delta V}{V} = 0.25 \text{ eV} \tag{4.13}$$

where ε_{zz} , ε_{yy} and ε_{yz} for the nano-stripe have been deduced from the FEM simulations. The calculated ΔE_V value is very close to that experimentally estimated using PEEM valence band mapping (0.28 eV). Moreover, within the framework of the $k \cdot p$ interaction method, it turns out that for the valence bands the dispersion along the uniaxial strain axis is greatly modified by the combination of strain and spin-orbit interaction, leading to a significant changes of the effective masses with respect to the bulk case. As schematically shown in Fig. 13 the curvature of the heavy hole band close to the valence band edge increases under compressive strain. This has been experimentally evidenced within the PEEM spectra shown in Fig. 4.12(b) by an increase of the band dispersion close to the valence band edge. This effect is thus responsible for a decrease of the hole effective mass and a correspondent enhancement of the hole mobility, μ ($\mu = \frac{e\tau}{m_h^*}$, where e is the electron charge, τ is the hole life time, and m_h^* is the hole effective mass).

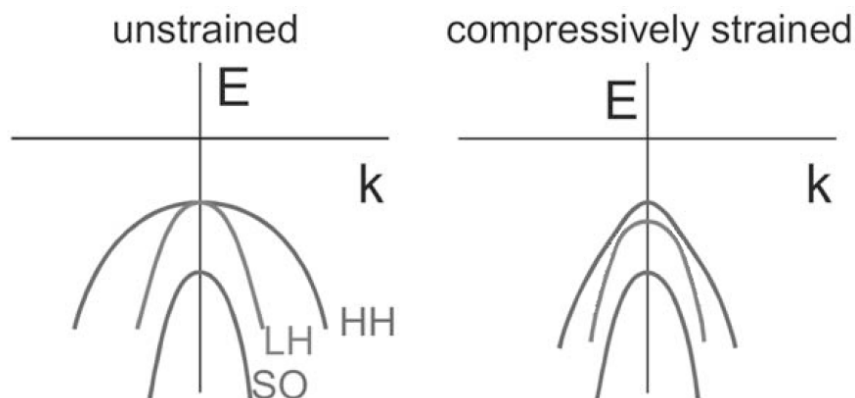


FIG. 4.13. Schematic representation of the degeneracy lifting at $k = 0$ and the change of the valence band character when Ge is subjected to a compressive strain as obtained within the framework of the $k \cdot p$ method. Note in particular the increase of the curvature of the heavy-hole band, corresponding to a decrease of its effective mass and thus to an increase of the mobility (from Ref. Von Kanel Lecture notes).

4.5 Conclusions

In this chapter, we have presented the spatial mapping with nanoscale resolution of strain, composition, work function and valence band structure of lithographically defined SiGe *embedded* nano-stripes by means of Tip Enhanced Raman Spectroscopy (TERS) and Energy-Filtered PhotoElectrons Emission Microscopy (EF-PEEM) techniques. First, we described the sample preparation methods and the experimental details for TERS and PEEM measurements. Then, we discussed the experimentally measured TERS spectra and the PEEM-derived elemental composition mapping, from which the perpendicular strain profile across a single nano-stripe is obtained with a spatial resolution of about 30 nm. The perpendicular strain (along the [001] direction) is tensile and becomes maximum (~ 0.014) at the center of the nano-stripe while decreasing close to zero at its boundaries. 3D Finite Element Modeling (FEM) calculations are successfully compared both qualitatively and quantitatively to the experimental results, and a preferential uniaxial stress along the longitudinal axis of the nano-stripe is deduced from the simulations. Finally, the local work function and the valence band mapping is presented from which the strain-induced conduction and valence band offsets for the SiGe nano-stripes with respect to the Ge(001) bulk case have been determined. The conduction band minimum shifts downward in energy of about 0.49 eV while the valence band maximum rises of 0.28 eV, showing a greater energy dispersion close to the valence band edge. The bands offset obtained from first-principles calculations considering both uniaxial and hydrostatic strain components correctly reproduce the experimental values.

Bibliography

- ¹ T. Irisawa et al., IEEE Transactions on electron devices **55**, 649 (2008)
- ² M. L. Lee et al., J. Appl. Phys. **97**, 011101 (2005)
- ³ B. Rössner, D. Chrastina, G. Isella, and H. von Känel, Appl. Phys. Lett. **84**, 3058 (2004)
- ⁴ S. Thompson et al., IEEE Transactions **53**, 1010 (2006). D. Buca, et al., Appl. Phys. Lett. **90**, 032108 (2007)
- ⁵ M.V. Fischetti, S.E. Laux, J. Appl. Phys. **80**, 2234 (1996)
- ⁶ E. Bonera, et al., J. Appl. Phys. **100** 033516 (2006); E. Bonera, et al., Appl. Phys. Lett. **87**, 111913 (2005)
- ⁷ N. Anderson, A. Hartschuh, L. Novotny, *Mat. Today* **8**(5) 50 (2005)
- ⁸ A. Hartschuh, *Angew. Chem. Int. Ed.* **47** 8178 (2008).
- ⁹ T. Yano, Y. Inouye, S. Kawata, *Nano Lett.* **6** 1269 (2006)
- ¹⁰ T. Yano, P. Verma, S. Kawata, Y. Inouye. *Appl. Phys. Lett.* **88** 093125 (2006)
- ¹¹ S. S. Kharintsev, G. G. Hoffmann, P. S. Dorozhkin, G. de With, and J. Loos. *Nanotechnology* **18** 315502 (2007).
- ¹² F. Ratto, S. Heun, et al., *Small* **2** 401 (2006)
- ¹³ F. De la Pena, N. Barrett, L.-F. Zagonel, M. Walls, O. Renault, *Surf. Sci.*, **604**, (2010) 1628-1636
- ¹⁴ L. Nataraj et al., Appl. Phys. Lett. **96**, 121911 (2010)
- ¹⁵ N. Mingo et al., *Nano Lett.* **9**, 711 (2009)
- ¹⁶ V. Yu. Fominski, O.I. Naoumenko, V.N. Nevolin, A.P. Alekhin, A.M. Markeev, and L.A. Vyukov, Appl. Phys. Lett. **68** 2243 (1996)
- ¹⁷ K. Choi, S. Ghosh, J. Lim, C.M. Lee, Appl. Surf. Sci. **206** 355-364 (2003)
- ¹⁸ W. Windl, P. Pavone, K. Karch, O. Schutt, D. Strauch, P. Giannozzi, S. Baroni, Phys. Rev. B **48** 3164 (1993)
- ¹⁹ A. Merlen et al., J. Raman Spectrosc. **40** 1361 (2009)
- ²⁰ Z. Yang, J. Aizpuruac and H. Xu, J. Raman Spectrosc. **40**, 1343–1348 (2009)
- ²¹ H.D. Fuchs et al., Phys. Rev. B **43** 4835 (1991)
- ²² W. Windl, K. Karch, P. Pavone, O. Schutt, and D. Strauch, J. Quantum Chemistry **56** 787 (1995)
- ²³ Pezzoli F, Grilli E, Guzzi M, Sanguinetti S, Chrastina D, Isella G et al., Mater Sci Semicond Process **9**, 541 (2006).
- ²⁴ M.Z. Hossain and H.T. Johnson, J. Appl. Phys. **107**, 073515 (2010)
- ²⁵ D. Mehtani et al., J. Raman Spectrosc. **36** 1068 (2005)
- ²⁶ Yeh, J. J.; Lindau, I. At. Data Nucl. Data Tables 1985, 32 (1), 1–155

-
- ²⁷ <http://www.openfoam.com/>
- ²⁸ Wang *et al.*, *Appl. Phys. Lett* **94**, 102115 (2009)
- ²⁹ Henke, B. L.; Smith, J. A.; Attwood, D. T. *J. Appl. Phys.* **1977**, *48* (5), 1852–1866.
- ³⁰ A. Bailly *et al.*, *Nano Letters* **8** 3709 (2008)
- ³¹ Henke, B. L.; Liesegang, J.; Smith, S. D. *Phys. Rev. B: Condens. Matter Mater. Phys.* **1979**, *19* (6), 3004.
- ³² Madden and Houston, *J. Appl. Phys.* **47** 3071 (1976)
- ³³ K. Unal and H.K. Wickramasinghe, *Appl. Phys. Lett.* **90**, 113111 (2007)
- ³⁴ P.W. Leu, A. Svizhenko, and K. Cho, *Phys. Rev B* **77**, 235305 (2008)
- ³⁵ B. Shan, K. Cho, *Phys. Rev. Lett.* **94** 236602 (2005)
- ³⁶ This hypothesis rests upon the basics assumptions of the Schottky model for the metal-semiconductor hetero-junctions (see H. Luth, *Solid Surfaces, Interfaces, and Thin Films*, Springer-Verlag, Fourth Edition)
- ³⁷ Y.H. Li *et al.*, *App. Phys. Lett.* **94** 212109 (2009)
- ³⁸ Maylis Lavayssiere, PhD Thesis, CEA-LETI (2010)
- ³⁹ C. Herring and E. Vogt, *Phys. Rev.* **101**, 944 (1956)
- ⁴⁰ L. Kipp, R. Manzke, and M. Skibowski, *Solid State Commun.* **93**, 603 (1995).
- ⁴¹ E. Landemark *et al.*, *Surf. Sci. Lett.* **236**, L359 (1990).
- ⁴² T. C. Hsieh, T. Miller, and T.-C. Chiang, *Phys. Rev. B* **30**, 7005 (1984).
- ⁴³ K. Prabhakaran, and T. Ogino, *Surf. Sci.* **325** (1995) 263
- ⁴⁴ P.Y. Yu and M. Cardona, *Fundamentals of Semiconductor: Physics and Material Properties*, Springer Fourth Edition
- ⁴⁵ Ch. G. Van de Walle and R.M. Martin, *Phys. Rev. B* **34**, 5621 (1986)

Chapter 5

Nanoscale elastic strain relief in SiGe nano-ridges studied by X-Ray Diffraction

5.1 Introduction

In the Chapter 4 we have extensively stressed that the enhancement of the charge carrier mobility is a key issue for the achievement of high performances MOSFET devices. As already discussed, high carrier mobility in SiGe devices can be obtained by controlling the strain of the MOSFET channel¹. Improvements in mobility have been demonstrated at room temperature² and further improvement has been observed at low temperature³. Moreover, we have also emphasized that as soon as the channel width approaches the limit for the carrier confinement, the channel strain depends also on the lateral boundary conditions due to elastic and plastic relaxation, resulting in uniaxial strain that provides even more significant carrier mobility enhancement⁴. Nevertheless it is worth noting here that to realize this potential, several strain reducing phenomena have to be prevented: nucleation of misfit dislocations, alloying, or intrinsic elastic deformation, the latter being particularly relevant when the lateral channel dimensions compare with its thickness (a few tens of nm). Thus it is of fundamental importance to know and control the strain in the channel, as a function of its shape and size, so that devices can be efficiently designed.

The strain information is *directly* obtained by wide beam X-Ray Diffraction (XRD)⁵ (see also Panel G), the conventional method for accurately determining composition and strain in $\text{Si}_{1-x}\text{Ge}_x$ heterostructures, whose results, however, represent *ensemble averages* over several square mm. When dealing with nanostructures this technique only relies on the assumption of a small dispersion of their properties, preventing the possibility to investigate morphologically different nanostructures present at the same time on the same sample. Mocuta *et al.*⁶ used X-ray *micro*-diffraction to analyze the strain and composition profiles in individual micronsized SiGe islands. Although this work is

the first demonstration of site selectivity within an ensemble, it relates with large size islands which are of limited interest for technological applications since the integration has already scaled down to tens of nanometers and the high degree of strain relaxation present there is something to be avoided. Strain profiles with a lateral resolution of tens of nm and sensitivity of 10^{-3} could be measured by transmission electron diffraction techniques⁷, but the possibility of strain relaxation due to thinning of the sample makes the correlation with real devices difficult.

The recent availability of the X-Ray *nano*-diffraction technique at the ID13 beamline of the European Synchrotron Radiation Facility (ESRF)⁸ has opened the possibility of measuring the lattice parameter of single nanostructures with spatial resolution down to 100 nm and sensitivity to relative lattice parameter variations better than 10^{-4} . The technique provides an unprecedented level of detail in the spatial strain mapping of single nanostructures with the considerable advantage to be non-destructive in contrast with Transmission Electron Microscopy.

In this chapter, we present the first results of the characterization of the strain state of lithographically defined SiGe nano-ridges on a Si(001) substrate, in layouts very close to those used in prototype devices, using nano-XRD technique. The sample preparation procedure, the experimental setup, the diffraction geometry and the post-acquisition data elaboration methods are presented. Strain values are extracted from the experimentally measured diffraction profiles, which are then compared with kinematical simulations performed on strain data obtained from Finite Element Modeling (FEM) calculations.

5.2 Experiment and Methods

5.2.1 Sample preparation

SiGe nano-ridges and large squares on Si(001) surface have been created by coupling Electron Beam Lithography (EBL) and Low Energy Plasma Enhanced Chemical Vapor Deposition (LEPECVD)⁹. The nano-ridges represent the prototypical structures for the investigation of the strain state when approaching lateral width of about several tens of nanometers, while the large squares have been used as test structures to verify the sensitivity of the measurements.

A $\text{Si}_{1-x}\text{Ge}_x$ fully strained alloy layer with $x = 0.11$ and thickness of 120 nm has been epitaxially grown on a Si(001) substrate at 600 °C by LEPECVD. The strain state, the alloy composition and the thickness for the SiGe film have been determined by means of wide beam x-ray diffraction about the (004) and $(\bar{2}\bar{2}4)$ reflections. PMMA photo-resist has been spin-coated on

the SiGe layer, and then exposed to the electron beam of a Converted Scanning Electron Microscope (SEM) along the designed pattern of large squares and small nano-ridges. A post-exposure bake at 105 °C is performed before the development of the PMMA removing the soluble exposed part of the resist. A reactive ion etching (RIE) has been finally performed to define the patterned structures.

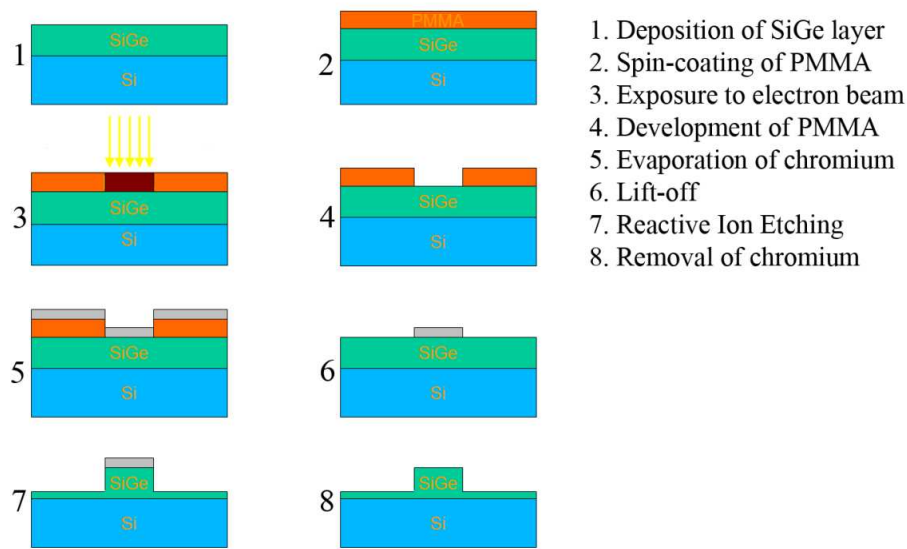


FIG. 5.1. Schematic representation resuming the main steps of the nano-lithographic process for the top-down formation of SiGe nano-structures on Si(001).

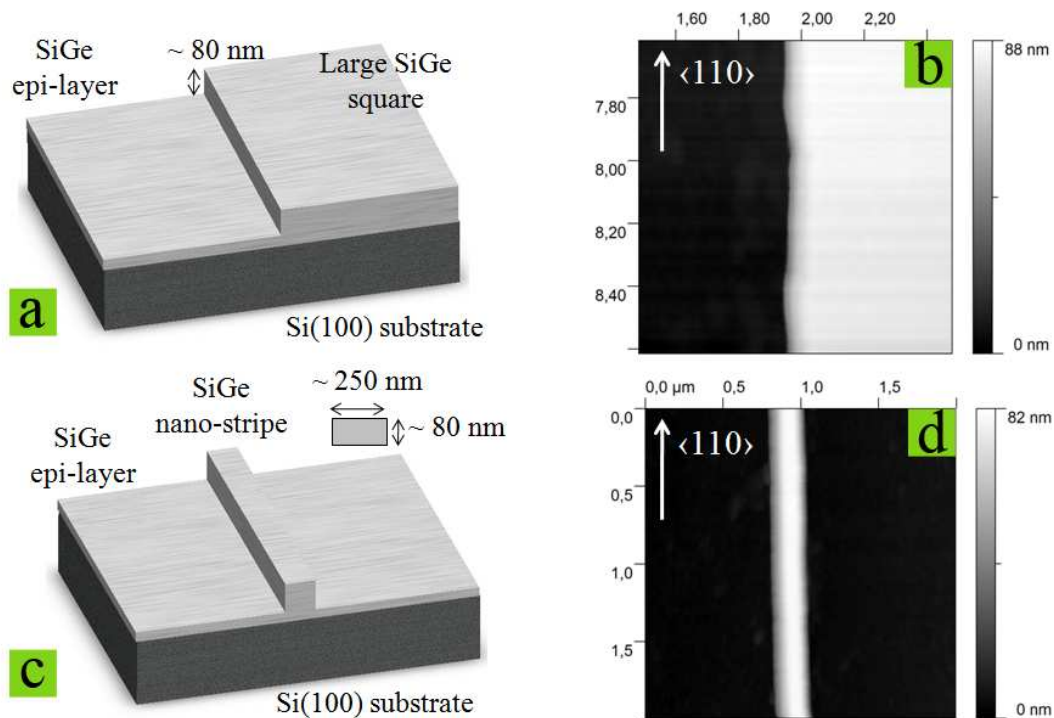


FIG. 5.2. Sketches (panels (a) and (c)) and atomic force microscopy images (panels (b) and (d)) of the step edge of a large square (panels (a) and (b)) and of a single nano-ridge (panels (c) and (d)) as obtained by electron beam lithography. The edges of the structures are aligned along $\langle 110 \rangle$ directions.

Fig. 5.1 resumes the main steps of the nano-lithographic process. The $\text{Si}_{1-x}\text{Ge}_x$ layer has not been completely etched away leaving a layer with thickness of about 40 nm, so that the strain outside the nanostructures could also be characterized from the same $\text{Si}_{1-x}\text{Ge}_x$ Bragg peak. Atomic force microscopy (AFM) images of the step edge of a large square and a single nano-ridge are shown in Fig. 5.2. The edges of the structures were aligned along $\langle 110 \rangle$ directions, which are the directions of highest hole mobility in the case of uniaxial strain in Si.

5.2.2 Diffraction experiment

The nano-diffraction experiment took place at the Nanofocus extension of the ID13 beamline at the ESRF in Grenoble. The basic principles of the XRD technique can be found in the Panel G. The wavelength of the incoming x-rays was set at 0.08130 nm, corresponding to an energy of 15.25 keV with $\Delta E/E=10^{-4}$. A spot size of ~ 100 nm was obtained using compound refractive x-ray lenses^{10,11,12} along with a flux of 10^8 photons/s. We present here diffraction measurements taken about the (004) Bragg peak, a symmetric reflection geometry (schematically shown in Fig. 5.3(a)) giving information about the lattice constant a_{\perp} perpendicular to the (001) sample surface since the scattering wave-vector q lies along the [001] direction. In the (004) geometry at this wavelength the scattering angle is $2\theta = 34.84^\circ$ for Si ($a_{\text{Si}} = 0.54310$ nm) and the incidence angle is $\omega = (2\theta)/2 = 17.42^\circ$.

In Fig. 5.3(b)-(d)-(e) is schematically reported the experimental setup: the x-ray beam is focused in two directions to a spot size of 100 nm using a final Kirkpatrick-Baez stage. A guard aperture protects the sample from the stray radiation. The horizontal focusing lens is fixed to the setup and can be aligned using the same hexapod table hosting the final experimental stage. The vertical focusing lens is then adjusted using a piezo-motor driven (picomotor) stage. The sample is mounted on a highly precise piezo stage (nanocube) and can be scanned through the beam. The scattered beam is collected by a two-dimensional (2D) detector made of a 256×256 pixels CCD “Maxipix” camera with an element size of $1.41 \text{ cm} \times 1.41 \text{ cm}$. During the (004) measurements the detector was 1.08 m from the sample as measured by hand and checked by means of the vertical alignment of the (001) truncation rod in the reciprocal space map (RSM). Simultaneously to the diffraction experiment a SiLi-detector records the fluorescence light emitted from the sample. A pre-aligned optical microscope is used for a coarse alignment of the beam on the sample surface on a micrometer scale, while the fluorescence detection is very useful for a fine adjustment of the sample position in case of nanosized structures.

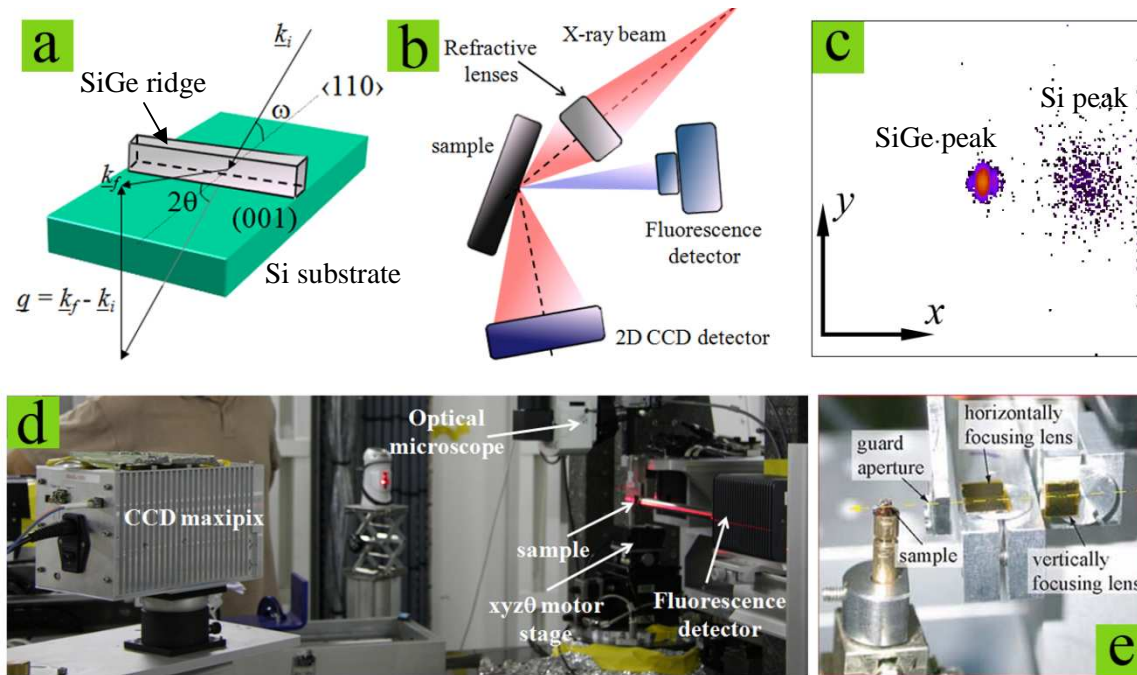


FIG. 5.3. Panel (a): schematic representation of the symmetric (004) reflection geometry; k_i , k_f and q are the incoming, the outgoing, and the scattered wave-vectors, respectively. The scattering angle is $2\theta = 34.84^\circ$ for Si ($a_{\text{Si}} = 0.54310$ nm) and the incidence angle is $\omega = (2\theta)/2 = 17.42^\circ$. Panel (b): schematic representation of the experimental layout. Panel (c): 2D CCD image acquired at a given ω from the Maxipix detector. Panel (d): large view picture of the experimental setup in the experimental hall of the ID13 beamline. Panel (e): close up picture of the horizontal and vertical x-ray focusing lens system.

The experiment was performed by scanning the x-ray beam across the lithographically defined structures. The line scans were constituted of 50–60 points spaced approximately 70 nm apart. This line scan was repeated for 25 ω values corresponding to the rocking curves around the $\text{Si}_{1-x}\text{Ge}_x$ (004) reflection in order to construct a Reciprocal Space Map (RSM) at each spatial point. We scanned across the step edge of a large (>100 μm) square, and across a small (~ 250 nm) ridge in order to evaluate the degree of elastic relaxation induced by nano-patterning of 2D and 1D structures. The Ge $K\alpha$ fluorescence signal was monitored during each scan, in order to track any drift of the x-ray spot relative to the nanostructures as ω was changed. The obtained diffraction patterns were then compared to kinematical simulations¹³ performed on strain maps obtained by 2D finite element modeling of the nanostructures^{14, 15}.

5.2.3 Construction of the reciprocal space maps

The 2D CCD image acquired at a given ω from the Maxipix detector (see Fig. 5.3(c) for an example) does not correspond to a section of the [001]-[1-10] plane of the reciprocal space we are interested in. Indeed, different pixels along the x -axis of the detector correspond to different scattering angles 2θ , relative to the position of the Si peak, according to the relation:

$$2\theta = (p_x - p_x(\text{Si})) \frac{w}{NL} \quad (5.1)$$

where p_x is the index of the pixel in the x direction and $p_x(\text{Si})$ is the pixel at which the Si reflection appears, $N = 256$ is the number of pixels, $L = 1.08$ m is the distance between sample and detector, and $w = 0.0141$ m is the width of the detector. In the CCD image of Fig. 5.3(c) only the line passing horizontally through the Si peak lies in the $[001]$ - $[1\bar{1}0]$ plane, while pixels displaced in the y direction away (above and below) from this line correspond to non-coplanar diffraction. To reconstruct the portion of the $[001]$ - $[1\bar{1}0]$ plane in the reciprocal space, the first step in the data processing was therefore to convert the 2D CCD image into a 1D line by summing the scattered signal at each x over all y . Then ω and $\theta = (2\theta)/2$ values were transformed into components of the scattering vector \vec{q} by (see Section G.3 in the Panel G):

$$\begin{aligned} q_{\perp} &= \frac{2}{\lambda} \sin \theta \cos(\omega - \theta) \\ q_{\parallel} &= \frac{2}{\lambda} \sin \theta \sin(\omega - \theta) \end{aligned} \quad (5.2)$$

By repeating this procedure as ω is changed during the “rocking” of the sample a 2D RSM is built up (see Fig. 5.4). It is worth noting that for the measurements of the Si peak we significantly reduced the intensity of the incoming x-ray beam of a factor $\sim 10^2$ (by detuning the beamline undulator) in order that the strong signal coming from the Si bulk reflection did not overwhelm the dynamic range of the CCD; otherwise, measurements of the SiGe peak were restricted to Bragg angles which did not excite the Si reflection and we used full intensity of the incoming x-ray beam. A complete reciprocal space map (RSM) is thus built up from two separate rocking curves, one acquired around the Si bulk reflection with a reduced intensity of the x-ray beam, and the other acquired around the SiGe peak with full intensity.

The RSM about the (004) reflection on a large unetched region, built up from separate scans over Si and $\text{Si}_{1-x}\text{Ge}_x$ peaks, is shown in Figure 5.4. In the symmetric (004) geometry, information on the perpendicular lattice constant a_{\perp} only is available; the $\text{Si}_{1-x}\text{Ge}_x$ peak is found at $q_{\perp} = 7.3117 \pm 0.001 \text{ nm}^{-1}$, so that $a_{\perp} = 4/q_{\perp} = 0.5471 \pm 0.0001 \text{ nm}$; the measured value of the perpendicular lattice parameter corresponds to a fully biaxially-strained $\text{Si}_{1-x}\text{Ge}_x$ thin film with $x = 0.1105 \pm 0.0001$ (while in the case of fully relaxed alloy with $x = 0.1105$ the SiGe peak would be found at $q_{\perp} = 7.3348 \text{ nm}^{-1}$). The fringes in the q_{\perp} direction indicate a sharp $\text{Si}_{1-x}\text{Ge}_x/\text{Si}$ interface, and the spacing of the minima of $\Delta q_{\perp} = 0.0083 \text{ nm}^{-1}$ corresponds to the layer thickness of $h = 1/\Delta q_{\perp} = 120 \text{ nm}$. The $\alpha \sim 1$ mrad divergence of the beam causes the RSM peaks to be elongated by $\alpha/\lambda \sim 0.01 \text{ nm}^{-1}$ along a direction which makes an angle ω with the q_{\perp} axis.

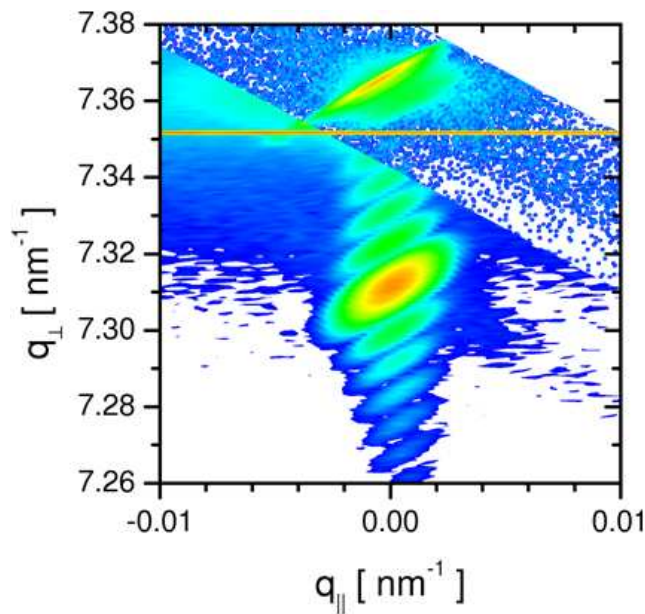


FIG. 5.4. Reciprocal space map (RSM), taken in an unetched region, combining separate scans over the (004) reflections of the Si and $\text{Si}_{1-x}\text{Ge}_x$ peaks. The Si peak is at $q_{\perp} = 4/a_{\text{Si}} = 7.3651 \text{ nm}^{-1}$ (and $q_{\parallel} = 0 \text{ nm}^{-1}$) with the $\text{Si}_{1-x}\text{Ge}_x$ peak below; the fringes above and below the peak indicate that the $\text{Si}_{1-x}\text{Ge}_x/\text{Si}$ interface is abrupt, and the fringe spacing $\Delta q_{\perp} = 1/h$ where the $\text{Si}_{1-x}\text{Ge}_x$ layer thickness $h=120\pm 1 \text{ nm}$. Diagonal elongation of each peak is related to the $\alpha \sim 1 \text{ mrad}$ beam divergence as explained in the text.

5.3 Strain relaxation at a step edge of a large square

In this section we present the results obtained from the scans across the step edge of a large square, used as test structure to verify the sensitivity of the measurements. In this case the incident and scattered x-ray beams were in the $[1\bar{1}0]$ plane corresponding to the (nominal) sidewall of the step, as shown in Figs. 5.5(a), 5.5(b), and 5.5(c), so that the spatial resolution in position across the step is given by the $\sim 100 \text{ nm}$ width of the beam. Fig 5.5(d) shows the measured RSM when the beam impinges on the etched region several microns away from the step, while Fig. 5.5(g) represents the intensity profile as a function of q_{\perp} at $q_{\parallel} = 0 \text{ nm}^{-1}$ across the SiGe peak. This profile has a sinc^2 -like form superimposed on the Lorentzian background from the Si peak and is centered at $q_{\perp} = 7.3115 \pm 0.001 \text{ nm}^{-1}$ corresponding to fully strained $\text{Si}_{0.8895}\text{Ge}_{0.1105}$ alloy.

Fig. 5.5(e) shows the RSM when the beam crosses the step edge of the large square. The significant emission at q_{\parallel} values far from 0 nm^{-1} is possibly due to a bending of $\sim 0.0235^\circ$ of the lattice planes at the sidewall of the step with respect to the (001) plane, responsible for a partial elastic strain relief as also revealed by the shift of the peak maximum toward higher q_{\perp} values (see Fig. 5.5(h)). Fig. 5.5(f) and 5.5(i) show the RSM measured on the unetched 120 nm thick layer far away from the step edge and the SiGe intensity profile as a function of q_{\perp} at $q_{\parallel} = 0 \text{ nm}^{-1}$, respectively. The narrowing of the sinc^2 -like profile of Fig. 5.5(i) as compared to the case of the etched layer (Fig. 5.5(g)), and the reduced spacing between the minima of contiguous fringes along the q_{\perp} direction are due to the increased thickness of the SiGe layer. The profile is centered at $q_{\perp} =$

$7.3115 \pm 0.001 \text{ nm}^{-1}$ corresponding to a fully strained alloy. These results are consistent with the following scenario: moving from the etched layer to the unetched region we observe a continuous transition from a compressive fully strained thin layer, to a partially relaxed step edge region, to a newly fully strained thick layer. Therefore, since the fully strained condition is experimentally evidenced for both the etched thin region and the unetched thicker layer far away from the step, the strain relaxation occurring at the step edge is believed to be elastic without the appearance of dislocations or defects.

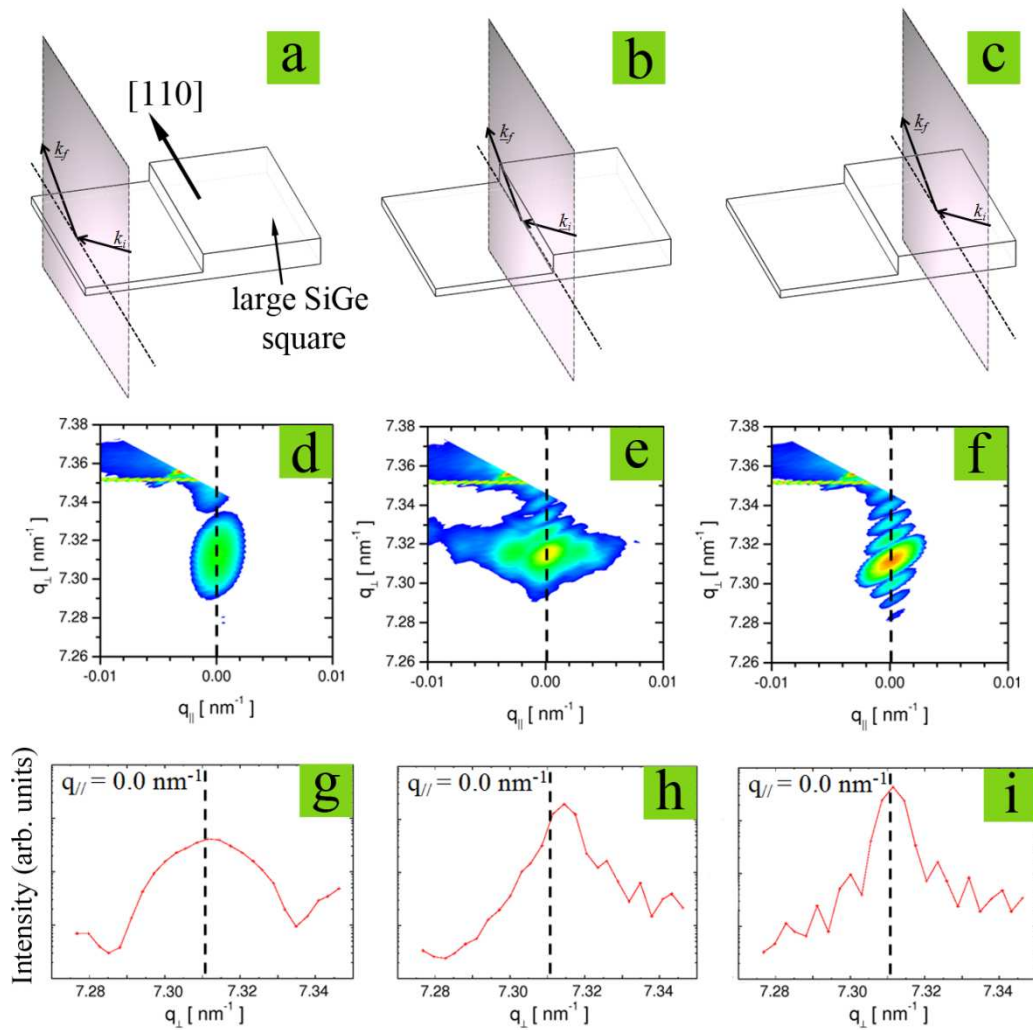


FIG. 5.5. Panel (a)-(b)-(c): schematic representation of the diffraction geometry when the beam impinges on the etched region (a), at the sidewall of the step (b), and on the unetched 120 nm thick layer (c). Panel (d)-(e)-(f): reciprocal space maps (RSMs) measured on the positions indicated in (a), (b) and (c), respectively. Panel (g)-(h)-(i): intensity profiles as a function of q_{\perp} at $q_{\parallel} = 0.0 \text{ nm}^{-1}$ across the SiGe peak measured on the positions indicated in (a), (b) and (c), respectively.

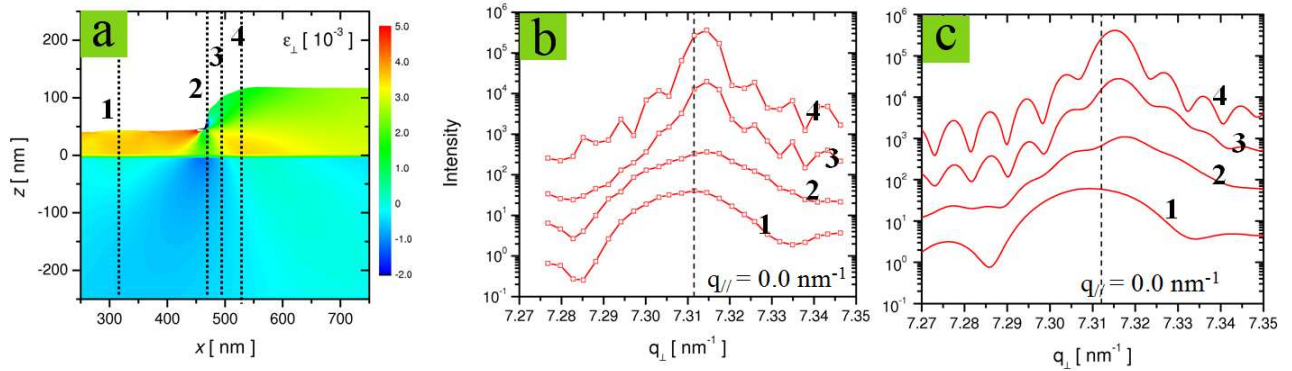


FIG. 5.6. Panel (a): Perpendicular strain ε_{\perp} (along the [001] direction) calculated by means of OpenFOAM package using the profile extracted by the AFM image of Fig. 2(b). The vertical dotted lines indicate the positions of the diffraction profiles shown in (b) and (c). Panel (b)-(c): experimentally measured (b) and 1D kinematical simulations (c) intensity profiles of the SiGe peak as a function of q_{\perp} for $q_{//} = 0 \text{ nm}^{-1}$ as the beam crosses the step structure in the positions shown in (a). Each trace has been offset by a factor of 10 in intensity for clarity. The dotted line is the position of the peak when the beam is several microns away from the step (on the unetched region) and corresponds to fully-strained material. The lowest trace corresponds to the beam impinging almost completely on the etched region; the next trace is just before the beam crosses the step. The highest trace corresponds to the beam impinging completely beyond the step. The latter has a narrower sinc²-like peak shape corresponding to the thick unetched material, and exhibits a displacement of the peak maximum toward higher q_{\perp} values, indicating elastic strain relief at the edge of the step.

To probe carefully the strain relaxation close and at the sidewall of the step, we monitored the RSMs around the SiGe peak at different position across its edge. In Fig. 5.6 the experimental intensity profiles as a function of q_{\perp} for $q_{//} = 0 \text{ nm}^{-1}$ are shown along with the results of 1D kinematical simulations performed on the strain data obtained from Finite Element Modeling (FEM) using OpenFOAM open source package¹⁶. In FEM calculations isotropic lattice constants were assumed, and the Ge content of the SiGe layer was taken into account as a mismatch $f = \Delta a/a_{\text{Si}} = 4.111 \times 10^{-3}$ in the $\text{Si}_{0.8895}\text{Ge}_{0.1105}$ layer with respect to the Si substrate. Simulations and measurements agree qualitatively and quantitatively, showing that strain relaxation is present close to the edge of the step. The only exception is the disagreement for the fringes structure at low q_{\perp} side between the measured and the calculated profiles in the position 3 of Fig. 5.6.

In the etched region close to the step (position 1 of Fig. 5.6(b)), the diffraction peak from the $\text{Si}_{1-x}\text{Ge}_x$ region is broad (since the $\text{Si}_{1-x}\text{Ge}_x$ layer is thin, $h \sim 40 \text{ nm}$) and is displaced towards smaller q_{\perp} values as compared to its position far from the edge (see Fig. 5(g)). This displacement suggests larger a_{\perp} and therefore positive ε_{\perp} . Since the perpendicular, a_{\perp} , and parallel, $a_{//}$, lattice parameters exhibit an inverse correlation due to the Poisson effect, a larger a_{\perp} would correspond to a smaller $a_{//}$, and then a negative $\varepsilon_{//}$. At the edge of the step (see for instance position 4 in Fig. 5.6(b)), a stronger diffraction pattern with a clear narrow sinc² shape is visible, displaced towards larger q_{\perp} values, and then smaller a_{\perp} and larger $a_{//}$ suggesting smaller ε_{\perp} and $\varepsilon_{//}$. To be more

quantitative, the measured relaxation of the perpendicular strain ε_{\perp} , calculated as the ratio between the values of ε_{\perp} measured at the step edge and on the thick layer, is estimated to be around 12 %.

The strain relaxation of $\varepsilon_{//}$ in the $[1\bar{1}0]$ direction perpendicular to the step edge, coupled to the boundary condition which maintains $\varepsilon_{//}$ constant in the $[110]$ direction along the step edge, leads to a preferential uniaxial compression along it. The close agreement between the kinematic simulations of Fig. 5.6(c) with the experimental results of Fig. 5.6(b) is a clear indication that the finite element model in Figure 5.6(a) would accurately describe the strain state of the structure, and that elastic relaxation is evident on a scale of hundreds of nanometers from the edge.

5.4 Strain relaxation of a single nano-ridge

In this section we present the results obtained from the scans across a single nano-ridge, which represents a prototypical structure for the investigation of the strain state when approaching lateral width of about several tens of nanometers. In this case, because of the experimental geometry and of the alignment of the nanostructures with respect to the scattering plane, the incident and scattered x-ray beams were perpendicular to the ridge, as shown in Figure 5.7(a), 5.7(b) and 5.7(c). This represents a strong limiting factor of the measurements in terms of spatial resolution and sensitivity. In fact it means firstly that the spot size across the ridge was increased by a factor of $1/\sin(\omega) \sim 3.3$ with respect to the beam width, and secondly that signals from the ridge are mixed with signals from the etched region next to the ridge. The Ge $K\alpha$ fluorescence signal (see Fig. 5.8) was monitored during each scan, so that the position of the ridge with respect to the x-ray spot could be verified as ω was varied.

Fig. 5.7 shows the measured RSMs and the correspondent intensity profiles as a function of q_{\perp} at $q_{//} = 0 \text{ nm}^{-1}$ and $q_{//} = 0.0045 \text{ nm}^{-1}$ across the SiGe peak when the beam impinges on a single nano-ridge (Fig. 7(e)-(h)) and on the thin etched regions besides it (Fig. 5.7(d)-(g) and Fig. 5.7(f)-(i)). As the spot passes over the ridge, fringes appear at $|q_{//}| = 0.0045 \text{ nm}^{-1}$ on either side of the main $q_{//} = 0 \text{ nm}^{-1}$ $\text{Si}_{1-x}\text{Ge}_x$ peak, due to the narrow lateral extent of the ridge ($\sim 250 \text{ nm}$). These fringes are centered at $q_{\perp} = 7.3145 \pm 0.004 \text{ nm}^{-1}$, shifted by $0.0030 \pm 0.005 \text{ nm}^{-1}$ with respect to the main $q_{//} = 0 \text{ nm}^{-1}$ peak from the etched layer (centered at $q_{\perp} = 7.3115 \pm 0.001 \text{ nm}^{-1}$).

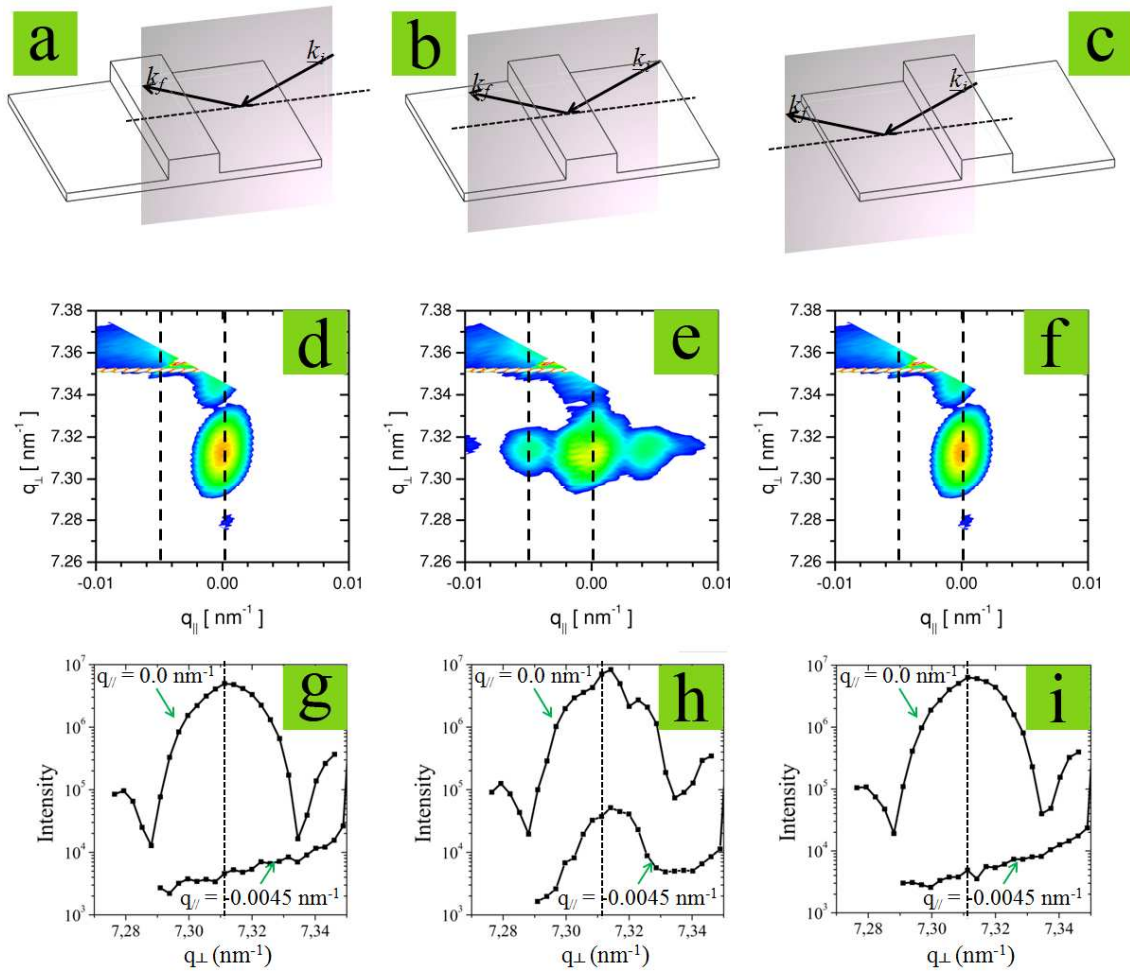


FIG. 5.7. Panel (a)-(b)-(c): schematic representation of the diffraction geometry when the beam impinges on a single nano-ridge (b) and on the thin etched region besides it (a)-(c). Panel (d)-(e)-(f): reciprocal space maps (RSMs) measured on the positions indicated in (a), (b) and (c), respectively. Panel (g)-(h)-(i): intensity profiles as a function of q_{\perp} at $q_{\parallel} = 0 \text{ nm}^{-1}$ and $q_{\parallel} = 0.0045 \text{ nm}^{-1}$ across the SiGe peak measured on the positions indicated in (a), (b) and (c), respectively.

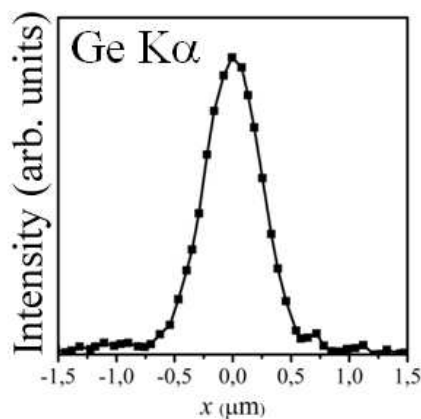


FIG. 5.8. Ge $K\alpha$ fluorescence signal, at 11 keV, as monitored during the scan over the ridge in the (004) geometry. Data from scans at all ω have been averaged, following the correction of the position shift related to the change in ω .

To probe carefully the strain state close to the ridge, we monitored the RSMs around the SiGe peak at different position across it. In Fig. 5.9 the experimental intensity profiles as a function of q_{\perp} for $q_{//} = 0 \text{ nm}^{-1}$ are shown along with the profiles extracted from 2D kinematical simulations. In the following we discuss first the physical information coming from the experimental data and then we compare them with the results of the simulations.

In a *gedanken* experiment where the beam spot size would be much smaller than the dimension of the ridge, the diffraction profile measured on the center of the ridge would be narrower than the profile measured on the etched layer, due to the reduced thickness in the latter case. In our case, the experimental diffraction profile at $q_{//} \sim 0 \text{ nm}^{-1}$ coming from the ridge is not a significantly narrower peak compared to the signal on the thin etched regions (see Fig. 5.9(b)). This indicates that most of the signal still comes from the etched region besides the ridge, which gives the most contribution to the diffraction signal. However, new rapidly varying features (see positions 2 and 3 of Fig 5.9(b)) appear within the profile measured on the ridge shifting the peak maximum and the minima in the regions of $q_{\perp} = 7.29$ and 7.34 nm^{-1} toward larger q_{\perp} values by 0.004 nm^{-1} with respect to the main $q_{//} = 0 \text{ nm}^{-1}$ peak from the etched layer approximately matching also the shift of the lateral fringes at $|q_{//}| = 0.0045 \text{ nm}^{-1}$. The intensity profile measured on the nano-ridge can be thus interpreted as a coherent superposition of the signals coming from etched layer and from the material in the ridge. From the shift of the peak maximum $\Delta q_{\perp} = 0.004 \text{ nm}^{-1}$, we estimate an experimental average perpendicular strain $\varepsilon_{\perp}^{ave-exp} \sim 2.5 \times 10^{-3}$, suggesting an average strain relaxation of about 12 %.

Parallel and perpendicular strain maps within the ridge have been calculated by Finite Element Modeling (FEM) using OpenFOAM package. As in the case of the step structure, isotropic lattice constants were assumed, and the Ge content of the SiGe layer was taken into account as a mismatch $f = \Delta a/a_{\text{Si}} = 4.111 \times 10^{-3}$ in the $\text{Si}_{0.8895}\text{Ge}_{0.1105}$ layer with respect to the Si substrate. For the FEM calculations an elliptical cross-section profile of the nano-ridge has been considered as derived from AFM imaging. In Fig. 5.9(a) is shown the perpendicular strain map obtained from the FEM calculations, which predicts a variation of the in-plane strain along the $[1\bar{1}0]$ direction from compressive ($\varepsilon_{//} = -3.3 \times 10^{-3}$) at the bottom to tensile ($\varepsilon_{//} = +7 \times 10^{-4}$) towards the top of the ridge (while the boundary conditions of the 2D finite element model mean that full compressive strain is maintained in the direction along the nanostructure perpendicular to the simulation plane). The perpendicular strain (along the $[001]$ direction) ε_{\perp} is predicted to evolve from $+3.4 \times 10^{-3}$ at the bottom to 1.3×10^{-3} at the top of the ridge with an average value of $\varepsilon_{\perp}^{ave-calc} \sim 2.3 \times 10^{-3}$, which is in good agreement with the experimentally measured value ($\sim 2.5 \times 10^{-3}$).

Kinematical simulations have been then performed on strain data obtained from FEM calculations using the elliptical cross-section profile of the ridge, and taken into account also the increased beam spot size with respect to the real beam width. The simulations, agree qualitatively and quantitatively with the experimental diffraction profiles (see Fig. 5.9(b) and 5.9(c)), showing that (i) the intensity profile obtained on the nano-ridge is actually a coherent superposition of the signals coming from etched layer and from the material in the ridge, and (ii) a strain relaxation is present within the ridge. The close agreement between the kinematical simulations of Fig. 5.9(c) with the experimental profiles of Fig. 5.9(b) suggests that the strain model developed for the ridge using FEM calculations, which predict a preferential uniaxial compression along its axis, is a realistic representation of the strain state of the ridge within the sensitivity limits of the measurements.

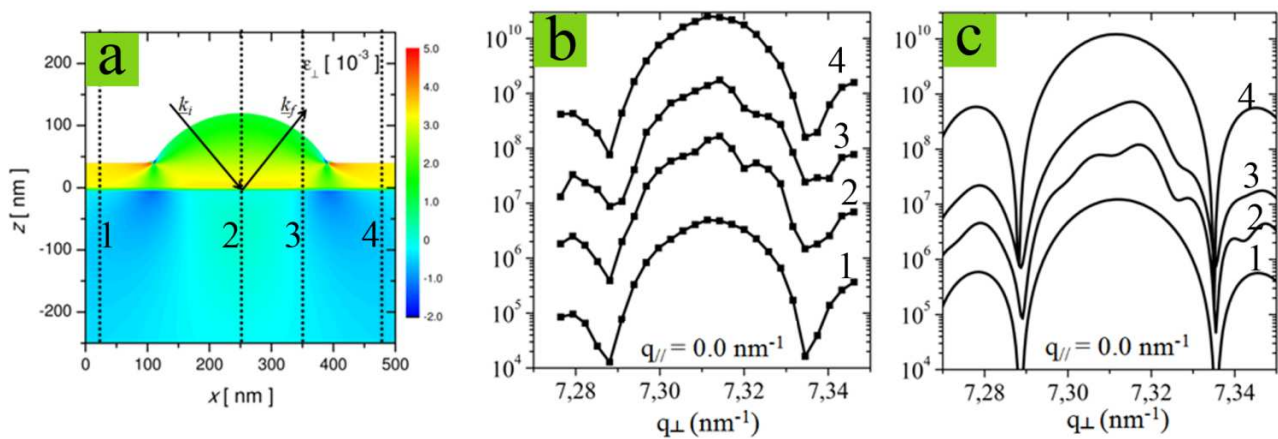


FIG. 5.9. Panel (a): Perpendicular strain ε_{\perp} (along the [001] direction) calculated by means of OpenFOAM package using an elliptical profile as derived by the AFM image of Fig. 2(d). The vertical dotted lines indicate the positions of the measured diffraction profiles shown in (b). Panel (b)-(c): experimentally measured (b) and 2D kinematical simulations (c) intensity profiles of the SiGe peak as a function of q_{\perp} for $q_{\parallel} = 0 \text{ nm}^{-1}$ as the beam crosses the ridge in the positions shown in (a). Each trace has been offset by a factor of 10 in intensity for clarity. The lowest and the highest traces correspond to the beam impinging completely on the etched regions besides the ridge. The trace at the position 2 corresponds to the beam impinging completely on the ridge. The most of the signal still comes from the etched region, however, the rapidly varying features appearing within this profile are related to the nano-structures. The peak maximum and the minima in the regions of $q_{\perp} = 7.29$ and 7.34 nm^{-1} shift toward larger q_{\perp} values by 0.004 nm^{-1} , indicating elastic strain relief of the ridge.

5.5 Conclusions

In this chapter we presented the first results of a X-Ray Diffraction study aimed to the strain state characterization on a nanometer scale of lithographically defined SiGe structures: the step edge of a large square and a single small nano-ridge. The latter represents the prototypical structure for the investigation of the strain state when approaching lateral width of about several tens of nanometers, while the former has been used as test structure to verify the sensitivity of the measurements. We have described the sample preparation procedure, the experimental setup, the diffraction geometry and the post-acquisition data elaboration methods. The experimental results clearly indicate an elastic strain relaxation on a sub-micron scale, in broad agreement with kinematical simulations performed on strain data obtained from Finite Element Modeling calculations. For ~ 250 nm wide ridge the close agreement between experimental data and simulations suggests that the strain model developed using FEM calculations, which predict a preferential uniaxial compression along its axis, is a realistic representation of its strain state. These results are of interest to the sub-micron scaling of strained Si and SiGe devices and to the physics of electronic transport in such devices, as well as demonstrating the capabilities of the relatively new technique of x-ray nano-diffraction.

Bibliography

-
- ¹ T. Irisawa et al., IEEE Transactions on electron devices **55**, 649 (2008)
 - ² M. L. Lee et al., J. Appl. Phys. **97**, 011101 (2005).
 - ³ B. Rössner, D. Chrastina, G. Isella, and H. von Känel, Appl. Phys. Lett. **84**, 3058 (2004).
 - ⁴ S. Thompson et al., IEEE Transactions **53**, 1010 (2006).
 - ⁵ T. U. Schüllli et al., Phys. Rev. Lett. **90**, 066105 (2003); T.U. Schüllli et al., Phys. Rev. Lett. **102**, 025502 (2009)
 - ⁶ C. Mocuta et al., Phys. Rev. B **77**, 245425 (2008)
 - ⁷ K. Usuda, T. Numata, T. Irisawa, N. Hirashita, and S. Takagi, Mater. Sci. Eng. B **124–125**, 143 (2005)
 - ⁸ M. Hanke et al., Appl. Phys. Lett. **92**, 193109 (2008); C. Riekkel, private communication
 - ⁹ G. Isella, D. Chrastina, B. Rössner, T. Hackbarth, H-J. Herzog, U. König, H. von Känel, Solid-State Electronic **48**, 1317-1323 (2004)

-
- ¹⁰ Schroer, C. G.; Lengeler, B. *Phys. Rev. Lett.* **94**, 054802 (2005).
- ¹¹ Boye, P.; Feldkamp, J. M.; Patommel, J.; Schwab, A.; Stephan, S.; Hoppe, R.; Schroer, C. G.; Burghammer, M.; Riekkel, C.; van der Hart, A.; Kuchler, M. *J. Phys. Conf. Ser.* **186**, 012063 (2009).
- ¹² Schropp, A. et al. *Appl. Phys. Lett.* **96**, 091102 (2010).
- ¹³ Grundmann, M.; Krost, A. *phys. stat. sol. (b)* **218**, 417–423 (2000).
- ¹⁴ Jasak, H.; Weller, H. G. *Int. J. Num. Meth. Eng.* **48**, 267–287 (2000).
- ¹⁵ Grönqvist, J.; Sondergaard, N.; Boxberg, F.; Guhr, T.; Åberg, S.; Xu, H. Q. *J. Appl. Phys.* **106**, 053508 (2009).
- ¹⁶ <http://www.openfoam.com/>

Conclusions

The relationship and the interplay among morphology, elemental composition, strain state and electronic structure of self-assembled and lithographically defined SiGe nanostructures have been experimentally investigated by means of several spectro-microscopy techniques. The research project, which took advantage from a joint effort of several experimental groups, aimed at a better understanding of several key factors that are still not fully understood for the development of emerging processes based on SiGe nanostructures, including the kinetics and thermodynamics of formation, the interplay between the strain relaxation mechanisms and the SiGe intermixing, and the control of the strain state and of the strain-induced modification of the electronic band structure when approaching to the nanometer length scale.

The initial part of the thesis dealt with the investigation of the surface diffusion dynamics of Ge on both C-free and C-covered Si(001) surface promoted by annealing at high temperatures in UHV of Ge stripes by means of *in-situ* Scanning Auger Microscopy. The temperature dependence of the Ge diffusion coefficient on a microscopic scale has been directly measured in case of a C-free Si surface and the results interpreted within a one-dimensional diffusion model. The Ge diffusion coefficient at 600 °C has been monitored as a function of the carbon coverage, exploiting a continuous spatial modulation obtained by ion sputtering a homogeneous carbon layer during an increasing time. The increase of the carbon coverage from 0.1 ML to 1 ML corresponded to a decrease of the diffusion coefficient from $\sim 3 \cdot 10^{-9} \text{ cm}^2/\text{s}$ to $\sim 3 \cdot 10^{-13} \text{ cm}^2/\text{s}$. This huge dependence has been discussed within a physical scenario where carbon is incorporated within the shallow volume of the Si substrate inducing increased surface roughness and a compressive local strain field. These two phenomena, together with the chemical interactions among Si, C and Ge, are the main factors influencing the diffusion modulation. This has been described through a linear dependence of the diffusion activation energy on the C coverage which correctly reproduced the experimental data.

The heart of the thesis is oriented to the study of the spontaneous nucleation of SiGe islands coexisting with the continuous surface diffusion of Ge from the source stripe.

Joining SAM and AFM analysis the critical overlayer thickness for nucleation has been measured, showing that island growth mode gradually evolves from Stranski-Krastanow (SK) in case of absence of surfactant to Volmer-Weber (VW) for high surfactant coverage. This observation supports the possibility of engineering the self-assembly of SiGe islands by a controlled C deposition. A semi-quantitative estimation of the C incorporation inside the Si substrate is then

deduced from the critical thickness. The carbon concentration inside the topmost Si substrate layer is found to increase linearly as a function of the carbon coverage, starting from a critical threshold $\theta_0 = 0.16 \pm 0.06$ ML. Below this critical coverage no sizable effect on the diffusion of Ge or on the nucleation of SiGe islands has been found.

Then, the growth process of SiGe islands obtained by the surface thermal diffusion of Ge from a source stripe on a *C-free* Si(001) surface has been experimentally investigated and discussed in detail, with a particular emphasis on key aspects such as the formation kinetics, SiGe intermixing, strain relaxation mechanisms and island ordering.

Using extensive AFM statistical analysis we have determined the size and density behavior exhibited by islands grown at different temperatures in the range $600 \div 700$ °C as a function of the distance from the source stripe. Our results give experimental evidence that the growth process mainly evolves within a diffusion limited regime where the island density follows a universal scaling distribution depending only on the Ge coverage. Moreover, we showed that the density behaviour has been successfully reproduced using a 1D model of nucleation which considers the probability of formation of a critical nucleus only dependant on local differences in the chemical potential of the wetting layer. In this scenario the island growth can be described by the Mulheran capture zone model. The model's validity has been verified by evaluating the correlation between the island volumes and the capture zone area, mathematically defined as the area of the Voronoi cell within the Voronoi tessellation of the island network. This findings suggest that kinetics rather than energetics crucially affect the competition between the islands to gather the available mass, represented by both Ge atoms diffusing on the surface and Si atoms from the substrate, penetrating into the islands leading to the formation of alloyed nanocrystals (SiGe intermixing).

To measure the composition of single islands we performed a STEM-EELS experiment giving both the vertical and the horizontal concentration profiles. We found a vertical compositional gradient from a Si-rich bottom to a Ge-rich topmost region and highly Si-intermixed boundaries. To explore the interplay between intermixing and size evolution, we measured the composition of single islands as a function of the distance from the stripe by means of micro-Raman spectroscopy and Scanning Auger Microscopy. Looking at the average island concentration, a greater Si incorporation has been found for islands nucleated farther away from the stripe at lower Ge coverage regions. This modulation of Ge composition is believed to be the origin of the experimentally observed increase of the island volume as a function of the distance from the stripe.

Moreover, we have experimentally studied the plastic strain relaxation of nucleated self-assembled SiGe islands. The aspect ratio distributions as a function of the base width gave a statistical indication of the coherent nature of the nucleated islands. This has been confirmed by the

structural analysis performed with TEM and LAADF-STEM on single islands. We have shown that islands grown by surface thermal diffusion remain dislocation-free for base width values greater by a factor ~ 3 -3.5 and ~ 1.5 -1.8 than those obtained by MBE and CVD, respectively. An enhanced SiGe intermixing is believed to be the origin of this suppression of the plastic relaxation. In fact the growth method used intrinsically promotes higher intermixing since the Ge supply occurs on a time scale longer with respect to the Si incorporation from the substrate, and thus intermixing becomes the dominant process for the strain relaxation leading to the quenching of the plastic channel.

In order to explore device engineering for nanoelectronics applications based on self-assembled SiGe islands, some crucial parameters must be controlled. From a mesoscopic point of view, island positioning and size distribution are the most important factors that can be managed. Hence, we have investigated the growth of SiGe islands on a Si(001) surface patterned with a 2D squared array of circular pits. The ordered island growth has been obtained by controlling the local atomic mobility and the length of the diffusion pathway of Ge atoms by means of a correct choice of the growth parameters (annealing time and temperature). Moreover, controlling the diffusion dynamics of Ge from the source stripe, we were able to obtain a controlled size evolution of the orderly nucleated islands as a function of the Ge coverage. Our observations are consistent with a physical scenario where island positioning is mainly determined by energetics, which predominate with respect to the local kinetics of diffusion, and the size evolution mainly depends on the local density of Ge atoms.

The last part of the thesis addresses the characterization of the strain state and of the strain-induced band structure modifications in lithographically defined SiGe nanostructures.

First, we presented the spatial mapping of strain, composition, work function and valence band structure of SiGe *embedded* nano-stripes by means of TERS and Energy-Filtered PEEM techniques. The perpendicular strain profile across a single nano-stripe is obtained with a spatial resolution of about 30 nm. The perpendicular strain (along the [001] direction) is tensile and becomes maximum (~ 0.014) at the center of the nano-stripe while decreasing close to zero at its boundaries. 3D Finite Element Modeling (FEM) calculations are successfully compared to the experimental results. From the local work function and the valence band mapping, the strain-induced conduction (-0.49 eV) and valence band ($+0.28$ eV) offsets for the SiGe nano-stripes with respect to the Ge(001) bulk case have been determined. The calculated offsets obtained within the framework of the linear deformation-potential theory correctly reproduce the experimental values.

Finally, the first results of a *direct* characterization of the strain state in lithographically defined SiGe nano-ridges by means of nanofocused XRD are presented. The experimental results clearly indicate an average elastic relaxation of the perpendicular strain of about 12 %, in broad

agreement with kinematical simulations performed on strain data obtained from Finite Element Modeling calculations. The close agreement between experimental data and simulations suggests that the strain model developed using FEM calculations, which predict a preferential uniaxial compression along its axis, is a realistic representation of its strain state.

We think that these systematic experimental results make a real contribution to a better understanding of the factors influencing the surface diffusion of Ge, the self-organization of SiGe islands, and strain relaxation mechanisms when approaching to the nanometer length scale. Moreover, we hope that they will act as a motivation for further experimental and theoretical work.

Panel A

Scanning Auger Microscopy

A.1 Introduction

Most physics-based techniques can be classified as scattering experiments: a particle is incident on the sample, and another particle is detected after the interaction with the sample. Surface sensitive techniques are no exception; we have an incident electron probe, with a well-defined energy, and the response particle in our case is another electron. If we understand the nature of the scattering process, then we can interpret the experiment and deduce corresponding characteristics of the sample. Here we concentrate on the imaging and spectroscopic capabilities of the Scanning Auger Microscopy (SAM) technique, which can be considered as the child of the Scanning Electron Microscopy (SEM) and the Auger Electron Spectroscopy (AES). The panel is organized as follows. First we introduce the basic principles behind the SEM technique and we discuss the physical aspects of the Auger process. Then the characteristic and performances of the elements constituting the illumination and detection stages of the PHI 660 SAM microscope used in this thesis work are presented. Finally the problem of the quantification of the Auger spectra is addressed.

A.2 Scanning electron microscopy (SEM)¹

The basic principle of SEM technique consists in scanning a focused electron beam (primary energy typically 2 – 25 keV) over the surface under study and simultaneously detecting electrons emitted from the surface. The *electron-electron* scattering involving primary electrons and bounded electrons within the sample causes the generation of *secondary electrons*, which propagate into the sample and possibly generate further ionizations and excitations. The intensity of this emitted signal determines the brightness of the spot on a TV tube. The formation of a topographical image is due to local variation of the electron emissivity of the surface. In fact the emission yield of the secondary electrons is strongly dependent on the topography of the sample surface. However, although to a minor extent, the secondary electron yield depends also on the ionization cross-section of the primary electrons, on the atomic number and on the work function of the sample. The operation of a SEM is schematically described in Fig. A.1. The scanned electron beam is produced in a electron microscope column. Electrons are emitted from a heated LaB₆ cathode (or field

emission cathode) and are focused by the Wehnelt cylinder and an anode aperture in the so-called *cross-over point*. The cross-over point is projected by a first magnetic lens onto a smaller image point, which is further reduced by a second magnetic lens onto the sample surface. The best SEM column can achieve a spot size of about 10 Å. However, the spatial resolution within a SEM image depend not only by the beam spot size, but also by the aberration of the optic column and by the lateral width of the region on the sample surface from which secondary electrons are emitted.

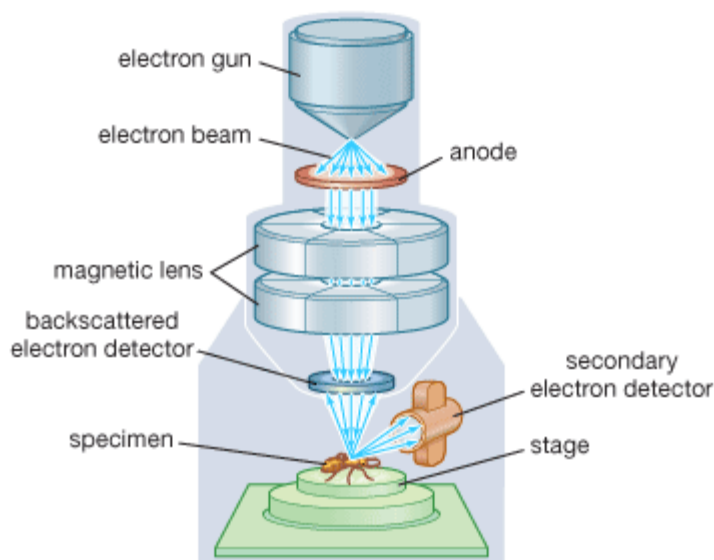


FIG. A.1. Schematic layout of a scanning electron microscope.

It is worth noting that the typical energies of the secondary electrons generating in a solid belong to the range 5 – 2000 eV. Electrons with energies in that range are strongly scattered in solids. Fig. A.2 shows a plot of the experimental values of the inelastic mean free path (IMFP) versus the electron kinetic energy. Though the data are energy and material dependent, the IMFP in the energy range 5 – 2000 eV changes from 5 to 50 Å. In this sense, scanning electron microscopy can be considered a surface sensitive technique.

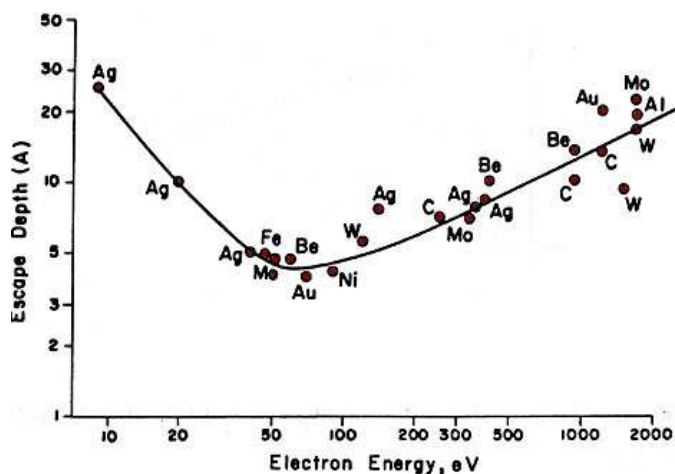


FIG. A.2. Inelastic Mean Free Path of electrons as a function of their kinetic energy collected for different materials (from Ref. 2).

A.3 Auger effect and chemical analysis¹

The principle of the Auger process is explained in Fig. A.3. The primary electron produces an initial hole by ionization of a core level (K or L shell). Both primary electron and core electron then leave the atom with an ill-defined energy; the escaping primary electron has lost its “memory” due to the complexity of the scattering process. The electronic structure of the ionized atoms rearranges such that the deep initial hole in the core level is filled by an electron originating from an energetically higher-lying shell. This transition may be accompanied by the emission of a characteristic X-Ray photon, or alternatively the deexcitation process might be a radiationless Auger transition, in which the energy gained by the electron that “fall” into the deeper atomic level is transferred to another electron of the same or a different shell. This latter electron is then emitted with a characteristic Auger energy, thereby leaving the atom in a double-ionized state [two holes in different (or the same) core levels]. The characteristic Auger energy is close to the characteristic X-Ray photon energy but, due to many-body interactions, it is not identical. In comparison to the X-ray emission process the final state of the atoms now has one more hole and is thus more highly ionized. In comparison to the X-ray emission process the final state of the atom now has one more hole and is thus more highly ionized.

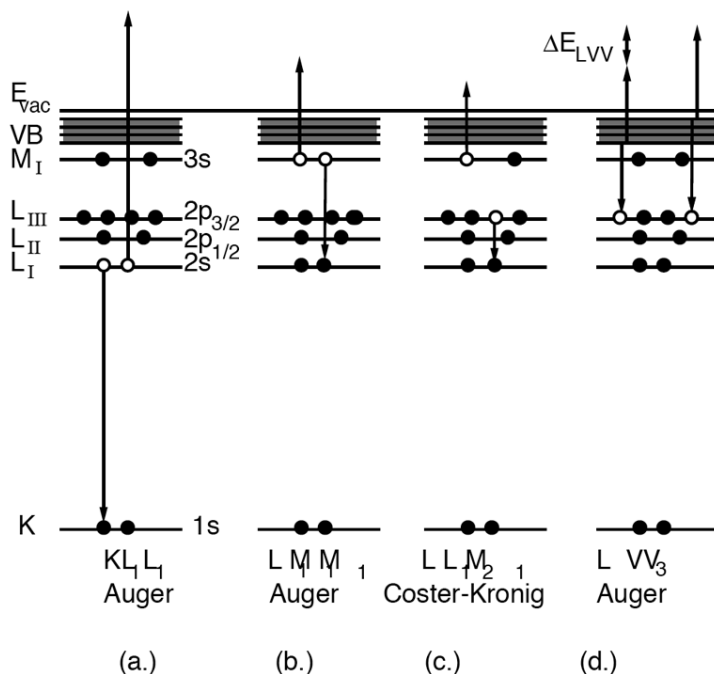


FIG. A.3 Explanation of the Auger process on the basis of atomic-level schemes in case of KLL (a), LMM (b), LLM (c) and LVV (d) transitions.

Since the emitted Auger electrons carries a well-defined kinetic energy that is directly related to the differences in core-level energies (see below), measurement of this energy can be used to identify the particular atom. Moreover, looking to the intensity of the Auger peaks a quantitative estimation of the elemental concentration within a composite sample can be also obtained with a

sensitivity of about 1% of a monolayer (see Section A.5). It is worth noting that a right quantification can be only obtained if the contribution of the elastic Auger electrons, which didn't suffer any energy loss escaping from the sample, is correctly separated from the inelastic background.

The nomenclature of the Auger transitions reflects the core level involved. When the primary hole is produced in the K shell, the Auger process is initiated by an outer electron from the L shell, e.g. the L_1 level as in Fig. A.3(a). This electron falls in the initial K vacancy giving up its transition energy to another electron from the L shell, e.g. the L_2 shell; such an Auger process is named KL_1L_2 process. Another possibility is shown in Fig. A.3(b). In this case the two final holes are both in the M_1 shell. Since the initial hole was in the L_1 shell, this transition is known as a $L_1M_1M_1$ process. If the initial hole is filled by an electron from the same shell (see Fig. A.3(c)), the process is called a *Coster-Kronig* transition (e.g. $L_1L_2M_1$). When the Auger process occurs in an atom that is bound in a solid, electronic bands may be involved in the transition, in addition to sharply defined core-levels. The process shown in Fig. A.3(d) involves the formation of a primary hole in the L_3 shell and deexcitation via an electron from the valence band (V), which transfers its transition energy to another valence electron. This process is correspondingly called L_3VV process. The strongest intensity is observed for processes in which the two final holes are produced in regions of high valence band density of states.

To illustrate the calculation of the characteristic energy of an Auger transition, we consider as an example the KL_1L_2 process of Fig. A.3(a). In a simple one-electron picture the kinetic energy of the outgoing Auger electron would be given by a difference between the corresponding core-level energies:

$$E_{KL_1L_2}^Z = E_K^Z - E_{L_1}^Z - E_{L_2}^Z \quad (\text{A. 1})$$

where Z is the atomic number of the element concerned. However the Auger process involves many-body interactions, and a further correction term is therefore used to describe the effect of the rearrangement of the other electrons in a double-ionized atom:

$$E_{KL_1L_2}^Z = E_K^Z - E_{L_1}^Z - E_{L_2}^Z - \Delta E(L_1L_2) \quad (\text{A. 2})$$

The correction term $\Delta E(L_1L_2)$ is small; it involves an increase in binding energy of the L_2 electron when L_1 electron is removed, and of the L_1 electron when an L_2 electron is removed. The detailed calculation of the correction term is, of course, difficult but there is an empirical formula, which relates the higher ionization states of the atom Z to the core-level energies of the atom with atomic number $Z+1$. The average increase in binding energy due to a missing electron in the L_1 shell is thus approximately expressed by $(E_{L_1}^{Z+1} - E_{L_1}^Z)/2$ and the correction term follows as:

$$\Delta E(L_1L_2) = \frac{1}{2}(E_{L_2}^{Z+1} - E_{L_2}^Z + E_{L_1}^{Z+1} - E_{L_1}^Z) \quad (\text{A.3})$$

The principal Auger electron energies of the elements are given versus atomic number Z in Fig. A.4. Three main branches, the KLL, LMM and the MNN processes can be distinguished. The stronger transitions are indicated by heavier points. The strong Z dependence of the binding energies and of the Auger energies is important for the application of Auger spectroscopy as a chemical technique.

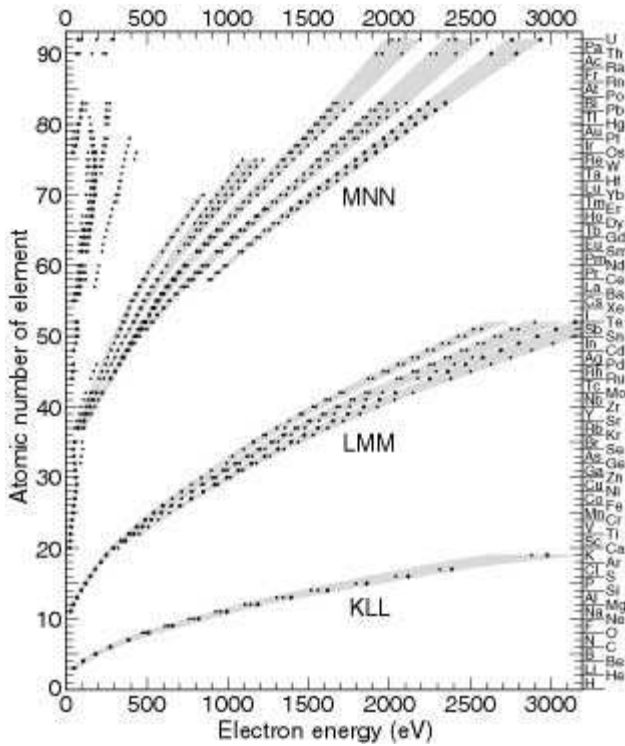


FIG. A.4. Auger electron energies as a function of atomic number Z for all the elements (with the exception of H, He).

A.4 Instrumentation

Figure A.5 shows the main components and the electron optics of the PHI 660 Scanning Auger microscope used in this thesis work. The SAM incorporates an electron-optical column, a sample stage with translational and turning movements, a detection unit for secondary, back-scattered and Auger electrons, and Ar^+ ion gun for sputtering purposes.

The electron source used in the SAM is a LaB_6 heated crystal. The electrons emitted from the source are focused by the Wehnelt cylinder and an anode aperture at the entrance of the optical system. This is made of axially-symmetric magnetic lenses and electrostatic deflectors. The first element of the optic column is the beam blanking, made of an annular electrode at which a retarding field is applied. The first lens is a condenser lens which operates a collimation of the electron beam: the lens collects the electrons arriving from the anode aperture on a wide angle and redirect them toward the optical axis. At this stage the beam is thus demagnified of a factor $\sim 1/100$, thus

requiring a very small focal length for the condenser lens. The final lens is the objective which focalizes the electron beam on the sample surface. Its design and performance (including aberrations) largely determine the spatial resolution of the instrument. Possible deviations of the electron beam from the coaxial condition are corrected using electrostatic steering plates located after the condenser and the objective lenses. Finally an electrostatic octopole, made of eight deflection plates arranged to form an octahedron, is used for the scanning of the beam on the sample surface and the corrections of the aberrations of the beam.

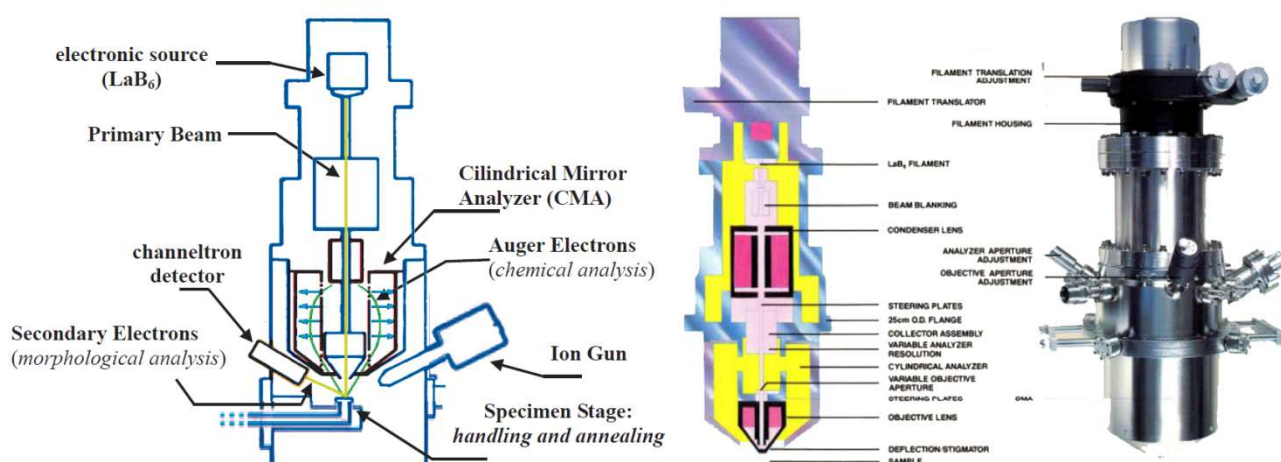


FIG. A.5. Schematic layout and electron optic column of the PHI 660 Scanning Auger Microscope used in this thesis work.

For the detection of the secondary electron signal during the scanning of the primary beam on the sample surface, a channeltron electron multiplier is used. It consists of a specially formulated lead silicate glass shaped like a cornucopia, and exhibits the properties of electrical conductivity and secondary electron emission. The input end is at ground or some positive potential while the output end (the tail) is at high positive voltage. An electron striking the input face of the channeltron produces 2-3 secondary electrons. These electrons are accelerated down the channel by the positive bias. Secondary electrons are progressively created along the channel length until at the output end a pulse of 10^7 to 10^8 electrons emerges.

The problem of measuring the electron energy spectrum is non-trivial. There are various possible geometries for the analyzers, and the measurements can be performed in an angle integrated or angle-resolved (AR) mode. The PHI 660 system uses an electrostatic angle-integrated cylindrical mirror analyzer (CMA). A CMA consists of two concentric metal cylinders arranged such that their axes are coincident. Different voltages are placed on each cylinder such that there is an electric field between the two cylinders. Electrons are injected from a point on the axis into the gap between the two cylinders. If the electrons are travelling very fast, they will impinge on the

outer cylinder. If they are travelling very slowly, they will be attracted to the inner cylinder. Hence only electrons in a narrow energy region (called the pass energy) succeed in getting all the way along the cylinders to the detector. The resolution is improved by apertures within the analyzer. The CMA operates in non-retarding mode. In this mode the electrons pass through the analyzer with their initial kinetic energy and the energy range is swept by varying the potential on the outer cylinder. The resolution is then fixed and depends on the width of the entrance and exit apertures of the analyzer. The spectrum actually reflects $E \cdot N(E)$, where E is the electron kinetic energy and $N(E)$ are the number of counted electrons at a given E .

A.5 Quantification of Auger spectra

The general equation governing the Auger electron current, I_A caused by a primary beam current I_p can be written down easily, but really needs a schematic drawing, such as Fig. A.6.

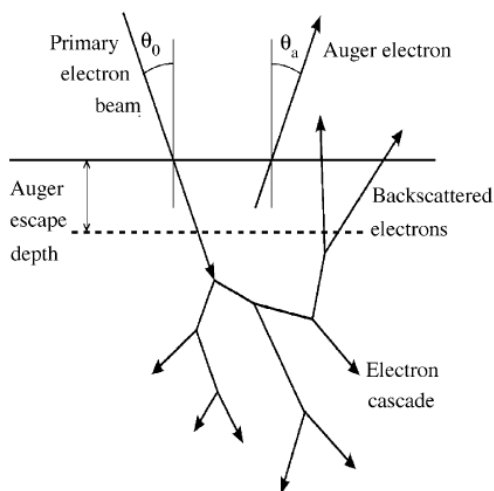


FIG. A.6. Schematic diagram of electron scattering in a solid, indicating the incident and detected angles, θ_0 and θ_a , plus the role of backscattered electrons in determining the Auger signal strength. The escape depth is qualitatively the thickness of the region from which most of the detected Auger electrons originate, of the same order as the inelastic mean free path λ discussed in the text (from Ref. 3).

For a bulk sample, the incoming electron causes an electron cascade below the surface, whose spatial extent is typically much greater than the IMFP. For example, the spatial extent is about $0.5 \mu\text{m}$ at an incident energy $E_0 = 20 \text{ keV}$, but also depends on the material and the angle of incidence, θ_0 . As a result Auger electrons can be produced by the incoming primary electron beam, and also by the backscattered electrons as they emerge from the sample; the Auger signal intensity thus contains the backscattering factor, R , which is a function of the sample material, E_0 and θ_0 . The ratio I_A/I_p can be expressed as a product of terms describing the production and detection of the Auger electrons, as first developed by Bishop and Rivière⁴. The Auger yield Y is the number of Auger electrons emitted into the total solid angle ($\Omega = 4\pi \text{ sr}$). It is therefore not dependent on the details of the analyzer. The detection efficiency D of the analyzer can be written as $(T\varepsilon)$, where T is a function

$f(\Omega_a/4\pi)$, Ω_a being the solid angle collected by the analyzer, and ε is the energy resolution $\Delta E/E$.

Thus:

$$\frac{I_A(z)}{I_P} = YD = (\sigma\gamma R) \sec \theta_0 (T\varepsilon) N_A \int \exp\left(-\frac{z}{\lambda_A \cos \theta_A}\right) dz \quad (\text{A. 4})$$

where z is the coordinate normal to the sample surface and increasing moving deeper along its depth. Here we have Y expressed as the cross-section for the initial ionization event (σ), the Auger efficiency (γ), and the factor R . The $\sec \theta_0$ term describes the extra ionization path length caused by having the primary beam at an angle θ_0 to the sample normal. λ_A is the Inelastic Mean Free Path, and the exponential term describes the probability that an Auger electron generating at a position z can escape from the surface without suffering any energy loss. Finally N_e is the effective number of atoms/unit area contributing to the (particular) Auger process. What we actually want to know is: given a measured signal I_A , how many A-atoms are there on the surface? Typically there is not a unique answer to such a simple question, because the signal depends not only on the number of atoms but also on their distribution in depth. In the simple case when the atoms are uniformly distributed in depth, like in bulk materials, the Auger intensity is thus given by:

$$\frac{I_A(z)}{I_P} = (\sigma\gamma R) \sec \theta_0 (T\varepsilon) N_A \int_0^{+\infty} \exp\left(-\frac{z}{\lambda_A \cos \theta_A}\right) dz = (\sigma\gamma R) \sec \theta_0 (T\varepsilon) N_A \lambda_A \cos \theta_A \quad (\text{A. 5})$$

Bibliography

-
- ¹ H. Luth, *Solid Surfaces, Interfaces, and Thin Films*, Springer Verlag, Fourth Edition
 - ² M.P. Seah and W.A. Dench, NPL Report Chem. (82) April 1978
 - ³ J.A. Venables, J. Liu *Journal of Electron Spectroscopy and Related Phenomena* **143** (2005) 205–218.
 - ⁴ H.E. Bishop, J.C. Riviere, *J. Appl. Phys.* **40** (1969) 1740

Panel B

Atomic Force Microscopy[§]

B.1 Introduction

The Atomic Force Microscopy (AFM) belongs to the broad family of scanning probe microscopy in which a proximal very sharp probe is exploited for investigating properties of surfaces with sub-nanometer resolution. The AFM, initially developed to overcome the limitations of his ancestor, the scanning tunneling microscope (STM), in imaging non-conducting samples, has provided a break-through in the ability to investigate the matter on the atomic scale. Since using this instrument the electrical conductivity of the sample is not required, it can virtually image any flat surface without the need for surface preparation. Thousands of AFM's are nowadays in use in university, public, and industrial research laboratories all over the world.

The aim of this panel is to illustrate how AFM represents a very useful tool for the measurement of highly magnified three dimensional images of a surface. The panel is organized as follows: first a brief description of basic principles and of the main characteristics of the AFM instrumentation are presented. Then the possible imaging modes are described with a particular emphasis toward that one used for the images shown in the thesis.

B.2 Basic principles

Unlike traditional microscopes, the AFM does not rely on electromagnetic radiation, such as photon or electron beams, to create an image. An AFM is a mechanical imaging instrument that measures the three dimensional topography as well as physical properties of a surface with a sharpened probe (see Fig. B.1).

The sharpened probe is positioned close enough to the surface such that it can interact with the force fields associated with the surface. Then the probe is scanned across the surface such that the forces between the probe and the sample remain constant. An image of the surface is then reconstructed by monitoring the precise motion of the probe as it is scanned over the surface. Typically the probe is scanned in a raster-like pattern.

[§] The most of information and images presented in this panel make reference to *Introduction to Atomic Force Microscopy*, Paul E. West.

In an AFM the probe is very sharp, typically less than 10 nm in diameter and the areas scanned by the probe are less than 100 μm . In practice the heights of surface features scanned with an AFM are less than 20 μm . Scan times can range from a fraction of a second to many 10's of minutes depending on the size of the scan and the height of the topographic features on a surface.

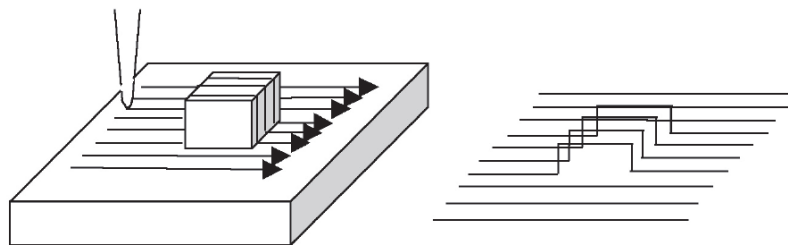


FIG. B.1. In the AFM, a sharp probe is scanned across a surface, left, and by monitoring the motion of the probe from each pass across the surface, a 2D line profile is generated. Then the line profiles are combined to create a three dimensional image of the surface, right.

Fig. B.2 illustrates the block diagram of an atomic force microscope. In the microscope, the force between a nanoscopic needle and the surface is measured with a force sensor, the output of the force sensor is then sent to a feedback controller that then drives a Z motion generator. The feedback controller uses the force sensor output to maintain a fixed distance between the probe and the sample. X-Y motion generators then move the probe over the surface in the X and Y axis. The motion of the probe is monitored and used to create an image of the surface.

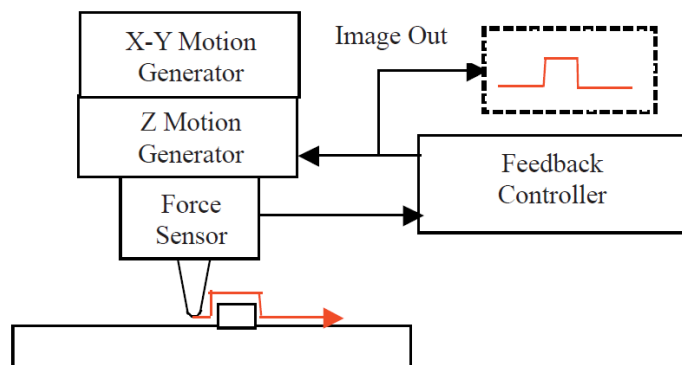


FIG. B.2. Basic block diagram of an AFM

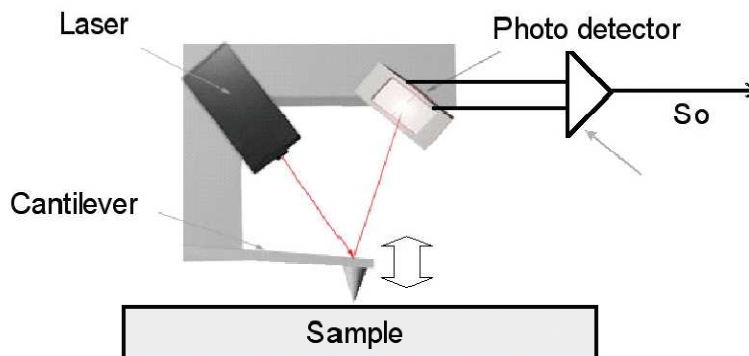


FIG. B.3. Illustration of a light lever force sensor

The force sensor in an atomic force microscope is typically constructed from a light lever, see (Fig. B.3). In the light lever, the output from a laser is focused on the backside of a cantilever and reflected into a photodetector with four sections. The output of each of the photo-detector sections is compared in a differential amplifier. When the probe at the end of the cantilever interacts with the surface, the cantilever bends, and the light path changes causing the amount of light in the two photo-detector sections to change. Thus the electronic output of the light lever force sensor, S_o , is proportional to the force between the probe and sample.

B.3 AFM Instrumentation

Fig. B.4 illustrates the primary components of an AFM stage. There is an AFM scanner that measures the force between the probe and surface and scans the probe over the surface. There is a motion control mechanism, the Z motor, which can move the AFM scanner towards the sample. There is also an X-Y positioning stage which is not required but is useful for positioning the feature for imaging under the probe as well as an optical microscope for viewing the probe and surface. A mechanical structure is required to support the AFM scanner.

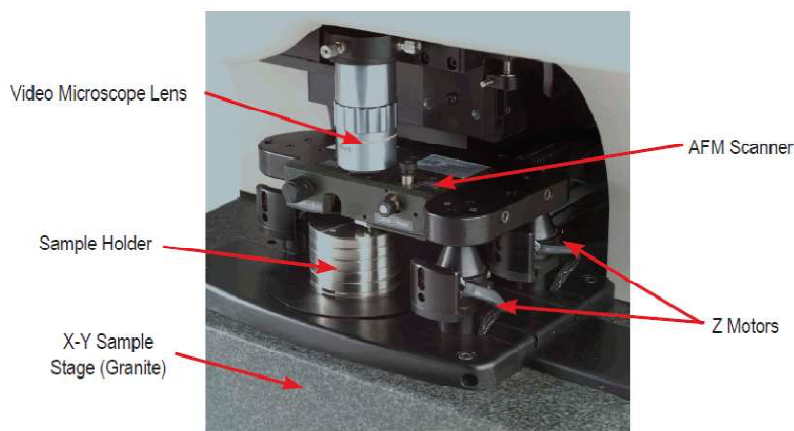
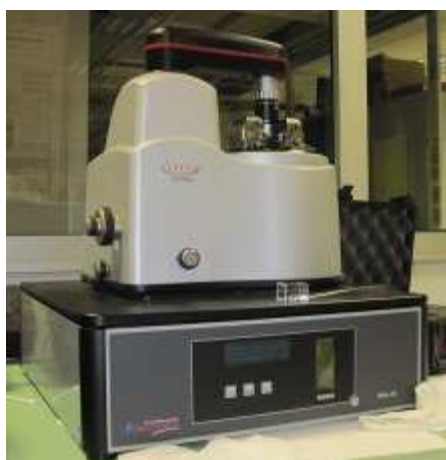


FIG. B.4. Left: photograph of the Veeco Innova AFM microscope at the Laboratory LNESS (Como) used for the measurements presented in this thesis. Right: details of an AFM stage.

B.3.1 AFM scanners

Typically, the scanners used for moving the probe relative to the sample in an AFM are constructed from piezoelectric materials. This is because piezo-materials are readily available, easily fabricated in desirable shapes, and cost effective.

The most common types of piezoelectric materials in use for AFM scanners are constructed from amorphous PdBaTiO_3 . The ceramics may be “hard” or “soft”, depending on the formulation. Hard ceramics have smaller coefficients of expansion, but are more linear. Soft ceramic

formulations have more non-linearities and have greater expansion coefficients. After fabrication, piezoelectric ceramics are polarized. Polarization may be lost by elevating the piezos to a temperature above their critical temperature or by giving them an over voltage.

All piezoceramics have a natural resonance frequency that depends on the size and shape of the ceramic. Below the resonance frequency, the ceramic will follow an oscillating frequency, at resonance there is a 90° phase change, and above resonance there is a 180 degree phase change. To a great extent, the resonance frequencies of the piezoelectric ceramics limit the scan rates of atomic force microscopes.

Ideally, the piezoelectric ceramics would expand and contract in direct proportion to the driving voltage. However, piezoelectric materials have two primary non-ideal behaviors, hysteresis and creep. Hysteresis, derived from the word history, causes the ceramic to maintain the shape that it was in. As the ceramic is expanding, there is a negative shaped non-linearity, and as the material is contracting, there is a positive shaped non-linearity. Creep occurs when the ceramic is subjected to a sudden impulse such as a voltage step function. These non-ideal behaviors must be corrected or they cause distortions in AFM images.

B.3.2 Light Lever Force Sensors

The force sensor in an AFM must be able to measure very low forces. This is because, if a small probe is used, the pressure, force/area, must be small so that the probe is not broken. Although a number of different force sensors have been tested and demonstrated to work with an AFM, the light lever is used routinely for measuring minute motions in scientific instrumentation. With the advent of microfabricated cantilevers the Light Lever AFM (LL-AFM) became the most widely used design for the force sensor in an AFM.

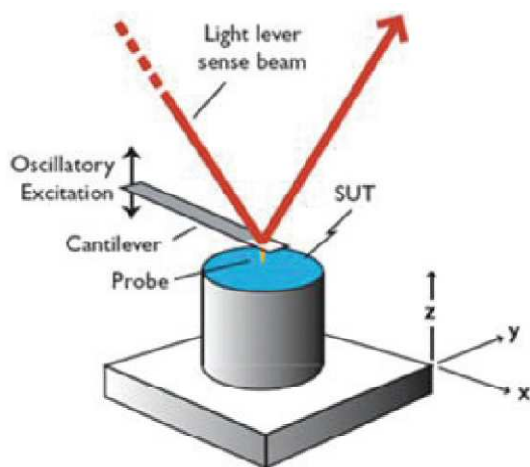


FIG. B.5. Illustration of the light lever AFM force sensor. In the LLAFM sensor the end of the cantilever bends and thus the angle between the probe and sample changes as the cantilever bends.

The design for a LL-AFM sensor is illustrated in Fig. B.5. A laser light is reflected off the back side of a cantilever into a 4 section photodetector. If a probe, mounted on the backside of the cantilever, interacts with the surface the reflected light path will change. The force is then measured by monitoring the change in light entering the 4 quadrant photo-detector. The light reflects off the parabolic end of the cantilever, which gives much of the amplification of the light path in the light lever. Geometrically, it is calculated that the deflection at the end of the cantilever is equal to the motion of the laser beam across the face of the photodetector.

The LL-AFM force sensor requires alignment each time a probe/cantilever is exchanged. Typically, alignment is accomplished by first positioning the laser light onto the cantilever, and then confirming that the light is reflected onto the photo-detector by looking at the photo-detectors electronic output.

B.3.3 Cantilevers and tips

An LL-AFM force sensor requires a cantilever with a probe at its end for operation. Typically these are fabricated using MEMS technology and are considered a disposable component of the AFM. In principle, an AFM probe should last forever; however, in practice the probe tip is often blunted when it touches a surface. Changing the probe typically takes only a few minutes. Fig. B.6 illustrates the geometry of a typical probe/cantilever/substrate.

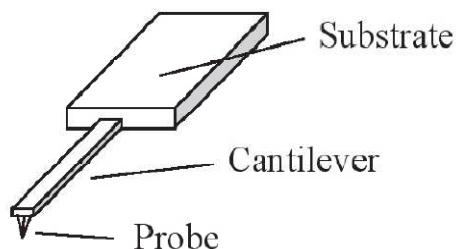


FIG. B.6 Illustration of an AFM cantilever/probe/substrate created by micromachining of Si or SiN. All commercially available probes have substrates with the same dimension.

The geometry of the probe is critical to the quality of images measured with an AFM. All AFM images are a convolution of probe geometry and surface. In principle, AFM cantilevers can be made of any material that can be fabricated into a spring-like cantilever. The first AFM cantilevers were fabricated from tungsten wire and had a probe etched in the silicon at the end. Early in the evolution of AFM it was discovered that the best AFM probes could be constructed from MEMS technology. There are two materials commonly used for AFM cantilevers: SiN and Si.

SiN is used for creating probes that have very low force constants. The thin films used for creating SiN probes must have very low stress so the cantilevers don't bend naturally from the stress. Practically, most SiN films have some residual stress and in fact, cantilevers made with SiN

tend to have curvature along their primary axis. Cantilevers fabricated from silicon tend to have less residual stress than SiN and tend not to suffer from bending. However, the Si probes that are fabricated at the end of the cantilever can be brittle and tend to chip if they contact a surface. Most of the cantilever/probes used in LL-AFM force sensors are constructed from Si.

Two basic geometries are used for AFM cantilevers, rectangular and triangular. The two primary shapes for probes are pyramidal and conical. Typically SiN probes are pyramidal and Si probes are conical, see Fig. B.7. AFM cantilevers were initially fabricated from SiN in a triangular shape. Because of the cantilevers bending, Si became the preferred material.

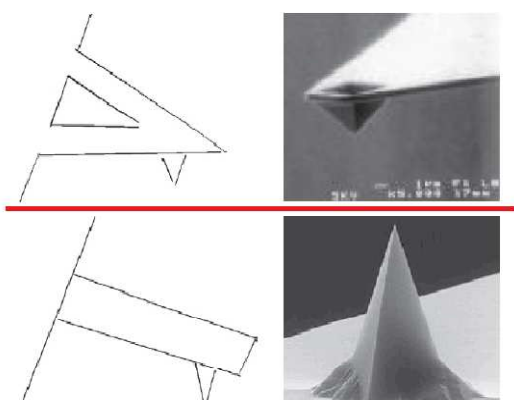


FIG. B.7 SiN cantilevers are typically triangular with two arms meeting at an apex. The probe on SiN probes are typically pyramidal and appear hollow at the top. (Top) Si cantilevers are typically rectangular and the probes tend to have a triangular shape to them. Si probes are crystalline and are prone to chipping and breaking if they crash into a surface. (Bottom)

B.4 Imaging modes

A force sensor in an AFM can only work if the probe interacts with the force field associated with a surface. In ambient air, the potential energy between the probe and surface is shown in Fig. B.8. There are three basic regions of interaction between the probe and surface: (i) free space, (ii) attractive region, and (iii) repulsive region.

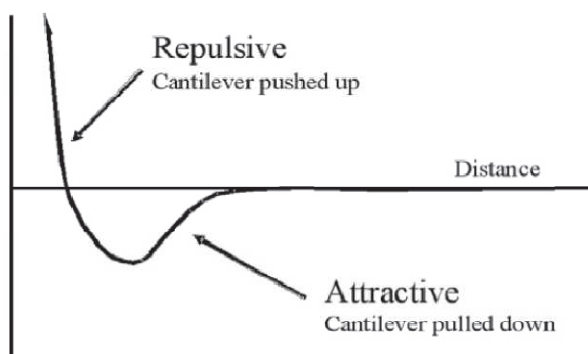


FIG. B.8. Potential energy diagram of a probe and sample. The attractive potential is caused by the capillary forces from surface contamination.

Attractive forces near the surface are caused by a nanoscopic layer of contamination that is present on all surfaces in ambient air. The contamination is typically an aerosol composed of water vapor and hydrocarbons. The amount of contamination depends on the environment in which the

microscope is being operated. Repulsive forces increase as the probe begins to “contact” the surface. The repulsive forces in the AFM tend to cause the cantilever to bend up.

There are two primary methods for establishing the forces between a probe and a sample when an AFM is operated. In contact mode the deflection of the cantilever is measured, and in vibrating mode the changes in frequency and amplitude are used to measure the force interaction. As a rule of thumb, the forces between the probe and surface are greater with contact modes than with vibrating modes.

B.4.1 Contact Mode

In contact mode, the cantilever is scanned over a surface at a fixed deflection (see Fig. B.9). Provided that the PID feedback loop is optimized, a constant force is applied to the surface while scanning. If the PID feedback parameters are not optimized, a variable force is exerted on the surface by a probe during a scan. The force constant may be calculated if the dimensions and material of the cantilever are known. Most commercially available cantilevers for the AFM are supplied with the approximate values for the force constant.

Contact mode is typically used for scanning hard samples and when a resolution of greater than 50 nanometers is required. The cantilevers used for contact mode may be constructed from silicon or silicon nitride. Resonant frequencies of contact mode cantilevers are typically around 50 KHz and the force constants are below 1 N/m.

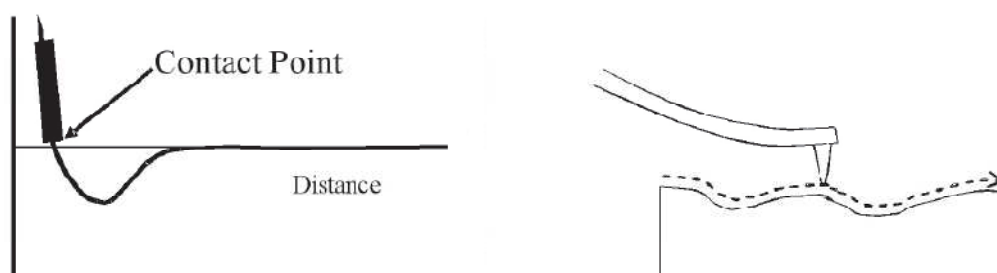


FIG. B.8. Left: Potential diagram showing the region of the probe while scanning in contact mode. Right: In contact mode the probe glides over the surface.

B.4.2 Vibrating Modes

In order to make more sensitive measurements requiring better signal/noise ratios in scientific instruments, it is common to modulate the signal being measured and use phase or amplitude detection circuits. Use of modulated techniques shifts the measurement to a higher frequency regime where there is less than $1/f$ noise. Such techniques were developed for the AFM soon after it was invented.

In order to make the S/N ratio higher, and thus be able to measure lower forces with the AFM, the probe is vibrated as it is scanned across a surface. As shown in Fig. B.9, the probe is vibrated in and out of surface potential. The modulated signal can then be processed with a phase or amplitude demodulator. The cantilever can be excited with a piezoelectric ceramic and exhibit natural resonant frequency is $\omega_0 = c\sqrt{k}$, where k is the force constant and c is a proportionality constant.

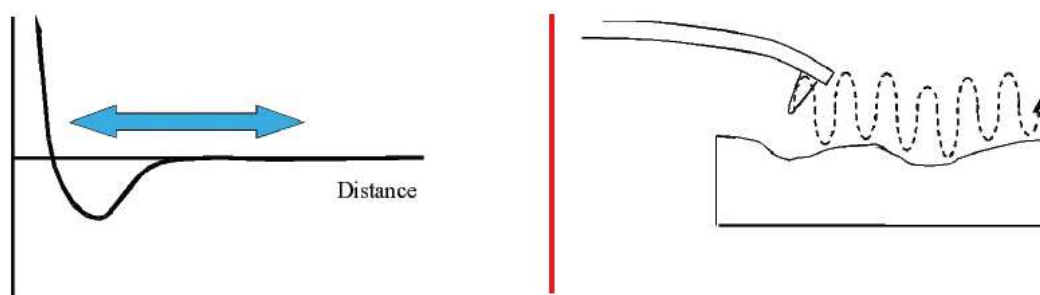


FIG. B.9. Left: Potential diagram showing the motion of the probe in vibrating mode. Right: The probe vibrates as it scans across a surface.

At the resonance frequency, there is a 90° phase shift. When the probe tip interacts with a surface, the resonance frequency shifts to a lower value, and there is a corresponding change in the phase. When scanning in the vibrating modes, a constant relationship is maintained by the feedback electronics, which keeps either the phase shift or amplitude constant at a given frequency, while scanning.

As mentioned before, there is a “contamination” layer on surfaces in ambient air with a thickness between 1 and 50 nm. The probe surface interaction forces are governed by the capillary forces between the probe and the contamination layer. The probe may be vibrated in three separated regimes as it is scanned across the surface, see Figure 4-9.

In the first regime, the probe is vibrated across the surface of the contamination layer. The vibration amplitude must be very small and a very stiff probe must be used. The images of the surface contamination layer are typically very “cloudy” and appear to have low resolution. This is because the contamination fills in the nanostructures at the surface.

In the second regime the probe is scanned inside the contamination layer⁶. This technique, named “near contact”, requires great care to achieve. The cantilever must be stiff so that the tip does not jump to the surface from the capillary forces caused by the contamination layer. Then very small vibration amplitudes must be used. Often very high resolution images are measured in this regime.

In the third regime the probe is vibrated in and out of the contamination layer. This mode is given several names such as intermittent contact or tapping. In this mode the energy in the vibrating cantilever is much greater than the capillary forces and the probe moves readily in and out of the

contamination layer. This mode is the easiest to implement but often results in broken probes because the tip is crashing into the surface upon each oscillation.

Vibrating methods are used when the highest resolution is required or if very soft samples are being scanned. The probes used for vibrating mode are often less than 10 nm in diameter.

Panel C

Transmission Electron Microscopy

C.1 Introduction

Advanced electron microscopy techniques, especially transmission electron microscopy (TEM), are indispensable for characterizing interfaces and defects, nano-devices, nanoparticles and catalysts, and other nano-systems. The single most important feature of a TEM instrument is its versatility: atomic resolution images, diffraction patterns from nanometer regions and nanometer-scale spectroscopy data can be obtained either simultaneously or sequentially from the same region of the sample. The availability of the various imaging, diffraction, and spectroscopy techniques within a single instrument makes TEM one of the most powerful microscope for characterizing the nature of nanoscale systems.

The panel is organized as follows. First the basic principles, the instrumentation and the imaging contrast for Conventional TEM are reviewed. Then the main aspects of Scanning TEM and Energy Filtered TEM are critically discussed. The sample preparation procedure for cross-section TEM using a Focused Ion Beam (FIB) microscope is then presented. Finally the application of TEM-STEM capabilities for imaging dislocations in a Ge/Si(100) system is discussed.

C.2 Conventional TEM

C.2.1 Basic principles¹

In transmission electron microscopy the image is formed by electron passing through the sample. The principle of operation is the same as that of an optical microscope, using magnetic lenses instead of glass lenses and electrons instead of photons. A beam of electrons emitted by an electron gun is focused by a condenser lens into a small spot ($\sim 2 \div 3 \mu\text{m}$) on the sample and after passing through the sample is focused by the objective lens to project the magnified image onto the screen (Fig. C.1). A very essential element is the aperture located at the back focal plane of the objective lens. As it will be show below, this determines the image contrast and the resolution limit of the microscope. It is worth noting that this simple scheme illustrates only the principle of image formation in TEM, not the actual TEM setup which is more sophisticated. Due to the limited penetration depth of electrons in solids the sample should be very thin: the acceptable thickness is

100 ÷ 1000 Å for conventional microscopes with accelerating voltages of 50 ÷ 200 kV, and a few thousand Å for high voltage microscopes with acceleration voltages up to 3 MV. Of course, the required sample thickness depends on the sample material: the larger the atomic number, the greater the electron scattering, hence a thinner sample should be.

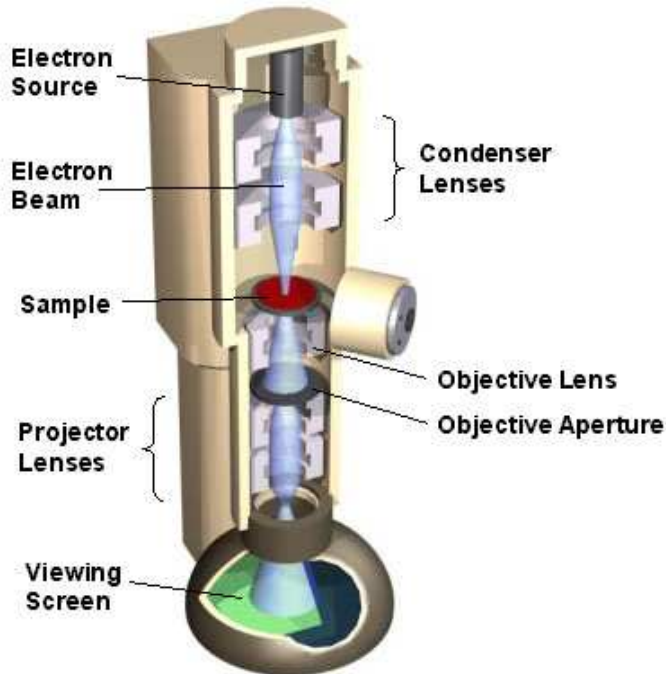


FIG. C.1. Schematic diagram illustrating the electron optic of a typical transmission electron microscope.

The diffraction for TEM resolution can be estimated from $\Delta = 0.5\lambda/\sin \alpha$, where λ is the electron wavelength and α equals one half the angular aperture, which can be approximated by the ratio of the objective diaphragm radius to the objective focal lens. For a voltage of 100 kV ($\lambda = 0.037$ Å), diaphragm radius of 20 μm , and focal length of 2 mm, the estimation yields $\Delta \sim 2$ Å. In practice the resolution is usually worse due to non ideality of the electronic optic system.

The formation of TEM image contrast will be discussed in more details in Section C.2.3. In brief it can be understood as follows. When passing through a sample, the electron flux loses part of its intensity due to scattering processes. This part is greater for thicker regions or regions with species of higher atomic number. If the objective aperture effectively cuts off the scattered electrons, the thicker regions and the regions of higher atomic number appear dark. The small aperture enhances the contrast (but leads to the loss of resolution as shown above). In crystals, the elastic scattering of electrons results in the appearance of diffraction contrast.

C.2.2 Instrumentation²

The overall flexibility of a TEM microscope is achieved with an electron-optical system containing an electron gun (which produces the beam of electrons) and several magnetic lenses,

stacked vertically to form a lens column (see Fig. C.1). It is convenient to divide the instrument into three sections: the illumination system, the sample stage, and the imaging system.

The *illumination system* comprises the electron gun, together with two or more condenser lenses that focus the electrons onto the sample. Its design and operation determine the diameter of the electron beam at the sample and the intensity level in the final TEM image. The electron gun produces a beam of electrons whose kinetic energy is high enough to enable them to pass through thin areas of the TEM sample. The gun consists of an electron source, also known as the cathode because it is at a high negative potential, and an electron-accelerating chamber. Hot filament, Schottky emission and Cold Field emission are the most used electron sources, exhibiting an increasing brilliance and a decreasing beam spot size going from the former to the latter. After emission from the cathode, electrons are accelerated to their final kinetic energy by means of an electric field parallel to the optic axis. This field is generated by applying a potential difference between the cathode and an anode, a round metal plate containing a central hole (vertically below the cathode) through which the beam of accelerated electrons emerges. Many of the accelerated electrons are absorbed in the anode plate and only around 1% pass through the hole, so the beam current in a TEM is typically 1% of the emission current from the cathode.

The TEM may be required to produce a highly magnified image of the sample on a fluorescent screen, or for viewing larger areas of sample the final-image magnification might need to be very low. In order to achieve the required flexibility, the condenser-lens system must contain at least two electron lenses. The first condenser lens is a *strong* magnetic lens, with a focal length f that may be as small as 2 mm and located 20 cm or more below the source, which accounts for the high magnification mode. The second condenser (C2) lens is a *weak* magnetic lens (f is around several centimeters) that provides little or no magnification but allows the diameter of illumination at the sample to be varied continuously over a wide range.

The *sample stage* allows samples to either be held stationary or else intentionally moved, and also inserted or withdrawn from the TEM. The mechanical stability of the sample stage is an important factor that determines the spatial resolution of the TEM image. To allow observation in different brands or models of microscope, TEM samples are always made circular with a diameter of 3 mm. Perpendicular to this disk, the sample must be thin enough (at least in some regions) to allow electrons to be transmitted to form the magnified image. The sample stage is designed to hold the sample as stationary as possible, as any drift or vibration would be magnified in the final image, impairing its spatial resolution (especially if the image is recorded by a camera over a period of several seconds). But in order to view all possible regions of the sample, it is also necessary to move the sample horizontally over a distance of up to 3 mm if necessary.

The *imaging system* contains at least three lenses that together produce a magnified image (or a diffraction pattern) of the sample on a fluorescent screen or on the monitor screen of an electronic camera system. The design of the imaging lenses (especially the first imaging lens, the objective) largely determines the spatial resolution that can be obtained from the microscope. The lens closest to the sample is called the objective. It is a strong lens, with a small focal length; because of its high excitation current, the objective must be cooled with temperature controlled water, thereby minimizing image drift that could result from thermal expansion of the sample stage. The TEM also has fine controls that enable the operator to make small fractional adjustments to the objective current, to allow the sample image to be accurately focused on the viewing screen. The objective produces a magnified real image of the sample at a distance of about 10 cm below the center of the lens. Because of the small value of f , the object distance is only slightly greater than the focal length, so the sample is usually located within the pre-field of the lens (that part of the focusing field that acts on the electron before it reaches the center of the lens). By analogy with a light microscope, the objective is therefore referred to as an immersion lens. When the final (C2) condenser lens produces a near-parallel beam, the pre-field focuses the electrons into a nanoprobe of typical diameter $1 \div 10$ nm (see Fig. C.2(a)). Alternatively, if the condenser system focuses electrons to a crossover at the front-focal plane of the pre-field, the illumination at the sample is approximately parallel (Fig. C.2.(b)). An objective diaphragm can be inserted located at the back-focal plane (BFP) of the post-field of the objective lens, the plane at which a diffraction pattern of the specimen is first produced. In this plane, *distance* from the optic axis represents the *direction* of travel (angle relative to the optic axis) of an electron that has just left the specimen.

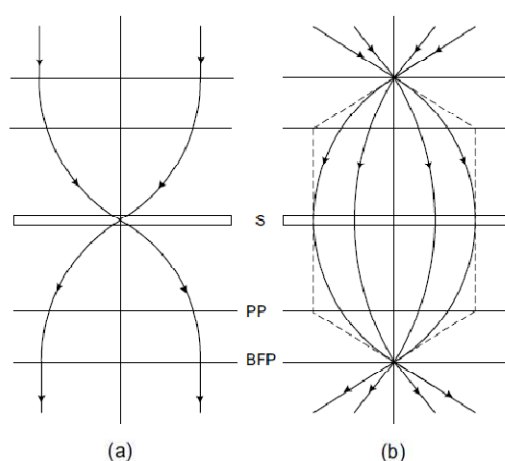


FIG. C.2 Formation of (a) a small-diameter nanoprobe and (b) parallel illumination at the sample, by means of the pre-field of the objective lens. S defines the sample, PP is the principal plane of the objective lens, and BFP is the back-focal plane.

A modern TEM contains several lenses between the objective and the final (projector) lens. At least one of these lenses is referred to as the intermediate. The intermediate lens serves two purposes. First, by changing its focal length in small steps, its image magnification can be changed, allowing the overall magnification of the TEM to be varied over a large range. Second, by making a

larger change to the intermediate lens excitation, an electron diffraction pattern can be produced on the TEM viewing screen. Finally, a projector lens is located after the intermediate and before the screen. The purpose of the projector lens is to produce an image or a diffraction pattern across the entire TEM screen, with an overall diameter of several centimeters.

C.2.3 Image contrast²

In a transmitted-light microscope, variation of intensity within an image is caused by differences in the absorption of photons within different regions of the sample. In the case of a TEM, however, essentially all of the incoming electrons are transmitted through the sample, provided it is suitably thin. Although not absorbed, these electrons are scattered (deflected in their path) by the atoms of the sample. The nature of this scattering process is essentially the electrostatic (Coulomb) interaction between charged particles. Interaction between the incoming fast electron and an atomic nucleus gives rise to *elastic* scattering where almost no energy is transferred. Interaction between the fast electron and atomic electrons results in *inelastic* scattering, in which process the transmitted electron can lose an appreciable amount of energy.

The amount and angular distribution of electron scattering within a *crystalline* material, which primarily affect the contrast within a TEM image, is strongly dependent on the *orientation* of the atomic planes relative to the incident electron beam. To understand why this orientation matters, we must abandon the particle description of the incident electrons and consider them as de Broglie (matter) waves. A useful comparison is with x-rays, which are diffracted by the atoms in a crystal (see Panel G and Chapter 5). The simplest way of understanding x-ray diffraction is in terms of Bragg reflection from atomic planes, which occurs only when the angle of incidence (here measured between the incident direction and the planes) is equal to a Bragg angle ϑ_B that satisfies the Bragg's law:

$$n\lambda = 2d \sin \vartheta_B \quad (\text{C.1})$$

Here, λ is the x-ray wavelength and d is the spacing between atomic planes, measured in a direction perpendicular to the planes; n is an integer that represents the order of reflection. The fast electrons used in a transmission electron microscope penetrate through many planes of atoms and are diffracted (elastically scattered) within crystalline regions of a solid, just like x-rays. However, their wavelength ($\lambda = 0.037 \text{ \AA}$ primary beam energy of 100 keV) is far below a typical atomic-plane spacing ($\sim 3 \text{ \AA}$) so the Bragg angles are small, as required by Eq. (C.1) when $\lambda \ll d$. The integer n in Eq. (C.1) is usually taken as one. Using the small-angle approximation, Eq. (C.1) can therefore be rewritten as:

$$\lambda \approx 2\vartheta_B d = \vartheta d \quad (\text{C.2})$$

where $\vartheta = 2\vartheta_B$ is the angle of scattering (deflection angle) of the electron resulting from the diffraction process.

Considering a polycrystalline sample made of a number of crystallites with different crystallographic orientations, for a few particular orientations of a crystallite relative to the incident beam Eq. (C.2) will be satisfied and a crystallite will strongly diffract the incident electrons. Provided the corresponding deflection angle ϑ exceeds the semi-angle α of the objective aperture, the diffracted electrons will be absorbed by the objective diaphragm and the crystallite will appear dark in the TEM image. Crystallites whose atomic-plane orientations do *not* satisfy Eq. (C.2) will appear bright, as most electrons passing through them will remain *undiffracted* (undeviated) and will pass through the objective aperture. This imaging mode when only the undiffracted beam is collected is generally called *bright-field*. Instead of selecting the undiffracted beam of electrons to form the image, we could horizontally displace the objective aperture so that it admits diffracted electrons. Strongly diffracting regions of the sample would then appear *bright* relative to their surroundings, resulting in a *dark-field* image because any part of the field of view that contains *no* sample would be dark.

Close examination of the TEM image of a polycrystalline sample shows there can be a variation of electron intensity *within* each crystallite. This diffraction contrast arises either from atomic-scale defects within the crystal or from the crystalline nature of the material itself, combined with the wave nature of the transmitted electrons. In fact in the vicinity of a crystal defect a strain field is present and a distortion of the crystallographic planes appear. Because the Bragg angles for electron diffraction are small, it is likely that, at some places within this strained region, the bending causes the angle between an atomic plane and the incident beam to become approximately equal to the Bragg angle ϑ_B . At such locations, electrons are strongly diffracted, and most of these scattered electrons will be absorbed at the TEM objective aperture. In addition to diffraction (or scattering) contrast, features seen in some TEM images depend on the *phase* of the electron waves at the exit plane of the sample. Although this phase cannot be measured directly, it gives rise to interference between electron waves that have passed through different regions of the specimen. Such electrons are brought together when a TEM image is *defocused* by changing the objective-lens current slightly. Unlike the case of diffraction-contrast images, a large-diameter objective aperture (or no aperture) is used to enable several diffracted beams to contribute to the image. Some examples of diffraction and phase contrast will be given in Section C.6 concerning the imaging of dislocations in case of a Ge/Si(100) system.

C.3 Scanning TEM³

The Scanning TEM works on the same principle as the normal scanning electron microscope (SEM), by forming a focused beam of electrons that is scanned over the sample while some desired signal is collected to form an image. Figure C.3 shows the main components comprising an aberration-corrected STEM. Electrons are accelerated from a source and focused into a point on the sample (see Section C.2.2 and Fig. C.2) by a set of condenser lenses and an objective lens. An objective aperture limits the maximum angle of illumination included in the incident probe, which is scanned across the sample by a set of scan coils.

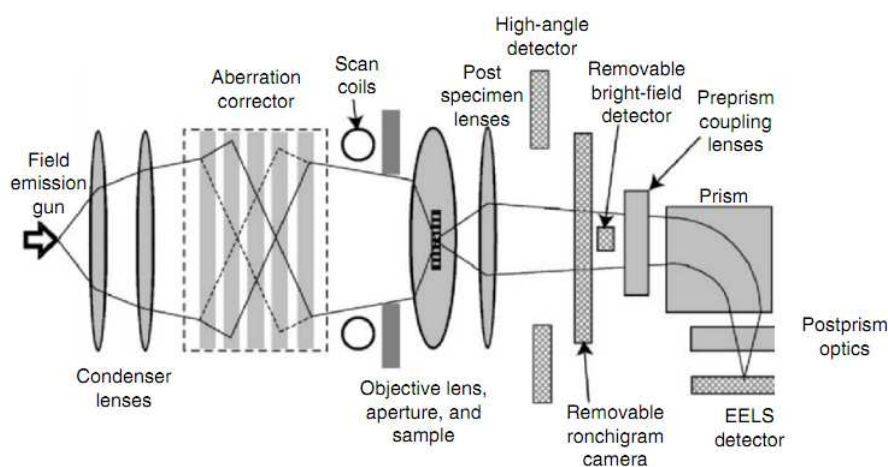


FIG. C.3. Schematic diagram of a high resolution Scanning TEM (From Ref. 3)

The output of a variety of possible detectors can then be used to form an image. In fact, multiple detectors can be used simultaneously to give different views of the sample, providing different but complementary information. The usual detectors include a bright field (BF) detector that intercepts the transmitted beam and an annular dark field (ADF) detector that surrounds the transmitted beam to collect scattered electrons. The inner angle of this detector can be changed with post-sample lenses from just outside the incident beam cone, which gives maximum efficiency for collecting scattered electrons (generally referred to as low angle ADF - LAADF), to several times this angle, that enhances the atomic number (Z) dependence of the image contrast. This latter configuration is often referred to as a Z -contrast or high-angle ADF (HAADF) image. Also, normally, part of the STEM is an EELS system (see Section C.4), comprising spectrometer and parallel detection system using a charge-coupled device (CCD).

C.4 Energy Filtered TEM⁴

Electrons scattered inelastically as a result of energy loss and wavelength change in the sample, are brought to a focus plane far distant from the viewing screen showing the elastic image.

This out-of-focus “inelastic”, as far as Conventional TEM, contributes only with a uniform background to the in-focus elastic image. However it contains a tremendous amount of both structural and chemical information. The interaction of the fast electron with the sample causes either collective excitations of electrons in the valence band (plasma oscillations), or discrete transitions between atomic energy levels with scattering angles of about $1 \div 2$ mrad for 100 keV primary beam energy. The ability to observe discrete atomic transitions allows compositional analysis to be performed since the transitions occur at characteristic binding energies for a given element. Furthermore, the transitions to unoccupied states above the Fermi level allows the degree of hybridization between atomic orbitals to be determined, i.e. information on local electronic structure (bonding) changes can be ascertained.

Measurement of the kinetic energy allowing analysis of fast electrons, can be done using an energy-loss system combined with the transmission electron microscope, i.e., the Energy-Filtering TEM. The filter, generally based on a magnetic-prism spectrometer, is able to analyze the energy distribution of initially monoenergetic electrons, after they have traversed the sample, and moreover recombines those electrons that have lost a selected energy, thus forming an energy filtered image on a two-dimensional CCD array as detector. Moreover, the energy filter can be also integrated within a Scanning TEM (see Fig. C.3), allowing to perform spectroscopic analysis on a single point with nanometric resolution. In fact, as can be seen from Fig. C.3, the annular detector used for Z-contrast imaging does not interfere with the low angle scattering used for EELS. This means that the Z-contrast image can be used to position the electron probe over a particular structural feature for acquisition of a spectrum.

C.5 Cross-section TEM sample preparation by FIB

A Focused Ion Beam (FIB) instrument looks and operates much like a scanning electron microscope (SEM). Both instruments rely on a focused beam to create a specimen image; an ion beam (generally Ga^+) for the FIB and an electron beam for the SEM. For both instruments, the intensity of the secondary electrons produced at each raster position of the beam is displayed to create an image of the sample. However, the FIB can be also used for micro and nano-machining due to the sputtering effect of the ion beam irradiation. In fact when a Ga^+ ion is accelerated toward the target sample, it enters the sample and creates a cascade of events which results in the ejection of a sputtered particle (which may be an ion or a neutral atom).

Another feature that is used extensively in the FIB is ion beam assisted chemical vapor deposition. The deposition of metal is used extensively in silicon semiconductor device

modification and is used in TEM sample preparation techniques to protect the top surface of interest from spurious sputtering. A needle is brought to close to the target surface (see Fig. C.4(a)). A suitable gas (e.g., $W(CO)_6$) is injected from the needle and adsorbs onto the target surface. The Ga^+ beam is raster over the desired sample region. The ion beam decomposes the gas, which leaves a deposited layer of metal (e.g., W), while the byproduct (e.g., CO) is removed through the vacuum system.

In the following we describe the procedure adopted for the sample preparation for cross-sectional TEM investigation of SiGe islands presented in Chapter 3, and performed at the Ecole Polytechnique and at the Université Paris-Sud 11. Initial sample preparation have been performed before the sample was placed into the FIB using the conventional TEM specimen preparation method. An area of interest was located and cut to < 3 mm in length. The sample has been then mechanically polished along the direction parallel to the surface (and parallel to the Ge stripes) down to $60 \mu m$ to reduce the FIB time. The sample has been mounted on a slotted TEM Cu grid that has been partially cut away (see Fig. C.4(d)). The sample is then positioned into the FIB. A W line is deposited on the area of interest (see Fig. C.4(b)) to prevent damage and spurious sputtering of the top portion of the sample and to also delineate the location of the area of interest. Large trenches are then sputtered on either side of the area of interest using a high Ga^+ beam current (see Fig. C.4(c)). The beam current is reduced and milling is performed on alternate sides of the sample to reduce re-deposition of sputtered material onto the surface of the sample (see Fig. C.4(c)). Milling is continued until the membrane is thinned to ~ 100 nm.

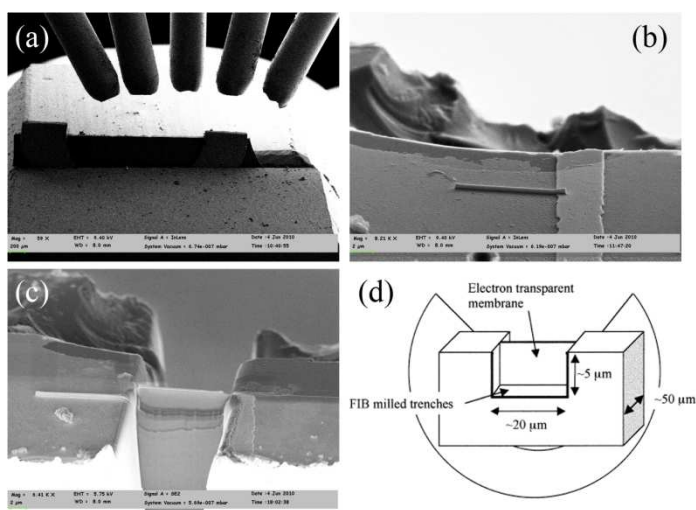


FIG. C.4. Panel (a): gas needles for ion assisted CVD. Panel (b): SEM image of a portion of the sample surface. The vertical lighter band is the Ge stripe; the thin horizontal line represents the W deposit to protect the island during the milling. Panel (c): SEM image of the thinned region after FIB processing; the large trenches on either side of the area of interest are clear. Panel (d): schematic of a conventionally prepared FIB TEM sample (not in scale).

C.6 Imaging dislocations in a Ge/Si system

Let's now consider the heteroepitaxial growth of Ge on top of a single crystalline Si(100) substrate. At the beginning the growth process evolves in layer-by-layer mode (see Chapter 1), and the Ge layer will first adapt its lateral lattice parameter to that of the substrate by deforming elastically. As the film grows thicker, more and more elastic energy will therefore accumulate until at some critical thickness it is no longer energetically favorable to strain the film to the substrate lattice constant. In hypothesis that island nucleation is kinetically prevented, the so-called *misfit dislocations* will start to form in the film. For diamond and zinc-blende crystal structures the dislocation structure is of mixed edge and screw character. Here, the glide planes are {111}-planes, and the most common dislocations are 60° -dislocations, where the Burgers vector makes an angle of 60° degrees with respect to the dislocation line⁵. The dislocation line is not located entirely in the interface plane. This is the case only for the *misfit segment* MD, while the so-called *threading segment* TD lies in the (111)-plane and extends to the surface of the film. The presence of this threading arm is related to the way in which dislocations are formed.

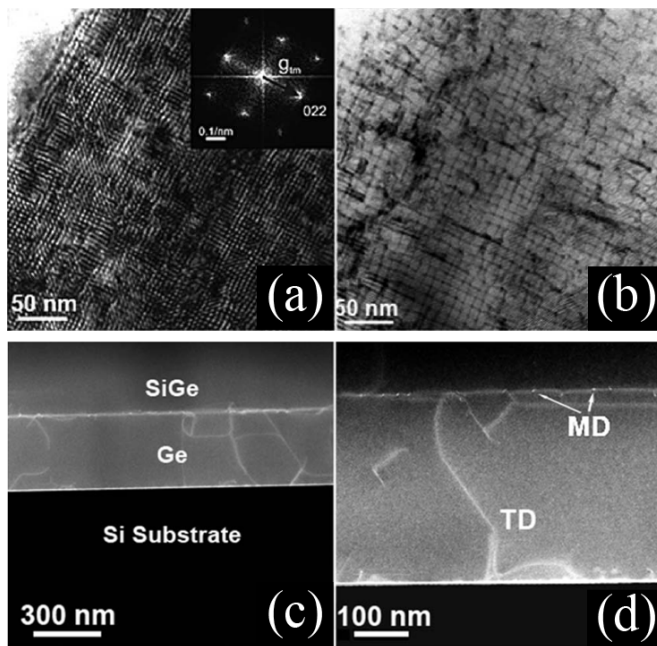


FIG. C.5. Panel (a) PV BF image in [100] axis beam condition of a Ge layer on Si(001). Panel (b): PV BF image in [220] axis beam condition of the same region shown in (a). Panel (c) and (d): LAADF-STEM images of the SiGe/Ge/Si(100) system.

Transmission electron microscopy allows to directly probe the presence of such a dislocations thanks to the diffraction and phase contrast capabilities, as recently shown by Capellini *et al.*⁶. Fig. C.5(a) shows plan view (PV) bright field (BF) image by Conventional TEM, under the [100] zone axis beam condition (the optic axis is aligned along the [100] direction normal to the sample surface). In this experimental condition, the primary electron beam generates a translational Moiré pattern due to the interference of the two electron beams transmitted by the two layers of the Ge/Si heteroepitaxial structure. The presence of several interruptions of their Moiré pattern in the Ge layer

is due to the presence of MDs. In Fig. C.5(b) is shown a Conventional TEM image obtained in weak beam-BF with a diffraction vector $g = [220]$, acquired in the same region of Fig. C.5(a). The regular network of dark lines represent the $[110]$ -oriented MDs at the Ge/Si interface as well as the presence of threading dislocation arms (line having irregular shapes), propagating both in plane and toward the sample surface. Figs. C.5(c) and C.5(d) display the cross sectional LAADF-STEM of a sample composed of a 200 nm thick Ge relaxed layer and a 400 nm thick SiGe top layer. The Ge/Si interface appears bright, owing to the high density of MDs scattering the electron beam. In fact, the contrast is due to the static random displacement of atoms around defects which causes extra scattering in the low angle region⁷. It is possible to observe also few threading arms of 60° MD (TD) departing from the Ge/Si interface propagating in the $\langle 110 \rangle / \{111\}$ slip system through the Ge layer.

Bibliography

-
- ¹ K. Oura, V.G. Lifshits, A.A. Saranin, A.V. Zotov, M. Katayama, *Surface Science – An Introduction*, Springer Verlag 2003
- ² R.F. Egerton, *Physical Principles of Electron Microscopy - An Introduction to TEM, SEM, and AEM*, Springer Science 2005
- ³ S. J. Pennycook, A. R. Lupini, M. Varela, A. Y. Borisevich, Y. Peng, M. P. Oxley and M. F. Chisholm, “*Scanning Transmission Electron Microscopy for Nanostructure Characterization*” pp. 152-191 in *Scanning Microscopy for Nanotechnology: Techniques and Applications*, ed. by W. Zhou and Z. L. Wang, Springer (2006).
- ⁴ G. Nicotra, PhD thesis – University of Catania (2006).
- ⁵ A.E. Blakeslee, *Mat. Res. Symp. Proc.* **148**, 217 (1989).
- ⁶ G. Capellini, M. De Seta, Y. Busby, M. Pea, F. Evangelisti, G. Nicotra, C. Spinella, M. Nardone, and C. Ferrari, *J. Appl. Phys.* **107**, 063504 (2010)
- ⁷ Z. Yu, D. A. Muller, and J. Silcox, *J. Appl. Phys.* **95**, 3362 (2004).

Panel D

Micro-Raman Spectroscopy

D.1 Introduction

Raman spectroscopy is a photon in-photon out technique based on the inelastic scattering of monochromatic light, usually from a laser source. The frequency of the incoming photons changes upon interaction with the sample due to the excitation of vibrational modes (generally referred as phonons in case of crystalline materials). Raman spectroscopy can be used to study solid, liquid and gaseous samples, and have wide applications for chemical analysis, since the vibrational excitations in a medium represent a fingerprint of its composition.

Moreover Raman spectroscopy has emerged as a promising and feasible solution for an accurate characterization of composition and strain in alloy of group IV and III-V semiconductors. In fact the optical phonon modes of the alloy are strongly affected by their composition and strain, with the additional advantage of being a fast and nondestructive technique.

The outline of this panel is as follows. First, the basic theory underlying Raman spectroscopy is reviewed. Then a typical experimental setup for micro-Raman is described. Finally the effects of composition and strain on the Raman modes in SiGe/Si systems are critically discussed.

D.2 Raman effect: general theory

The vibrations of a crystal are described not in terms of the vibrations of individual atoms but in terms of collective motions in the form of waves, called lattice vibrations. Each possible vibration j of the lattice is characterized by a wavevector \mathbf{q}_j and a frequency ω_j . The vibration amplitude, at position \mathbf{r} , is given by^{1,2}:

$$Q_j = A_j \exp[\pm i(\mathbf{q}_j \cdot \mathbf{r} - \omega_j t)] \quad (\text{D. 1})$$

where Q_j is the normal coordinate of the vibration and A_j is a constant. Such a quantized lattice vibration is called a normal mode or a phonon. These lattice vibrations may cause a variation in the electrical susceptibility of the crystal, which can give rise to ‘‘Raman scattering’’. A *classical* way to explain Raman scattering is the following. When monochromatic light of frequency ω_i is incident on a crystal in a direction \mathbf{k}_i , the associated electric field \mathbf{E} will induce at position \mathbf{r} an electric moment \mathbf{P} , which is related to \mathbf{E} through:

$$\mathbf{P} = \varepsilon_o \chi \mathbf{E} = \varepsilon_o \chi \mathbf{E}_0 \exp[i(\mathbf{k}_i \cdot \mathbf{r} - \omega_j t)] \quad (\text{D. 2})$$

where χ is the susceptibility tensor, which describes the response of the crystal to the electric field. If the atoms of the sample are vibrating, the susceptibility may change as a function of these vibrations. This can be expressed by expanding χ , for each normal mode of vibration j , in a Taylor series with respect to the normal coordinate of this vibration Q_j :

$$\chi = \chi_0 + \left(\frac{\partial \chi}{\partial Q_j} \right)_0 Q_j + \left(\frac{\partial \chi}{\partial Q_j \partial Q_k} \right)_0 Q_j Q_k + \dots \quad (\text{D. 3})$$

which can be redefined as:

$$\chi = \chi_0 + \chi_j^1 Q_j + \chi_j^2 Q_j Q_k + \dots \quad (\text{D. 4})$$

The first term will give rise to Rayleigh scattering, the second to first-order Raman scattering, and the third to second-order Raman scattering (two phonons are involved). For simplicity, we neglect the third and higher-order terms. Combining equations (D.1) to (D.3) results in:

$$\mathbf{P} = \varepsilon_o \chi_0 \mathbf{E}_0 \exp[i(\mathbf{k}_i \cdot \mathbf{r} - \omega_j t)] + \varepsilon_o \mathbf{E}_0 \left(\frac{\partial \chi}{\partial Q_j} \right)_0 A_j \exp[-i(\omega_i \pm \omega_j)t] \exp[i(\mathbf{k}_i \pm \mathbf{q}_j) \cdot \mathbf{r}] \quad (\text{D. 5})$$

From this it follows that the induced moment will reradiate light which has three distinct frequency components: ω_i , which is called Rayleigh scattering, and $\omega_i + \omega_j$ and $\omega_i - \omega_j$, which are called anti-Stokes and Stokes Raman scattering respectively. This will only be observed if χ_j^1 differs from zero. The scattering efficiency, I , depends on the polarization vector of the incident \mathbf{e}_i and scattered \mathbf{e}_s light, and is given by:

$$I = C \sum_j |\mathbf{e}_i \cdot \mathbf{R}_j \cdot \mathbf{e}_s|^2 \quad (\text{D. 6})$$

where C is a constant and \mathbf{R}_j is the Raman tensor of the phonon j . The \mathbf{R}_j are obtained from group theoretical considerations^{2,3}. They are second-rank tensors which are proportional to χ_j^1 , and they are used to calculate the polarization selection rules. Loudon³ derived the Raman tensors for each of the 32 crystal classes (symmetry point groups). It is worth noting that the expansion (D.5) is limited only to the first order term in the susceptibility. If considering also the second order term, the polarization \mathbf{P} becomes:

$$\mathbf{P} = z.o. + f.o. + \varepsilon_o \mathbf{E}_0 \left(\frac{\partial \chi}{\partial Q_j \partial Q_k} \right)_0 A_j \exp[-i(\omega_i \pm \omega_j \pm \omega_k)t] \exp[i(\mathbf{k}_i \pm \mathbf{q}_j \pm \mathbf{q}_k) \cdot \mathbf{r}] \quad (\text{D. 7})$$

where *z.o.* and *f.o.* mean zero order and first order, respectively. From this it follows that, if χ_j^2 differs from zero, the induced moment will reradiate light which has all the possible combinations among ω_i and $\pm\omega_j$ and $\pm\omega_k$.

From a *quantum physical* point of view, Raman scattering involves the destruction of a photon with frequency ω_i , incident from a light source, and the creation of a photon with frequency ω_s . Fig. D.1 shows a typical Feynman diagram and the related energy levels for a first-order Stokes scattering process. The scattering cross section can be calculated by treating this three-step process using third-order perturbation theory³. An electron–hole pair is created through interaction of the incident photon (frequency ω_i), with an electron. By this interaction, the electron goes from the ground state $|0\rangle$ to a state $|l\rangle$. By electron–phonon interaction, where a phonon of frequency ω_j is created (or annihilated in anti-Stokes), the electron goes from state $|l\rangle$ to state $|m\rangle$. By recombination of the electron–hole pair, a photon with frequency ω_s is emitted, where $\omega_s = \omega_i - \omega_j$ (for anti-Stokes it would be $\omega_i + \omega_j$). Because conservation of momentum is required for each intermediate step, whereas conservation of energy is required only for the overall process, both real and virtual intermediate states are allowed. Further, the three steps described above are taking place instantaneously, so the order in which they occur is not important. This results in six types of this kind of process.

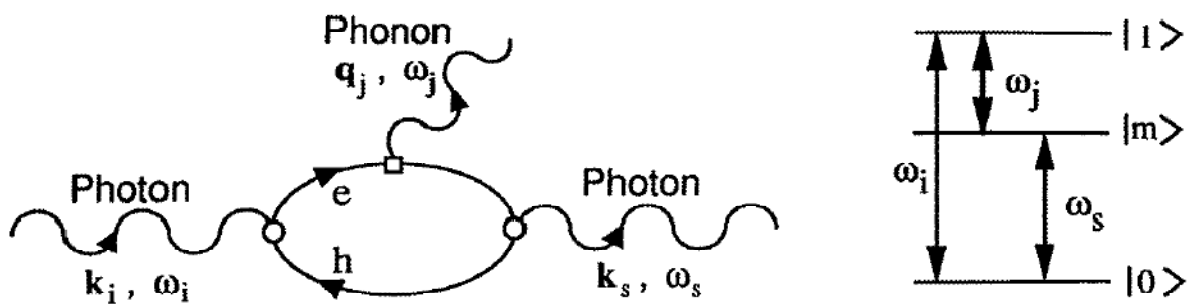


FIG. D.1. Feynman diagram and related energy levels for a first-order Stokes scattering process.

D.3 Experimental setup

Raman scattering is a second-order inelastic scattering process, and therefore, its intensity is very weak compared with first-order effects such as elastic Rayleigh scattering. Typically about one photon out of 10^{12} is inelastically scattered. For this reason, very sensitive detectors are required, and the monochromator should have a high rejection ratio of the Rayleigh-scattered light (double monochromator). Fig. D.2 shows a typical experimental set-up of a Raman spectroscopy system. The incident light is provided by a laser. This light is focused on the sample, either directly through a cylindrical lens (often a 50 mm lens, this is called macro-Raman spectroscopy), or through a microscope (as shown in the figure), in which case one speaks about micro-Raman spectroscopy. The microscope, often *confocal*, allows one to change the analyzed surface from about $1\ \mu\text{m}$ to a few μm ($100\times$ to $10\times$ objective). For reliable local mechanical stress measurements, the basis of the

microscope should be an automatic XY stage, allowing the sample to be moved in small steps in a well controlled manner. The scattered light of the sample is collected, either in back scattering (micromode) through the same microscope, or in back scattering, near back scattering or 90° scattering for the macro-mode, and directed into the double pre-monochromator through the entrance slit (S1) and into the spectrograph through the exit slit (S3). The double pre-monochromator consists, in general, of two identical units which are separated by the intermediate slit (S2). Each unit has two spherical mirrors and one grating. These gratings are typically blazed at 600 or 1800 grooves/mm. The spectrograph is composed of two spherical mirrors and a grating, in general with 1800 grooves/mm. The position of the gratings of the pre-monochromator and spectrometer, and the width of the slits is controlled through a computer. The aperture of the entrance and exit slits determines the resolution, i.e. the width at half maximum height of the spectral peak. The smaller the slit, the better the resolution, but the weaker the signal. The main role of the intermediate slit is to reduce scattered light. At the exit plane of the spectrograph, a photomultiplier, multichannel detector or CCD detector is mounted.

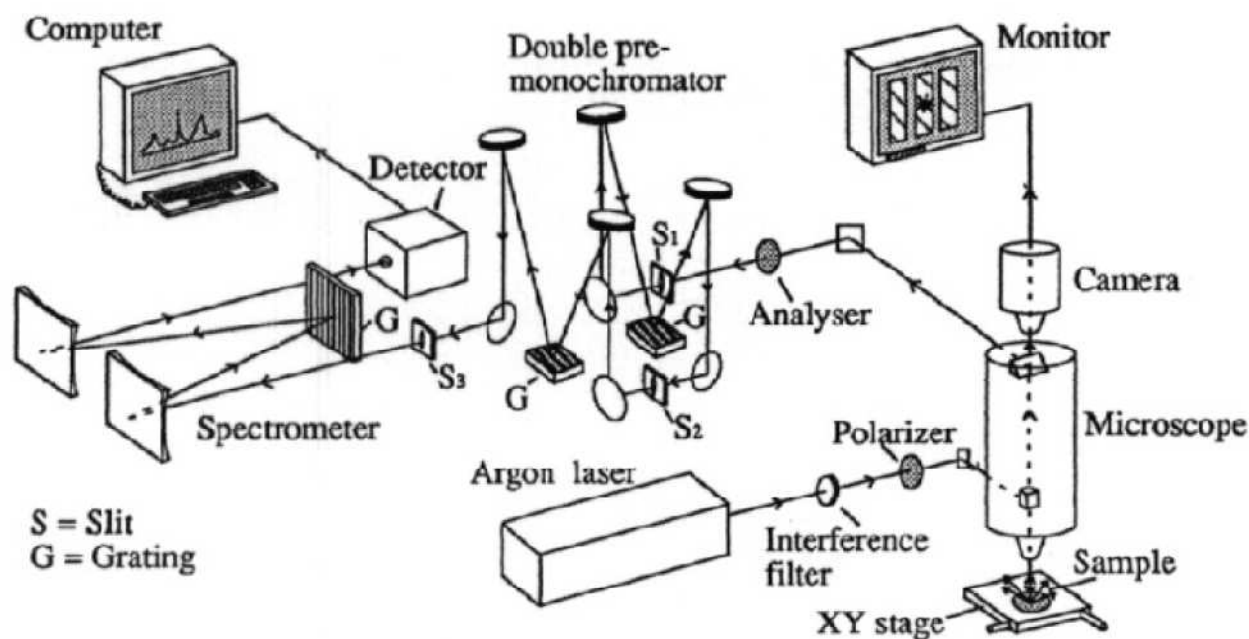


FIG. D.2 Experimental setup of a micro-Raman Spectrometer

D.4 Application to a strained SiGe/Si system

A fundamental issue in heteroepitaxial SiGe/Si systems is to be able to determine the epilayer strain ϵ and the composition x , because these parameters affect the electronic and optical properties of the material. Raman spectroscopy is expected to be a very useful technique for characterization

of SiGe/Si heterostructures, since the frequencies of the optical modes are entirely determined by ε and x . Nevertheless, precise measurements of these parameters can be performed only if relations describing the dependence of the Raman active phonon frequencies on ε and x are well known.

In $\text{Si}_{1-x}\text{Ge}_x$ alloys, three first-order Raman modes are presents: the Ge-Ge, the Si-Ge, and the Si-Si nearest neighbors vibrations. For a given alloy composition grown pseudomorphically on material with in-plane lattice parameter a_{\parallel} , the biaxial strain due to lattice mismatch induce a frequency shift of the Raman mode given by⁴:

$$\Delta\omega_j(x, \varepsilon) = \omega_j(x, \varepsilon) - \omega_{0j}(x) = b_j\varepsilon = b_j \frac{a_{\parallel} - a_{epi}}{a_{epi}} \quad (\text{D.8})$$

where ω_j and ω_{0j} are, respectively, the j mode Raman frequency of the strained and relaxed alloy, a_{epi} is the relaxed epilayer lattice constant and b_j is the so-called strain shift coefficient.

In Fig. D.3(a) are reported the Raman mode frequencies measured by Pezzoli *et al.*⁵ as a function of the Ge concentration x of $\text{Si}_{1-x}\text{Ge}_x$ relaxed layers. For the Si-Si and Ge-Ge lines there is an almost linear variation of the peak position with the composition, while the Si-Ge mode behavior is highly non linear. In Fig. D.3(b) are shown the Ge-Ge, Si-Ge and Si-Si Raman spectra measured by Pezzoli *et al.*⁵ for a $\text{Si}_{0.4}\text{Ge}_{0.6}$ layer under different biaxial strain conditions, as obtained by tailoring the lattice parameter of the substrate. They found that the peak shift to lower energy as the epilayer changes from a compressive to a tensile stress state. Repeating this type of experiment for different composition x , they were able to determine the behavior of the phonon strain shift coefficients b_j for the three modes as a function of x (see Fig. D.3(c)). Their results evidenced negligible variations through all the composition range.

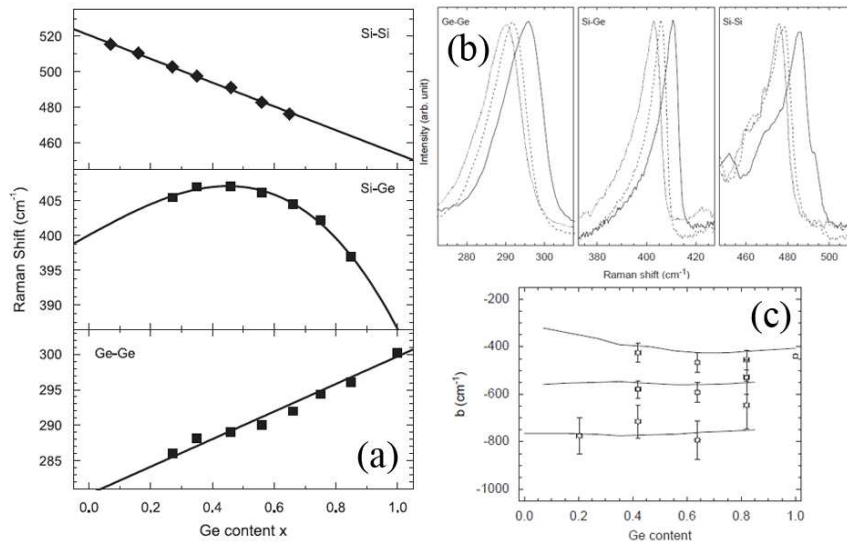


FIG. D.3. Panel (a): frequency of the three optical modes as a function of the Ge concentration x in unstrained $\text{Si}_{1-x}\text{Ge}_x$ alloys (full squares). Panel (b): Ge-Ge, Si-Ge, and Si-Si Raman spectra for $\text{Si}_{0.4}\text{Ge}_{0.6}$ epilayers relaxed (dashed line) and under a compressive (full line) or tensile (dotted line) strain. Panel (c): experimental strain shift coefficients for the Si-Si (diamonds), Si-Ge (squares), and Ge-Ge (circles) Raman modes. Solid lines are valence force field calculation results⁶.

Bibliography

- ¹ Bruesch P 1981 *Phonons: Theory and Experiments. Lattice Dynamics and Models of Interatomic Forces (Springer Series in Solid-State Sciences 34)* (Berlin: Springer)
- ² Cardona M 1982 *Light Scattering in Solids II (Topics in Applied Physics 50)* ed M Cardona and G Guntherodt (Berlin: Springer)
- ³ Loudon R 1964 *Adv. Phys.* **13** 423–80
- ⁴ J.M. Hartmann, B. Ghallas, J. Zhang, J.J. Harriss *Semicond. Sci. Technol.* **15**, 370 (2000)
- ⁵ F. Pezzoli, E. Bonera, E. Grilli, M. Guzzi, S. Sanguinetti, D. Chrastina, G. Isella, H. von Kanel, E. Wintersberger, J. Stangl, G. Bauer, *Materials Science in Semiconductor Technology* **11**, 279-284 (2008)
- ⁶ Pezzoli F, Grilli E, Guzzi M, Sanguinetti S, Chrastina D, Isella G et al., *Mater Sci Semicond Process* **9**, 541 (2006).

Panel E

Tip Enhanced Raman Spectroscopy

E.1 Introduction

The main drawback of Raman spectroscopy is the extremely low cross section ($\frac{d\sigma}{d\omega} = 10^{-28} \text{ cm}^{-2} \text{ sr}^{-1}$) of the Raman event compared with the much higher probability of other optical processes such as the Rayleigh scattering or fluorescence. Thus, powerful exciting sources, very sensitive detectors and a large number of scattering atoms are needed in order to record a Raman spectrum. The last constraint would make Raman spectroscopy rather unsuitable for surface studies, where usually one has to deal with a small amount of material, down to the monolayer level, or even less.

In contrast to this expectation, some twenty years ago, at first Fleischmann^{1,2} and then Van Duyne *et al.*³ reported huge Raman intensities observed for certain adsorbates at rough silver electrodes. Van Duyne concluded that the signal arises due to a tremendous enhancement of the Raman cross section for the adsorbed molecules. A suitable choice of the metal (copper, silver and gold being the most used) and a *roughening* of the surface turned out to be the key factors for the enhancement. Since then, this effect is known as the surface enhanced Raman scattering (SERS) and has been widely studied^{4,5,6,7,8}. Today, it is commonly accepted that the enhancement arises mainly due to two different mechanisms operating at the same time. In the literature, these are usually named the *electromagnetic* enhancement and the *chemical* enhancement; together, they may provide enhancement factors between 10^6 and 10^8 ; yet, the exact partition between the two is still a matter of debate.

However, SERS suffers of a severe limitation due to the essential need to have the sample surface heavily roughened. Moreover, because of the random distribution of the surface roughness, even considering a uniform coverage of the effective area, two different positions on the surface will never give the same enhancement, thus making a quantitative analysis rather delicate. Most of the above mentioned limitations could be circumvented by using an external field enhancing unit, as for instance a metallic object of sub-micrometer dimensions placed a few Å above a crystalline sample surface. This simple geometry actually describes the junction formed in a scanning tunneling microscope (STM) with the piezo-elements controlling, at atomic resolution, the height and lateral movement of the scanning tip and a conductive sample to close the electric circuit and to

enable the current feedback loop. This approach has been called Tip Enhanced Raman Spectroscopy (TERS)⁹. There are more features that make it very appealing. First of all the possibility to have a local (in the sub-wavelength domain) non-invasive analytical tool: as far the illumination is concerned, Raman spectroscopy and SERS may be regarded as far field optical techniques, where the laser spot size and subsequent lateral resolution cannot be lower than half the wavelength of the excitation beam, due to the diffraction limit of light. In contrast, the extension of the tip induced enhanced field depends mainly on the size of the tip itself. A number of theoretical investigations point out that the highest fields are expected for tips with a small radius, between 10 nm and 200 nm. To a first approximation, only the area directly below the tip, shadowed by it, will be influenced by the external field. Such an area is by far smaller than the average diffraction limited laser spot (0.5-2 μm).

The panel is organized as follows: first we describe the basic physical principles underlying the field enhancement effects, and then we discuss the case of near-field enhancement induced by a metallic tip in tunneling contact with a crystalline surface. Finally, the possible operating modes of a TERS system are described and the method for the fabrication of Au tip is presented.

E.2 Surface plasmon polaritons

The so-called electromagnetic effect involves the excitation of surface plasmon polaritons (SPP) at the metal tip apex. Since these modes will play a major role in all the forthcoming discussion, it is worthwhile introducing them here. As long as the free electron model is consistent, a metal behaves like a plasma of an electron gas, the electrons being the mobile charge carriers, and the dielectric function may be expressed as:

$$\varepsilon(\omega) = 1 - \frac{Ne^2}{\varepsilon_0 m_e \omega^2} = 1 - \frac{\omega_{BP}^2}{\omega^2} \quad (\text{E. 1})$$

where:

$$\omega_{BP} = \frac{Ne^2}{\varepsilon_0 m_e \omega^2} \quad (\text{E. 2})$$

is defined as the (bulk) plasma frequency for the metal; ω is the frequency of light, e and m_e are the electron charge and mass, ε_0 is the permittivity of free space and N is the electron density of the metal. Using the general relation for the optical dispersion of an electromagnetic wave in an isotropic medium:

$$\varepsilon(\omega, k)\omega^2 = c^2 k^2 \quad (\text{E. 3})$$

the dispersion curve for the bulk plasma is obtained:

$$\omega^2 - \omega_{BP}^2 = c^2 k_{BP}^2 \quad (\text{E. 4})$$

The oscillating electron cloud of a metal behaves as a collection of coupled harmonic oscillators with a characteristic resonance frequency given by Eq. (E.2), where the *plasmon polariton* is the quasi-particle of the excited mode.

This assumes so far a bulk (volume) plasma. Next, an air/metal phase boundary system with the metal surface at $z = 0$ and $\varepsilon(\omega) = \varepsilon_M(\omega)$ for $z < 0$ is considered. Solutions for the Laplace equation that fulfill the boundary conditions for the tangential components of the electric field and for the normal component of the electronic displacement exhibit the form:

$$E_z = E_{0z} \exp[i(kx - \omega t)] \exp(-k_z z) \quad (\text{E. 5})$$

the dispersion relationship reads as follows:

$$k_{sp} = \frac{\omega}{c} \sqrt{\frac{\varepsilon_M}{\varepsilon_M + 1}} \quad (\text{E. 6})$$

The limiting frequency for the oscillating charges at the surface, the surface plasma frequency, is defined by:

$$\omega_{sp} = \frac{\omega_{BP}}{\sqrt{2}} \quad (\text{E. 7})$$

The wave described in Eq. (E.5) is an evanescent wave, i.e. it is a wave propagating along the interface and decaying exponentially in intensity as it penetrates the less dense medium. This is also seen in Fig. E.1, where the dispersion curve of the surface plasma is confined below the propagating wave domain. It means that volume plasmons may be excited by any incident light with $\vartheta_i < \vartheta_c$ (the critical angle), if $k_x(\omega, \vartheta_i) = k_{BP}(\omega)$ (the red dotted line intersects the dispersion curve) but not surface plasmons, for which $k_x(\omega, \vartheta_i) < k_{sp}(\omega)$. This is why they are usually described as radiative and non radiative processes, respectively.

In the foregone discussion a planar surface was considered to derive the surface plasmon dispersion curves. However, a small perturbation of the regular surface structure (like a metallic tip in tunneling contact with the surface) may also provide the missing momentum to satisfy the law of momentum conservation:

$$k_x + G_p = k_{sp} \quad (\text{E. 8})$$

where G_p is the reciprocal of the perturbation extent (such a possibility is often called the *umklapp* process¹⁰), so that also surface plasmon modes may be excited and radiate.

The surface plasmons are therefore electromagnetic waves propagating along a flat surface. Any structure in their way acts as an hindrance or scattering center that can convert the delocalized mode into a localized one (LSP), the electromagnetic wave being confined into sub-wavelength structures. The local field strength, amplitude and the resonant condition associated with the charge

oscillations are all governed by the size and geometry of each structure as well as by their spatial arrangement(s).

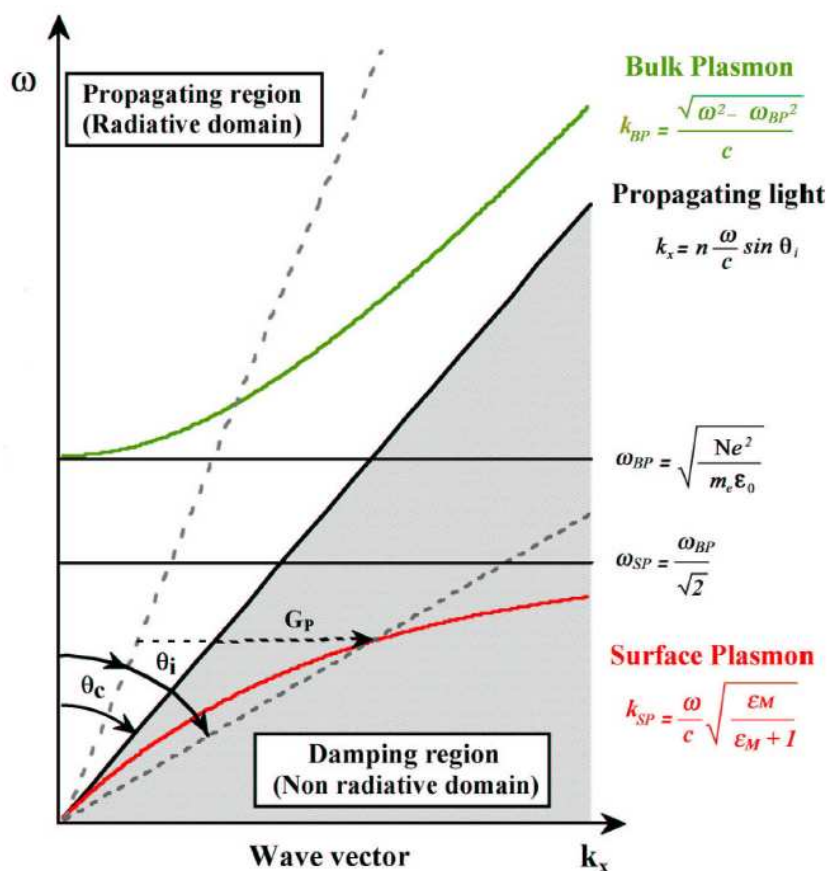


FIG. E.1. Dispersion curves for bulk and surface plasmons. Excitation of bulk plasmon in the metal is allowed at the frequency defined by the crossing point between the dispersion curve and the dotted line (angle of incidence $\vartheta_i < \vartheta_c$). Excitation of surface plasmon is normally forbidden (the required angle of incidence is larger than the critical angle ϑ_c).

E.3 Electromagnetic enhancement at the tip apex

Let us consider first the electronic processes taking place at a metal sub-wavelength particle due to illumination with a monochromatic light source (see diagram in Fig. E.2). The above mentioned LSP are excited by the absorption of a photon with energy $\hbar\omega_i$; the particle is now found in an excited state and will relax to the ground state (relaxation time, τ , in the order of 10^{-15} s) with the annihilation of the LSP mode and the creation of a second photon.

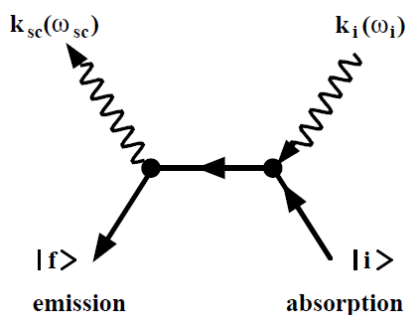


FIG. E2. Rayleigh scattering by a metal surface.

This process is also a Rayleigh scattering with the particle acting as the scatterer of light: the frequency of the emitted photon remains the same as for the incident photon $\omega_{sc} = \omega_i$. The emitted electromagnetic field is thus represented by the local field enhanced by the induced oscillations of the electrons in the metal particle. Since the cross section for the Raman process scales with the fourth power of the electromagnetic field enhancement¹¹, a moderately enhanced field gives an extremely enhanced Raman intensity.

Let us consider now a metallic tip of sub-micrometer dimensions placed a few Å above the sample surface (see Fig. E.3). By the illumination of such a cavity, plasmon modes will be excited that are localized below the tip, i.e. at the gap formed by the tip apex and the surface. This approach should bring a substantial Raman enhancement since the field associated with the external body should extend over several nanometers, thus reaching the underlying surface if the tip is at tunneling distance. In a figurative way, the tip may be considered as playing the role of a particle, where the enhancing field is extremely localized, facing over the surface. Since it is mainly the tip which provides the electromagnetic enhancement, the sample may have a smooth surface contrary to the SERS case. Such an improvement, i.e., the availability of a vibrational spectroscopy with high spatial resolution, would be extremely valuable for the study of surface processes on crystalline material. Moreover, Raman studies could be extended to any kind of samples: only the choice for the tip material is restricted, but virtually any conductive surface may be chosen as substrate, also a semiconductor.

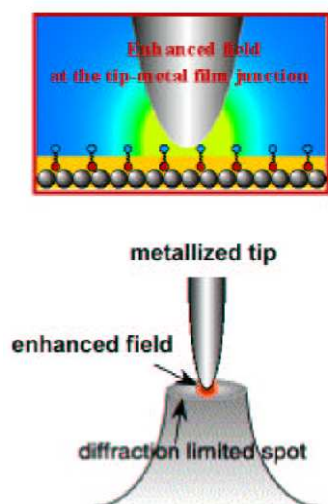


FIG. E.3. Schematic diagram of the field enhancement at the apex of a metallic tip in case of TERS configuration.

The dominant contribution producing the enhancement factor in TERS is thus associated with the large local field enhancement due to the excitation of localized surface plasmons at the tip-substrate system when illuminated by the incoming radiation. The strength of the localized surface plasmon resonance and the corresponding TERS enhancement is dependent on many factors, such as the size and shape of the tip, the materials of the tip and substrate, the distance between the tip

and substrate, and the dielectric environments of TERS. The strong near-field coupling effect between the tip and substrate usually plays a key role in producing efficient enhancement in a real TERS system. Figure E.4(a) and E.4(b) show Finite Difference Time Domain (FDTD) simulations performed by Yang *et al.*¹² of the calculated optical field enhancement in TERS with and without a gold substrate, respectively. The Au tips are modeled as a metal cone with a radius of curvature 25 nm. The 632.8 nm monochromatic plane wave is incident at an angle $\phi = 60^\circ$, with the polarization in the plane of incidence, from the side. The distance d between the tip and substrate is set to be 2 nm. The maximum field enhancement, defined as the ratio between the maximum local field E_{loc} and the incoming field E_{in} amplitude, $M = |E_{loc}|/|E_{in}|$, in a single tip is only about 20 (Fig. E.4(a)), which is much smaller than the field enhancement factor of 189 in a tip–substrate coupled system (Fig. E.4(b)).

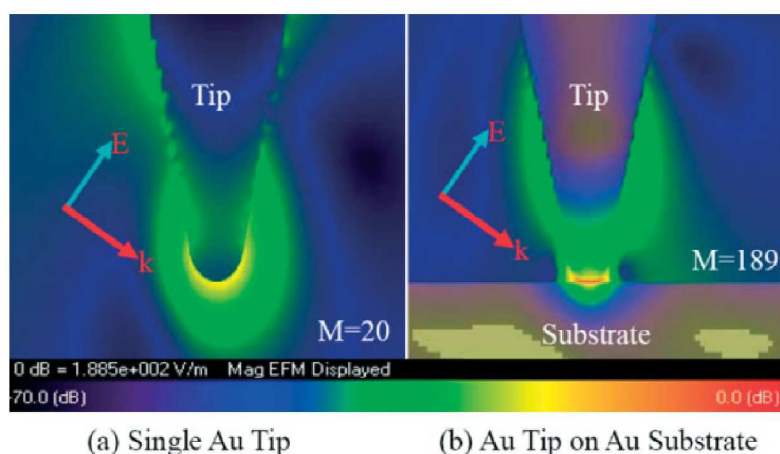


FIG. E.4. FDTD simulations of the electric field distribution for a single Au tip (a), and a gold tip held at distance $d = 2$ nm from a gold substrate surface. The polarization E and wave vector k of the incoming light are displayed in the schematics. M stands for the maximum. (From Ref. 12)

In Fig. E.5 are shown the FDTD simulations¹² of the maximum field enhancement at the surface of a Au substrate when probed with gold tips of different sizes under p -polarized laser excitation with a wavelength of 632.8 nm illuminated from the side at an incident angle of 60° . The tip–substrate distance is fixed in all cases at a value of $d = 2$ nm. The radius of curvature of the tip ranges from 5 to 80 nm. The calculations show that the field enhancement does not change very much as the tip size changes. The value of the enhancement factor is in the range of 180 to 220. The TERS enhancement increases slowly when the tip radius increases from 15 to 50 nm. Further increase of the tip radius does not provide additional enhancement.

Moreover the tip radius significantly affects the spatial resolution of TERS. Due to the highly localized electromagnetic fields, TERS can provide very high spatial resolution, smaller than the size of the tip apex, mainly determined by the tip geometry. The field distribution in a plane

parallel to and 1 nm above the substrate is shown as an inset in Fig. E.5 corresponding to a tip radius r of 5, 25, and 50 nm, respectively. The figure clearly indicates that the center of the area underneath the tip apex gives the highest enhancement, and the spatial resolution, quantified as the full width at half-maximum (FWHM) of the Raman enhancement, is strongly dependent on the tip radius. Decreasing the tip radius can improve dramatically the spatial Raman resolutions of TERS, and therefore tips with sharp ends (small radius of curvature) are preferable in TERS.

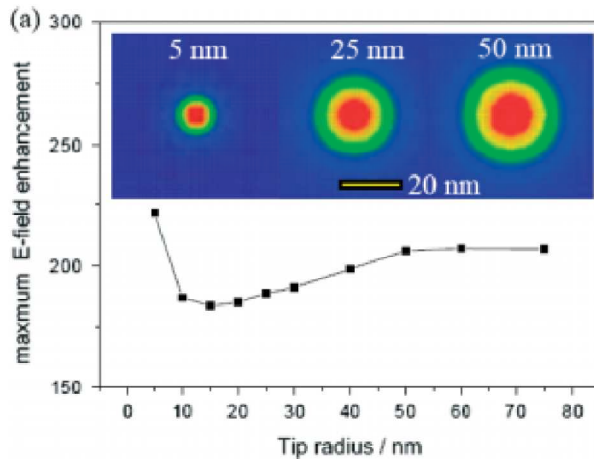


FIG. E.5. Tip size dependence of the maximum field enhancement and spatial resolutions of TERS. Maximum electric field enhancement in the gap as a function of tip radius. The inserts give the spatial field distribution for tip radius $r = 2, 25$, and 50 nm respectively, from left to right. The yellow scale bar is 20 nm. (From Ref. 12)

E.4 Instrumentation

The crucial attribute of a TERS experiment is a field enhancing metal object which is raster scanned across a sample surface. An essential pre-requisite for any TERS experiment is a scanning probe microscope of some sort to provide a scanning stage that controls precisely the distance between the object and the surface. Either AFMs or STMs are presently used for this purpose. The latter can control the distance more easily, even if the use is restricted to either conductive samples or very thin layers of non-conductive samples on a conductive support.

E.4.1 TERS configurations

A TERS experiment can be performed in two different operating modes: back-illumination and side illumination. Fig. E.6(a) shows a schematic diagram of a TERS setup working in back-illumination mode. An inverted Raman microscope is coupled with a scanning probe microscope for synchronized use. The Raman microscope is required to illuminate the metal tip. The back scattered Raman signal is collected through the same objective and notch or edge filter are used to block the laser line. After this filter stage, the signal is coupled to a spectrometer equipped with a cooled charge-coupled device (CCD) for spectrally resolved measurements. This configuration is,

however, limited to transparent samples based on thin glass cover slips, whereas, obviously, not all materials of interest can be deposited on transparent substrates. Moreover, an important requirement for attaining maximum enhancement under the tip is the orientation of the electric field of the incident light along the tip axis¹³. This condition is difficult to achieve in the bottom-illumination geometry. Thus, despite the many advantages provided by bottom illumination, it is not the optimum geometry for TERS. The side-illumination TERS configuration, see Fig. E.6(b) for a schematic diagram, working in reflection mode is more versatile as it can be performed on any kind of samples including bulk and opaque ones. Unfortunately, owing to geometrical constraints, only long-working-distance objectives can be used, with numerical apertures (NA) limited to ~ 0.5 and typically producing spots of some square micrometers in the visible range. Under such conditions, larger field enhancement factors would be required to have the ratio between the TERS signal and the far field background greater than 1.

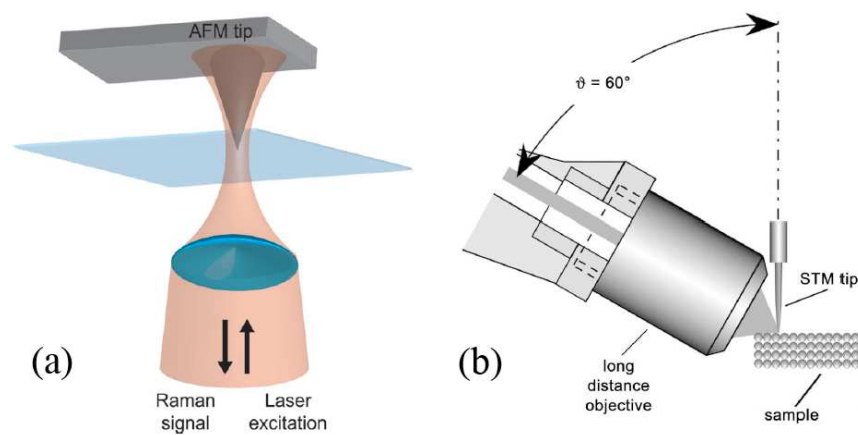


FIG. E.6. TERS operation modes: back-illumination (a), and side-illumination (b)

E.4.2 Scanning Tunnelling Microscopy (STM)

The concept of the operation of STM is as follows. A very sharp metallic tip is placed so close to the probed surface that the wave functions of the closest tip atoms and the surface atoms overlap. This take place at tip-sample gap of $\sim 5 \div 10 \text{ \AA}$. If one applies a bias voltage U between the tip and the sample, a tunneling current will flow through the gap. In simplified form the tunneling current density j is given by:

$$j = \frac{D(U)U}{d} \exp(-Ad\sqrt{\phi_B}) \quad (\text{E. 9})$$

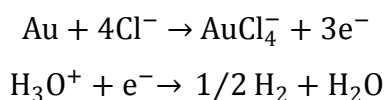
where d is the effective tunneling gap, $D(U)$ reflects the electron state density, A is a constant, and ϕ_B is the effective barrier height of the junction. The success of resolving the atomic structures of

conductive surfaces with the STM is based on the exponential distance dependence of the tunneling current¹⁴.

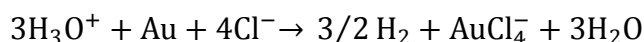
In the usual topographic studies (generally performed in the constant current mode), the tunneling bias is kept much below ϕ_B and the tunneling current is set to a fixed value. A metal tip is laterally scanned over the surface by piezo-elements. Via an internal electrical loop the z-elongation of the piezos (onto which the tip is mounted) is adjusted in order to have always the set current between tip and sample. The voltage(s) applied are recorded and processed to produce an “image” of the surface.

E.4.3 Tip fabrication

In the TERS experiment presented in the Chapter 4 we used gold tips fabricated by electrochemical dissolution in a proper etching solution^{15,16}. For gold, a concentrated hydrochloric acid solution was used. The overall electrochemical reaction is:



and thus:



A small electrochemical cell was used to etch the wire, as depicted in Fig. E.7(a). The counter electrode was a small gold ring (diameter of the ring 1 cm) surrounding the wire (diameter 0.25 mm). A constant voltage of 3.0 V was applied to the cell. When the wire was partially immersed into the electrolyte, the etching of the metal proceeded as a necking in around the region closer to the counter electrode but material was also removed from the lower part of the wire. The etching was stopped manually when the lower end finally dropped. Fig. E.7(b) shows a SEM image of typical gold tip obtained by this method.

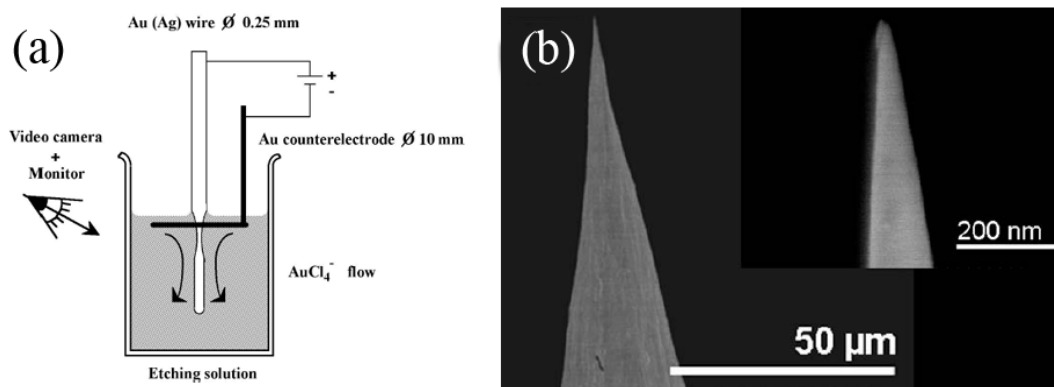


FIG. E.7. Panel (a): diagram of the electrochemical cell used for etching metal tips. SEM images of a gold tip obtained by the method shown in (a) (From Ref. 17).

Bibliography

- ¹ M.Fleischmann, P.J. Hendra and A.J. McQuillan, Chem. Phys. Lett. **26**, 163-166 (1974).
- ² M.Fleischmann, P.J. Hendra and A.J. McQuillan, J. Chem. Soc.-Chem. Comm. 80-81 (1973).
- ³ D.L. Jeanmarie and R.P. Van Duyne, J. Electroanal. Chem. **84**, 1-20 (1977).
- ⁴ Chang. R.K. and Furtak T.E., *Surface Enhanced Raman Spectroscopy* (Plenum Press, New York (1986)
- ⁵ Z. Tian, Ren B. and D. Wu, J. Phys. Chem. **106**, 9463-9482 (2002).
- ⁶ M. Moskovits, Rev. Mod. Phys. **57**, 783-826 (1985).
- ⁷ A. Campion and P. Kambhampati **27**, 241-250 (1998).
- ⁸ G.C. Schatz, Acc. Chem. Res. **17**, 307-376 (1984).
- ⁹ M. A. Young, J. A. Dierger, R. P. Van Duyne, *Advances in Nano-Optics and Nano-Photonics* (Eds: S. Kavata, V. M. Shalaev), Elsevier: Amsterdam (2007), pp 1.
- ¹⁰ Kittel C., *Introduction to Solid State Physics* (Wiley, New York, 1986)
- ¹¹ Loudon R., *The Quantum Theory of Light* (Clarendon Press, Oxford, 1984).
- ¹² Z. Yang, J. Aizpuruac and H. Xu, J. Raman Spectrosc. **40**, 1343–1348 (2009)
- ¹³ O.J.F. Martin, C. Girard, Appl. Phys. Lett. **70**, 705 (1997).
- ¹⁴ Chen C.J., *Introduction to Scanning Tunneling Microscopy* (Oxford Press, New York, 1993)
- ¹⁵ J.P. Ibe, P.P. Bey, D.P. DiLella and R.J. Colton, J. Vac. Sci. Technol. A **8**, 3570-3575 (1995).
- ¹⁶ L. Libioulle, Y. Houbion and J.M. Gilles, J. Vac. Sci. Technol. B **13**, 1325-1331 (1995).
- ¹⁷ M. Chaigneau, G. Picardi, R. Ossikovski, Surface Science **604** 701–705 (2010)

Panel F

PhotoElectron Emission Microscopy

F.1 Introduction

The worldwide advances in nanoscience and nanotechnology have strongly pushed the development and improvement of adequate analytical methods. In the field of microscopy there has been dramatic progress in imaging performance. Today scanning tunneling microscopy (see Panel E) and transmission electron microscopy (see Panel C) are standard tools for imaging of surfaces with atomic resolution. Less progress has been achieved in the field of nano-spectroscopy. The spectroscopic mode of STM works very well within a few eV from the Fermi edge¹, but gives no access to core levels, being the ‘fingerprint’ of elements and their chemical environment in a compound. Scanning Auger Microscopy (see Panel A) and Energy-filtered TEM (see Panel C) allows for a spatially resolved chemical characterization of the sample, but have difficult access to the investigation of the electronic band structure, which plays the dominant role in determining the electrical and optical properties of a material.

Looking at the problem with the eyes of a spectroscopist, photoelectron spectroscopy represents one of the most powerful technique. In fact energy analysis of the electrons yields the core level binding energies. This facilitates a fingerprint-like detection of elements and their chemical states in compounds, and allows direct access to the valence band structure of the investigated material. It is near at hand that the combination of photoemission with microscopy provides an attractive surface analytical tool. There have been several approaches to implement laterally resolved photoemission. A straightforward way is to focus the photon beam in a small spot and scan the surface, taking spectra at each point. This concept is used in various laboratories² and in a commercial instrument³, but its spatial resolution is limited to the x-ray beam spot size. The alternative way is parallel image acquisition via a magnifying lens system and an imaging energy analyzer. This approach provides both a higher data acquisition rate and the possibility to take energy-filtered images at selected photoelectrons lines and in real time.

The panel is organized as follows. After having introduced the basic principles of the photoemission process and the most used photon sources in condensed matter physics and nanoscience, we describe in detail the operation modes and the characteristics of the NanoESCA⁴ Energy-Filtered PhotoElectron Emission Microscope used for the measurements performed during

the thesis work, which exploits a double-hemispherical analyzer as aberration-corrected energy-filtering stage.

F.2 Basic principles of photoemission spectroscopy⁵

Photoemission spectroscopy performed with UV photons (UPS) and with X-ray photons (XPS) is based on the well-known photoelectric effect. The solid is irradiated by monochromatic photons which excite electrons from occupied states to empty states (within the solid), whence they are released into vacuum (free-electron-plane-wave states) and detected by an electron energy analyzer. Thus the kinetic energy of the emitted photoelectron is determined and its wave-vector outside the solid can be derived from its energy and the direction of the analyzer aperture with respect to the sample orientation. Since for the electron wave escaping from the crystal, the surface represents a 2D scattering potential (braking of translational symmetry), the wave vector perpendicular to the surface is not conserved.

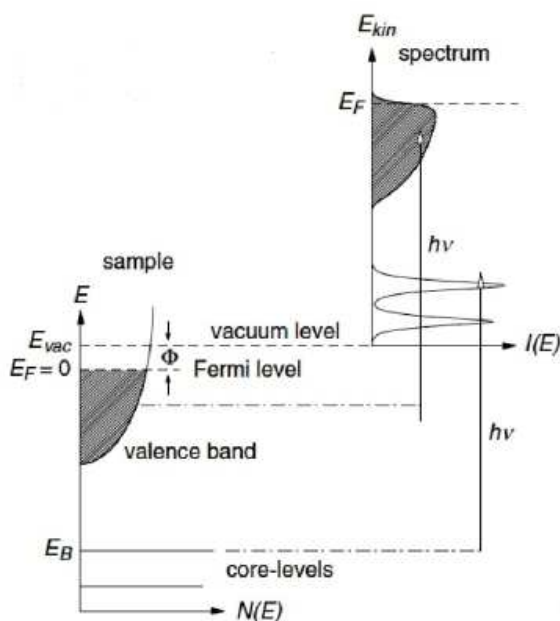


FIG. F.1. Schematic showing the principle of photoemission. An electron in a bound state is excited by a photon of energy $h\nu$: the electron is detected in its final state outside the sample at a kinetic energy given by $E_{kin} = h\nu - E_B - \Phi$, allowing one to deduce its initial state and binding energy. (From Ref. 6)

The basic relation for the photoemission process becomes clear from the Fig. F.1, where a schematic state density of occupied and empty states is plotted. Optical excitation by a fixed photon energy $\hbar\omega$ populates the empty states in the crystal above the vacuum level and the corresponding energy distribution of the electrons measured outside the crystal yields a qualitative image of the distribution of the occupied crystal states (valence and core-level states). The measured distribution of sharp peaks is superimposed to the true secondary background, which arises from electrons that have lost quasi-continuous amount of energy due to multiple scattering in the crystal. The sharp peak in the spectrum corresponds to a kinetic energy of the externally detected electrons given by:

$$E_K = \hbar\omega - E_i - \phi \tag{F.1}$$

where E_i is the binding energy of the initial state and ϕ the work function which has to be overcome by electrons reaching vacuum states. All energies in such a photoemission experiment are conveniently referred to the Fermi level of the sample.

F.3 Photon Sources

For XPS, the choice of the X-Ray laboratory photon sources is very limited. In fact, few materials combine high resistance to the electron beam, high cross-section for fluorescence emission, and a small natural width of the emitted X-ray lines. Actually only Al K α (1486.7 eV), Mo K α (1253 eV), and Si K α (1740 eV) can be envisaged. In the case of UPS, the most used laboratory photon sources are He discharge lamps, delivering photons at 21.2 eV (He-I) and 40.8 eV (He-II), with an intensity of 10^{16} photons/s·sr if working in He-I mode. Other noble gases can be also used, like Ar (Ar-I at 11.6 eV), Kr (Kr-I 12.6 eV), and Ne (Ne-I and II at 16.7 and 26.8 eV, respectively).

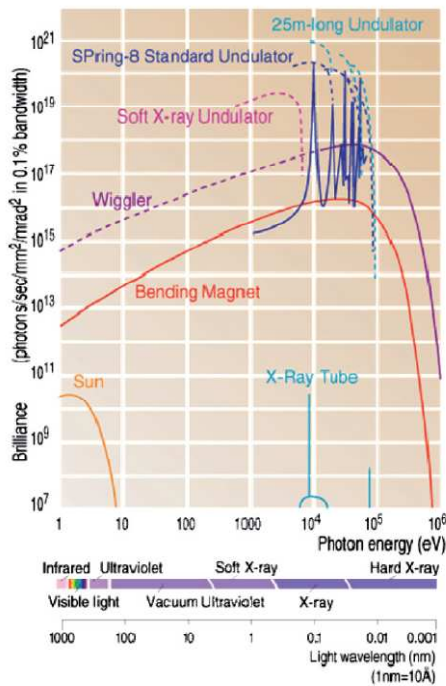


FIG. F.2. Comparison of the brilliance of different synchrotron radiation sources as a function of photon energy with that from a standard Al K α laboratory X-ray source.

Nowadays synchrotron radiation has come to play a vital role in photoemission spectroscopy, even if its beginnings were extremely modest. Its existence was known since of decades like a by-product of the particles accelerators, and its use was restricted to a parasitic mode. The first storage rings as ADONE in Frascati (Italy) or ACO in Orsay (France) were synchrotron radiation sources of this type. But the properties of the emitted radiation, the tunability on a wide energy range, its high

intensity, and the preferential emission within the orbit plane of the electrons moving into the ring, made the synchrotron radiation a source of photons out of pair in physics and chemistry of the condensed matter. The two limitations to the sensitivity of the photoemission spectroscopy with laboratory sources have been surmounted by the use of the synchrotron radiation. The high brilliance of the photon beam delivered by an undulator on a 3rd generation synchrotron is about six orders of magnitude greater than that one of a laboratory X-Ray source (see Fig. F.2), making accessible some physics phenomena which cannot be detected in laboratory. The continuous spectrum of the synchrotron radiation allows to adjust continuously the photon energy in order to optimize the photoionization cross-sections for the elements constituting the investigated sample. Moreover, the possibility to tune the photon energy allows to modulate the escape depth without changing the detection angle.

F.4 The NanoESCA spectro-microscope

The NanoESCA is an imaging analyzer derived from an electrostatic photoemission electron microscope (PEEM) column, combined with an aberration compensated double hemispherical analyzer. A schematic of the optical layout and a photograph of the instrument indicating the operation modes are shown in Fig. F.3.

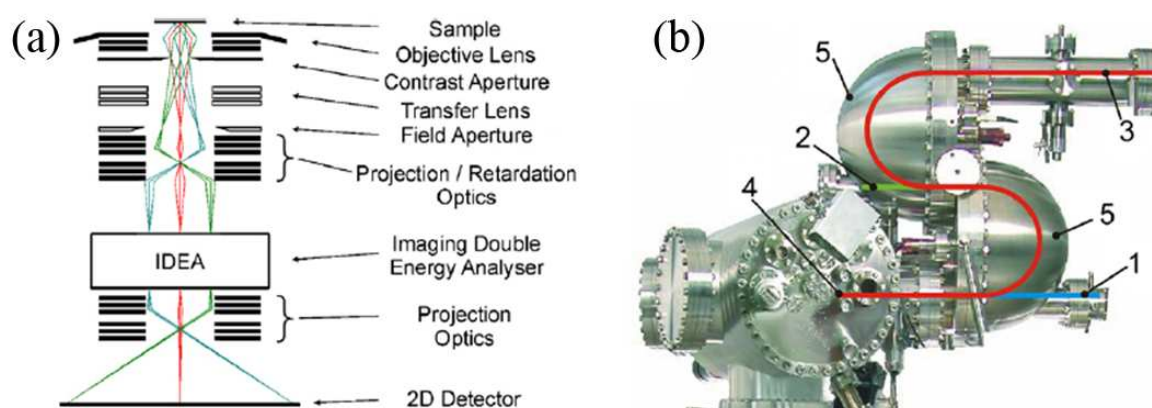


FIG. F.3. Panel (a): scheme of the optical layout of the NanoESCA instrument for real space imaging. Panel (b): photograph of the instrument. The optical path for the three working modes: direct non-energy filtered PEEM (1), small-spot spectroscopy with a channeltron detector (2), and energy filtered imaging (3) are indicated by the colored lines. (4) sample position, (5) double hemispherical analyzer. (From Ref. 7)

The PEEM column works as follows. Photons are incident on the sample surface at an angle of 65° with respect to the sample normal. The sample is at a potential close to zero, and a high tension, typically between 10 and 20 kV, allows an extractor lens, situated some millimeters away from the sample, to collect the photoelectric emission on a large range of emission angles. Then, a

lens system is used to focus the photoemitted electrons and to create a first intermediate image. Finally, a projective lens system allows the magnification of this first image. Three operating modes are available: direct non-energy-filtered PEEM; small spot, area selected spectroscopy; and energy filtered imaging. The fully electrostatic PEEM column is either used for direct (secondary electron) PEEM-imaging or as the entrance lens for the analyzer. The good lateral resolution of the microscope is accomplished by the immersion objective lens with an extraction voltage of up to 16 kV. In contrast to other cathode lenses described in literature^{8,9} the objective lens works with asymmetrical voltages where the electrons are decelerated in the focusing field of the lens towards the low voltage column typically at 1000 eV drift energy. The objective lens is equipped with exchangeable and adjustable contrast apertures of different sizes and an octopole stigmator to compensate for axial astigmatism. A continuously adjustable iris acts as a field aperture for small spot spectroscopy or angular imaging. The low column energy allows the retardation of the electrons toward the low pass energies which are needed for high transmission operation. The projection lenses project and retard the electrons into the analyser entrance or, in PEEM-mode with the energy analyzer deactivated, magnify it onto the image intensifier for non-energy filtered operation. A channeltron detector located behind the first hemisphere can be used to acquire fast small-spot overview spectra. A set of projection lenses after the second analyzer is used to obtain the final magnification in energy filtered operation. The magnification can be adjusted over a large range between $< 5 \mu\text{m}$ up to $> 650 \mu\text{m}$ field of view. In energy filtered operation, image stacks are recorded by scanning the sample voltage with fixed analyser pass energy and automatic refocussing of the objective lens. The three-dimensional data stack, $I(x,y,E)$, therefore contains at each image pixel microscopic and spectroscopic information, and can be analyzed off-line by standard data reduction techniques, as described in the Chapter 4.

The analyzer and the entrance lens used for imaging of the photoelectrons set the limits to the performance of the instrument, as the energy resolving power and lateral resolution are closely linked to the achievable transmission. A higher resolution is generally only feasible if the transmission of the instrument is reduced by inserting apertures, either angular apertures to enhance the lateral resolution or apertures in a dispersive plane to achieve a higher energy resolution.

F.4.1 Energy resolution and transmission

Most of the properties of an ideal hemispherical analyzer (HSA) can be easily deduced from its approximate (second order) imaging properties in the dispersive plane. Neglecting the fringe field effects at the entrance and exit slits, electrons entering the hemispherical field at the entrance slit with an excess energy of ΔE_{kin} over the pass energy E_{pass} of the analyzer at a point x_1 from the

slit centre and an angle α_1 with respect to the optical axis of the analyzer are transferred to the exit slit plane according to:

$$x_2 = -x_1 + 2R\varepsilon - 2R\alpha_1^2 \quad (\text{F. 2})$$

$$\alpha_2 = -\alpha_1 \quad (\text{F. 3})$$

where x_2 and α_2 are the coordinates in the exit slit plane (see Fig. F.6), R is the mean radius of the HSA and $\varepsilon = \Delta E_{kin}/E_{pass}$ is the relative energy difference of the electrons¹⁰. In the non-dispersive direction the electron coordinates are mirrored by the optical axis without second-order aberrations. Assuming a continuous energy distribution of the incoming electrons, the energy filtering action of the HSA described by Eq. (F.2) and (F.3) with an entrance slit of width w_1 and an exit slit of width w_2 results in a band pass with a base width of ΔE which is given by:

$$\Delta E = E_{pass} \left(\frac{w_1 + w_2}{2R} + \alpha^2 \right) \quad (\text{F. 4})$$

These considerations are only strictly valid in the dispersive direction of the analyzer and one would open the apertures in the non-dispersive direction for non-imaging spectroscopy. The situation changes for energy filtering of images. The angular and lateral spreads at the analyzer entrance correspond to angular and lateral apertures in the microscope column. The angular aperture defines the lateral resolution and one uses round apertures to have the same lateral resolution in both dispersive and non dispersive directions. The field of view imaged has also comparable sizes in both directions due to the lens bore geometry and matching to the circular image detector. Thus, the phase space accepted by the analyzer can be calculated as:

$$\Omega = \frac{\Delta E^3 R^2}{E_{pass}^2} \quad (\text{F. 5})$$

Fig. F.4 shows the maximum possible phase space as a function of pass energy (full lines) for three different analyzer energy resolutions and the analyzer entrance slit (dashed lines) needed to obtain it, calculated with Eq. (F.3) and (F.4). High transmission with good energy resolution is only possible at low pass energies.

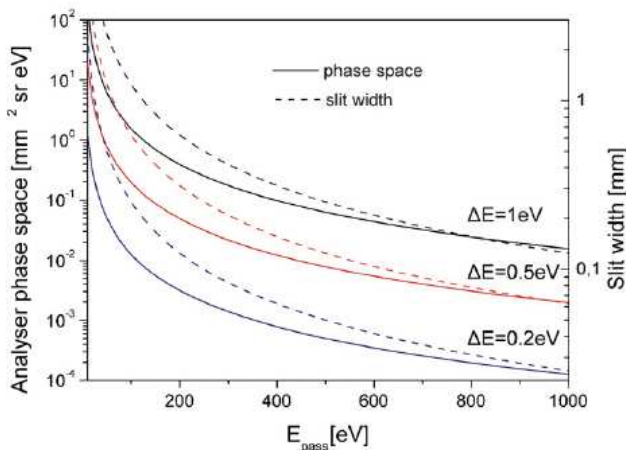


FIG. F.4. Calculated maximum phase space (solid lines) accepted by a hemispherical analyzer with $R = 125$ mm for three different energy resolutions ΔE using Eq. (F.5). The slit widths needed for a given energy resolution are shown as dashed lines. (From Ref. 7)

F.4.2 Spatial resolution

Considering the properties of the objective lens, the lateral resolution is limited by the electron optical aberrations. The objective lens of the NanoESCA, like in most photoelectron emission microscopes, is an immersion lens, i.e. the sample is immersed in a strong electrical field. This field accelerates the electrons into the focusing part of the lens and simultaneously reduces the axial angle of the electrons inside the lens. The bending of the electrons trajectories strongly reduces the amount of spherical and chromatic aberrations of the focusing lens but, simultaneously, aberrations of the extracting field are introduced. These field aberrations have been easily calculated analytically⁷ and depend mainly on the field strength at the sample surface. Moreover, the aperture's size can be reduced until diffraction at the aperture plays the dominant role, and resolution deterioration by diffraction have been also estimated analytically⁷. The total resolution of the objective lens can be approximated by the geometric mean of the size of the spherical and chromatic aberrations and diffraction discs. The calculated resolution in a case typical of core level XPS imaging is displayed in Fig. F.4 for electrons with a kinetic energy of 100 eV and an energy width of 0.5 eV for three different values of the extraction potential.

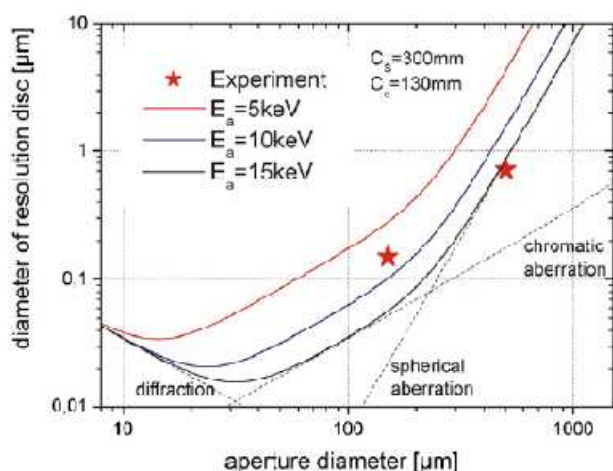


FIG. F.5. Calculated lateral resolution of the NanoESCA objective lens for electron with 100 eV kinetic energy. Two experimentally obtained values with 12 kV extractor voltage are marked with symbols. The contributions of diffraction, spherical and chromatic aberration for the highest extracting field are marked with dashed lines. (From Ref. 7)

A hemispherical analyzer also limits the lateral resolution of the microscope. To understand this behavior we will go into the details of the image transfer through the hemispheres. If a real image plane is introduced to the entrance plane of the hemispheres, the dispersion of the hemispherical field destroys the image at the exit plane whereas angles are preserved. To circumvent this problem a reciprocal image, i.e. an angular image plane, is used for energy filtering. The reciprocal image is created by a coupling lens in front of the analyzer. It is then transmitted through the analyzer and transferred back to a real image by an identical coupling lens behind the analyzer. The distance of the real image plane to the slit plane of the analyzer is twice the focal length f of the coupling lens. However, this setup is quite problematic in terms of aberrations. In

fact combining the coupling lens action with the focusing properties of the hemisphere, a mixing of the analyzer's α^2 term, dispersion and higher order terms with the lens action and spherical aberration of the coupling lenses lead to deterioration of the lateral resolution by first and second order terms in the angle α_i and energy spread ε (see Fig. F.6). This is not the case for the double hemispherical analyzer IDEA used by the NanoESCA. The second analyzer compensates the dispersion of the first analyzer, thus eliminating all dependence on the energy spread ε of the analyzer. Imaging of the double analyzer can be described as achromatic, leaving only the aberrations of the coupling lenses as additional terms.

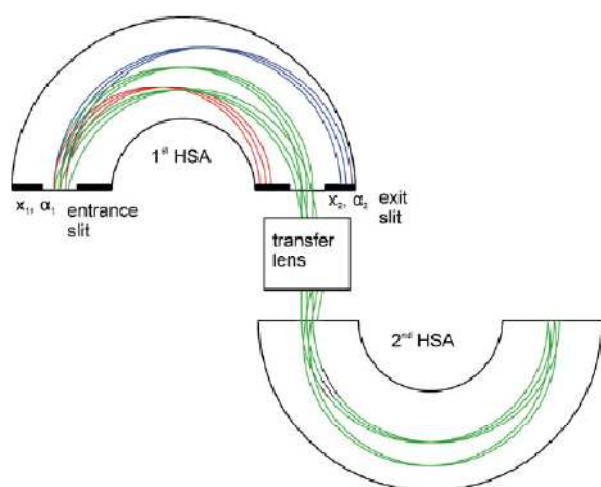


FIG. F.6. Scheme of the optical layout of the IDEA-Analyzer showing the two hemispheres and schematic electron trajectories. In the first hemisphere (left) the dispersive action on electron beams of different energy, shown in different color, is shown. The transfer lens transfers an reciprocal image at the exit of the first analyzer to the entrance of the second analyzer. The α^2 aberration of the first hemisphere can be seen for an off-axis image-point at the exit of the first analyzer and is compensated by the second analyzer. (From Ref. 7)

Bibliography

- ¹ X. de la Broise *et al.*, Appl. Phys. Lett. **76**, 3142 (2000)
- ² Thieme J, Rudolph D, Schmahl G and Umbach E (ed) 1996 *X-Ray Microscopy and Spectromicroscopy* (Berlin: Springer)
- ³ Quantera SXM, product information, Physical Electronics (ULVAC-PHI)
- ⁴ M. Escher, N. Weber, M. Merkel, C. Ziethen, P. Bernhard, G. Schonhense, S. Schmidt, F. Forster, F. Reinert, B. Kromker and D. Funnemann, J. Phys.: Condens. Matter **17** (2005) S1329–S1338
- ⁵ H. Luth, Solid Surfaces, Interfaces and Thin Films, Springer-Verlag, Fourth Edition
- ⁶ F. Reinert and S. Hufner, New J. Phys. **7**, 97 (2005)
- ⁷ M. Escher, K. Winkler, O. Renault, N. Barrett, Journal of Electron Spectroscopy and Related Phenomena **178–179** (2010) 303–316
- ⁸ J. Chmelik, L. Veneklasen, G. Marx, Optik **83** (1989) 155–160.
- ⁹ J. Feng, H. Padmore, D.H. Wei, S. Anders, Y. Wu, A. Scholl, D. Robin, Rev. Sci. Instr. **73**, 1514–1517 (2002).
- ¹⁰ B.P. Tonner, Nucl. Instr. Methods Phys. Res. A **291**, 60–66 (1990).

Panel G

X-Ray Diffraction

G.1 Introduction

In x-ray scattering, intensity distributions in reciprocal space are recorded instead of real-space images, and in most cases the interpretation of experimental data requires model assumptions and fitting routines. As in electron microscopy, the incident beam is diffracted. Due to the lack of x-ray lenses, however, it is not possible to form an image out of the diffraction pattern; the pattern itself is recorded. As only intensities can be measured, the phase information on scattered x rays is lost, which is certainly a drawback of the X-Ray Diffraction (XRD). The measurements usually require no special sample environment or preparation. The penetration depth of x rays between several nm and several hundred nm allows for the nondestructive investigation of both buried and surface structures. Choosing the proper scattering geometry, one can tune the penetration depth so that information is gained either about the surface or about the bulk. Different means of contrast can be used, e.g., differences in the refractive index are exploited in x-ray reflectivity and grazing-incidence small-angle x-ray scattering, while the strain fields are measured in coplanar x-ray diffraction and grazing-incidence diffraction. In fact, one particular strength of XRD is its very high sensitivity to the strain. In the following we first describe the basic principles of the x-ray diffraction from a crystalline sample, and then we discuss the x-ray reciprocal space mapping in case of Ge/Si heterostructures.

G.2 Basic Principles¹

A sketch of a scattering geometry is shown in Fig. G.1. Commonly, the intensity distribution of an x-ray scattering experiment is plotted in *reciprocal space*, i.e., the space spanned by the momentum transfer between incident radiation with wave vector \mathbf{k}_i and scattered radiation with wave vector \mathbf{k}_f : $\mathbf{Q} = \mathbf{k}_f - \mathbf{k}_i$ (scattering vector). Here we consider elastic scattering with $|\mathbf{k}_f| = |\mathbf{k}_i| = k = 2\pi/\lambda$, where λ is the x-ray wavelength. As the penetration depth is considerably smaller than the sample dimensions, only radiation with positive incident and exit angles α_{if} can be used in the reflection geometry, the so-called Bragg case. This puts restrictions on the accessible range in reciprocal space, indicated by the three half spheres in the Fig. G.1. The outer half sphere, with a

radius of $2k$, marks the limit due to the maximum scattering angle of $2\theta = \pi$ (backscattering). In the Bragg case, only the region between the large half sphere and the two small half spheres is accessible, as for \mathbf{Q} within the latter either α_i or α_f becomes negative. These regions, the so-called *Laue zones*, are accessible only in transmission. Note that the orientation of the x axis is always along the projection of \mathbf{k}_i into the xy plane. A review of especially surface-sensitive x-ray diffraction techniques was presented by Robinson and Tweet². The characterization of self-assembled nanostructures by diffuse x-ray scattering has been reviewed by Schmidbauer, Hanke, and Köhler³.

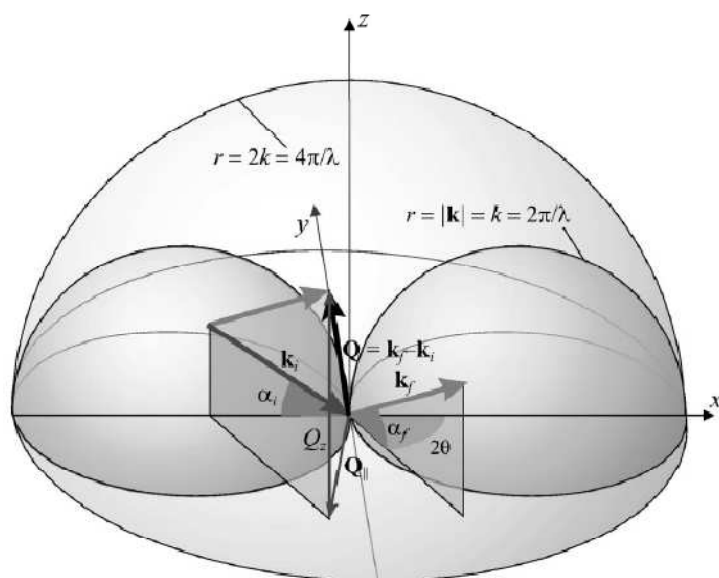


FIG. G.1. Reciprocal space sketch of a generic x-ray scattering experiment in reflection geometry (From Ref. 1).

G.3 Reciprocal space mapping of a Ge/Si(001) system⁴

Fig. G.2 shows a plane of the reciprocal lattice of a fully relaxed Ge layer on a unstrained Si substrate. The plane of diffraction is defined by the incident and diffracted x-ray beams which are chosen to lie in the plane determined by the two crystallographic [001] and [110] directions. The two small half-circles (Laue zones, radius π/λ) and the large one (radius $2\pi/\lambda$) indicate the limits of accessibility for the diffractometric measurements in the Bragg (reflection) geometry. The Ewald sphere construction is shown for the Si(115) high incidence reflection. The Bragg condition is fulfilled when the diffraction vector \mathbf{Q} equals a reciprocal lattice vector. The incidence angle ω is defined as that between the incident (\mathbf{k}_{inc}) beam and the sample surface, and the angle 2θ is that between the incident and the diffracted (\mathbf{k}_{diff}) beams.

Three possible scan directions, i.e., the $\omega/2\theta$ (“a”), the ω - (“b”), and the 2θ - (“c”) scan directions, as depicted in Fig. G.2. An ideal diffractometer collects intensity transversal in reciprocal space (arrow “b”) along a circle with center in (000), the origin of the reciprocal lattice, if

the sample is rotated, i.e., if ω is changed (ω -scan direction). If the detector is moved with the sample position being fixed (i.e., the angle 2θ changes), intensity will be collected along the Ewald sphere (arrow “c”, 2θ -scan direction). Finally, if the detector is rotated twice as fast around the diffractometer axis as the sample, the scan direction in reciprocal space is radial from (000) (arrow “a”, $\omega/2\theta$ -scan direction). Reciprocal space mapping is usually done by making a series of $\omega/2\theta$ scans at different ω settings. It is worth noting that in the 2D CCD image acquired at a given ω by the Maxipix detector used for the nanofocused XRD experiment at ID13 beamline of ESRF, different pixels along the horizontal axis of the detector corresponds to different 2θ values (arrow “c”).

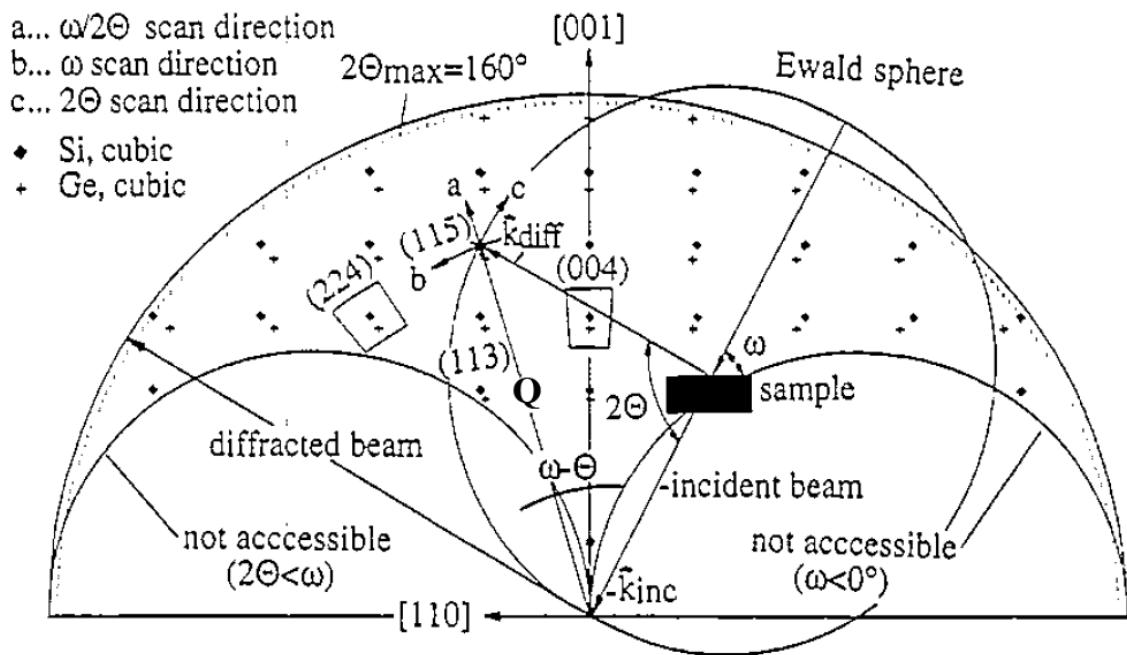


FIG. G.2. Schematic representation of the reciprocal space lattice points (RELPs) of fully relaxed [001] oriented Si (full diamonds) and Ge (+) accessible by XRD in the diffraction plane in reciprocal space with [110] azimuth.

For the strain analysis one needs to map the regions marked in Fig. G.2 by measuring a sets of $\omega/2\theta$ scans at different ω positions in the vicinity of the symmetrical (004) and asymmetrical (224) reciprocal lattice points (RELPs) originating from the layer of interest. The substrate is assumed to be unstrained, and from the relative position of the substrate and the layer RELP maxima in this two maps, one directly obtains the in-plane (a_p) and out-of-plane (a_n) lattice constants of the layer as described in Fig. G.3. The distance between a layer RELP maximum and the origin (000) along the direction [110] is inversely proportional to the in-plane lattice constant. If a Ge layer, which has a larger lattice parameter than that of Si substrate, is grown pseudomorphically, i.e., tetragonally distorted (Ge^{pseu} in Fig. G.3), it has the same in-plane lattice constant as the substrate. Its RELP maximum lies underneath that of the Si substrate along the growth direction [001] both in the

symmetric and asymmetric reciprocal maps. In the other extreme, if the Ge layer is fully relaxed and cubic (Ge^{rel} in Fig. G.3), asymmetrical lattice planes of layer and substrate are parallel to each other, and the layer RELP maximum lies underneath that of the substrate along the direction $[hkl]$ through the (hkl) substrate RELP maximum as shown in Fig. G.3. Obviously a partially relaxed Ge layer gives rise to a RELP located in between these two extreme positions of substrate and layer RELPS described above (bold arrows in Fig. G.3).

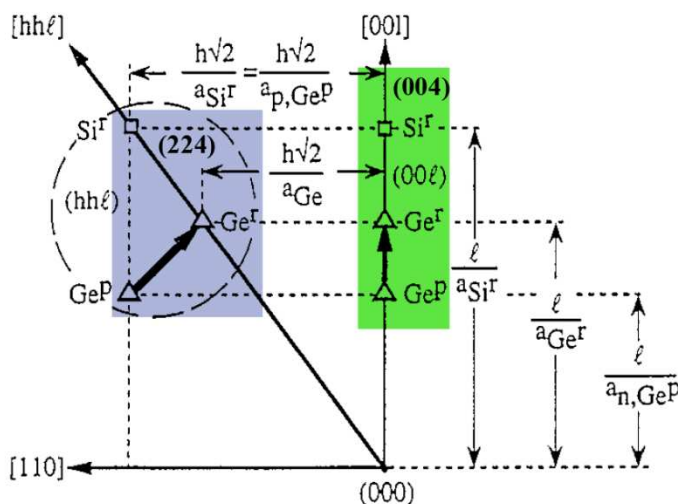


FIG. G.3. Schematic representation of correlation between distances in the reciprocal space and lattice constants along and perpendicular the $[001]$ growth directions for pseudomorphic and fully relaxed Ge on Si. The colored zones defines the reciprocal space regions explored by the symmetric (004) and asymmetric (224) reflections.

From the angular positions of the layer peaks in the reciprocal space maps, the reciprocal lattice vector components $b_{[001]}$ and $b_{[110]}$ of the layer can be calculated⁵:

$$b_{[001]} = \frac{2}{\lambda} \sin \Theta \cos(\omega - \Theta) \quad \text{and} \quad b_{[110]} = \frac{2}{\lambda} \sin \Theta \sin(\omega - \Theta)$$

For the (001) surface and in case of the symmetrical (004) reflection only $b_{[001]} = 4/a_n$ can be determined, while in case of the asymmetrical (224) reflection the two reciprocal lattice vector components corresponds to $b_{[001]} = 4/a_n$ and $b_{[110]} = 2\sqrt{2}/a_p$.

Bibliography

- ¹ J. Stangl, V. Holy, G. Bauer, Reviews of Modern Physics **76** (2004)
- ² Robinson, I. K., and D. J. Tweet, Rep. Prog. Phys. **55**, 599 (1992)
- ³ Schmidbauer, M., M. Hanke, and R. Köhler, Cryst. Res. Technol. **36**, 1 (2002).
- ⁴ G. Bauer, J. Li, E. Koppensteiner, J. Cryst. Growth **157** 61-61 (1995)
- ⁵ E. Koppensteiner, G. Bauer, H. Kibbel and E. Kaspel, Appl. Phys. Lett. **76** 3489 (1994)

Acknowledgements



Politecnico di Milano
A. Tagliaferri; M. Zani



Università Milano-Bicocca
E. Bonera; F. Montalenti



École Polytechnique, Paris
H.-J. Drouhin; G. Rizza;
M. Chaigneau; R. Ossikovski



IMM-CNR Catania
G. Nicotra



Università Roma Tre
G. Capellini



L-NESS (Como)
M. Bollani; D. Chrastina
G. Isella; J. Osmond;
R. Sordan



CEA
N. Barrett; O. Renault;
M. Lavayssière



SOLEIL
F. Sirotti; M. Silly



ESRF
M. Burghammer;
S. Schoeder

First and foremost I want to thank my advisor Alberto Tagliaferri. He has taught me, both consciously and un-consciously, how good experimental physics is done. I appreciate all his contributions of time, ideas, and expertise to make my PhD experience productive and stimulating. A special thank goes to Maurizio Zani for his continuous support. The joy and enthusiasm he has for the experimental research was contagious and motivational for me.

I would like to acknowledge the Prof. Henri-Jean Drouhin to have given me the possibility to work for several months at the Ecole Polytechnique. A special thank goes to Marc Chaigneau and to the Prof. Razvigor Ossikovski for the opportunity to work with them in their group. Thanks to Giancarlo Rizza and Pierre-Eugene Coulon for their continuous availability and their experimental abilities.

I am very grateful to Nick Barrett for his capacity to instill enthusiasm, for the ability to share his knowledge and for believe in me, and to all members of the XPEEM group at the CEA: Maylis Lavayssiere, Claire Mathieu, Jocelyne Leroy, Bruno Delomez, and Olivier Renault. The group has been a source of friendships as well as good advice and collaboration.

Many of the studies discussed in this thesis would not have been possible without the high-quality samples from the SiGe epitaxy group of the LNESS laboratory, and a special thanks goes to Giovanni Isella, Johann Osmond, Monica Bollani, Danny Chrastina, and Davide Colombo.

A special thank goes to Francesco Montalenti, Giovanni Capellini and Giuseppe Nicotra for their ideas, support, expertise, optimism, and for all the fruitful discussions and the time spent with me.

I would like also to acknowledge the Prof. Franco Ciccacci, the coordinator of my Ph.D. course, for his affection for the students, and the Prof. Ezio Puppini to have suffered me as his neighbor.

Thanks to everybody working at the Department of Physics, and especially the PhD students of the XXIII cycle (Marco Moretti, Federico Ferrari, Laura Cattaneo, Matteo Savoini, Marco Donolato, Michele Garbugli, Marta Mroz) to have shared with me all the official moments of this PhD.

A very special thank goes to the many funny and good friends I have been fortunate to come across, without whom life would be bleak.

I wish to thank my great family: Mamma, Papà, Davide, Nonna Maruccella, Zia Luisa, Zio Piero and Zia Liliana, Zia Pina and Zio Raffaele, Zio Salvatore and Zia Annamaria, Zia Anna and Zio Salvatore, Raffaella (and Marco), Raffaele, Alfonso, Mariella, Antonella, Eleonora, Marianna, Zia Emilia, Zia Nina, Zia Carmela, Zia Teresa and Zio Dino, Aurora and Andrea, Irma and Marco, Manuel and Elena, Sara and Christian, Daniele, Gianni, Enrico, Settimio and Gilda, Fabrizio,

Giovanna and MariaAdele, Gianni and Dacia, Doris and Johnny. Without their continuous support all the important goals I have reached in my life would not have been possible. I would like to thank them for their patience and sympathy, even during the most difficult periods. Moreover, a special thought goes to Nonno Raffaele, Nonno Giovanni, Zia Angelina, Zio Ciccio, Nonna Maria, Nonna Margherita and Stefano because I'm sure that you have been and you will be always with me.

Thanks to Alfredo, Maria Lucia, Vincenzo and Alessandra, to be the new part of my family, I appreciate a lot your love.

Finally, the most special thank goes to Milena, friend and lover.

Gianmaria

List of publications

November 2010

G. M. Vanacore, G. Nicotra, M. Zani, M. Bollani, E. Bonera, G. Capellini, G. Isella, F. Montalenti, J. Osmond, A. Picco, and A. Tagliaferri, *Delayed plastic relaxation in SiGe islands grown by Surface Thermal Diffusion on Si(001)*, submitted to Phys. Rev. B

D. Chrastina, **G. M. Vanacore**, M. Zani, M. Bollani, S. Schöder, M. Burghammer, P. Boye, G. Isella, R. Sordan, and A. Tagliaferri, *Nano-scale strain relief in lithographically defined SiGe nano-structures studied by Nano-Beam X-Ray Diffraction*, to be submitted

August 2010

G.M. Vanacore, M. Zani, M. Bollani, D. Colombo, G. Isella, J. Osmond, R. Sordan, and A. Tagliaferri, *Size evolution of ordered SiGe islands grown by surface thermal diffusion on pit-patterned Si(100) surface*, Nanoscale Res. Lett. **5** (2010) 1921 – 1925

M. Bollani, E. Bonera, D. Chrastina, A. Fedorov, V. Montuori, A. Picco, A. Tagliaferri, **G.M. Vanacore** and R. Sordan, *Ordered Arrays of SiGe Islands from Low-Energy PECVD*, Nanoscale Res. Lett. **5** (2010) 1917 – 1920

G.M. Vanacore, M. Zani, G. Isella, J. Osmond, M. Bollani, and A. Tagliaferri, *Quantitative investigation of the influence of carbon surfactant on Ge surface diffusion and island nucleation on Si(100)*, Physical Review B **82**, 125456 (2010)

G.M. Vanacore, L.F. Zagonel, and N. Barrett, *Surface enhanced covalency and Madelung potentials in Nb doped SrTiO₃ (100), (110) and (111) single crystals*, Surface Science **604** (2010) 1674-1683

August 2009

A. Pancotti, N. Barrett, L. F. Zagonel, and **G. M. Vanacore**, *Multiple scattering x-ray photoelectron diffraction study of the SrTiO₃(100) surface*, Journal of Applied Physics **106**, 034104 (2009).

June 2009

F. Ghezzi, M. Zani, S. Magni, **G.M. Vanacore**, A. Tagliaferri, *Surface and bulk modification of W-La₂O₃ armor mock-up*, Journal of Nuclear Materials **393** (2009) 522–526.